VOLUME 81 APRIL 7, 1977 NUMBER 7

JPCHAx

THE JOURNAL OF PHYSICAL CHEMISTRY

PUBLISHED BIWEEKLY BY THE AMERICAN CHEMICAL SOCIETY

THE JOURNAL OF

PHYSICAL CHEMISTRY

Published by the
AMERICAN CHEMICAL SOCIETY
BOOKS AND JOURNALS DIVISION
D. H. Michael Bowen, Director
Marjorie Laflin, Assistant to the Director

Editorial Department: Charles R. Bertsch, Head; Marianne C. Brogan, Associate Head; Celia B. McFarland, Joseph E. Yurvati, Assistant Editors
Magazine and Production Department: Bacil Guiley, Head
Research and Development Department: Seldon W. Terrant, Head

Advertising Office: Centcom, Ltd., 50 W. State St., Westport, Conn. 06880.

Published biweekly by the American Chemical Society at 20th and Northampton Sts., Easton, Pennsylvania 18042. Second class postage paid at Washington, D.C. and at additional mailing offices.

Editorial Information

Instructions for authors are printed in the first issue of each volume. Please conform to these instructions when submitting manuscripts.

Manuscripts for publication should be submitted to *The Journal of Physical Chemistry*, Department of Chemistry, University of Minnesota, Minneapolis, Minn. 55455. Correspondence regarding **accepted papers and proofs** should be directed to the Editorial Department at the ACS Easton address.

Page charges of $60.00 per page may be paid for papers published in this journal. Ability to pay does not affect acceptance or scheduling of papers.

Bulk reprints or photocopies of individual articles are available. For information write to Business Operations, Books and Journals Division at the ACS Washington address.

Requests for **permission to reprint** should be directed to Permissions, Books and Journals Division at the ACS Washington address. The American Chemical Society and its Editors assume no responsibility for the statements and opinions advanced by contributors.

Subscription and Business Information

1977 Subscription rates—including surface postage

	U.S.	PUAS	Canada, Foreign
Member	$24.00	$33.00	$34.00
Nonmember	96.00	105.00	106.00
Supplementary material	15.00	19.00	20.00

Air mail and air freight rates are available from Membership & Subscription Services, at the ACS Columbus address.

New and renewal subscriptions should be sent with payment to the Office of the Controller at the ACS Washington address. **Changes of address** must include both old and new addresses with ZIP code and a recent mailing label. Send all address changes to the ACS Columbus address. Please allow six weeks for change to become effective. **Claims for missing numbers** will not be allowed if loss was due to failure of notice of change of address to be received in the time specified: if claim is dated (a) North America—more than 90 days beyond issue date, (b) all other foreign—more than 1 year beyond issue date; or if the reason given is "missing from files". Hard copy claims are handled at the ACS Columbus address.

Microfiche subscriptions are available at the same rates but are mailed first class to U.S. subscribers, air mail to the rest of the world. Direct all inquiries to Special Issues Sales, at the ACS Washington address or call (202) 872-4554. **Single issues** in hard copy and/or microfiche are available from Special Issues Sales at the ACS Washington address. Current year $4.75. Back issue rates available from Special Issues Sales. **Back volumes** are available in hard copy and/or microform. Write to Special Issues Sales at the ACS Washington address for further information. **Microfilm** editions of ACS periodical publications are available from volume 1 to the present. For further information, contact Special Issues Sales at the ACS Washington address. **Supplementary material** mentioned in the journal appears in the microfilm edition. Single copies may be ordered directly from Business Operations, Books and Journals Division, at the ACS Washington address.

	U.S.	PUAS, Canada	Other Foreign
Microfiche	$2.50	$3.00	$3.50
Photocopy			
1–7 pages	4.00	5.50	7.00
8–20 pages	5.00	6.50	8.00

Orders over 20 pages are available only on microfiche, 4 × 6 in , 24X, negative, silver halide. Orders must state photocopy or microfiche if both are available. Full bibliographic citation including names of all authors and prepayment are required. Prices are subject to change.

American Chemical Society
1155 16th Street, N.W.
Washington, D.C. 20036
(202) 872-4600

Member & Subscription Services
American Chemical Society
P.O. Box 3337
Columbus, Ohio 43210
(614) 421-7230

Editorial Department
American Chemical Society
20th and Northampton Sts.
Easton, Pennsylvania 18042
(215) 258-9111

Notice to Authors last printed in the issue of January 13, 1977

THE JOURNAL OF

PHYSICAL CHEMISTRY

Volume 81, Number 7 April 7, 1977

JPCHAx 81(7) 593–686 (1977)

ISSN 0022-3654

COMMUNICATIONS TO THE EDITOR

■ Supplementary and/or miniprint material for this paper is available separately (consult the masthead page for ordering information); it will also appear following the paper in the microfilm edition of this journal.

* In papers with more than one author, the asterisk indicates the name of the author to whom inquiries about the paper should be addressed.

AUTHOR INDEX

THE JOURNAL OF
PHYSICAL CHEMISTRY

VOLUME 81, NUMBER 7 APRIL 7, 1977

Kinetics of Symmetric Proton Transfer Reactions in Alcohols and Amines by Ion Cyclotron Resonance Spectroscopy. Relaxation Mechanisms for Epithermal Ion Energy Distributions

T. B. McMahon[1] and J. L. Beauchamp*[2a]

Arthur Amos Noyes Laboratory of Chemical Physics,[2b] California Institute of Technology, Pasadena, California 91125 *(Received January 3, 1977)*

Rates of symmetric proton transfer have been measured for a number of simple aliphatic alcohols and amines both by the conventional ion cyclotron resonance intensity vs. pressure methods and using trapped-ion techniques. For the systems studied symmetric proton transfer was found to be very fast, occurring essentially at the ion–molecule encounter rate. The implications of the speed of these reactions with respect to the relaxation of epithermal ion energy distributions is discussed.

Introduction

Numerous factors can frequently lead to production of nonthermal energy distributions for gas phase ions. A substantial fraction of ions formed by electron impact or photoionization above the adiabatic ionization threshold will often possess considerable internal excitation. In some cases ions may be subjected to accelerating fields which lead to varying degrees of translational excitation dependent on the nature of the experimental apparatus. In formation of fragment ions considerable translational energy may be released from dissociation of the excited parent ion, particularly if the ionization occurs by a transition to a repulsive electronic state of the ion. In addition, product ions resulting from exothermic ion–molecule reactions may possess a substantial fraction of the exothermicity of reaction as internal and translational excitation. Haney and Franklin[3] have recently examined the partitioning of excess energy between translational and internal degrees of freedom for both fragmentation processes and ion–molecule reactions and have found that vibrational excitation of fragment and product ions may be appreciable.

Experimental observations have shown that most ion–molecule reactions are efficient, with reaction often taking place on every collision which brings the reactants in close contact. Thus, in the absence of a nonreactive diluent gas excess internal and translational excitation will not be relaxed prior to reaction. Hence most observed processes are not representative of thermal ion energy distributions.

Failure to thermalize reactant ions is of particular concern in cases where thermochemical inferences are made from the preferred direction of reaction or in favorable cases from equilibrium constants for reversible bimolecular ion–molecule reactions.[4] This concern is justified on the basis of disagreements which exist in the literature for thermochemical quantities determined by different investigators using different experimental conditions and, possibly, different ion energy distributions. It is thus important to determine the conditions which promote rapid thermalization of gas phase ions.

General agreement among various research groups using different experimental techniques has been obtained for alkylamine basicities.[5] This lends support to the conjecture that highly accurate thermochemical data may be derived from gas phase proton transfer equilibria measurements of the type generalized by

$$B_1H^+ + B_2 \rightleftarrows [B_1HB_2^+]^* \rightleftarrows B_1 + B_2H^+ \qquad (1)$$

where B_1 and B_2 represent n-donor bases. It has recently been demonstrated that symmetric proton transfer reactions of the form of eq 1 where B_1 and B_2 are identical, may be an efficient means of relaxing excited ions.[6]

Considerable experimental evidence suggests that proton transfer reactions proceed via an intermediate proton bound dimer as indicated in eq 1.[7] This intermediate may dissociate with the labile proton bound to either of the n-donor bases involved. If the intermediate has a lifetime which is short relative to the time scale for redistribution of vibrational energy then the neutral product, B_1, for reaction 1 proceeding to the right, will carry off the bulk of the excess energy in a single proton transfer event. If the lifetime of the proton bound dimer is long compared to the time for redistribution of vibrational energy then dissociation of the intermediate will likely involve partitioning of the excess energy between the ionic and neutral fragments based on statistical considerations involving the relative numbers of degrees of freedom in the products. In either case it is apparent that symmetric proton transfer reactions in which an n-donor base interacts with its own conjugate acid will provide an efficient means of thermalizing reactant ions if such processes are fast.

For a partially deuterated species MH_n where n hydrogens are directly bonded to the n-donor site it is often observed that the parent ion MH_n^+ reacts with the parent neutral to form MH_nD^+. This species in turn undergoes the reaction

$$MH_nD^+ + MH_n \rightarrow MH_{n+1}^+ + MH_{n-1}D \quad (2)$$

resulting in the disappearance of labile deuterium in the conjugate acid. For example, methanol-d_3, CD_3OH, undergoes reactions 3 and 4 with the product of reaction 4

$$CD_3OH^+ + CD_3OH \rightarrow CD_3OH_2^+ + CD_3O \quad (3)$$

$$CD_3OH^+ + CD_3OH \rightarrow CD_3OHD^+ + CD_2OH \quad (4)$$

$$CD_3OHD^+ + CD_3OH \rightarrow CD_3OH_2^+ + CD_3OD \quad (5)$$

$$CD_3OH_2^+ + CD_3OH \rightarrow (CD_3)_2OH^+ + H_2O \quad (6)$$

subsequently being consumed in reaction 5. Sieck, Abramson, and Futrell[8] have noted that labile deuterium does not appear in a product of condensation reaction such as reaction 6 indicating that the symmetric proton transfer reaction 5 is fast compared to protonated dimethyl ether formation (6).

Munson[9] has also studied the generalized process 2 for deuterated ammonium ions. Reaction 7, in which NH_3D^+

$$NH_3D^+ + NH_3 \rightarrow NH_4^+ + NH_2D \quad (7)$$

is formed by deuteron transfer employing CD_4 as a chemical ionization reagent, was found to be relatively fast ($k_7 = 1 \times 10^{-9}$ cm^3 molecule^{-1} s^{-1}). This compares favorably with our own value of $k_8 = 1.2 \times 10^{-9}$ cm^3 molecule^{-1} s^{-1} for reaction 8[10] determined using trapped-ion ICR ion

$$^{14}NH_4^+ + {}^{15}NH_3 \rightleftharpoons {}^{15}NH_4^+ + {}^{14}NH_3 \quad (8)$$

ejection techniques. Related and more extensive studies have been reported by Harrison and co-workers.[10] Using CD_4 as a reagent gas they examined symmetric proton transfer reactions involving NH_3, CH_3NH_2, $(CH_3)_2NH$, CD_3OH, and CH_3SH.

In the present study we report kinetic data for reactions analogous to reaction 5 for specifically labeled methanol, ethanol, methylamine, and dimethylamine as well as reactions and rate constants for accompanying processes. The site specificity of processes analogous to reactions 3 and 4 is analyzed for the first time in several of the systems studied. Rate constants are derived both by consideration of the variation of ion abundance with pressure[12] and the variation of ion abundance with time at fixed pressure in trapped-ion ICR experiments.[13] The results are discussed in terms of models for proton transfer and the implications arising for the deexcitation of protonated n-donor bases are considered.

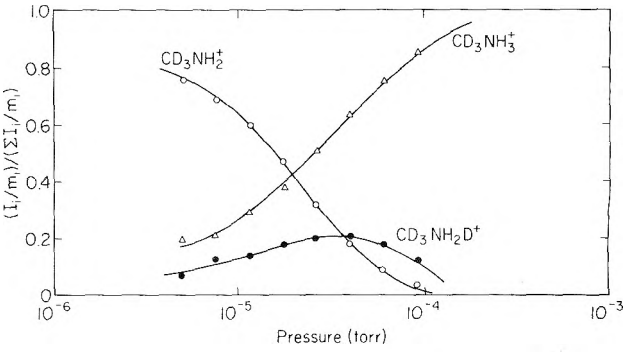

Figure 1. Variation of ion abundance with pressure for CD_3NH_2 at 11.0 eV. The solid line indicates the variation of ion intensity with pressure calculated from the average rate constant obtained from several determinations. The points indicate experimentally determined intensities.

Experimental Section

All experiments in this study were carried out at ambient temperature (23 °C) on a Varian Instruments V-5900 ICR spectrometer modified to permit trapped-ion experiments to be carried out routinely. Pressures below 10^{-5} Torr were monitored using an ionization gauge of the Shulz–Phelps design.[14] Above 10^{-5} Torr absolute pressures were measured by an MKS Instruments Baratron capacitance manometer which also permitted calibration of the ionization gauge. Rate constants from trapped-ion spectra were obtained from semilogarithmic plots of relative ion abundance vs. time. Rate constants from intensity vs. pressure data were calculated by iterative computer solution to the ICR power absorption equations formulated by Marshall and Buttrill.[12] The Marshall–Buttrill equations treat the case of a single primary ion reacting to produce several secondary ions which each may subsequently react to form different tertiary ions. Complications arise in the kinetic analysis when an ion may be both a secondary and a tertiary ion (for example, $CD_3OH_2^+$ in reactions 3 and 5). In this, and related cases, the different contributions to $CD_3OH_2^+$ were analyzed separately in computations of rate constants but were summed to compare calculated to observed ion intensities. The set of rate constants reported for each system are those which give the best fit of calculated to observed intensity vs. pressure data.

Methylamine-d_3 and dimethylamine-d_6 were obtained from Merck Sharpe and Dohme of Canada Ltd. Methanol-d_3 and ethanol-d_5 were prepared by refluxing the fully deuterated analogues, obtained from Merck Sharpe and Dohme of Canada Ltd., with magnesium turnings to produce the dialkoxy magnesium salts. These salts were subsequently treated with H_2O and distilled to obtain the exchanged alcohols. All samples were routinely degassed by bulb-to-bulb distillation. Analysis by mass spectrometry indicated the isotopic purity to be greater than 99 atom % D at the labeled sites.

Results

1. *Methylamine.* At sufficiently low electron energies only the parent ion of methylamine is formed. In the case of CD_3NH_2 this species undergoes reactions 9 and 10

$$CD_3NH_2^+ + CD_3NH_2 \rightarrow CD_3NH_3^+ + CD_3NH \quad (9)$$

$$CD_3NH_2^+ + CD_3NH_2 \rightarrow CD_3NH_2D^+ + CD_2NH_2 \quad (10)$$

producing $CD_3NH_3^+$ and $CD_3NH_2D^+$, respectively. It can be seen from the variation of ion abundance with both

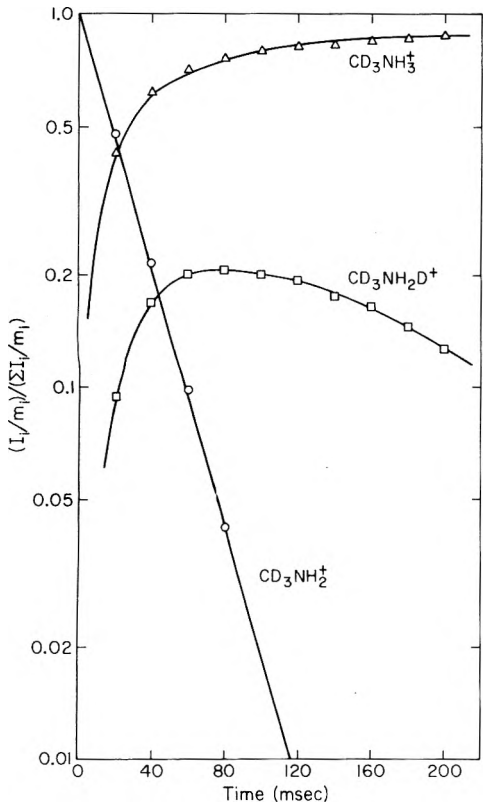

Figure 2. Variation of ion abundance with time for CD_3NH_2 at 12.0 eV and 6.5 × 10^{-7} Torr with a 6-ms electron beam pulse.

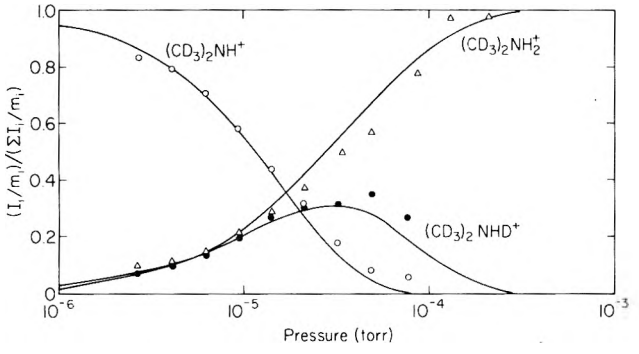

Figure 3. Variation of ion abundance with pressure for $(CD_3)_2NH$ at 11.0 eV. The solid line indicates the variation of ion intensity with pressure calculated from the average rate constant obtained from several determinations. The points indicate experimentally determined intensities.

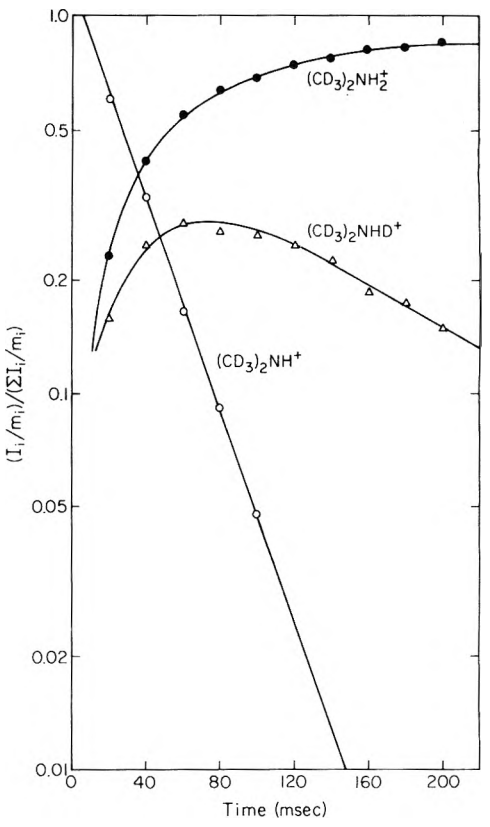

Figure 4. Variation of ion abundance with time for $(CD_3)_2NH$ at 10.5 eV and 7.5 × 10^{-7} Torr with a 6-ms electron beam pulse.

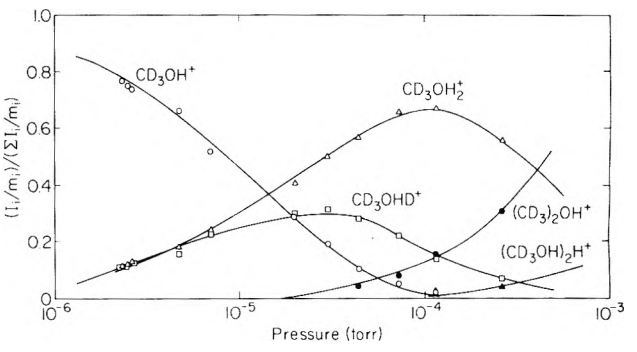

Figure 5. Variation of ion abundance with pressure for CD_3OH at 11.0 eV. The solid line indicates the variation of ion intensity with pressure calculated from the average rate constant obtained from several determinations. The points indicate experimentally determined intensities.

pressure (Figure 1) and time (Figure 2) that the ratio of $CD_3NH_3^+$ to $CD_3NH_2D^+$ is not constant as the reaction sequence progresses. The deuterated species is converted to the protonated ion by the symmetric proton transfer reaction

$$CD_3NH_2D^+ + CD_3NH_2 \rightarrow CD_3NH_3^+ + CD_3NHD \quad (11)$$

Rate constants for reactions 9–11 as well as the rate constant for formation of $CH_3NH_3^+$ from CH_3NH_2 are summarized in Table I. Included for comparison are available literature data for these reactions.

2. *Dimethylamine.* Reactions 12–14 are observed for

$$(CD_3)_2NH^+ + (CD_3)_2NH \begin{cases} \rightarrow (CD_3)_2NH_2^+ + (CD_3)_2N & (12) \\ \rightarrow (CD_3)_2NHD^+ + CD_3NHCD_2 & (13) \end{cases}$$

$$(CD_3)_2NHD^+ + (CD_3)_2NH \rightarrow (CD_3)_2NH_2^+ + (CD_3)_2ND \quad (14)$$

$(CD_3)_2NH$ in direct analogy with the related processes occurring in methylamine. Rate constants for reactions 12–14 as determined from the variation of ion abundance with pressure (Figure 3) and time (Figure 4) are summarized in Table I together with data for the unlabelled species.

3. *Methanol.* The ion–molecule reactions of simple alcohols are slightly more complex than those for alkylamines due to formation of protonated dialkyl ethers by nucleophilic displacement reactions.[15-17] The sequence of reactions 3–6 is apparent in the variation of ion abundance with pressure (Figure 5) and time (Figure 6). In the trapped-ion experiment it was necessary to operate at slightly higher electron energy resulting in the production of CD_2OH^+ as well as the parent ion. This species reacts exclusively by proton transfer to form $CD_3OH_2^+$. Proton bound dimer formation is also observed at pressures above 10^{-4} Torr (Figure 5). The absence of the proton bound dimer in the trapped ion data of Figure 6 indicates that collisional stabilization of the excited intermediate formed in the reaction of $CD_3OH_2^+$ with CD_3OH is required to observe this species. Rate constants for ion–molecule

TABLE I: Rate Constants for Ion-Molecule Reactions of Simple Alcohols and Amines

Reaction	Rate constant ($\times 10^{10}$ cm^3 molecule^{-1} s^{-1}) This work: Intensity vs. pressure	This work: Intensity vs. time	Other
1. Methylamine			
$CH_3NH_2^+ + CH_3NH_2 \rightarrow CH_3NH_3^+ + CH_4N$	20.6	16.4	21.0,[a] 9 ± 1,[b] 16,[c] 12.2,[d] 12.1[d]
$CD_3NH_2^+ + CD_3NH_2 \rightarrow CD_3NH_3^+ + CD_3NH$	12.2	18.9	
$CD_3NH_2^+ + CD_3NH_2 \rightarrow CD_3NH_2D^+ + CD_2NH_2$	5.8		
$CD_3NH_2D^+ + CD_3NH_2 \rightarrow CD_3NH_3^+ + CD_3NHD$	4.8	3.1	6.4 ± 0.2[e]
2. Dimethylamine			
$(CH_3)_2NH^+ + (CH_3)_2NH \rightarrow (CH_3)_2NH_2^+ + C_2H_6N$	14.9	12.8	12,[a] 6 ± 1,[b] 11.6,[d] 10.2,[d] 10.2[d]
$(CD_3)_2NH^+ + (CD_3)_2NH \rightarrow (CD_3)_2NH_2^+ + (CD_3)_2N$	7.5	13.5	
$(CD_3)_2NH^+ + (CD_3)_2NH \rightarrow (CD_3)_2NHD^+ + CD_3NH(CD_2)$	7.0		
$(CD_3)_2NHD^+ + (CD_3)_2NH \rightarrow (CD_3)_2NH_2^+ + (CD_3)_2ND$	3.4	2.8	3.1 ± 0.2[f]
3. Methanol			
$CH_3OH^+ + CH_3OH \rightarrow CH_3OH_2^+ + CH_3O$	21.7	20.8	25.3[g]
$CH_3OH_2^+ + CH_3OH \rightarrow (CH_3)_2OH^+ + H_2O$	1.0	1.1	
$CD_3OH^+ + CD_3OH \rightarrow CD_3OH_2^+ + CD_3D$	12.7	24.0	9.9[g]
$CD_3OH^+ + CD_3OH \rightarrow CD_3OHD^+ + CD_2OH$	14.6		12.0[g]
$CD_3OHD^+ + CD_3OH \rightarrow CD_3OH_2^+ + CD_3OD$	4.4	4.2	4.0 ± 0.5[h]
$CD_3OH_2^+ + CD_3OH \rightarrow (CD_3)_2OH_2^+ + H_2O$	1.5	1.3	
4. Ethanol			
$CH_3CH_2OH^+ + CH_3CH_2OH \rightarrow CH_3CH_2OH_2^+ + C_2H_5O$		17.8	
$CH_3CHOH^+ + CH_3CH_2OH \rightarrow CH_3CH_2OH_2^+ + CH_3CHO$		11.2	
$CH_3CH_2OH_2^+ + CH_3CH_2OH \rightarrow (CH_3CH_2)_2OH^+ + H_2O$	~2.2	2.4	
$CD_3CD_2OH^+ + CD_3CD_2OH \rightarrow CD_3CD_2OH_2^+ + CD_3CD_2O$		13.6	
$CD_3CD_2OH^+ + CD_3CD_2OH \rightarrow CD_3CD_2OHD^+ + CD_3CDOH$			
$CD_3CDOH^+ + CD_3CD_2OH \rightarrow CD_3CD_2OH_2^+ + CD_3CDO$		10.4	12.0[i]
$CD_3CD_2OHD^+ + CD_3CD_2OH \rightarrow CD_3CD_2OH_2^+ + CD_3CD_2OD$	~3.7	2.8	
$CD_3CD_2OH_2^+ + CD_3CD_2OH \rightarrow (CD_3CD_2)_2OH^+ + H_2O$	~1.7	1.4	

[a] M. S. B. Munson, *J. Phys. Chem.*, 70, 2034 (1966). [b] E. G. Jones and A. G. Harrison, *Can. J. Chem.*, 45, 3119 (1967). [c] M. J. Henchman, *Discuss. Faraday Soc.*, 39, 63 (1965). [d] L. Hellner and L. W. Sieck, *Int. J. Chem. Kinet.*, 5, 177 (1973). [e] Reference 10 (rate constant reported for $CH_3NH_2D^+$). [f] Reference 10 (rate constant reported for $(CH_3)_2NHD^+$). [g] S. K. Gupta, E. G. Jones, A. G. Harrison, and J. J. Myher, *Can. J. Chem.*, 45, 3107 (1967). [h] Reference 10. [i] L. W. Sieck, F. P. Abramson, and J. H. Futrell, *J. Chem. Phys.*, 45, 1655 (1966).

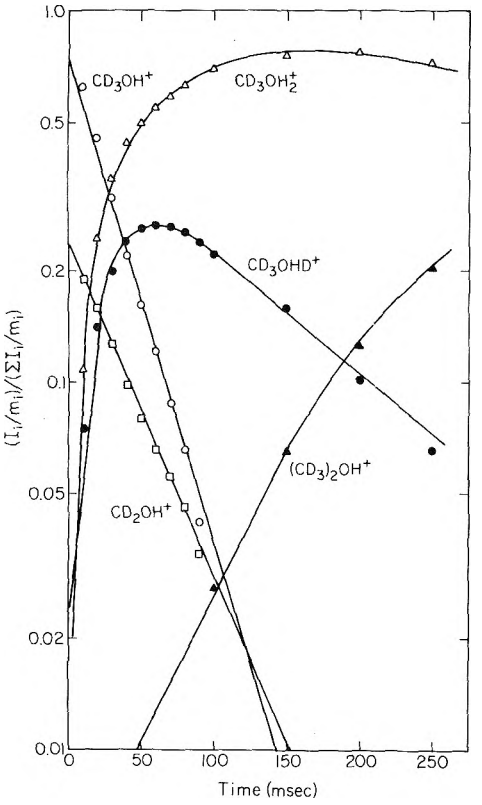

Figure 6. Variation of ion abundance with time for CD_3OH at 14.0 eV and 3.5 × 10^{-7} Torr with a 6-ms electron beam pulse.

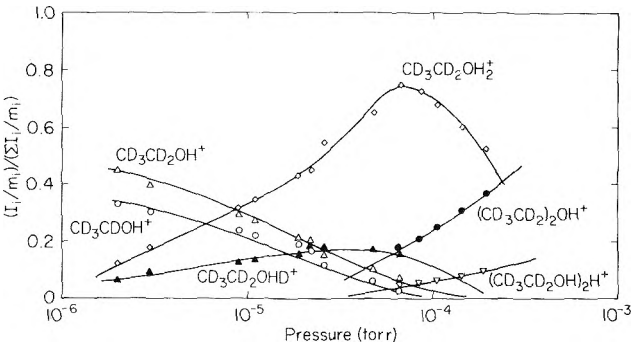

Figure 7. Variation of ion abundance with pressure for CD_3CD_2OH at 12.0 eV.

reactions in CH_3OH and CD_3OH are summarized in Table I. Rate constants for symmetric proton transfer (reaction 5) and protonated dimethyl ether formation (reaction 6) are derived from an analysis of the kinetics of disappearance of the deuterated and protonated parent molecules, respectively.

4. *Ethanol.* In addition to the parent ion of ethanol, it was found necessary to operate even in the pressure variation experiment (Figure 7) with the α-cleavage fragment, CH_3CHOH^+, present. At the slightly higher electron energy used in the trapped ion experiment (Figure 8) the fragment CH_2OH^+ also appears. In both cases the fragment ions are protonated aldehydes and react exclusively via proton transfer to form the protonated parent ion. The complications introduced by the presence of CH_3CHOH^+ in the data of Figure 7 made application of the Marshall–Buttrill analysis difficult since two primary ions react to produce the same secondary ion. However rate constants for reaction of all three primary ions in the data of Figure 8 are easily determined due to the greater

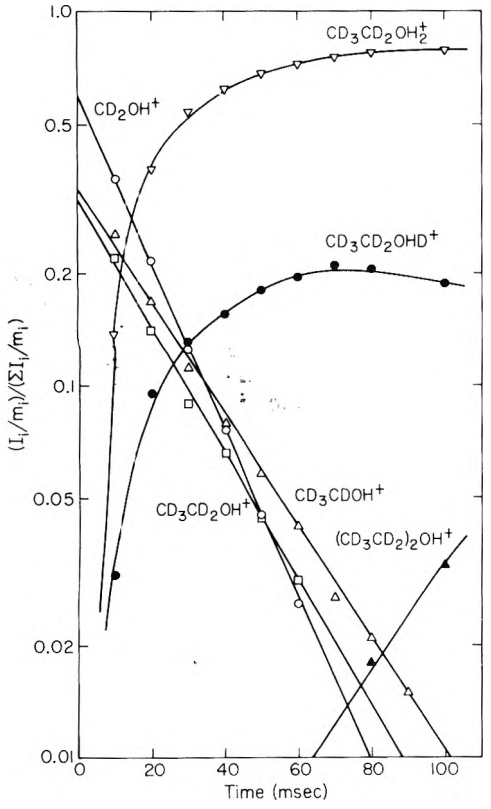

Figure 8. Variation of ion abundance with time for CD_3CD_2OH at 16.0 eV and 8.0 × 10^{-7} Torr with a 6-ms electron beam pulse.

ease of kinetic analysis by the trapped ion method.

The ion chemistry initiated by the parent ion of ethanol is described by the sequence of reactions 15–18 analagous

$$CD_3CD_2OH^+ + CD_3CD_2OH \longrightarrow \begin{cases} CD_3CD_2OH_2^+ + CD_3CD_2O & (15) \\ CD_3CD_2OHD^+ + C_2D_4OH & (16) \end{cases}$$

$$CD_3CD_2OHD^+ + CD_3CD_2OH \longrightarrow CD_3CD_2OH_2^+ + CD_3CD_2OD \quad (17)$$

$$CD_3CD_2OH_2^+ + CD_3CD_2OH \longrightarrow (CD_3CD_2)_2OH^+ + H_2O \quad (18)$$

to reactions 3–6 observed for methanol. Again it is observed that no deuterium is incorporated into the ionic product of reaction 18 indicating that the symmetric proton transfer process, reaction 17, is fast compared to the condensation reaction. The rate constants for reactions 17 and 18 were thus taken from the limiting slope for the disappearance of the deuterated and protonated ions, respectively. Rate data for the labeled and unlabeled ethanol are summarized in Table I.

Discussion

1. *Deexcitation Mechanisms.* In order to meaningfully compare theoretical rate constants to the experimentally measured rate of conversion of deuterated to protonated parent molecules various statistical corrections must be applied which depend upon the mechanism of the proton transfer reaction. The occurrence of fast, symmetric proton transfer and the formation of collisionally stabilized proton bound dimers at higher pressures are convincing evidence for an excited proton bound dimer as the intermediate in the reactions of protonated alcohols and amines with their parent neutrals. Such an intermediate formed in the interaction of the deuterated alcohol, $ROHD^+$, with the parent alcohol, ROH, may take the form

TABLE II: Comparison of Parent Ion and Proton Transfer Rate Constants

Species	Total reaction rate of parent ion[a]	Statistically corrected proton transfer encounter rate[a,b]	ADO[a,c] theory	Langevin[b]
NH_3	15.5[d]	12.0[e]	21.5	11.6
CD_3NH_2	18.5	11.9	15.9	11.1
$(CD_3)_2NH$	14.0	12.4	13.6	10.9
$(CD_3)_3N$	5.1[f]	5.5[f]	10.9	10.9
CD_3OH	25.6	17.2	17.8	10.0
CD_3CD_2OH	13.6	13.2	16.2	10.3

[a] All rate constants × 10^{10} cm^3 $molecule^{-1}$ s^{-1}. [b] See text. [c] Reference 10. [d] W. T. Huntress, Jr., and R. F. Pinizzotto, Jr., *J. Chem. Phys.*, 59, 4742 (1973). [e] Reference 11. [f] Reference 20.

of either a deuteron bound dimer, I, or proton bound

I II

dimer, II, with equal probability ignoring any deuterium isotope effect. Dissociation of intermediate I will never lead to the isotopically exchanged ionic product ROH_2^+. However intermediate II has equal probabilities of dissociating to yield ROH_2^+ and $ROHD^+$. Thus only one-fourth of the total encounters of $ROHD^+$ with ROH will lead to observable reaction. In order to obtain the total encounter rate then, the observed rate of isotopic exchange must be multiplied by a factor of 4.

A similar consideration of the possible intermediates formed between $CD_3NH_2D^+$ and CD_3NH_2 and between $(CD_3)_2NHD^+$ and $(CD_3)_2NH$ leads to statistical correction factors of three in the methylamine case and four in the dimethylamine case.

The statistically corrected proton transfer rate constants for the systems studied here are shown in Table II together with the total rate of reaction of the parent ions and the encounter rate constants predicted on the basis of the Langevin model[18] and the ADO theory.[19] Also included for comparison are the rates for similar reactions in ammonia and trimethylamine which have been reported elsewhere.[10,20] The summarized data show generally good agreement with rate constants calculated from the ADO theory, indicating that a proton bound dimer intermediate is likely formed in almost every ion–neutral encounter. This conclusion has important implications for the deexcitation of protonated alcohols and amines formed with appreciable amounts of internal or translational energy. If the lifetime of the proton bound dimer intermediate is long compared to the time necessary for redistribution of energy throughout the complex then roughly one-half of the excess energy will appear in both the ionic and neutral products of reaction. If, however, the lifetime of the intermediate is short enough that no energy flows from the excited to the thermal part of the complex during the proton transfer event then there is a probability of one-half that all of the excess energy will remain in the ionic product. In this latter case one-half of the ion–molecule encounters lead tc complete thermalization of the ions while in the former case each collision results in loss of one-half of the excess energy of the

ion. In both cases it may be assumed that even if the original excitation of the protonated molecule is as much as 100 kcal/mol after as few as 10 collisions the system will be thermalized within the detectable limit of 0.1 kcal/mol. This result is extremely important in considering the validity of thermochemical measurements made from observation of gas phase proton transfer equilibria. Assuming an encounter rate of 10^{-9} cm^3 $molecule^{-1}$ s^{-1} in trapped ion ICR experiments at 10^{-6} Torr each ion will undergo more than six collisions in a total reaction time of 200 ms which will be more than sufficient to thermalize an ion with 3 kcal/mol excess energy. Since 3 kcal/mol is the maximum free energy difference which may be conveniently measured in ICR observations of bimolecular equilibria it is fairly certain that under typical experimental conditions all ions will have been completely thermalized and a true thermodynamic equilibrium achieved. It has been for this reason that generally good agreement has been obtained among the various diverse techniques for observing ion–molecule equilibria. It should be noted that in cases where symmetric proton transfer is very slow it will take a much higher number of collisions to thermalize ions and the time necessary to achieve thermodynamic equilibrium will be greatly extended.

2. *Rate Constants from ICR Experiments.* An interesting and extremely important aspect of the results presented here is the good agreement obtained between rate constants determined using the Marshall–Buttrill analysis of intensity vs. pressure data and those determined using the ICR trapped-ion technique. In addition to providing corroboration of rate determinations the two techniques frequently provide complementary results. For example, in the case of ethanol where a secondary ion is produced by more than one primary ion no rate constants may be readily obtained from intensity vs. pressure data. However using trapped-ion techniques rate constants for reaction of each of the primary ions are easily determined. Conversely, when a single primary ion reacts to give two or more reactive secondary ions it is difficult to obtain individual rate constants for production of each secondary ion from a simple analysis of the trapped-ion data. However using the Marshall–Buttrill analysis of intensity vs. pressure data the individual rate constants are all obtained. From the above observations it is therefore highly desirable to be able to carry out both types of ICR experiment on a routine basis to completely characterize the kinetics of moderately complex systems. The advantage of the spectrometer such as the one used in these studies which is able to carry out both experiments facilely is thus evident.

Conclusion

The results summarized above show that ICR experiments involving appropriately isotopically labeled compounds may be conveniently used to determine rates of symmetric proton transfer reactions. These reactions have been demonstrated to be efficient in the relaxation of epithermal ion energy distributions and hence the symmetric proton transfer rate constant provides a measure of the conditions necessary for thermalization of ionic reactants. This knowledge is extremely useful in assessing the validity of thermochemical inferences made from observation of ion–molecule equilibria.

Acknowledgment. This work was supported in part by the Energy Research and Development Administration under Grant No. AT(04-3)767-8. T. B. McMahon thanks the National Research Council of Canada for fellowship support.

References and Notes

(1) Present address: Department of Chemistry, University of New Brunswick, Fredericton, New Brunswick, Canada.
(2) (a) Camille and Henry Dreyfus Teacher–Scholar, 1971–1976. (b) Contribution No. 5264.
(3) M. A. Haney and J. L. Franklin, *J. Chem. Phys.*, **48**, 4093 (1968).
(4) R. H. Staley and J. L. Beauchamp, *J. Chem. Phys.*, **62**, 1998 (1975).
(5) J. P. Briggs, R. Yamdagni, and P. Kebarle, *J. Am. Chem. Soc.*, **94**, 5128 (1972); D. H. Aue, H. M. Webb, and M. T. Bowers, *ibid.*, **94**, 4726 (1972); W. G. Henderson, M. Taagepera, D. Holtz, R. T. McIver, Jr., J. L. Beauchamp and R. W. Taft, *ibid.*, **94**, 4728 (1972).
(6) See, for example, J. J. Leventhal and L. Friedman, *J. Chem. Phys.*, **50**, 2928 (1969); M. L. Vestal, C. R. Blakley, P. W. Ryan, and J. H. Futrell, *ibid.*, **64**, 2094 (1976).
(7) J. L. Beauchamp in "Interactions between Ions and Molecules", P. Ausloos, Ed., Plenum Press, New York, N.Y., 1975, pp 413–444 and references contained therein.
(8) L. W. Sieck, F. P. Abramson, and J. H. Futrell, *J. Chem. Phys.*, **45**, 1655 (1966).
(9) M. S. B. Munson and F. H. Field, *J. Am. Chem. Soc.*, **87**, 4242 (1965).
(10) A. G. Harrison, P. H. Lin, and C. W. Tsang, *Int. J. Mass Spectrom. Ion Phys.*, **19**, 23 (1976).
(11) T. B. McMahon, P. G. Miasek, and J. L. Beauchamp, *Int. J. Mass Spectrom. Ion Phys.*, **21**, 63 (1976).
(12) A. G. Marshall and S. E. Buttrill, Jr., *J. Chem. Phys.*, **52**, 2752 (1970).
(13) T. B. McMahon and J. L. Beauchamp, *Rev. Sci. Instrum.*, **43**, 509 (1972).
(14) G. J. Shulz and A. V. Phelps, *Rev. Sci. Instrum.*, **28**, 1051 (1957).
(15) K. R. Ryan, L. W. Sieck, and J. H. Futrell, *J. Chem. Phys.*, **41**, 111 (1964).
(16) S. K. Gupta, E. G. Jones, A. G. Harrison, and J. J. Myher, *Can. J. Chem.*, **45**, 3107 (1967).
(17) J. M. S. Henis, *J. Am. Chem. Soc.*, **90**, 844 (1968).
(18) (a) P. Langevin, *Ann. Chim. Phys.*, **5**, 245 (1905); (b) G. Gioumousiss and D. P. Stevenson, *J. Chem. Phys.*, **29**, 294 (1958).
(19) T. Su and M. T. Bowers, *J. Chem. Phys.*, **50**, 3027 (1973).
(20) T. B. McMahon, Ph.D. Thesis, California Institute of Technology, 1973. The rate constant for symmetric proton transfer involving $(CD_3)_3N$ is estimated as the average of the forward and reverse rate constants for the proton transfer equilibrium $(CD_3)_3NH^+ + (CH_3)_3N \rightleftharpoons (CD_3)_3N + (CH_3)_3NH^+$.

Electron Capture Reactions in Mixtures of HCl and HBr

Surjit S. Nagra and David A. Armstrong*

Department of Chemistry, University of Calgary, Calgary, Alberta T2N 1N4, Canada *(Received November 11, 1976)*

Publication costs assisted by the National Research Council of Canada

The gas phase ^{60}Co radiolysis of mixtures of HCl and HBr has been studied at room temperature. Using SF_6 as a thermal electron scavenger, the rates of electron capture determined by competition kinetics were higher by a factor of 3 or more than the combined contributions of $(HCl)_2$ and $(HBr)_2$ dimers. The net increase in the rates is proportional to the product of the concentrations of HCl and HBr in the mixtures and can be explained by contributions of mixed (HCl, HBr) dimer species. The magnitude of the electron capture rate constant, $1.4 \pm 0.2 \times 10^{-28}$ cm^6 molecule^{-2} s^{-1}, of the mixed dimers is very similar to $1.0 \pm 0.1 \times 10^{-28}$ cm^6 molecule^{-2} s^{-1} observed in pure HBr, and it is suggested that the main reaction of the electron–mixed dimer ions is dissociation to H + ClHBr.

Introduction

Although reaction 1 is likely to be the most important

$$e^- + HX \rightarrow H + X^- \quad (X = I, Br, Cl) \tag{1}$$

electron reaction in gaseous hydrogen iodide,[1] previous studies in this laboratory[2-4] and elsewhere[5] have shown that it is relatively unimportant for HBr and HCl. The capture of low energy electrons in these systems is of higher order in hydrogen halide and obeys the stoichiometry of reaction 2. A mechanism based on the addition of

$$e^- + 2HX \rightarrow H_2 + \text{other products} \tag{2}$$

electrons to $(HX)_2$ dimer molecules as the initial event has been shown to hold for both halides.[3,4] However, the two molecules differ to the extent that dissociation of the transient $(HX)_2^{-*}$ complex dominates when HX = HBr, while stabilization to $(HX)_2^-$ and reactions with additional HX are most important in the case of HCl.

This investigation was undertaken with the object of examining the kinetics of electron capture in mixtures of HBr and HCl, where mixed dimers may be expected to occur. If one assumes that hydrogen bonding forces dominate,[6] then it is conceivable that the two species HCl–HBr and HBr–HCl may be near linear and thus distinguishable. To describe electron capture by these species the mechanism given in ref 4 is generalized below by replacing one HX of the original $(HX)_2$ dimer by HY.

$$HX + HY \overset{K_3^{HX,HY}}{\rightleftharpoons} (HX\text{-}HY) \tag{3}$$

$$e^- + (HX\text{-}HY) \underset{k_a}{\overset{k_c}{\rightleftharpoons}} (HX\text{-}HY)^{-*} \tag{4}$$

$$(HX\text{-}HY)^{-*} \xrightarrow{k_r} H + XHY^- \tag{5}$$

$$(HX\text{-}HY)^{-*} + HX \rightarrow (HX\text{-}HY)^- + HX \tag{6a}$$

$$(HX\text{-}HY)^{-*} + HX \rightarrow H + XH\text{-}Y^-\text{-}HX \tag{6b}$$

$$(HX\text{-}HY)^{-*} + HY \rightarrow (HX\text{-}HY)^- + HY \tag{6c}$$

$$(HX\text{-}HY)^{-*} + HY \rightarrow H + XH\text{-}Y^-\text{-}HY \tag{6d}$$

$$H + HY \rightarrow H_2 + Y \tag{7a}$$

$$H + HX \rightarrow H_2 + X \tag{7b}$$

As in ref 4 the rate of capture by hydrogen halide dimer species is defined as the effective first-order rate constant: $k_{HX,HY} = -(d[e]/dt)/[e]$ s^{-1}. For the $(HBr)_2$ dimers (i.e., HX = HY = HBr) $k_r \gg k_a > (k_{6a} + k_{6b})[HBr]$ at normal pressures[3,4] and $k_{HBr,HBr}$ is simply equal to $K_3^{HBr,HBr}k_c$. $[HBr]^2$, where $K_3^{HBr,HBr}k_c = 1.0 \pm 0.1 \times 10^{-28}$ cm^6 molecule^{-2} s^{-1} at 298 K. For the case of HX = HY = HCl on the other hand $k_a > (k_{6a} + k_{6b})[HCl] \gg k_r$ at normal pressures, and the rate of capture, $k_{HCl,HCl}$, is $K_3^{HCl,HCl}k_c(k_{6a} + k_{6b})k_a^{-1}[HCl]^3 = 10.4 \pm 0.7 \times 10^{-30}$ [HCl]^3 s^{-1} at 298 K. With the mixtures studied here the observed value of $k_{HX,HY}$ will be the sum of these two contributions plus those of the mixed dimers HBr–HCl and HCl–HBr, which will be designated as $k_{HBr,HCl}$ and $k_{HCl,HBr}$, respectively. The total rate was measured by the competition technique with sulfur hexafluoride as the scavenger in reaction 8. The

$$e^- + S \rightarrow S^- \tag{8}$$

contributions of $(HCl)_2$ and $(HBr)_2$ dimers, calculated with the above rate expressions, were then subtracted to determine the following: (a) whether mixed dimers played a significant role; and (b) the rates of their reactions, and whether they resembled $(HCl)_2$ or $(HBr)_2$ in their kinetics.

Experimental Section

The source and methods of purifying and storing the hydrogen halides and sulfur hexafluoride were described in ref 2 and 4. Mixtures of the gases of the required compositions were prepared in a mercury-free vacuum line and introduced into the 10-cm diameter 360-cm^3 volume pyrex irradiation cells.[2,4] Irradiations were carried out at 298 ± 2 K in a ^{60}Co Gamma cell 220, supplied by Atomic Energy of Canada Ltd. Dose rates were determined as discussed in ref 2 and lay in the range $1.8–2.0 \times 10^{18}$ eV g^{-1} h^{-1}, while typical absorbed doses were $0.9–1.0 \times 10^{18}$ eV g^{-1}. After irradiation noncondensibles were transferred to a gas-measuring system, where the hydrogen content was determined.

Results

The total yields of hydrogen in the mixtures, $G_m(H_2)$, were measured in molecules per 100 eV of absorbed energy for several different compositions. In the absence of sulfur hexafluoride the increase of $G_m(H_2)$ from 8.0 molecules per 100 eV in HCl to 9.8 molecules per 100 eV in HBr[1] was within experimental error (±0.2 molecules per 100 eV) a linear function of Z, the stopping power fraction of HBr defined in ref 2.

As previously shown,[2,4,5] the competition for low energy electrons between sulfur hexafluoride and the hydrogen halides may be described in terms of expression i, where

$$\{\Delta G(H_2)\}^{-1} = g_{es}^{-1}\{1 + k_{HX,HY}/k_8[S]\}$$

$\Delta G(H_2)$ is the reduction in hydrogen yield caused by capture of electrons via reaction 8 and g_{es} the yield per 100 eV of scavengable low-energy electrons. Plots of $\{\Delta G(H_2)\}^{-1}$

TABLE I: Rates of Electron Capture in HCl-HBr Mixtures

Concn (10^{19} molecule cm^{-3})		Electron capture rates, 10^9 s^{-1}			$k'_{HCl,HBr}/[HCl]\cdot[HBr]$ (10^{-28} cm^6 $molecule^{-2}$ s^{-1})
[HCl]	[HBr]	$k_{HX,HY}$ [a]	$k_{HCl,HCl} + k_{HBr,HBr}$ [b]	$k'_{HCl,HBr}$ [c]	
1.94	0.320	9.6 ± 1.0	1.9 ± 0.2	7.7 ± 1.2	$1.2_3 \pm 0.3_0$
1.94	0.640	22.1 ± 2.2	5.2 ± 0.5	16.9 ± 2.5	$1.3_4 \pm 0.2_0$
1.94	0.960	39.7 ± 4.0	10.6 ± 1.1	29.1 ± 5.1	$1.5_5 \pm 0.3_0$
3.89	0.640	45.1 ± 5.0	11.3 ± 1.1	33.8 ± 5.1	$1.3_4 \pm 0.2_0$
					Mean 1.4 ± 0.2

[a] Observed total rate. [b] Combined contributions of $(HCl)_2$ and $(HBr)_2$. [c] Net contribution of mixed dimer species.

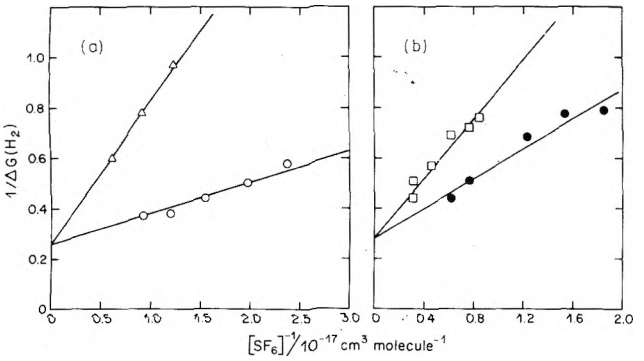

Figure 1. Reciprocal of $\Delta G(H_2)$ vs. the reciprocal of SF_6 concentration for mixtures of HCl and HBr: Concentrations of HCl and HBr in molecules cm^{-3} were respectively: (a) 1.94×10^{19} and 0.32×10^{19} (○), 3.89×10^{19} and 0.64×10^{19} (△); (b) 1.94×10^{19} and 0.64×10^{19} (●), 1.94×10^{19} and 0.96×10^{19} (□).

vs. $[SF_6]^{-1}$ are shown in Figure 1a and b for mixtures of four different compositions of HBr and HCl. The total rates of capture by hydrogen halide dimer species, $k_{HX,HY}$, were obtained from the (slope) × (intercept)$^{-1}$ (= $k_{HX,HY}k_8^{-1}$) for each of these plots and with $k_8 = 2.0 \times 10^{-7}$ cm^3 $molecule^{-1}$ s^{-1} as in ref 4. They are given in Table I along with the concentrations of HCl and HBr in each mixture. Column four of this table presents the combined contributions of $(HCl)_2$ and $(HBr)_2$. These were calculated with the rate coefficients given in the Introduction for pure HCl and HBr, but in the case of HCl an additional rate contribution equal to $K_3^{HCl,HCl}k_c(k_{6e} + k_{6f})k_a^{-1}$ was included in $k_{HCl,HCl}$ to take account of reactions 6e and 6f. For this

$$(HCl)_2^{-*} + HBr \rightarrow (HCl)_2^- + HBr \quad (6e)$$

$$(HCl)_2^{-*} + HBr \rightarrow H + ClH\text{-}Cl^-\text{-}HBr \quad (6f)$$

purpose $(k_{6e} + k_{6f}) = 0.88 \times 10^{-9}$ cm^3 $molecule^{-1}$ s^{-1} was calculated from ion-molecule reaction rate theory.[7] Comparison with 1.16×10^{-9} cm^3 $molecule^{-1}$ s^{-1} calculated in ref 4 for the corresponding reactions of $(HCl)_2^{-*}$ with HCl showed that the overall rate coefficient $K_3^{HCl,HCl}k_c(k_{6e} + k_{6f})k_a^{-1}$ should be $0.76\ K_3^{HCl,HCl}k_c(k_{6a} + k_{6b})k_a^{-1}$ for HX = HY = HCl. Since HCl was usually present in excess the contributions of reactions 6e and 6f are not large in any case, and, in the absence of experimental values of $(k_{6e} + k_{6f})$, the above procedure is therefore satisfactory.

For every mixture the magnitude of $k_{HX,HY}$ in column three exceeds $(k_{HCl,HCl} + k_{HBr,HBr})$ by a factor of 3 or more. Thus reactions of the mixed dimer species must make a substantial contribution to the rate of capture. The magnitudes of these contributions were obtained from the differences between the rates in columns three and four. They are referred to subsequently as $k'_{HCl,HBr}$ and are listed in column five of the table.

Clearly the concentrations of both (HCl–HBr) and (HBr–HCl) dimers will be proportional to [HCl][HBr] and column six of Table I gives the values of $k'_{HCl,HBr}$ divided by this product. The quotients are within experimental error equal and independent of [HBr] and [HCl].

Discussion

If one or more of reactions 6a–d were important for the mixed dimers, then $k'_{HCl,HBr}/[HCl][HBr]$ should be a function of the total hydrogen halide concentration. This is clearly not the case for the concentration regimes used here. Also the magnitude of the mean value of $k'_{HCl,HBr}/[HCl][HBr]$ in column six of Table I, $1.4 \pm 0.2 \times 10^{-28}$ cm^6 $molecule^{-2}$ s^{-1}, is very similar to $1.0 \pm 0.1 \times 10^{-28}$ cm^6 $molecule^{-2}$ s^{-1} observed in pure HBr. It appears therefore that the kinetics of electron capture by the mixed dimer (or dimers) of HCl and HBr resemble those $(HBr)_2$ and are such that $k_r \gg k_a > (k_{6a} + k_{6b})[HX] \simeq (k_{6c} + k_{6d})[HY]$.

The foregoing conclusion requires the absence of a significant energy barrier for reaction 5. As pointed out in ref 4, the energy change $\Delta E_{298}°_{(5)}$ for this reaction is the same as that of reaction 5′, which in turn can be calculated

$$e + (HX\text{-}HY) \rightarrow H + XHY^- \quad (5')$$

$$e + HX + HY \rightarrow H + YHY^- \quad (2a)$$

from $\{\Delta E_{298}°_{(2a)} - \Delta E_{298}°_{(3)}\}$. Yamdagni and Kebarle[8] have estimated $D_{Br^-HCl} = 16$ kcal mol^{-1} at 298 K from their results for gas-phase ion–molecule association energies. From this and standard thermochemical data[9] and electron affinities[10] $\Delta E_{298}°_{(2a)}$ is ~−7 kcal mol^{-1} for X = Cl and Y = Br. The energy change for reaction 5′ will be less exothermic by the absolute magnitude of $\Delta E_{298}°_{(3)}$, which may obviously be different for HCl–HBr and HBr–HCl dimer configurations. However, since $\Delta E_{298}°_{(3)}$ for HX = HY = HCl is ~−2.4 kcal mol^{-1} and $\Delta E_{298}°_{(3)}$ for HX = HY = HBr smaller,[4] it seems probable that $|\Delta E_{298}°_{(3)}|$ for both dimer configurations would be less than 7 kcal mol^{-1}. Based on current thermochemical data reaction 5 should not therefore have a significant energy barrier.

In summary the present observations are consistent with the capture of electrons by mixed HCl,HBr dimers having values of $K_3^{HX,HY}$ and k_c similar to those for $(HCl)_2$ and $(HBr)_2$. The subsequent reactions of the transient mixed dimer anions closely resemble those for the HBr system.

Acknowledgment. This research was supported by Canadian National Research Council Grant A3571.

References and Notes

(1) D. E. Wilson and D. A. Armstrong, *Radiat. Res. Rev.*, **2**, 297 (1970).
(2) S. S. Nagra and D. A. Armstrong, *Can. J. Chem.*, **53**, 3305 (1975).
(3) S. S. Nagra and D. A. Armstrong, *J. Phys. Chem.*, **79**, 2875 (1975).
(4) S. S. Nagra and D. A. Armstrong, *Can. J. Chem.*, **54**, 3580 (1976).
(5) G. R. A. Johnson and J. L. Redpath, *Trans. Faraday Soc.*, **66**, 861 (1970).
(6) See the discussion of $(HX)_2$ dimers in ref 4. One may note that HCl–HBr chains have been observed in crystals, but information on gaseous mixed dimers appears to be lacking. G. L. Hiebert and D. F. Hornig, *J. Chem. Phys.*, **28**, 316 (1958).
(7) T. Su and M. T. Bowers, *Int. J. Mass. Spectrum Ion Phys.*, **12**, 347 (1973), and references cited therein.
(8) R. Yamdagni and P. Kebarle, *J. Am. Chem. Soc.*, **93**, 7139 (1971).
(9) JANAF Thermochemical Tables, *Natl. Stand. Ref. Data Ser., Natl. Bur. Stand.*, **No. 37** (1971).
(10) L. G. Christophorou in "Atomic and Molecular Radiation Physics", Wiley, New York, N.Y., 1971.

Electron-Transfer between Iron, Ruthenium, and Osmium Complexes Containing 2,2′-Bipyridyl, 1,10-Phenanthroline, or Their Derivatives. Effects of Electrolytes on Rates[1,2]

Nelson D. Stalnaker, John C. Solenberger, and Arthur C. Wahl*

Department of Chemistry, Washington University, St. Louis, Missouri 63130 *(Received October 21, 1976)*

Publication costs assisted by the National Science Foundation

The rates of a number of electron-transfer reactions between the ML_3^{3+} and $M'L'_3{}^{2+}$ complex ions have been measured by the stopped-flow method, the symbols M and M′ representing iron, ruthenium, or osmium and L and L′ representing 2,2′-bipyridyl, 1,10-phenanthroline, or their derivatives. Both aqueous and nonaqueous solutions were used as reaction media, and the temperature was 25 °C. For several reaction systems it was shown that the reaction followed a second-order rate law, first order in each reactant concentration, and values of k in the range of 5×10^5 to $\geq \sim 5 \times 10^7$ M^{-1} s^{-1} were observed. When M = Fe, M′ = Os, and L = L′ = 4,4′-dimethyl-2,2′-bipyridyl and the solvent is acetonitrile, the rate of electron transfer is influenced strongly by the concentration and nature of the anion present; the rate law determined is rate = $(k_1 + k_2[ClO_4^-] + k_3[PF_6^-])[FeL_3^{3+}][OsL_3^{2+}]$. The rate constants determined at 25 °C are $k_1 = (5.0 \pm 0.6)10^5$ M^{-1} s^{-1}, $k_2 = (1.3 \pm 0.1)10^{10}$ M^{-2} s^{-1}, and $k_3 = (5.6 \pm 0.3)10^9$ M^{-2} s^{-1}. The formal potential of the reaction was measured to be $E_f = 0.225$ V by use of a cell having the same concentrations (6×10^{-5} or 3×10^{-4} M) of each member of each couple. Electrical conductivity measurements of acetonitrile solutions of the reactant or similar perchlorate compounds indicated that the reactant compounds were essentially completely dissociated in the very dilute solutions investigated. The experimental value of k_1 is nearly two orders-of-magnitude smaller than predicted by the Marcus theory of adiabatic electron-transfer reactions applied to spherical reactants 14 Å in diameter in a continuous, unsaturated dielectric medium.

Introduction

Electron-transfer reactions between the large complex cations, ML_3^{3+} and $M'L'_3{}^{2+}$, are of interest for several reasons. (The symbols M and M′ represent iron, ruthenium, or osmium, and L and L′ represent 2,2′-bipyridyl (bpy), 1,10-phenanthroline (phen), or their derivatives.) (1) Since the complexes are substitution inert, electron transfer must occur via the outer-sphere mechanism with the aromatic ligands most likely particpating in the transfer. Thus, measured rates of electron transfer might reasonably be compared to the predictions of the Marcus theory of adiabatic outer-sphere electron-transfer reactions.[3] (2) The effect of electrolytes on the reaction rates between the large cations (radii $\simeq$ 7 Å) is of interest for comparison with the catalytic effects associated with specific cations found for the MnO_4^{2-}–MnO_4^- and $Fe(CN)_6^{4-}$–$Fe(CN)_6^{3-}$ electron-exchange reactions.[4,5]

Previous work had indicated that electron-transfer reactions between ML_3^{3+} and $M'L'_3{}^{2+}$ were very rapid ($k > \sim 10^5$ M^{-1} s^{-1} at 25 °C),[6-13] so stopped-flow measurements were undertaken with reactants at very low concentrations ($\sim 10^{-5}$ M). The measurements were possible because the 2+ ions have large molar extinction coefficients in the visible region. The low reactant concentrations not only slowed reactions to measurable rates but also made possible rate measurements at small electrolyte concentrations, so that ideal conditions were approached.

In addition to the kinetic measurements, some conductivity measurements were made to investigate the degree of dissociation of a typical reactant compound in acetonitrile. Also, measurements were made of the potential between the couples of reaction 1, which was the

$$Fe(me_2bpy)_3^{3+} + Os(me_2bpy)_3^{2+} = Fe(me_2bpy)_3^{2+} + Os(me_2bpy)_3^{3+}$$

reaction most thoroughly investigated. The symbol me_2bpy represents 4,4′-dimethyl-2,2′-bipyridyl.

Results

The rates of a number of electron-transfer reactions were measured in several different solvents, and the results are summarized in Table I. When reactant concentrations were varied, the second-order rate constant, k, first order with respect to each reactant concentration, remained essentially constant. The most careful investigation of the rate law was carried out in acetonitrile for the reaction represented by eq 1, and the results are given in Tables II and III. Since the rate is very dependent on the electrolyte concentration, as is discussed below, $Co(me_2bpy)_3(ClO_4)_3$ was added to maintain an essentially constant ionic strength and ClO_4^- concentration.

Variation of the electrolyte concentration in acetonitrile resulted in large changes in the rate constant for reaction 1; as shown in Figure 1, the magnitude of the effect depends on the nature of the electrolyte, and the increase in k with anion concentration is much greater than predicted by the Brønsted–Debye–Hückel limiting law.[14] Experiments at 30 °C with added $LiClO_4$ gave results at low concentration similar to those shown for $NaClO_4$ at 25 °C in Figure 1; however, at higher concentrations ($[ClO_4^-] > 10^{-3}$ M) rate constants were large, $>2 \times 10^7$ M^{-1} s^{-1}, and it was difficult to obtain reproducible results. A rate law of the following form well represents the data obtained at 25 °C and low concentrations:

$$\text{rate} = (k_1 + k_2[ClO_4^-] + k_3[PF_6^-])[Fe(me_2bpy)_3^{3+}] \times [Os(me_2bpy)_3^{2+}] \quad (2)$$

A least-squares fit of the data for $[ClO_4^-] \leq 2 \times 10^{-4}$ M gives $k_1 = (5.0 \pm 0.6)10^5$ M^{-1} s^{-1} and $k_2 = (1.3 \pm 0.1)10^{10}$ M^{-2} s^{-1}, and use of these values with the data obtained when KPF_6 was added gives $k_3 = (5.6 \pm 0.1)10^9$ M^{-2} s^{-1}. If ion-atmosphere effects are considered by inclusion of the Debye–Hückel limiting law in the calculation, $k_1 = (4.0 \pm 0.5)10^5$ M^{-1} s^{-1}, $k_2 = (1.0 \pm 0.1)10^{10}$ M^{-2} s^{-1}, and $k_3 = (3.4$

TABLE I: Summary of Measured Rate Constants at 25 °C

Reactants (concn range, μM)[a]	Solvent[b]	k, 10^6 M^{-1} s^{-1} [c]
$Fe(phen)_3^{3+}$ (4-8), $Os(phen)_3^{2+}$ (2)	5×10^{-4} M H_2SO_4 (aq)	47 ± 5 (9)
$Fe(phen)_3^{3+}$ (10-26), $Os(phen)_3^{2+}$ (4-8)	HCOOH	~17 (3)
$Fe(phen)_3^{3+}$ (5), $Os(phen)_3^{2+}$ (2)	~90% HCOOH, ~10% H_2O	~24 (2)
$Fe(phen)_3^{3+}$ (12), $Os(phen)_3^{2+}$ (7)	CH_3CN	~14 (2)
$Fe(bpy)_3^{3+}$ (7-18), $Os(phen)_3^{2+}$ (4-7)	HCOOH	19 ± 2 (4)
$Fe(bpy)_3^{3+}$ (5), $Os(phen)_3^{2+}$ (4)	90% HCOOH, 10% H_2O	~52 (1)
$Fe(bpy)_3^{3+}$ (16), $Os(bpy)_3^{2+}$ (43)	CH_3CN	~1.0 (1)
$Fe(4,4'\text{-}me_2bpy)_3^{3+}$ (4-11), $Os(phen)_3^{2+}$ (2)	5×10^{-4} M H_2SO_4 (aq)	32 ± (15)
$Fe(4,4'\text{-}me_2bpy)_3^{3+}$ (9-20), $Os(phen)_3^{2+}$ (3-6)	HCOOH	0.49 ± 0.03 (3)
$Fe(4,4'\text{-}me_2bpy)_3^{3+}$ (3-21), $Os(phen)_3^{2+}$ (1-5)	90% HCOOH, 10% H_2O	3.5 ± 0.3 (9)
$Fe(4,4'\text{-}me_2bpy)_3^{3+}$ (5-30), $Os(4,4'\text{-}me_2bpy)_3^{2+}$ (3-12)	CH_3CN	1.9 ± 0.2[d] (8)
$Fe(4,7\text{-}me_2phen)_3^{3+}$ (5), $Os(4,7\text{-}me_2phen)_3^{2+}$ (2)	~90% HCOOH, ~10% H_2O	~20 (1)
$Fe(5,6\text{-}me_2phen)_3^{3+}$ (6), $Os(5,6\text{-}me_2(phen)_3^{2+}$ (2)	~90% HCOOH, ~10% H_2O	~12 (1)
$Fe(bpy)_3^{3+}$ (5), Os (3,5,6,8-me_4phen)$_3^{2+}$ (2)	~90% HCOOH, ~10% H_2O	~13 (1)
$Fe(3,5,6,8\text{-}me_4phen)_3^{3+}$ (3), $Os(3,5,6,8\text{-}me_4phen)_3^{2+}$ (2)	5×10^{-4} M H_2SO_4 (aq)	~47 (1)
$Fe(3,5,6,8\text{-}me_4phen)_3^{3+}$ (7-15), $Os(3,5,6,8\text{-}me_4phen)_3^{2+}$ (2)	~90% HCOOH, ~10% H_2O	44 ± 3 (3)
$Ru(3,4,7,8\text{-}me_4phen)_3^{3+}$ (25), $Fe(3,4,7,8\text{-}me_4phen)_4^{2+}$	~90% HCOOH, ~10% H_2O 0.13 M H_2SO_4	≥~20 (1)
$Ru(4,7\text{-}Ph_2phen)_3^{3+}$ (13), $Fe(4,7\text{-}Ph_2phen)_3^{2+}$ (13)	0.13 M H_2SO_4	≥~40 (1)
$Ru(4,7\text{-}ch_2phen)_3^{3+}$ (10), $Fe(4,7\text{-}ch_2phen)_3^{2+}$ (10)	0.13 M H_2SO_4	≥~50 (1)

[a] The symbol me represents methyl, Ph represents phenyl, and ch represents cyclohexyl. All reactant compounds were perchlorate salts. [b] Percentages are weight percent. [c] Uncertainties given are standard deviations of the average derived from the number of measurements given in parentheses. [d] Average of data given in Tables II and III.

TABLE II: Rate Dependence on the $Fe(me_2bpy)_3^{3+}$ Concentration in CH_3CN[a]

$[Fe(me_2bpy)_3^{3+}]$, M	k, M^{-1} s^{-1}
1.19×10^{-4}	1.75×10^6
1.77×10^{-5}	1.80×10^6
2.38×10^{-5}	1.82×10^6
3.05×10^{-5}	1.70×10^6
	(Av 1.77×10^6)

[a] $[Os(me_2bpy)_3^{2+}] = 7.62 \times 10^{-6}$ M, $[ClO_4^-] = 1.08 \times 10^{-4}$ M, $\mu = 2.09 \times 10^{-4}$ M, temperature = 25 °C.

TABLE III: Rate Dependence on the $Os(me_2bpy)_3^{2+}$ Concentration in CH_3CN[a]

$[Os(me_2bpy)_3^{2+}]$, M	k, M^{-1} s^{-1}
3.08×10^{-6}	1.77×10^6
5.50×10^{-6}	2.04×10^6
7.82×10^{-6}	2.02×10^6
11.8×10^{-6}	2.20×10^6
	(Av 2.01×10^6)

[a] $[Fe(me_2bpy)_3^{3+}] = 1.84 \times 10^{-5}$ M, $[ClO_4^-] \simeq 1.17 \times 10^{-4}$ M, $\mu \simeq 2.26 \times 10^{-4}$ M, temperature = 25 °C.

± 0.2)10^9 M^{-1} s^{-1}. A modification of the ORGLS general least-squares computer program[15] was used; 10% uncertaninties in the k values were assumed; and the fit of the function to the data was good. The function also satisfactorily represents the data at the higher perchlorate-ion concentrations, as shown in Figure 1, except for the two data at the highest perchlorate-ion concentrations ($Co(me_2bpy)_3(ClO_4)_3$ added). These data could be in error since the rate constants are near our limit of ~2×10^7 M^{-1} s^{-1} for reliable measurements, or the calculated perchlorate-ion concentration could be high if the added $Co(me_2bpy)_3(ClO_4)_3$ were only partially dissociated at the higher concentrations.

Conductance measurements were made at 25 °C with acetonitrile solutions of $Fe(me_2bpy)_3(ClO_4)_2$, and it was found that the solutions were highly conducting. The decrease in equivalent conductance at low concentration with increasing $c^{1/2}$, $\Lambda = 178\text{–}1015\ c^{1/2}$ ohm^{-1} cm^{-2} $equiv^{-1}$, is consistent with the Onsager–Debye–Hückel limiting law,[16] indicating that the compound is a strong electrolyte in acetonitrile. Kolthoff and Thomas[17] made conductivity measurements for $Fe(phen)_3(ClO_4)_2$ and for $Fe(phen)_3$-

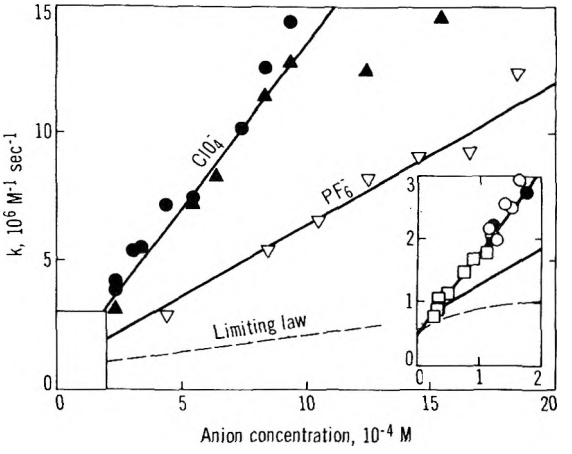

Figure 1. Variation of the rate constant for reaction 1 with anion concentration: (□) reactant perchlorate compounds, (■) reactant concentrations varied (averages of data from Tables II and III), (○) $[ClO_4^-]$ varied at constant ionic strength, (●) $NaClO_4$ added, (▲) $Co(me_2bpy)_3(ClO_4)_3$ added, (▽) KPF_6 added to reactants present as perchlorates ($[ClO_4^-] = 3.4 \times 10^{-5}$ M). Lines represent eq 2 with $k_1 = 5 \times 10^5$ M^{-1} s^{-1}, $k_2 = 1.3 \times 10^{10}$ M^{-2} s^{-1}, and $k_3 = 5.6 \times 10^9$ M^{-1} s^{-1}. The dashed line represents the Brönsted–Debye–Huckel limiting law, $k = 5 \times 10^5 \exp(43.8\mu^{1/2})$ M^{-1} s^{-1}, for equal reactant concentrations up to 2×10^{-5} M plus $NaClO_4$ or KPF_6.

$(ClO_4)_3$ in acetonitrile and concluded that both are strong electrolytes. It will be assumed, therefore, for treatment of the kinetic data that the reactant compounds $Os(me_2bpy)_3(ClO_4)_2$ and $Fe(me_2bpy)_3(ClO_4)_3$ are essentially completely dissociated in acetonitrile.[18]

Direct potentiometric measurements with a Beckman Model G.S. pH meter were made with cells of the type

$$Pt|Os(me_2bpy)_3^{2+}, Os(me_2bpy)_3^{3+}\,\|\,Fe(me_2bpy)_3^{2+}, Fe(me_2bpy)_3^{3+}|Pt \qquad (3)$$

to determine the formal potential of the reaction, the anion being ClO_4^-. The couples were contained in a U-tube and were separated by a fine or medium porosity fritted disk, and bright or platinized platinum electrodes were used. With the concentrations of each ion near 6×10^{-5} M or near 3×10^{-4} M, stable cells were made with potentials of 0.225 V at 25 ± 1 °C. Reduction of the concentrations below 6×10^{-5} M or addition of considerable $NaClO_4$

(≥0.008 M) resulted in unstable cells.

Discussion

The data in Table I show for a number of outer-sphere electron-transfer reactions in several different reaction media that the rate constants are large ($k = 5 \times 10^5$ to $\geq \sim 5 \times 10^7$ M^{-1} s^{-1}) at 25 °C. The large variation in rate constants may be due to differences in the free-energy changes, electrolyte concentrations, solvents, and ligands. However, only for the $Fe(me_2bpy)_3^{3+}$–$Os(me_2bpy)_3^{2+}$ reaction in acetonitrile has the free-energy change been measured and the electrolyte effect investigated in some detail, and this system is discussed below.

The rate law given in eq 2 for reaction 1 suggests that the reaction may proceed via the following paths:[19]

$$Fe(me_2bpy)_3^{3+} + ClO_4^- = Fe(me_2bpy)_3ClO_4^{2+} \quad K_c$$

$$Fe(me_2bpy)_3^{3+} + PF_6^- = Fe(me_2bpy)_3PF_6^{2+} \quad K_p$$

$$Fe(me_2bpy)_3^{3+} + Os(me_2bpy)_3^{2+} \xrightarrow{k_1}$$

$$Fe(me_2bpy)_3ClO_4^{2+} + Os(me_2bpy)_3^{2+} \xrightarrow{k_c}$$

$$Fe(me_2bpy)_3PF_6^{2+} + Os(me_2bpy)_3^{2+} \xrightarrow{k_p} \quad (4)$$

The rate law for the reaction proceeding via the above paths is given by

$$\text{rate} = \frac{k_1 + k_c K_c[ClO_4^-] + k_p K_p[PF_6^-]}{1 + K_c[ClO_4^-] + K_p[PF_6^-]} \times [Fe^{III}][Os^{II}] \quad (5)$$

Equation 5 reduces to eq 2 when the products of the ion-association constants and anion concentrations are much less than unity so that the $[Fe^{III}] \simeq [Fe(me_2bpy)_3^{3+}]$ and $[Os^{II}] \simeq [Os(me_2bpy)_3^{2+}]$, a condition that is indicated by conductivity measurements. Under these conditions $k_2 = k_c K_c$ and $k_3 = k_p K_p$, and values of K_c and K_p are need for interpretation of these terms.[18]

The Marcus theory of adiabatic electron-transfer reactions[3] predicts a rate dependence on the free-energy change of the reaction, and this can be derived from the emf measurements, which were made at low and equal concentrations for the components of the two couples, so the measured formal potential of 0.225 V should be close to the $E°$ value, and $\Delta G° = 5.2$ kcal/mol.

The Marcus theory applied to spherical reactants 14 Å in diameter in a continuous, unsaturated dielectric medium predicts a value of $k_1 \simeq 2 \times 10^7$ M^{-1} s^{-1}, which is nearly two orders of magnitude too large. The values were calculated as follows, ΔG_c^* and ΔG_o^* being the free energies of activation due to the Coulombic effect and the necessity of rearranging the outer-sphere solvation layers, respectively.

$$k = 10^{11} e^{-\Delta G^*/RT}$$

$$\Delta G^* = \Delta G_c^* + \Delta G_o^* + \Delta G°/2 + (\Delta G°)^2/16\Delta G_o^* \quad (6)$$

$$\Delta G^* = 4.0 + 3.1 - 2.1 = 5.0 \text{ kcal/mol} \quad (7)$$

The discrepency, which can be expressed as the ΔG^* value being 2.2 kcal/mol too small, could be due to neglect of the inner-sphere reorganizational free energy of activation, ΔG_i^*, which was assumed to be zero. However, the value of k predicted by theory with the same assumption is less than a factor of 2 smaller than the measured value of 1.5×10^9 M^{-1} s^{-1} (2.0×10^{-9} M^{-1} s^{-1} corrected for diffusion) at 25 °C for the $Cr(bpy)_3$–$Cr(bpy)_3^+$ electron-exchange system in *N,N*-dimethylformamide,[20] and the ΔG_i^* values should be similar for the two systems with similar electronic structures and bonding. The discrepency is probably due to defects in the simple model that was assumed, and the defects may well be related to the ionic charges, e.g., partial dielectric saturation may occur, as was postulated for $Fe(CN)_6^{4-}$–$Fe(CN)_6^{3-}$ electron-exchange reaction.[5] If partial dielectric saturation were a major cause for the discrepency, it would be necessary that ΔG_c^* be increased more than ΔG_o^* is decreased by the effect, a possiblity that seems reasonable.

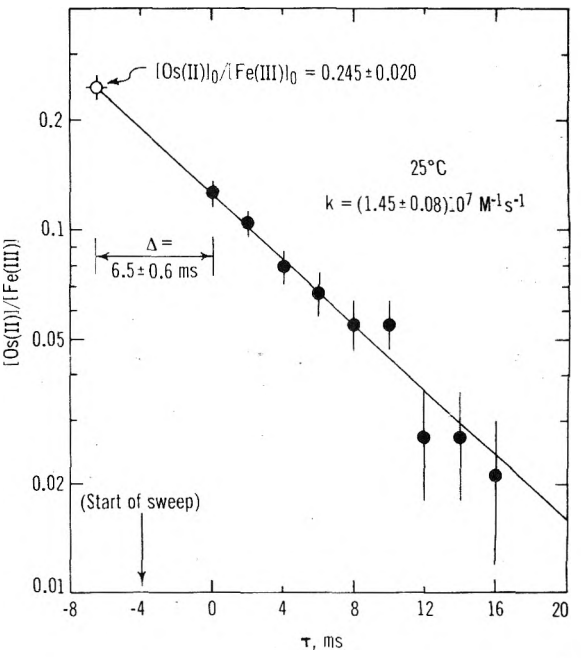

Figure 2. Plot of data for reaction 1 with $NaClO_4$ added ($[ClO_4^-] = 9.4 \times 10^{-4}$ M) in the manner suggested by eq 9. The line was calculated from the values for k and Δ shown that were determined from the data and eq 10 by the method of least-squares. Initial reactant concentrations were 2.3×10^{-6} M $Os(me_2bpy)_3^{2+}$ and 9.4×10^{-6} M $Fe(me_2bpy)_3^{3+}$ in CH_3CN.

Experimental Section

The stopped-flow measurements were made with a Durram instrument, Model 13000, modified to include an electrically operated pneumatic drive for the syringes. The photographs of the oscilloscope screen were measured to determine the transmittance as a function of time. Typically, the transmittance changed from 85 or 90% to 95% during the course of a reaction, and about ten transmittance values were read from a photograph. Most data were interpreted by use of eq 10, which was programmed for least-squares analysis with the ORGLS program.[15] Some data were plotted as illustrated in Figure 2.

The fraction F of a reaction which occurred up until time t is given by

$$F = \frac{x}{a} = \frac{D_0 - D_t}{D_0 - D_\infty} \quad (8)$$

The symbols a and x represent the concentrations of a reactant (the one not in excess) at the start of the reaction and of a product at time t, respectively, and D_0, D_t, and D_∞ represent the optical densities of the solution at the start, at time t, and at the completion of the reaction, respectively. Equation 8 combined with eq 9 for a second-order rate law, when $a \neq b$, b representing the initial concentration of the reactant in excess, gives eq 10. The

$$kt = \frac{1}{b-a} \ln \frac{a(b-x)}{b(a-x)} = \frac{1}{b-a} \ln \frac{[1-(a/b)F]}{(1-F)} \quad (9)$$

$$T = \exp(-2.303D_t) = \exp\left\{-2.303\left[D_0 - (D_0 - D_\infty)\left(\frac{1 - \exp[k(b-a)t]}{(a/b) - \exp[k(b-a)t]}\right)\right]\right\} \quad (10)$$

symbol T represents the measured transmittance, and k represents the second-order rate constant.

In the computer programs t was replaced by $\Delta + \tau$, the "dead-time" plus the time lapse after the first reading, and k and Δ were determined. The Δ values were used only to help determine if an experiment gave reliable results; generally it was required that Δ be a reasonable value of 1–5 ms plus the time interval between the start of the oscillograph sweep and the first reading. A measured value of T was corrected for the small difference between the measured T_∞ and the value calculated from the optical densities of the reactant solutions. The molar extinction coefficients at 4500 Å used for the 4,4′-dimethyl-2,2′-bipyridyl complexes in acetonitrile are as follows: Os(II) 13 456, Fe(II) 3525, Os(III) 705, Fe(III) 466.

Uncertainties in T of ±0.003 were assumed and allowed satisfactory fits of the data by eq 10. Uncertainties in the k values of ~5% were given by the least-squares calculations, and these were increased to ~10% to allow for the uncertainties in k caused by uncertainties in the extinction coefficients.

Conductivity measurements were made using a Beckman conductivity bridge (Model RC-18A) operating at 1000 or 3000 Hz. Conductivity cells were thermostated in a Fisher Isotemp water bath equipped with a Precision Scientific portable cooler. The temperature was kept at 25.0 ± 0.1 °C.

Iron(II) complex ions were prepared in aqueous solution by mixing stoichiometric amounts of $FeSO_4 \cdot 7H_2O$ and ligand, purchased from the G. F. Smith Co., allowing several hours for reaction at room temperature, and then filtering. Iron(III) complex ions were prepared from the iron(II) complex ions by oxidation with lead dioxide or cerium(IV) ammonium sulfate in aqueous sulfuric acid solution. Compounds of both complex ions were prepared by addition of a soluble salt containing the appropriate anion (e.g., ClO_4^- or PF_6^-), filtering, washing with water, and drying at 40–60 °C under reduced pressure.

Preparation of coordination compounds of ruthenium, osmium, and cobalt required higher temperatures, longer times, and various solvents, and procedures given in the literature were generally followed.[21-24] The few modifications that were made are described elsewhere.[25]

Compounds were analyzed spectrophotometrically if the molar extinction coefficients were known,[26-31] or, if not, by carbon and hydrogen analysis. A number of osmium compounds were also analyzed for osmium;[32] however, *difficulty was encountered with perchlorate salts due to violent reactions that occurred at the elevated temperature required for sodium peroxide fusion.* The analyses indicated that the compounds used were ≥~99% pure.

Distilled water was redistilled from basic premanganate solution in a pyrex system. Fisher pesticide grade acetonitrile was dried over calcium hydride powder (~10 g/L) for 1 or more days, decanted or filtered into a distillation flask containing phosphorous pentoxide (~5 g/L), and distilled through a 1-m column containing small pieces of glass tubing. Eastman practical grade formic acid (97+%) was dried over Baker's Purified boric anhydride (~70 g/L) for 1 day or more and then distilled from fresh boric anhydride (~20 g/L). (In our earlier work[25] formic acid was distilled from calcium hydride; it was later found that formic acid prepared in this way contained ~10% water.)

References and Notes

(1) Supported by the National Science Foundation under Grants No. GP-5939X, GP-28260X, and CHE76-02473.
(2) Presented in part at the 157th and 169th National Meetings of the American Chemical Society, Minneapolis, Minn., April 13–18, 1969 and Los Angeles, Calif., April 1–4, 1974, respectively. A portion of this article was abstracted from the Ph.D. Thesis of John C. Solenberger, Washington University, St. Louis, Mo., 1969.
(3) R. A. Marcus, *J. Chem. Phys.*, **43**, 679 (1965).
(4) J. C. Sheppard and A. C. Wahl, *J. Am. Chem. Soc.*, **79**, 1020 (1957).
(5) R. J. Campion, C. F. Deck, P. King, Jr., and A. C. Wahl, *Inorg. Chem.*, **6**, 672 (1967).
(6) F. P. Dwyer and E. C. Gyarfas, *Nature (London)*, **166**, 481 (1950).
(7) L. Eimer and A. I. Medalia, *J. Am. Chem. Soc.*, **74**, 1592 (1952).
(8) P. George and D. H. Irvine, *J. Chem. Soc.*, 587 (1954).
(9) E. Eichler and A. C. Wahl, *J. Am. Chem. Soc.*, **80**, 4145 (1958).
(10) M. W. Dietrich and A. C. Wahl, *J. Chem. Phys.*, **38**, 1591 (1963).
(11) D. W. Larsen and A. C. Wahl, *J. Chem. Phys.*, **41**, 908 (1964).
(12) D. W. Larsen and A. C. Wahl, *J. Chem. Phys.*, **43**, 3765 (1965).
(13) M.-S. Chan, J. B. De Roos, and A. C. Wahl, *J. Phys. Chem.*, **77**, 2163 (1973).
(14) See, for example, K. J. Laidler, "Chemical Kinetics", McGraw-Hill, New York, N.Y., 1950, p 126.
(15) L. A. Busing and H. A. Levy, Oak Ridge National Laboratory Report No. ORNL-TM-2771, 1962 (unpublished).
(16) J. O'M. Bockris and A. K. N. Reddy, "Modern Electrochemistry", Vol. 1, Plenum Press, New York, N.Y., 1970, pp 430–438.
(17) I. M. Kolthoff and F. G. Thomas, *J. Phys. Chem.*, 69, 3049 (1965).
(18) Preliminary results of conductance measurements by T. Braga in our laboratory with dilute acetonitrile solutions of $Co(me_2bpy)_3(ClO_4)_3$ indicate that the compound is essentially a strong electrolyte but that some ion association may occur. Although the interpretation of the data is by no means straightforeward, the data appear to be consistent with a value of $K_c \simeq 10^3$ (eq 5). This value would indicate that ≤~5% of the $Fe(me_2bpy)_3^{3+}$ reactant is associated with ClO_4^- at $[ClO_4^-] \leq 2 \times 10^{-4}$ M, the concentration range used for the data analysis.
(19) Other paths, e.g., those involving ion association of $Os(me_2bpy)_3^{2+}$, are also consistent with the rate law given in eq 2, and eq 6 could be made more general so as to include these paths. However, the data do not allow distinction between the several possible sets of paths, and the set given in the text is illustrative of how the available data can be interpreted.
(20) T. Saji and S. Aoyagui, *Bull. Chem. Soc. Jpn.*, **46**, 2101 (1973).
(21) B. Kratochvil and D. A. Zatko, *Anal. Chem.*, **36**, 527 (1964).
(22) F. H. Burstall, *J. Chem. Soc.*, 172 (1936).
(23) F. P. Dwyer, N. A. Gibson, and E. C. Gyarfas, *J. Proc. R. Soc. N.S. Wales*, **84**, 69 (1950).
(24) F. H. Burstall, F. P. Dwyer, and E. C. Gyarfas, *J. Chem. Soc.*, 953 (1950).
(25) J. C. Solenberger, Ph.D. Thesis, Washington University, 1969.
(26) M. L. Moss and M. G. Mellon, *Ind. Eng. Chem., Anal. Ed.*, **14**, 862 (1942).
(27) F. W. Cagle, Jr., and G. F. Smith, *J. Am. Chem. Soc.*, **69**, 1860 (1947).
(28) W. W. Brandt and D. K. Gullstrom, *J. Am. Chem. Soc.*, **74**, 3532 (1952).
(29) W. W. Brandt and G. F. Smith, *Anal. Chem.*, **21**, 1313 (1949).
(30) H. Diehl and G. F. Smith, "The Iron Reagents", 2nd ed, G. Frederick Smith Chemical Co., 1965, p 13.
(31) M. H. Ford-Smith and N. Sutin, *J. Am. Chem. Soc.*, **83**, 1830 (1961).
(32) F. P. Dwyer and N. A. Gibson, *Analyst*, **76**, 104 (1951).

Hydrogen Atom Spin Trapping in γ-Irradiated Fluorinated Alcohols. Solvent Effects on Coupling Constants and Relative Radical Yields

A. Campbell Ling

Nuclear Chemistry Facility, San Jose State University, San Jose, California 95192

and Larry Kevan*

Department of Chemistry, Wayne State University, Detroit, Michigan 48202 *(Received July 12, 1976; Revised Manuscript Received November 30, 1976)*

H atoms and radicals in γ-irradiated $(CF_3)_2CHOH$ and $CF_3CF_2CF_2CH_2OH$ liquids have been spin trapped with phenyl *tert*-butyl nitrone. The H adduct yields are comparable to the radical adduct yields in contrast to the nonfluorinated alcohols in which the H adduct yield is only about 10^{-2} of the radical adduct yield. The coupling constants in the partially fluorinated alcohols ($A^N \sim 17$ G and $A_\beta^H \sim 10$ G) are significantly larger than in the nonfluorinated alcohols ($A^N \sim 15$ G and $A_\beta^H \sim 8$ G) and change smoothly with mole fraction of the partially fluorinated alcohols.

Introduction

Thermal hydrogen atoms in γ-irradiated liquids have recently been detected by a spin trapping technique.[1] Spin trapping involves the addition of a short-lived reactive free radical to a nitroso or nitrone function to form a stable spin adduct nitroxide that can be observed by electron paramagnetic resonance (EPR) to identify the original radical. We use phenyl *tert*-butyl nitrone (PBN) as the spin trap for which the EPR spectra of various spin adducts have been discussed.[2] The spin adduct of PBN with H atoms has a characteristic β-proton splitting of ~7 G which distinguishes it from the spin adducts with other C, H, O, N containing radicals with $A_\beta^H = 1.5$–4 G.[3]

In γ-irradiated systems we have detected H-atom spin adducts with PBN in alkanes,[1] methanol,[4] and nitriles.[5] However in all of these systems the yield of H adduct has been quite low in comparison to the yields of alkyl radical spin adducts, methanol radical spin adducts, and cyanoalkyl radical spin adducts. The intensity of a certain spin adduct depends on the spin trapping efficiency, the stability of the spin adduct and other factors. We postulate that one reason for the low yields of H atom spin adducts in the systems previously is that the H atom can also react by H abstraction with the solvent molecules so that the net spin trapping efficiency by PBN is relatively low. To test this hypothesis we have looked for H-atom spin adducts in partially fluorinated solvents. We do find much higher yields of H atom spin adducts in partially fluorinated alcohols and we also find a relatively large solvent effect on the A_β^H splitting for the H adduct.

Experimental Section

Carbon tetrachloride, 1-butanol, and 2-propanol were supplied by Mallinckrodt Chemical Co.; hexafluoro-2*H*-propanol [$(CF_3)_2CHOH$] and heptafluorodi-1*H*-1-butanol ($CF_3CF_2CF_2CH_2OH$) were supplied by PCR Inc.; di-*tert*-butyl nitroxide was supplied by Eastman Kodak; and phenyl *tert*-butyl nitrone (PBN) was supplied by Dr. N. LeBel of the Wayne State University Chemistry Department. All chemicals were used directly as received. Samples were made by standard vacuum line techniques, degassed three to four times, and sealed under a vacuum of <10 μ pressure. All concentrations are given in mol %. EPR spectra were taken on a Varian Associates E-4 X-band spectrometer. A Co-60 γ source with a dose rate of 0.19 Mrad h^{-1} was used for all irradiations. Doses were in the range of 0.002–0.2 Mrad. Fresh samples were used for each irradiation. Hyperfine coupling constants were calibrated against $^{55}Mn^{2+}$ in MgO at room temperature, using the value of 86.8 G given by Low[6] for the separation of the center two lines of the exhibited hyperfine sextet.

Results

Figure 1 shows the EPR spectrum of γ-irradiated $CF_3CF_2CF_2CH_2OH$ containing 3 mol % PBN at room temperature. This spectrum can be interpreted as due to two spin adducts. One spin adduct is characterized by a triplet of doublets as marked on the figure and is assigned to an alkyl type of radical species with coupling constants of $A^N = 15.5$ G and $A_\beta^H = 3.0$ G. This radical species is tentatively assigned as $CF_3CF_2CF_2\dot{C}HOH$. The other spin adduct is characterized by a triplet of triplets which overlap with coupling constants of $A^N = 16.4$ G and $A_\beta^H = 9.7$ G. The large β proton coupling constant indicates that this radical is the H atom spin adduct of PBN. It is seen in Figure 1 that the relative intensities of the two spin adducts are comparable. This is in contrast to the methanol system, for example, where the H atom spin adduct is only a few percent of the radical spin adduct.[4]

The H atom spin adduct in Figure 1 begins to exhibit microwave power saturation at about 10 mW and the optimum power for observation seems to be about 2 mW. Typically no spin adducts were observable below 1 mol % PBN and below 0.003 Mrad radiation dose. Studies were made of the spectral intensity vs. PBN concentration and the optimum results were obtained between 1 and 3 mol % PBN. Higher concentrations of PBN up to 25 mol % gave little increase in the total radical intensity. Between 0.003 and 0.15 Mrad there was a slow increase in the overall spectral intensity. Increasing radiation dose appears to have little affect on the ratio of the H atom adduct to the radical adduct, although there is perhaps a twofold increase in the lower dose range.

Figure 2 shows the spin adducts observed in γ-irradiated $(CF_3)_2CHOH$ containing 10 mol % PBN at room temperature. This spectrum appears more complicated than that in Figure 1 because of the presence of an additional radical spin adduct. The spectrum can be interpreted as due to a total of three spin adducts. Two of these are triplets of doublets with a relatively small A_β^H coupling characteristic of alkyl type radical addition to PBN. The

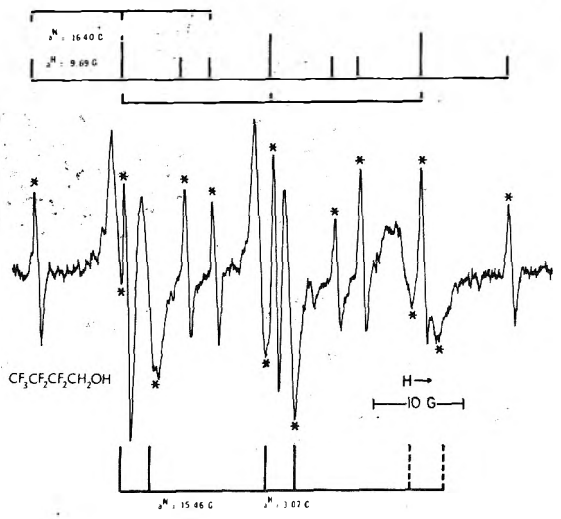

Figure 1. EPR spectrum of 3 mol % PBN in $CF_3CF_2CF_2CH_2OH$ γ irradiated to 0.1 Mrad at room temperature. The H atom adduct is denoted by the triplet of triplets (which overlap) marked by asterisks at the top of the spectrum. The radical adduct is denoted by the triplet of doublets marked by asterisks at the bottom of the spectrum.

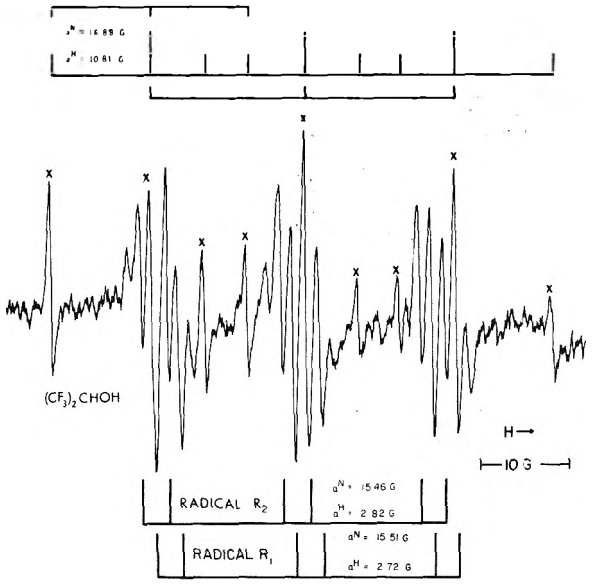

Figure 2. EPR spectrum of 10 mol % PBN in $(CF_3)_2CHOH$ γ irradiated to 0.05 Mrad at room temperature. The H atom adduct is denoted by the triplet of triplets (which overlap) marked by asterisks at the top of the spectrum. Two radical adducts are denoted by two sets of triplets of doublets.

H atom spin adduct is also clearly observed with its now characteristic spectrum of a triplet of triplets which overlap. The coupling constants for these spin adducts are summarized in Table I. We suggest that one of the radical spin adducts is due to the trapping of $(CF_3)_2\dot{C}OH$ but a tentative identification for the other radical that is trapped is difficult. Cleavage of C–C bonds has been observed in γ-irradiated perfluoroalkanes by spin trapping.[7] We suggest that fluorine atom loss does not occur with very great probability and suspect C–C bond cleavage as a possibility to produce other radicals. This could lead to CF_3 and to CF_3CHOH radicals. The CF_3 spin adduct has been observed previously in benzene but in this solvent it has much lower coupling constants than those observed in Figure 2, i.e., A^N = 13.3 G, A_β^H = 1.54 G, and A_γ^F = 1.54 G. Although the coupling constants might be considerably changed by the fluorinated solvent here, we feel we can exclude the CF_3 spin adduct since we do not see a fluorine coupling.

TABLE I: Hyperfine Coupling Constants of *tert*-Butyl α-Substituted Benzyl Nitroxides [$C_6H_5CHRNOC(CH_3)_3$] at Room Temperature

R	Solvent	$A^{N,a}$ G	$A_\beta^{H,a}$ G
H	$CF_3CF_2CF_2CH_2OH$	16.40	9.69
H	$CH_3CH_2CH_2CH_2OH$	15.4	8.1
H	$(CF_3)_2CHOH$	16.89	10.81
H	$(CH_3)_2CHOH$	15.6	7.8
$CF_3CF_2CF_2\dot{C}HOH$?	$CF_3CF_2CF_2CH_2OH$	15.46	3.02
R_1 [b]	$(CF_3)_2CHOH$	15.51	2.72
R_2 [b]	$(CF_3)_2CHOH$	15.46	2.82

[a] ± 0.1 G when given to nearest 0.1 G; ± 0.03 G when given to nearest 0.01 G. [b] Either R_1 or R_2 is tentatively assigned to $(CF_3)_2\dot{C}OH$; the other radical is unassigned.

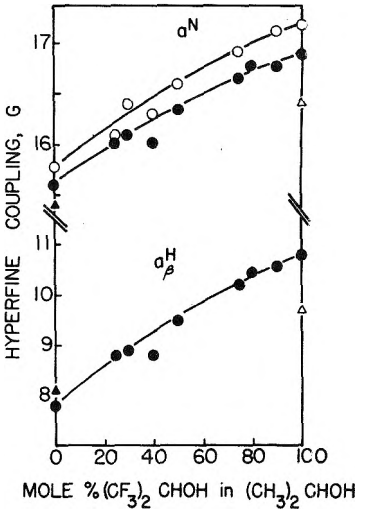

Figure 3. Hyperfine coupling constant variation in mixtures of $(CF_3)CHOH$ in $(CH_3)_2CHOH$ at room temperature for a^N in di-*tert*-butyl nitroxide (○) and a^N and a_β^H in the H atom adduct with PBN (●). The a^N and a_β^H values for the H adduct with PBN are also shown in pure $CH_3CH_2CH_2CH_2OH$ (▲) and in pure $CF_3CF_2CF_2CH_2OH$ (△).

The effects of PBN concentration and radiation dose on the intensities of the spin adducts in γ-irradiated $(CF_3)_2CHOH$ are similar to those found for $CF_3CF_2CF_2CH_2OH$.

We felt that it was rather striking that the H atom adducts in these partially fluorinated alcohols had significantly larger coupling constants than those observed in nonfluorinated alcohols. From Table I it is seen that the A^N values of 16.5–17.5 G are significantly larger than the ~14–15 G observed for a variety of protiated solvents including benzene, alkanes, alcohols, and nitriles.[1-5] Also the A_β^H values of about 10 G in Table I are much larger than the ~7-G values observed in protiated solvents. We therefore studied the coupling constants for the H atom adduct of PBN in mixtures of $(CF_3)_2CHOH$ and $(CH_3)_2CHOH$ at room temperature. The results are summarized in Figure 3. To test whether these results were characteristic of nitroxides in general, we also studied the nitrogen coupling for di-*tert*-butyl nitroxide in the same mixed solvent at room temperature. The results for this nitroxide parallel those for the H adduct with PBN. There is a smooth trend in coupling constants with mole fraction of the partially fluorinated alcohol.

As previously noted, the ratio of the H atom spin adduct to the radical spin adduct in the partially fluorinated alcohol is much larger than that in protiated solvents. To investigate this difference more quantitatively we studied the radical yields in mixtures of $(CF_3)_2CHOH$ and $(CH_3)_2CHOH$. The overall radical yield increases 2–3-fold as the composition changes from the partially fluorinated

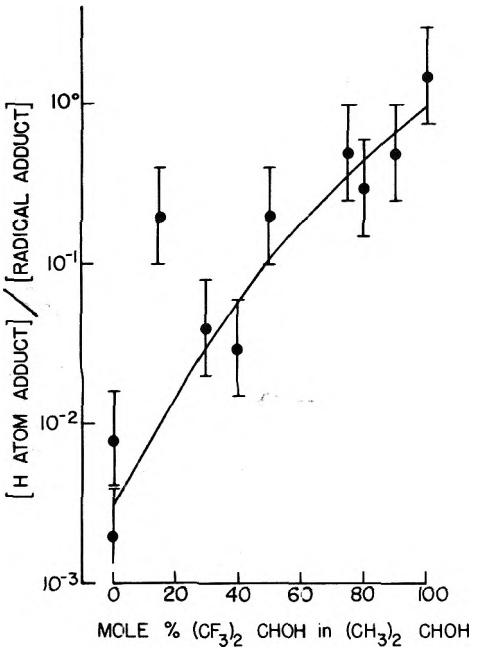

Figure 4. Relative yield of H atom adduct of PBN to one radical adduct of PBN in γ-irradiated (0.1 Mrad) mixtures of $(CF_3)_2CHOH$ and $(CH_3)_2CHOH$ at room temperature.

solvent to the protiated solvent. However, the relative mole percent of the protiated solvent increases. This latter trend is shown in Figure 4.

The H atom spin adducts appeared to decay by second-order kinetics and decayed more rapidly in partially fluorinated solvents than in fully protiated solvents.

Discussion

We have found that the relative yields of the H adduct and radical adducts are comparable in partially fluorinated alcohols (Figures 1 and 2) in contrast to fully protiated alcohols. In mixtures of protiated and fluorinated alcohols the overall radical yield decreases by 2–3-fold as 100 mol % protiated alcohol is reached. This reflects either a difference in the radiation stability of the protiated and fluorinated alcohols or more effective spin trapping of $(CH_3)_2\dot{C}OH$ compared to $(CF_3)_2\dot{C}OH$ by PBN. However, the major feature of the yield in the mixed solvent experiments is that the ratio of H adduct yield to radical adduct yield increases by over 100-fold on going from the protiated to the fluorinated alcohol. This presumably reflects a change in the loss pathways for H atoms as a function of solvent nature. In the protiated alcohols the H atoms can decay by H abstraction from any position in the alcohol. In the partially fluorinated alcohols F abstraction by H atoms has a much higher activation energy which hinders H loss by this mechanism. Thus, PBN competes more effectively for the H atom and increases the relative H adduct yield in partially fluorinated solvents.

Figure 3 shows that the origin of the large hyperfine constants of the H adducts in partially fluorinated alcohols is clearly a solvent effect associated with fluorine substitution in the solvent. The increase in A^N may be due to specific solvation effects at the nitroxide moiety. The relatively large (20–40%) increase in A_β^H is most reasonably attributed to rather small conformational changes due to solvation. The β-proton splitting is related to the dihedral angle θ between the β-hydrogen–carbon–nitrogen plane and the carbon–nitrogen–p-orbital plane. From the approximate relationships[8] A_β^H (G) $\sim 50 \cos^2 \theta \rho_N$ and A^N (G) $\sim 35.6\rho_N$ the coupling constant changes from $(CH_3)_2CHOH$ to $(CF_3)_2CHOH$ only correspond to a change in θ from 53.4 to 47.6° ($\Delta\theta \sim 6°$) and the coupling constant changes from $CH_3CH_2CH_2CH_2OH$ to $CF_3CF_2CF_2CH_2OH$ only correspond to 52.3 to 49.5° ($\Delta\theta \sim 3°$).

Acknowledgment. We are grateful to the Energy Research and Development Administration for partial support of this research under Contract No. E(11-1)-2086. A.C.L. wishes to thank the West Virginia University Senate Grant Committee for a summer stipend.

References and Notes

(1) S. W. Mao and L. Kevan, *J. Phys. Chem.*, **78**, 91 (1974).
(2) E. G. Janzen, *Acc. Chem. Res.*, **4**, 31 (1971).
(3) E. G. Janzen and B. J. Blackburn, *J. Am. Chem. Soc.*, **91**, 4481 (1969).
(4) S. W. Mao and L. Kevan, *Chem. Phys. Lett.*, **24**, 505 (1974).
(5) S. W. Mao and L. Kevan, *J. Phys. Chem.*, **80**, 2330 (1976).
(6) W. Low, *Phys. Rev.*, **101**, 1827 (1956).
(7) G. B. Caflisch and A. C. Ling, unpublished work.
(8) E. G. Janzen, B. R. Knauer, L. T. Williams, and W. B. Harrison, *J. Phys. Chem.*, **74** 3025 (1970).

The Effect of Nonclassical Behavior on the Solubilities of Gases in Liquids

Saul Goldman

Guelph-Waterloo Centre for Graduate Work in Chemistry, Guelph Campus, Department of Chemistry, University of Guelph, Guelph, Ontario N1G 2W1, Canada *(Received October 12, 1976)*

Publication costs assisted by the National Research Council of Canada

The Leonard–Henderson–Barker perturbation theory of mixtures was extended to include first-order Helmholtz free energy terms that accounted for the nonclassical translational behavior of the solute and the solvent in a binary liquid solution. From thermodynamics and this equation, expressions were obtained for the Henry's law constant, the heat of solution, and the partial molar volume of a solute in a solvent. The equation for the Henry's law constant contained two terms that explicitly represented the first-order quantum correction due to nonclassical behavior of the two solution components. The equations were applied to the following systems at low temperatures: H_2 in N_2, Ar, CH_4; He in N_2, Ar, CH_4; Ne in N_2, Ar; and to each of H_2, He, and Ne in benzene at ordinary and elevated temperatures. Inclusion of the quantum correction was important, and resulted in improved agreement with experiment, relative to the classical calculation, for all the simple systems. The agreement with experiment was very good for those simple systems wherein H_2 and Ne were the solutes, and was fair for those in which He was the solute. For all the systems studied, the effect of including the quantum correction was to increase the calculated values of the Henry's law constant, the heat of solution, and the partial molar volume of the solute. The effect of the correction was greatest on the heat of solution and least on the partial molar volume. The quantum correction was estimated to be small, but not quite negligible, for H_2 in benzene at ordinary temperatures. The corrections were negligible for He and Ne in benzene at ordinary and elevated temperatures.

Introduction

The thermodynamic perturbation theories[1-3] developed over the past 10 years represent the most promising theoretical approach to the liquid state that is now available. These theories have all been extended to binary mixtures of simple liquids,[4-6] and can be used as the basis for the derivation of a truly fundamental solubility theory. Thus, Neff and McQuarrie[7] used the Leonard–Henderson–Barker first-order mixture theory[4] to derive explicit expressions for the Henry's law constant, K,[8] the heat of solution at infinite dilution, $\Delta H_s^\bullet$, and the partial molar volume at infinite dilution, $\bar{V}_2^\bullet$, for a gas in a liquid. These authors applied their expressions to the system Ne in Ar, and found that their results agreed quite well with the corresponding experimental values.

In this work, the Leonard–Henderson–Barker first-order theory is modified so as to include first-order correction terms for the quantum behavior of both the solute and the solvent in a binary liquid mixture. Subsequent thermodynamic manipulations lead to quantum-corrected expressions for ln K, $\Delta H_s^\bullet$, and $\bar{V}_2^\bullet$. These expressions are applied to solutions of H_2, He, and Ne in simple solvents at low temperatures and to solutions of H_2, He, and Ne in benzene at ordinary and elevated temperatures.

The purpose of carrying out this work was twofold. First, it was considered desirable to improve on previously published semiempirical quantum corrections for liquid solutions,[9,10] by deriving theoretical expressions for the correction terms. Second, it was suspected that the effect of these corrections might be larger than had previously been supposed so that this problem merited detailed consideration. This suspicion arose from the physical picture outlined below.

Consider the problem of a particle in a box.[11] The sum that defines the particle partition function

$$q = \sum_{\substack{n_x,n_y,\\ n_z=1}}^{\infty} e^{-\epsilon_{n_x,n_y,n_z}/kT}$$

is well approximated by an integral (i.e., the classical limit) if

$$\Delta\epsilon/kT << 1$$

or, for a cubic box if

$$MTl^2 >> 2.4 \times 10^{-14} \text{ g cm}^2 \text{ K/mol} \quad (1)$$

In eq 1, M is the molecular weight of the particle, T is the absolute temperature, and l is the length of one edge of the box. For purposes of this illustration we identify l with the mean free path (mfp) of a solute. Clearly, the mfp of a solute dissolved in a liquid solvent will be very much smaller from its value in the gas phase. Specifically, consider the mfp of Ne, first when it is present at infinite dilution in a medium of gaseous Ar at 1 atm of Ar at the normal boiling point of Ar (87.29 K), and then again when it is present at infinite dilution in liquid Ar at this temperature.

The mfp of the solute (component 2) in a binary mixture can be estimated from kinetic theory by[12]

$$l_2 = \left(\sqrt{2}\,\pi\rho_2 d_{22}^2 + \pi\rho_1 d_{12}^2\left[1 + \frac{M_2}{M_1}\right]^{1/2}\right)^{-1} \quad (2)$$

where ρ_i, M_i are respectively the particle number density and the molecular weight of component i, and d_{ij} is the diameter between particles i and j. By applying eq 2 to Ne in gaseous Ar at 1 atm and 87.29 K, with $d_{12} = 3.077 \times 10^{-8}$ cm (Table I):

$$\lim_{\rho_2 \to 0} l_2 = 3.3 \times 10^{-6} \text{ cm}$$

Substituting this value for l into inequality 1:

$$MTl^2 = 1.9 \times 10^{-8} >> 2.4 \times 10^{-14} \text{ g cm}^2 \text{ K/mol}$$

From eq 2 applied to Ne at infinite dilution in liquid Ar at 87.29 K ($\rho_1 = 2.101 \times 10^{22}$ cm^{-3}):[13]

$$\lim_{\rho_2 \to 0} l_2 = 1.3 \times 10^{-8} \text{ cm}$$

TABLE I: Lennard-Jones 6-12 Pair Potential Parameters σ (cm), ϵ/k (K), and ξ_{12}

Pair	$10^8\sigma$[a]	ϵ/k[a]	ξ_{12}[b]
H_2-H_2	2.928	37.00	
He-He	2.556	10.22	
Ne-Ne	2.748	35.58	
Ar-Ar	3.405	119.80	
N_2-N_2	3.620	100.15	
CH_4-CH_4	3.742	151.67	
C_6H_6-C_6H_6	4.860	432.00	
H_2-Ar	3.167	66.58	1.00
H_2-N_2	3.274	59.05	0.97
H_2-CH_4	3.335	72.66	0.97
H_2-C_6H_6	3.894	(126.43)	(1.00)
He-Ar	2.981	27.29	0.78
He-N_2	3.088	23.99	0.75
He-CH_4	3.149	23.62	0.60
He-C_6H_6	3.708	(66.45)	(1.00)
Ne-Ar	3.077	56.15	0.86
Ne-N_2	3.184	53.13	0.89
Ne-C_6H_6	3.804	(123.98)	(1.00)

[a] The values of σ and ϵ/k for all like pair interactions except those for C_6H_6-C_6H_6 were taken from Henderson and Leonard.[21] These values derive from second virial coefficient data and, for the heavier species Ar, N_2, CH_4, they are consistent with the thermodynamic properties of the pure liquids. The values for C_6H_6-C_6H_6 were taken from Goldman,[22] who obtained them by fitting an analytic form of the Chandler-Weeks-Andersen theory to vapor pressure data for pure benzene. The values of σ and ϵ/k for all unlike pair interactions were obtained from $\sigma_{12} = {}^1/_2(\sigma_{11} + \sigma_{22})$ and $\epsilon_{12} = \xi_{12}(\epsilon_{11}\epsilon_{22})^{1/2}$, respectively. [b] The values of ξ_{12} for all unlike pair interactions, except those involving C_6H_6, were taken from the mixture second virial coefficient data reported in ref 10. The values of ξ_{12} for the unlike pair interactions involving C_6H_6 were arbitrarily set equal to one; these highly approximate pair potentials were used only to obtain a rough estimate of the magnitude of the quantum effects in benzene.

Substituting this value for l into inequality 1 one obtains:

$$MTl^2 = 3.0 \times 10^{-13} \text{ g cm}^2 \text{ K/mol}$$

which is only ~10 times greater than 2.4×10^{-14} g cm^2 K/mol. Hence the condition required to ensure the applicability of the classical limit for calculating thermodynamic functions is not nearly as well-met for a solute in a liquid phase as it is for the same solute at the same temperature in the gas phase. This six order of magnitude difference in the validity of the classical limit, and the result that the behavior of Ne in liquid Ar at the normal boiling point of Ar is not overwhelmingly classical, suggested the need for the correction terms derived below.

Derivation

For a system in which the total potential energy is given by a sum of pair potentials, the Leonard–Henderson–Barker theory[4] provides the following expression for the Helmholtz free energy of the mixture:

$$A(\text{classical}) = A^{HS} - (4\pi\rho_1 N_2 d_{12}^2/\beta) g_{12}^{HS}(d_{12})[d_{12} - \delta_{12}] + 2\pi \sum_{i,j} \rho_i N_j \int_{\sigma_{ij}}^{\infty} r^2 u_{ij}(r) g_{ij}^{HS}(r)\, dr \qquad (3)$$

where β is $1/kT$, A is the Helmholtz free energy of the real system, A^{HS} and $g_{ij}^{HS}(r)$ are respectively the Helmholtz free energy and the two-body radial distribution function for the hard-sphere reference mixture, d_{ij} is the hard-sphere diameter between particles i and j, $u_{ij}(r)$ is the potential energy of interaction between particles i and j, ρ and N are the particle number density and number of particles respectively, $g_{12}^{HS}(d_{12})$ is the two-body hard-sphere contact radial distribution function between particles 1 and 2, σ_{ij} is the distance at which $u_{ij}(r)$ is zero and

$$\delta_{12} = \int_0^{\sigma_{12}} (1 - e^{-\beta u_{12}(r)})\, dr$$

$$d_{11} = \int_0^{\sigma_{11}} (1 - e^{-\beta u_{11}(r)})\, dr$$

$$d_{22} = \int_0^{\sigma_{22}} (1 - e^{-\beta u_{22}(r)})\, dr$$

$$d_{12} = {}^1/_2(d_{11} + d_{22})$$

If, in the above pair-wise additive system, the quantum deviations are small, then one can expand the free energy in powers of h^2 to obtain, to order h^2:[14,15]

$$A = A(\text{classical}) + A(\text{quantum})$$

$$A(\text{quantum}) = \frac{h^2}{24\pi^2} \beta \sum_{i,j} \frac{N_i \rho_j}{m_i} \int_{d_{ij}}^{\infty} r^2 \nabla^2 u_{ij}(r) g_{ij}^{HS}(r)\, dr \qquad (4)$$

where h is Plank's constant, m is the molecular mass, and A(classical) is given by eq 3. From eq 4 and the definition of the chemical potential in a binary system:

$$\mu_2 = (\partial A/\partial N_2)_{N_1 TV} \qquad (5)$$

it follows that

$$\mu_2 = \mu_2(\text{classical}) + \mu_2(\text{quantum}) \qquad (6)$$

where

$$\mu_2(\text{classical}) = (\partial A(\text{classical})/\partial N_2)_{N_1 TV}; \mu_2(\text{quantum}) = (\partial A(\text{quantum})/\partial N_2)_{N_1 TV}$$

From thermodynamics

$$\ln K = \beta[(\mu_2^\circ)_l - (\mu_2^\circ)_g] \qquad (7)$$

where

$$(\mu_2^\circ)_l = \lim_{X_2 \to 0} [(\mu_2)_l - \beta^{-1} \ln X_2]$$

In eq 7 the superscript degree denotes standard state, the outer subscripts l and g denote liquid and gaseous phases respectively, X denotes mole fraction, and K is the Henry's law constant. The standard state for the solute in the gas is the ideal gas at 1 atm and temperature T, and its standard state in solution is the hypothetical unit mole fraction solution at T.

Since in all the systems to be studied here, the gas phase will be sufficiently attenuated and at a high enough temperature to be considered both ideal and classical

$$(\mu_2^\circ)_g = -\frac{1}{\beta} \ln \left[\left(\frac{2\pi m_2 kT}{h^2} \right)^{3/2} \beta^{-1} \right] \qquad (8)$$

Combining eq 6–8, and using the supercript • to denote the limit $X_2 \to 0$, one obtains after rearrangement

$$\ln K = \ln (RT/\bar{V}_1) + \beta\mu_2^\bullet(\text{classical}) + \beta\mu_2^\bullet(\text{quantum}) \qquad (9)$$

where

$\bar{V}_1$ = molar volume of the pure solvent

$$\beta\mu_2^\bullet(\text{classical}) = \beta\mu_2^\bullet(\text{hard sphere}) + 4\pi\rho_1 d_{12}^2 (d_{12} - \delta_{12}) g_{12}^{HS}(d_{12}) + I_{11}^\bullet + I_{12}^\bullet$$

$$\beta\mu_2^\bullet(\text{hard sphere}) = \beta f^\bullet + N_1 \left(\frac{\partial(\beta f)}{\partial N_2} \right)^\bullet_{N_1 TV}$$

(see Appendix)

$$I_{11}^\bullet = 2\pi\rho_1 N_1 \beta \int_{\sigma_{11}}^{\infty} r^2 u_{11}(r) \left(\frac{\partial g_{11}^{HS}(r)}{\partial N_2} \right)^\bullet_{N_1 TV} dr$$

$$I_{12}^{\bullet} = 4\pi\rho_1\beta\int_{\sigma_{12}}^{\infty} r^2 u_{12}(r) g_{12}^{HS\bullet}(r)\, dr$$

$$\beta\mu_2^{\bullet}(\text{quantum}) = Q_{11}^{\bullet} + Q_{12}^{\bullet}$$

$$Q_{11}^{\bullet} = \frac{h^2\beta^2 N_1\rho_1}{24\pi m_1}\int_{d_{11}}^{\infty} r^2\nabla^2 u_{11}(r)\left\{\frac{\partial g_{11}^{HS}(r)}{\partial N_2}\right\}_{N_1TV}^{\bullet} dr$$

$$Q_{12}^{\bullet} = \frac{h^2\beta^2\rho_1(m_1+m_2)}{24\pi m_1 m_2}\int_{d_{12}}^{\infty} r^2\nabla^2 u_{12}(r) g_{12}^{HS\bullet}(r)\, dr$$

The significance of the various terms in eq 9 is of interest. The first term accounts for the difference in the standard state of the solute in the two phases. The second term consists of a term due to the hard-sphere reference system, the difference term that arises from the fact that the hard-sphere diameters are taken to be additive,[4] and the integrals $I_{11}^{\bullet}$ and $I_{12}^{\bullet}$ that come from the perturbation potentials in the system. Our classical term differs from one derived elsewhere,[7] in that here the somewhat more accurate equation of state due to Mansoori et al.[15] is used for the reference system, rather than the equation of state from the Percus–Yevick theory used with the compressibility relationship. The expressions for $\beta f^{\bullet}$ and $(\partial(\beta f)/\partial N_2)^{\bullet}$ are lengthy but straightforward and are given in the Appendix.

The term $\beta\mu_2^{\bullet}$(quantum) is new to solubility theory. The integral $Q_{12}^{\bullet}$ corrects from quantum deviations that arise in the calculation of the solute–solvent interaction energy. The physical significance of the $Q_{11}^{\bullet}$ term is somewhat more subtle. It accounts for the perturbing influence of the solute on the quantum correction that arises in the calculation of the solvent–solvent interaction energy. In all our calculations, it was found that $Q_{12}^{\bullet}$ and $Q_{11}^{\bullet}$ were both positive, and that $Q_{12}^{\bullet}$ was always larger than $Q_{11}^{\bullet}$.

Calculations

Lebowitz' solution of the Percus–Yevick equation for a binary hard-sphere mixture[17] was used for the Laplace transform of $rg_{ij}^{HS}(r)$. Therefore the integrals in eq 9 were recast as follows:[18]

$$I_{12}^{\bullet} = 4\pi\rho_1\beta\int_{\sigma_{12}}^{\infty}(ru_{12}(r))(rg_{12}^{HS\bullet}(r))\, dr$$
$$= 4\pi\rho_1\beta\left[\int_0^{\infty} U_{12}(s) G_{12}^{\bullet}(s)\, ds - \int_{d_{12}}^{\sigma_{12}} r^2 u_{12}(r) g_{12}^{HS\bullet}(r)\, dr\right]$$

$$I_{11}^{\bullet} = 2\pi\rho_1 N_1\beta\int_{\sigma_{11}}^{\infty}(ru_{11}(r))\left(r\left(\frac{\partial g_{11}^{HS}(r)}{\partial N_2}\right)_{N_1TV}^{\bullet}\right) dr$$
$$= 2\pi\rho_1 N_1\beta\left[\int_0^{\infty} U_{11}(s)\left(\frac{\partial G_{11}(s)}{\partial N_2}\right)_{N_1TV}^{\bullet} ds - \int_{d_{11}}^{\sigma_{11}} r^2 u_{11}(r)\left(\frac{\partial g_{11}^{HS}(r)}{\partial N_2}\right)_{N_1TV}^{\bullet} dr\right]$$

$$Q_{12}^{\bullet} = \frac{h^2\beta^2\rho_1(m_1+m_2)}{24\pi m_1 m_2}\int_{d_{12}}^{\infty}(r\nabla^2 u_{12}(r))(rg_{12}^{HS\bullet}(r))\, dr$$
$$= \frac{h^2\beta^2\rho_1(m_1+m_2)}{24\pi m_1 m_2}\int_0^{\infty} U_{12}'(s) G_{12}^{\bullet}(s)\, ds$$

$$Q_{11}^{\bullet} = \frac{h^2\beta^2\rho_1 N_1}{24\pi m_1}\int_{d_{11}}^{\infty}(r\nabla^2 u_{11}(r))(r)\left(\frac{\partial g_{11}^{HS}(r)}{\partial N_2}\right)_{N_1TV}^{\bullet} dr$$
$$= \frac{h^2\beta^2\rho_1 N_1}{24\pi m_1}\int_0^{\infty} U_{11}'(s)\left(\frac{\partial G_{11}(s)}{\partial N_1}\right)_{N_1TV}^{\bullet} ds$$

where

$$G_{ij}(s) = \int_{d_{ij}}^{\infty} e^{-sr} r g_{ij}^{HS}(r)\, dr$$

$$ru_{ij}(r) = \int_0^{\infty} e^{-sr} U_{ij}(s)\, ds$$

$$r\nabla^2 u_{ij}(r) = \int_0^{\infty} e^{-sr} U_{ij}'(s)\, ds$$

Radial Distribution Function. Explicit expressions for $G_{11}(s)$ and $G_{12}(s)$ for a binary hard-sphere mixture of any composition have been given elsewhere.[17] From these expressions it may be shown that

$$G_{12}^{\bullet}(s) = s^2 e^{sd_{12}}\{[0.75(-\eta_1 d_{11}^3)(d_{22}-d_{11}) - d_{12}(1 + (\xi^{\bullet}/2))]s - (1+2\xi^{\bullet})\}/D^{\bullet}(s)$$

$$N_1\left(\frac{\partial G_{11}(s)}{\partial N_2}\right)_{N_1T,V}^{\bullet} = \frac{s}{12\eta_1 D^{\bullet}(s)}\left(a + b(s) + \frac{L_2^{\bullet}(s) e^{sd_{22}}\gamma^{\bullet}(s)}{D^{\bullet}(s)}\right)$$

with

$$\xi^{\bullet} = \pi\rho_1 d_{11}^3/6 = \eta_1 d_{11}^3$$

$$D^{\bullet}(s) = S^{\bullet}(s)e^{2sd_{12}} - L_2^{\bullet}(s)e^{sd_{22}}$$

$$L_2^{\bullet}(s) = 12\eta_1[(1 + (\xi^{\bullet}/2))]d_{11}s^2 + 12\eta_1(1+2\xi^{\bullet})s$$

$$S^{\bullet}(s) = [12\eta_1(1+2\xi^{\bullet})]s - 18(\eta_1 d_{11}^2)^2 s^2 - 6(\eta_1 d_{11}^2)(1-\xi^{\bullet})s^3 - (1-\xi^{\bullet})^2 s^4$$

$$\gamma^{\bullet}(s) = a + b(s) - e^{sd_{11}}X(s) + e^{2sd_{12}}Y(s)$$

$$Y(s) = a + s[2\pi\rho_1(1+2\xi^{\bullet}) + 4\pi\rho_1 d_{22}^3\eta_1 - (d_{11}+d_{22})a] - 6\pi s^2\rho_1 d_{22}^3(\eta_1 d_{11}^2) + \pi\rho_1 d_{22}^3 s^3(\eta_1 d_{11}^2) - d_{22}^2\rho_1\pi s^3(1-\xi^{\bullet}) + (\pi/3)\rho_1 d_{22}^3(1-\xi^{\bullet})s^4$$

$$X(s) = 2\pi d_{22}s^2\rho_1[(1 + (\xi^{\bullet}/2)) + {}^3/_2\eta_1 d_{11}^2(d_{22}-d_{11})] + a + s[2\pi\rho_1(1+2\xi^{\bullet}) - d_{11}a]$$

$$b(s) = -e^{sd_{22}}\{12\eta_1 d_{11}s^2[(\pi/12)d_{22}^3\rho_1 + (\pi/4)d_{22}^2(d_{11}-d_{22})\rho_1] + s[4\pi\eta_1 d_{22}^3\rho_1 - 6\pi\eta_1 d_{22}(d_{22}-d_{11})^2\rho_1] + a\}$$

$$a = 6\pi\eta_1\rho_1(d_{22}-d_{11})^2$$

Intermolecular Potential Energy. The Lennard-Jones 6–12 pair potential is used for both $u_{11}(r)$ and $u_{12}(r)$. Thus

$$u_{ij}(r) = 4\epsilon_{ij}[(\sigma_{ij}/r)^{12} - (\sigma_{ij}/r)^6] \qquad r > d_{ij}$$

$$\nabla^2 u_{ij}(r) = \frac{\partial^2 u_{ij}(r)}{\partial r^2} + \frac{2}{r}\frac{\partial u_{ij}(r)}{\partial r} = 24\epsilon_{ij}\left[22\left(\frac{\sigma_{ij}^{12}}{r^{14}}\right) - 5\left(\frac{\sigma_{ij}^6}{r^8}\right)\right] \qquad r > d_{ij}$$

Hence

$$U_{ij}(s) = L^{-1}\{ru_{ij}(r)\} = 4\epsilon_{ij}[\sigma_{ij}^{12}(s^{10}/10!) - \sigma_{ij}^6(s^4/4!)]$$

$$U_{ij}'(s) = L^{-1}\{r\nabla^2 u_{ij}(r)\} = 24\epsilon_{ij}[22\sigma_{ij}^{12}(s^{12}/12!) - 5\sigma_{ij}^6(s^6/6!)]$$

where $L^{-1}\{f(r)\}$ means the inverse Laplace transform of f(r).

Method of Calculation. Gauss quadrature was used to obtain values for the integrals: d_{11}, d_{22}, δ_{12}, $Q_{11}^{\bullet}$, $Q_{12}^{\bullet}$, and the two larger integrals (the integrals over s) required for the calculation of $I_{11}^{\bullet}$ and $I_{12}^{\bullet}$. The small integrals (d_{11} to σ_{11} and d_{12} to σ_{12}) were approximated as described elsewhere,[7] and the contact radial distribution function needed for the term containing $(d_{12}-\delta_{12})$ was obtained from Lebowitz' solution of the Percus–Yevick equation.[17] For the integrations performed by Gauss quadrature, the intervals of integration were subdivided into seven sub-

TABLE II: Comparison of Calculated and Experimental Values of ΔH_s^* (cal/mol) and $\bar{V}_2^*$ (cm³/mol) for Simple Systems (T, K)

System	T	ΔH_s^*			$\bar{V}_2^*$		
		Classical[a]	Quantum[b]	Expt[c]	Classical[c]	Quantum[b]	Expt[c]
H_2 in N_2	77.35	−121	264	270	25.8	30.0	35–45
	90.00	23	350	315	34.3	39.4	
He in CH_4	95.00	531	641	1010	16.9	17.7	26
	125.00	716	795	1230	25.0	25.7	32
Ne in Ar	87.29	59	132	201	22.5	23.1	20–30
	87.42	60	132	232	22.6	23.2	
	115.80	386	437	597	39.7	40.5	40–50

[a] These values were obtained from eq 9–11, with the $\beta\mu_2^*$(quantum) term set equal to zero, and the parameters in Table I. [b] These values were obtained from eq 9–11, with the $\beta\mu_2^*$(quantum) term retained, and the parameters in Table I. [c] The experimental values for H_2 in N_2 and He in CH_4 were all taken from ref 23. The experimental values for ΔH_s^* for Ne in Ar are from ref 24 and those for $\bar{V}_2^*$ for Ne in Ar are from ref 25.

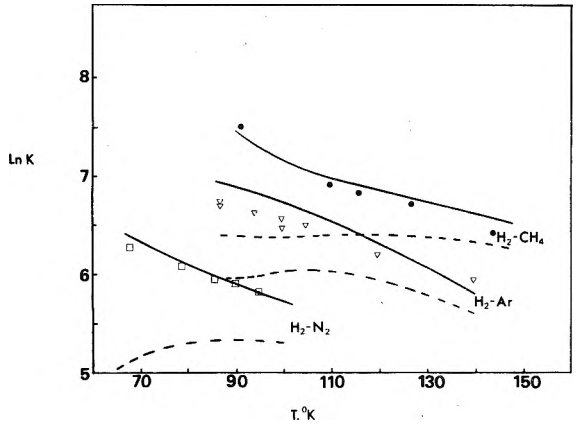

Figure 1. Calculated and experimental Henry's law constants for hydrogen. The solid and broken curves give the quantum-corrected and classical results, respectively. The solid curves were calculated by eq 9 and the parameters in Table I; the broken curves were obtained using the same parameters, but with the $\beta\mu_2^*$(quantum) term in eq 9 set equal to zero. The data source was ref 28: (●) H_2 in CH_4; (▽) H_2 in Ar; (□) H_2 in N_2.

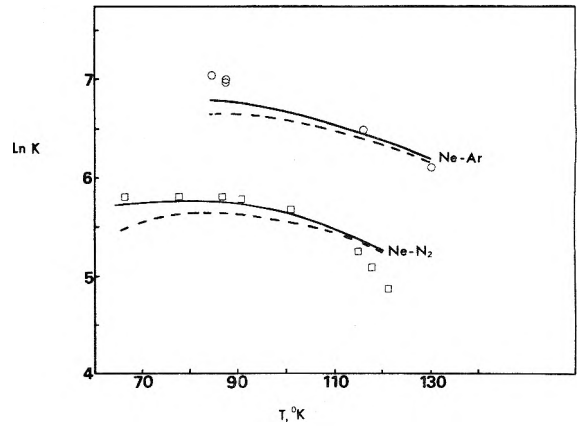

Figure 2. Calculated and experimental Henry's law constants for neon. Curves as explained in caption for Figure 1. The data sources were as follows: Ne–Ar, ref 24; Ne–N_2, ref 29: (O) Ne in Ar; (□) Ne in N_2.

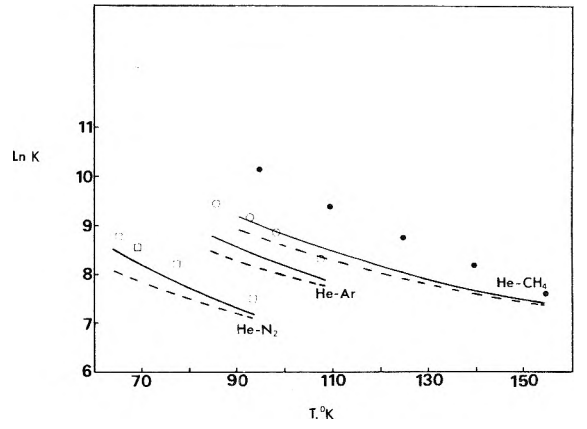

Figure 3. Calculated and experimental Henry's law constants for helium. Curves as explained in caption for Figure 1. The data source was ref 30: (●) He in CH_4; (O) He in Ar; (□) He in N_2.

intervals, each of which was integrated using 20 Gaussian points. Trial calculations wherein 40 Gaussian points were used in each subinterval resulted in the same answer to 10 figures. The Gaussian points were of 15 figure accuracy and double precision arithmetic was used throughout.

Once values for the Henry's law constant are calculable, then so too are the molar heat of solution of the solute at infinite dilution $\Delta H_s^\bullet$, and the partial molar volume of the solute at infinite dilution in the solvent $\bar{V}_2^\bullet$. From thermodynamics these quantities are connected to K by the relations

$$\Delta H_s^* = -RT^2 (\partial \ln K/\partial T)_p \quad (10)$$

$$\bar{V}_2^* = RT (\partial \ln K/\partial p)_T \quad (11)$$

The values of $\Delta H_s^\bullet$ and $\bar{V}_2^\bullet$ were obtained by numerical differentiation of eq 9. The accuracy of the calculations of K, $\Delta H_s^\bullet$, and $\bar{V}_2^\bullet$ was confirmed by applying our program, mutatis mutandis, to previously published work.[7]

Results

Values for K, $\Delta H_s^\bullet$, and $\bar{V}_2^\bullet$ were calculated by eq 9–11 over a range of temperatures for the following systems: H_2 in each of N_2, Ar, CH_4, C_6H_6; He in each of N_2, Ar, CH_4, C_6H_6; Ne in each of N_2, Ar, C_6H_6. These particular systems were chosen for the following reasons: (1) they all contained at least one light component; (2) for the simple systems (i.e., those in which the solvent was either N_2, Ar, or CH_4) meaningful comparisons with experimental data could be made; (3) the calculations in the complex liquid benzene were done in order to get an estimate of the quantum effect in a common solvent at ordinary and high temperatures.

Solvent densities are needed in eq 9, the constant pressure coefficient of thermal expansion of the solvent (α_p) is needed in eq 10, and the coefficient of isothermal compressibility of the solvent (β_T) is needed in eq 11. In all these calculations smoothed experimental values, taken from ref 13, were used for these quantities.

The values of the Lennard-Jones 6–12 pair potential parameters used are given in Table I.

Simple Systems. The experimental and calculated values of K for these systems are presented graphically in Figures 1–3, and the values obtained for $\Delta H_s^\bullet$ and $\bar{V}_2^\bullet$ (at temperatures where experimental values exist) are given in Table II. The calculations were performed using eq

TABLE III: Deviations between the Classically Calculated Values of K, $\bar{V}_2^*$, and ΔH_s^* and the Corresponding Quantum-Corrected Values for H_2, He, and Ne in C_6H_6 (t, °C; ΔH_s^*, cal/mol)

	K(quantum)/K(classical)[a]			$\bar{V}_2^*$(quantum)/$\bar{V}_2^*$(classical)[a]			ΔH_s^*(quantum) − ΔH_s^*(classical)[a,b]		
t	H_2	He	Ne	H_2	He	Ne	H_2	He	Ne
20	1.066	1.021	1.008	1.022	1.008	1.003	90	29	12
60	1.047	1.015	1.006	1.018	1.007	1.003	77	25	10
100	1.035	1.012	1.004	1.016	1.006	1.002	68	22	8.7
150	1.024	1.008	1.003	1.013	1.005	1.002	62	20	7.9
200	1.017	1.006	1.002	1.011	1.004	1.001	59	19	7.4

[a] The experimental values of K, $\bar{V}_2^*$, and ΔH_s^* for H_2 in C_6H_6 at 25 °C are 3.38×10^3 atm, 35 cm³/mol, and 1520 cal/mol, respectively.[26,27] [b] The results for the quantum effect on ΔH_s^* are expressed as a difference rather than a ratio, since ΔH_s^* for the H_2 in C_6H_6 system goes through zero in the range 20–200 °C.

9–11; the classically calculated values were obtained by setting the term $\beta\mu_2^\bullet$(quantum) in these equations equal to zero.

It is seen from Figure 1 that for all the simple systems containing H_2 as the solute, the quantum-corrected calculations for K give values that are either within, or very nearly within, experimental error. On the other hand, the classically calculated values of K for these systems, particularly at the lower temperatures, are poor. Clearly the quantum correction is essential for the interpretation of these systems.

The results for the Ne in Ar and Ne in N_2 systems are shown in Figure 2. Again, the agreement with the experimental values is good, although the calculated values of K appear to be somewhat low in Ar at the low temperatures and somewhat high in N_2 at the high temperatures. The discrepancy at low temperatures in Ar is probably due to experimental error, and/or uncertainties in the values of the Lennard-Jones parameters. Small changes in the values of σ, ϵ, and ξ_{12} have a large effect on the calculated values of K and on the shape of the ln K vs. T curve. However the discrepancy at high temperatures in N_2 is probably due, at least partly, to an inadequacy in the theory. Specifically, the adequacy of the first-order approximation for the free energy falls off at low densities,[19] and the density of N_2 is low and falls rapidly with temperature for temperatures above 110 K (ρ_{N_2}* (T = 110 K) = 0.633; ρ_{N_2}* (T = 120 K) = 0.537).[15] It is also apparent from Figure 2 that although Ne is the heaviest of our three solutes it is still sufficiently light to require the inclusion of a quantum correction in the vicinity of the triple points of N_2 and Ar (63.18 and 83.81 K, respectively).

It is seen from Figure 3 that the agreement with experiment for the He-containing systems is generally worse than it is for the H_2-containing and Ne-containing systems. Also, the size of the deviations follows the order He–CH_4 > He–Ar > He–N_2. Since He is intermediate in mass between H_2 and Ne, it seems unlikely that the discrepancies in the He-containing systems are due to any fault in our first-order quantum term. It is known, however, that when first-order perturbation theory is applied to mixtures, it accounts better for the excess properties (which are thermodynamically related to solubilities) when the ratios $\epsilon_{11}/\epsilon_{22}$ and σ_{11}/σ_{22} are about 1, than it does when these ratios deviate considerably from 1. Thus it seems likely that the discrepancies, apparent in Figure 3, result from the inability of the classical first-order perturbation theory (i.e., eq 3) to handle the very large ratios of $\epsilon_{11}/\epsilon_{22}$ that occur with the He-containing systems ($\epsilon_{11}/\epsilon_{22}$ = 9.80, 11.72, 14.84 for He–N_2, He–Ar, and He–CH_4, respectively). The relative effect of this problem will be greatest in the He-containing systems, since He has by far the smallest ϵ_{22} value of all the species here considered (Table I).

The calculated values of $\Delta H_s^\bullet$ and $\bar{V}_2^\bullet$ for the simple systems in which experimental comparisons are possible are given in Table II. It is seen from Table II that the effect of the quantum correction is to increase the calculated values of $\Delta H_s^\bullet$ and $\bar{V}_2^\bullet$, and that the effect is considerable on $\Delta H_s^\bullet$ but is fairly small on $\bar{V}_2^\bullet$. As may be anticipated from Figures 1–3, and the above discussion, the agreement with experiment of the quantum-corrected calculation is quite good for H_2 in N_2 and Ne in Ar but is only fair for He in CH_4. Uncertainties in the standard deviations of the experimental values of $\Delta H_s^\bullet$ and $\bar{V}_2^\bullet$ preclude the usefullness of a more detailed analysis of discrepancies between calculated and experimental values.

It is worthwhile noting that while the effect of the quantum correction was found to be substantial in many of these systems, the relative magnitude of the quantum terms is small. Specifically, $Q_{11}^\bullet$ and $Q_{12}^\bullet$ were never greater than 20% of $I_{11}^\bullet$ and $|I_{12}^\bullet|$, respectively. This result provides some justification for truncating the expansion in h^2 after the first term. The reason that $Q_{11}^\bullet$ and $Q_{12}^\bullet$ have an appreciable effect on the value of K despite their relatively small size is that the effect of the perturbation potentials, i.e., $(I_{11}^\bullet + I_{12}^\bullet)$ in eq 9 to a considerable degree cancels the effect of $\beta\mu_2^\bullet$(hard sphere). This occurs because the sum $(I_{11}^\bullet + I_{12}^\bullet)$ is negative and usually is comparable in magnitude to $\beta\mu_2^\bullet$(hard sphere) which is positive.

Solutions in Benzene. It seemed worthwhile to pursue the question of quantum effects on solubility by examining these effects at higher temperatures in a noncryogenic solvent. Benzene, because it is a very common solvent, was selected for this purpose. Of course, benzene is a complicated anisotropic liquid, it is not in corresponding states with our gaseous solutes, and its pair potential with these gases will not be well-represented by a simple Lennard-Jones expression. Consequently these calculations cannot and did not yield results that were in good agreement with experiment. However by taking ratios of or differences between the classically calculated and the quantum-corrected functions some of these uncertainties will cancel, so that an estimate of the size of the quantum effect in these systems may still be obtained.

Equations 9–11 together with the values of the parameters entered in Table I were used for these calculations, and the results are given in Table III. It may be concluded from this table that the classically calculated values of K and $\Delta H_s^\bullet$ for H_2 in C_6H_6 at ordinary temperatures are in error by 5–10%. The error in the classical result for $\bar{V}_2^\bullet$ for H_2, He, and Ne in C_6H_6 is essentially negligible, as is the error in the classical result for K and $\Delta H_s^\bullet$ for He and Ne in C_6H_6. In other words except for its effect on K and $\Delta H_s^\bullet$ for H_2 in C_6H_6 at ordinary temperatures, the quantum effect is negligible in these benzene systems. As expected from eq 9, and in line with out results on simple systems, the error entailed by omitting the quantum correction diminishes with increasing temperature.

Discussion

It is clear from even a cursory examination of Figures 1–3 and Table II that inclusion of the quantum correction results in improved agreement with experiment (relative to the classical result) for all the simple systems studied. The improvement is dramatic for systems containing H_2 as the solute (Figure 1). However even for the heaviest of our solutes, Ne, the effect of the quantum correction in the vicinity of the triple points of N_2 and Ar is not negligible. In this respect we have found that the effect of the quantum correction on calculated solubilities is greater than was hitherto supposed. Specifically in two previous studies where the solubility of Ne in condensed gases was considered[7,10] Ne was assumed to behave classically.

While the quantum correction resulted in improved agreement with experiment for all the simple He-containing systems, the accuracy of the final values obtained for K, ΔH_s^*, and $\bar{V}_2^*$ for these systems was only fair (Figure 3, Table II). As mentioned previously, these discrepancies are very likely due to the inability of the classical components of the theory to handle the large ratios of $\epsilon_{11}/\epsilon_{22}$ that occur in these systems. Consequently, improved agreement can be expected by either including a second-order term in the Leonard–Henderson–Barker mixture theory, or by using another first-order theory, such as the variational theory, that more accurately handles the problem of large $\epsilon_{11}/\epsilon_{22}$ and σ_{11}/σ_{22} ratios.[20] These calculations are presently under way.

The result that an infinitely dilute solution of H_2 in a solvent such as benzene manifests significant nonclassical behavior at ordinary temperatures has not (to the best of the author's knowledge) been previously reported, and was certainly not anticipated when these calculations were initiated. The conceptional explanation for this result (based on the rough analogy that may be made between a particle in a box and a solute in a solvent) may be stated as follows. For H_2 in liquid C_6H_6, the combined effects of the small mass of the particle and the small dimensions of the box, offset the otherwise nullifying effect that ordinary temperatures have on translational quantization (eq 1). The more precise explanation that comes out of our analysis is that because of the low value of m_2 for H_2, the Q_{12}^* term in eq 9 becomes large enough to be significant relative to the sum of the other terms on the right-hand side of eq 9 (the Q_{11}^* term for this system was only about 2% of the Q_{12}^* term).

The result that translational quantization is more important for a solute in a liquid than for the same solute in a gas has implications that go beyond solubility theory. To cite an example it seems likely that this effect would arise in the study of clathrates in which the caged molecule is light.

Acknowledgment. The author is grateful to the National Research Council of Canada for financial assistance.

Appendix

The equation of state of Mansoori et al.[16] is used for the reference state. The integrated form of this equation of state may be expressed in the form[5]

$$\frac{A - A(\text{ideal gas})}{NkT} = \beta f(\text{hard sphere})$$

$$= \frac{3 - 3y_1 - 3y_2 - y_3}{2(1-\eta)^2} + \frac{3y_2 + 2y_3}{1-\eta} - (1 - y_3)$$

$$\times \ln(1-\eta) - {}^3/_2(1 - y_1 + y_2 + y_3)$$

where

$$\eta = (\pi/6)(\rho_1 d_{11}^3 + \rho_2 d_{22}^3) = \eta_1 + \eta_2$$

$$y_1 = \frac{s_{12}(d_{11} + d_{22})}{(d_{11}d_{22})^{1/2}}$$

$$y_2 = s_{12}\left(\frac{\eta_1}{\eta}\frac{(d_{11}d_{22})^{1/2}}{d_{11}} + \frac{\eta_2}{\eta}\frac{(d_{11}d_{22})^{1/2}}{d_{22}}\right)$$

$$y_3 = \left(\left(\frac{\eta_1}{\eta}\right)^{2/3} x_1^{1/3} + \left(\frac{\eta_2}{\eta}\right)^{2/3} x_2^{1/3}\right)^3$$

$$s_{12} = \frac{(\eta_1\eta_2)^{1/2}}{\eta}\left(\frac{(d_{11} - d_{22})^2}{d_{11}d_{22}}\right)(x_1x_2)^{1/2}$$

$$N = N_1 + N_2$$

From this equation and the definition of the chemical potential in a binary system, one obtains for the limit $X_2 \to 0$

$$\beta\mu_2^*(\text{hard sphere}) = \beta f^* + N_1\left(\frac{\partial\beta f}{\partial N_2}\right)^*_{N_1TV}$$

where

$$\beta f^* = \frac{1}{(1-y)^2} + \frac{2}{(1-y)} - 3$$

$$N_1\left(\frac{\partial\beta f}{\partial N_2}\right)^*_{N_1TV} = T1 + T2 + T3 + T4$$

$$T1 = \frac{-3\left(N_1\frac{\partial y_1}{\partial N_2}\right)^* - 3\left(N_1\frac{\partial y_2}{\partial N_2}\right)^* - \left(N_1\frac{\partial y_3}{\partial N_2}\right)^*}{2(1-y)^2} + \frac{(\pi/3)d_{22}^3\rho_1^*}{(1-y)^3}$$

$$T2 = \frac{3\left(N_1\frac{\partial y_2}{\partial N_2}\right)^* + 2\left(N_1\frac{\partial y_3}{\partial N_2}\right)^*}{(1-y)} + \frac{(\pi/3)d_{22}^3\rho_1^*}{(1-y)^2}$$

$$T3 = \left(N_1\frac{\partial y_3}{\partial N_2}\right)^* \ln(1-y)$$

$$T4 = \frac{3}{2}\left[\left(N_1\frac{\partial y_1}{\partial N_2}\right)^* - \left(N_1\frac{\partial y_2}{\partial N_2}\right)^* - \left(N_1\frac{\partial y_3}{\partial N_2}\right)^*\right]$$

$$N_1\left(\frac{\partial y_1}{\partial N_2}\right)^* = \frac{(d_{11} + d_{22})(d_{11} - d_{22})^2}{d_{11}^3}$$

$$N_1\left(\frac{\partial y_2}{\partial N_2}\right)^* = \frac{(d_{11} - d_{22})^2 d_{22}}{d_{11}^3}$$

$$\left(N_1\frac{\partial y_3}{\partial N_2}\right)^* = \left[\left(\frac{d_{22}}{d_{11}}\right)^2 - 1\right]$$

$$y = \pi\rho_1^* d_{11}^3/6$$

References and Notes

(1) J. A. Barker and D. Henderson, *J. Chem. Phys.*, **47**, 4714 (1967).
(2) G. A. Mansoori and F. B. Canfield, *J. Chem. Phys.*, **51**, 4958 (1969).
(3) J. D. Weeks, D. Chandler, and H. C. Andersen, *J. Chem. Phys.*, **54**, 5237 (1971).
(4) P. J. Leonard, D. Henderson, and J. A. Barker, *Trans. Faraday Soc.*, **66**, 2439 (1970).
(5) G. A. Mansoori and T. W. Leland, Jr., *J. Chem. Phys.*, **53**, 1931 (1970).
(6) L. L. Lee and D. Levesque, *Mol. Phys.*, **26**, 1351 (1973).
(7) R. O. Neff and D. A. McQuarrie, *J. Phys. Chem.*, **77**, 413 (1973).
(8) The Henry's law constant K of a solute is defined by

$$K \equiv \lim_{x_2 \to 0} p_2/x_2$$

where p_2 is the partial pressure of the solute over the solution and x_2 is the mole fraction of the solute in the solution.
(9) R. C. Miller and J. M. Prausnitz, *Ind. Eng. Chem., Fundam.*, **8**, 449 (1969).
(10) R. C. Miller, *J. Chem. Phys.*, **55**, 1613 (1971).
(11) T. L. Hill, "An Introduction to Statistical Thermodynamics", Addison-Wesley, Reading, Mass., 1960, p 74.
(12) E. A. Moelwyn-Hughes, "Physical Chemistry", Pergamon Press, London, 1961, p 51.
(13) J. S. Rowlinson, "Liquids and Liquid Mixtures", Butterworths, London, 1969, pp 34, 46, 48, 51.
(14) H. S. Green, *J. Chem. Phys.*, **19**, 955 (1951).
(15) S. Kim, D. Henderson, and J. A. Barker, *Can. J. Phys.*, **47**, 99 (1969).
(16) G. A. Mansoori, N. F. Carnahan, K. E. Starling, and T. W. Leland, Jr., *J. Chem. Phys.*, **54**, 1523 (1971).
(17) J. L. Lebowitz, *Phys. Rev. A*, **133**, 895 (1964).
(18) H. L. Frisch, J. L. Katz, E. Praestgaard, and J. L. Lebowitz, *J. Phys. Chem.*, **70**, 2016 (1966).
(19) D. Henderson and J. A. Barker in "Physical Chemistry, An Advanced Treatise", Vol. VIIIA, H. Eyring, D. Henderson, and W. Jost, Ed., Academic Press, New York, N.Y., 1971, pp 377–412.
(20) G. A. Mansoori, *J. Chem. Phys.*, **56**, 5335 (1972).
(21) D. Henderson and P. J. Leonard in "Physical Chemistry, An Advanced Treatise", Vol. VIIIB, H. Eyring, D. Henderson, and W. Jost, Ed., Academic Press, New York, N.Y., 1971, p 420.
(22) S. Goldman, *J. Phys. Chem.*, **80**, 1697 (1976).
(23) L. A. K. Staveley, *J. Chem. Phys.*, **53**, 3136 (1970).
(24) W. B. Streett, *J. Chem. Phys.*, **42**, 500 (1965).
(25) W. B. Streett, *J. Chem. Phys.*, **46**, 3282 (1967).
(26) E. B. Smith and J. Walkley, *J. Phys. Chem.*, **66**, 597 (1962).
(27) J. H. Hildebrand and R. L. Scott, "Regular Solutions", Prentice-Hall, Englewood Cliffs, N.J., 1962.
(28) M. Orentlicher and J. M. Prausnitz, *Chem. Eng. Sci.*, **19**, 775 (1964).
(29) W. B. Streett, *Cryogenics*, **5**, 27 (1965).
(30) K. A. Solen, P. L. Chueh, and J. M. Prausnitz, *Ind. Eng. Chem., Process Des. Dev.*, **9**, 310 (1970).

Bends in Globular Proteins. A Statistical Mechanical Analysis of the Conformational Space of Dipeptides and Proteins[1-3]

S. Scott Zimmerman,[4a,b] Lester L. Shipman,[4b,c] and Harold A. Scheraga*[4b,d,e]

Department of Chemistry, Cornell University, Ithaca, New York 14853 and Department of Biophysics, Weizmann Institute, Rehovoth, Israel *(Received October 7, 1976)*

Average $C^{\alpha}_{i}\cdots C^{\alpha}_{i+3}$ distances and probabilities of formation of bends were calculated for the nine *N*-acetyl-*N'*-methylamide dipeptides containing alanine, glycine, and proline, using three methods of approximation. In the first method, conformational space was represented by summing the Boltzmann factors of the conformational energy at each of the local minima; in the second, by summing the statistical weights, which take into account librational entropy, at the local minima; and, in the third, by summing the Boltzmann factors of the conformational energy at specified intervals (usually 30° in each of the variable dihedral angles) over all conformational space. The results indicate that the conformational space of isolated dipeptides can be described adequately by considering only the local minima if librational entropy is taken into account properly. The probability distribution function, conformational volume distribution function, and probability density distribution function also were used to describe and compare the conformational space of the various dipeptides. A comparison of the calculated probabilities for formation of bends in isolated dipeptides with the results of a survey of the corresponding dipeptide sequences in the x-ray structures of 20 globular proteins suggests that, for many dipeptide sequences, bends in proteins are stabilized primarily by local interactions (i.e., those between atoms within the dipeptide) and not primarily by longer-range interactions. The analysis of x-ray structures also indicates that, although bends in proteins are not structurally as well defined as the α helix and β-pleated sheet, they are nevertheless distinguishable in a natural way from other nonregular structures in terms of their $C^{\alpha}_{i}\cdots C^{\alpha}_{i+3}$ distances and their average relative stabilities.

I. Introduction

The importance of the α helix and the β-pleated sheet in the structure of polypeptides and proteins has been recognized for some time.[5] However, many conformations of amino acid residues in proteins cannot be classified into one of these regular structures. One of the problems in understanding the factors which stabilize protein conformation and in predicting protein structure is the ambiguity in the classification of these nonregular structures[6] of proteins. In an effort to alleviate this problem to some extent, the bend conformation[7] has been proposed[8-12] as a type of structure which may play an important role in the folding of a polypeptide chain and in the stabilization of the native protein conformation. Recent theoretical[3,12-20] and experimental[18,21-23] work has sought to examine the occurrence of bends in peptides and to describe the properties of bends. The major purposes of the present study are (a) to assess the validity of three methods of approximation for calculating the conformational properties of dipeptides, (b) to analyze the effects of composition and sequence on the propensity for formation of bends in these dipeptides, (c) to assess the importance of local interactions[24] on the occurrence of bends in globular proteins, (d) to determine if bends are distinguishable in some natural way from other nonregular structure in proteins, and (e) to assess the usefulness of probability distribution functions, conformational volume distribution functions, and probability density distribution functions in characterizing bend and nonbend regions of the conformational space of a protein.

II. Molecules Examined

A. *Dipeptides.* Just as *N*-acetyl-*N'*-methylamides of single amino acid residues have served as models for an individual residue in a polypeptide chain,[25] *N*-acetyl-*N'*-methylamide dipeptides (see Figure 1) can serve as models for dipeptide segments in proteins. Moreover, these blocked dipeptides are the simplest polypeptides which can form a bend conformation. This paper deals with the nine *N*-acetyl-*N'*-methylamide dipeptides (which

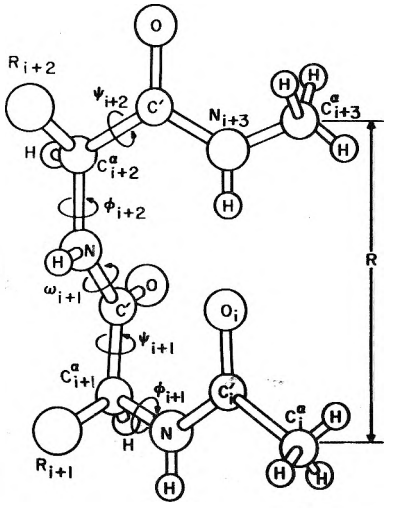

Figure 1. Schematic diagram of an *N*-acetyl-*N'*-methylamide dipeptide, showing the definition of the $C^{\alpha}_i \cdots C^{\alpha}_{i+3}$ distance *R*.

will be called simply "dipeptides"[26]) containing Ala, Gly, and Pro, viz., Ala-Ala, Ala-Gly, Ala-Pro, Gly-Ala, Gly-Gly, Gly-Pro, Pro-Ala, Pro-Gly, and Pro-Pro.

B. *Globular Proteins.* The x-ray structures of 20 globular proteins were examined to determine the conformational preferences of each of the dipeptide segments which have sequences corresponding to those of the nine *N*-acetyl-*N'*-methylamide dipeptides listed above. The 20 proteins, which are the same as those analyzed in a recent paper from this laboratory,[27] are myoglobin,[28] thermolysin,[29] cytochrome *b*,[30] tosyl elastase,[31] A, B, and C chains of tosyl α-chymotrypsin,[32] carboxypeptidase A,[33] papain,[34] bovine pancreatic trypsin inhibitor,[35] concanavalin A,[36] high potential iron protein,[37] hen egg-white lysozyme,[38] carp myogen,[39] subtilisin BPN',[40] ribonuclease S,[41] staphylococcal nuclease,[42] cytochrome c_2,[43] D-glyceraldehyde-3-phosphate dehydrogenase,[44] clostridial flavodoxin,[45] α and β chains of human deoxyhemoglobin,[46] and sea lamprey hemoglobin.[47]

The atomic coordinates of these proteins were supplied by the Protein Data Bank (Brookhaven National Laboratories, Upton, N.Y.), except those of tosyl elastase[31] and bovine pancreatic trypsin inhibitor,[35] which were taken directly from the references cited. Dihedral angles were calculated directly from these sets of x-ray coordinates and, therefore, in some cases, do not agree with the dihedral angles published by the crystallographer, who may have determined dihedral angles from coordinates at a different stage of refinement. The conformational states of all residues in these proteins, as determined from the atomic coordinates, are given in the supplement to ref 27.

Although four protein chains in the data set were globins (myoglobin, α and β chains of human deoxyhemoglobin, and sea lamprey hemoglobin), this does not bias the results since helical regions of the proteins were not included in the analysis (see Methods); and, considering only the nine dipeptide sequences containing Ala, Pro, or Gly, there is no occurrence of identical dipeptide sequences at homologous positions in the nonhelical regions of these globins.

III. Definitions and Methods

The nomenclature and conventions used here are those adopted by an IUPAC-IUB Commission.[48]

A. *Definitions of Conformation-Dependent Quantities.* Figure 1 illustrates certain quantities associated with the conformations of an *N*-acetyl-*N'*-methylamide dipeptide or of a dipeptide segment in a protein. The dihedral angles (ϕ, ψ, ω) are defined by the standard convention.[48] Of special interest to this discussion are the following definitions.

1. *The $C^{\alpha}_i \cdots C^{\alpha}_{i+3}$ Distance, R.* The quantity *R* is defined as the distance in the *N*-acetyl-*N'*-methylamide dipeptides between the methyl carbon of the acetyl group on the amino end and the methyl carbon of the *N'*-methyl group on the carboxyl end (see Figure 1). Analogously, *R* in proteins is defined as the distance between the C^{α} of a particular residue *i* and the C^{α} of residue *i* + 3.

2. *Definition of a Bend.* A bend is defined[9] as a conformation of an *N*-acetyl-*N'*-methylamide dipeptide in which $R \leq 7$ Å. In proteins, a bend is defined as a conformation of a dipeptide segment in which $R \leq 7$ Å and in which at least one of the residues is not in an α helix. This definition of a bend is independent of the presence or absence of an *i* + 3 to *i* (NH···OC) hydrogen bond.

3. *Definition of an α Helix in Proteins.* In proteins, if four or more consecutive residues have dihedral angles, $-130° \leq \phi \leq -10°$ and $-90° \leq \psi \leq -10°$, these residues are considered to be part of a right-handed α helix.[27,49] It should be noted that the average value of *R* for dipeptide segments in an α helix is about 5 Å,[12] which is within the same region of *R* as bends ($R \leq 7$ Å). Therefore, each dipeptide segment must be checked to see if it is part of an α helix before considering it a bend. If *both* residues are part of an α helix, the dipeptide is not considered a bend even though $R \leq 7$ Å.

4. *Definition of Extended Structure in Proteins.* In proteins, if four or more consecutive residues have dihedral angles, $-180° \leq \phi < 180°$ and $110° \leq \psi < 180°$, or $-180° \leq \phi < 180°$ and $-180° \leq \psi \leq -110°$, these residues are considered to be part of an extended structure. These ranges of dihedral angles are expanded from those given in ref 49 in order to conform to the definition of the ε conformational state as given in ref 27, from which the conformational states of the protein residues were obtained. The average value of *R* for dipeptide segments in an extended structure is about 10 Å.[12]

B. *Conformational Energy Calculations.* Conformational energy calculations were carried out using ECEPP (empirical conformational energy program for peptides), available from the Quantum Chemical Program Exchange.[50] The empirical potential energy functions and energy parameters are those described previously.[51] The total conformational energy *E* is the sum of the electrostatic energy, the nonbonded energy, and the torsional energy.[51] The hydrogen-bond energy is included in the nonbonded energy component.[51] Solvent was not taken into consideration explicitly in these calculations.

All bond lengths and bond angles were taken, without modification, from the standard ECEPP[50] data for all residues and end groups. The proline ring was taken in the "puckered down" position.[50,52] All non-Gly residues were taken in the L configuration.

C. *Energy Minimization.* The method used to search for the global minimum and all local low-energy minima has been described elsewhere.[20] In brief, the method involved the minimization of the total conformational energy from starting points which consisted of all combinations of single-residue minima,[53] standard bend conformations,[12] and a limited number of other selected conformations.[20] Minimization first was carried out using the algorithm of Powell.[54] Minimization was terminated when any of the following conditions was met: (a) the energy changed by less than 0.002 kcal/mol between any two iterations, (b) each of the variable dihedral angles changed by less than 0.02° between any two iterations, or

(c) ten iterations were completed. To refine the value of each dihedral angle to within less than 0.001° of a local minimum (so that accurate second derivatives at the minimum could be evaluated numerically), a multidimensional Newton–Raphson[55] procedure was then employed. During minimization, all backbone dihedral angles (and in the case of Ala, the side-chain dihedral angle) in the dipeptides were allowed to vary, except ω, which was held fixed at 180°. Dihedral angles in the end groups also were held fixed at 180°. Since ϕ of Pro is part of the pyrrolidine ring, it too was held fixed (at −75°) during minimization.

D. *Evaluation of Average Values of Conformation-Dependent Quantities.* Assuming that classical statistical mechanics are valid in this analysis,[56,57] the average or expectation value of a particular conformation-dependent quantity A is given by

$$\langle A\rangle_W = (1/W) \int_{q_1} \cdots \int_{q_r} A(q_1,\ldots,q_r) \times \exp[-U(q_1,\ldots,q_r)/RT]\mathrm{d}q_1 \ldots \mathrm{d}q_r \quad (1)$$

where W, the classical configuration integral,[58] is given by

$$W = \int_{q_1} \cdots \int_{q_r} \exp[-U(q_1,\ldots,q_r)/RT]\mathrm{d}q_1 \ldots \mathrm{d}q_r \quad (2)$$

and where q_1, ..., q_r are the r internal coordinates which determine the conformation of the molecule, the function $U(q_1, ..., q_r)$ describes the potential energy surface, and RT is the usual gas constant times the absolute temperature. Since integration over all conformational space is not feasible, eq 1 was approximated by three different methods, as follows.

1. *Summation of Boltzmann Factors at Minimum-Energy Points.* In this first method of approximation (which we shall call the Q approximation), the average value of A is given by

$$\langle A\rangle_Q = (1/Q)\sum_{i=1}^{n} A_i \exp[-E_i/RT] \quad (3)$$

where

$$Q = \sum_{i=1}^{n} \exp[-E_i/RT] \quad (4)$$

A_i is the value of the property A at the ith conformational-energy minimum; E_i is the conformational energy determined by ECEPP at the ith local low-energy[59] minimum; and n is the number of such minima in conformational space. For $\langle A\rangle_Q$ to be a good approximation of $\langle A\rangle_W$, the widths of the potential energy wells at the minima must be about the same for all minima, and the potential energy wells must be separated by sufficiently high barriers.

2. *Summation of Statistical Weights at Minimum-Energy Points.* To take into account possible differences in the relative widths of the potential energy wells at the local minima, the statistical weights w_i', given by[57,60]

$$w_i' = (2\pi RT)^{k/2} (\det \mathbf{F}_i)^{-1/2} \exp[-E_i/RT] \quad (5)$$

can be substituted for the Boltzmann factors in eq 3 to give (the Z approximation)

$$\langle A\rangle_Z = (1/Z)\sum_{i=1}^{n} A_i w_i' \quad (6)$$

where

$$Z = \sum_{i=1}^{n} w_i' \quad (7)$$

In eq 5, k is the number of variable dihedral angles in the molecule, and $\mathbf{F}_i$ is the matrix of second derivatives[60] at the ith minimum. For $\langle A\rangle_Z$ to be a good approximation of $\langle A\rangle_W$, the potential energy wells must be sufficiently deep (i.e., there can be only small fluctuations in the conformation about each of the minima), and the wells must be sufficiently parabolic in shape (although their widths may vary). The assumption that all low-energy minima can be located is implicit in eq 3 and 6.

In an earlier work,[60b] it was determined that the approximation of Gō et al.[60] (eq 5 in the present paper) adequately described the relative librational entropy of the three minima of lowest energy in cyclo(glycylglycylglycylprolylprolyl), a cyclic peptide having two independent variables.[60b] In the present study, the evaluation of the approximation of Gō et al.[60] is extended to determine conformational properties by taking into consideration *all* low-energy minima of linear dipeptides having *more* than two independent variables.

3. *Summation of Boltzmann Factors at Intervals Over All Conformational Space.* The third method of approximation (the Ω approximation) is by numerical integration, where a finite number of sets of q_1, ..., q_r are taken rather than integrating continuously over all the variables. This can be expressed by the equation

$$\langle A\rangle_\Omega = (1/\Omega)\sum_{i=1}^{M} A_i \exp[-E_i/RT] \quad (8)$$

where

$$\Omega = \sum_{i=1}^{M} \exp[-E_i/RT] \quad (9)$$

and where M is the number of points in conformational space at which E and A are evaluated. In this study, the locations of these points were specified by taking the variable backbone dihedral angles independently at 30° (and in some selected cases at 5 or 10°) steps over the full 360° range (i.e., from −180 to +180°). For the dipeptides in which ϕ and ψ of each residue are variables, $k = 4$ and, with a grid step size of 30°, $M = (360°/30°)^4 = 12^4 = 20\,736$. The side-chain dihedral angle χ^1 of Ala was held fixed at 60° during the numerical integration.

4. *Determination of Averages and Bend Probabilities.* In this study, eq 3, 6, and 8 were used to calculate, for each *N*-acetyl-*N'*-methylamide dipeptide, (a) $\langle R\rangle_X$, the average $C^\alpha_i \cdots C^\alpha_{i+3}$ distance, where $X = Q$, Z, or Ω in eq 3, 6, and 8, respectively, and $A_i = R_i$; and (b) $P_{X,b}$, the probability of occurrence (or mole fraction) of bend conformations, where $\langle A\rangle_X = P_{X,b}$; $X = Q$, Z, or Ω; and $A_i = 1$ if the ith conformation is a bend ($R \leq 7$ Å) or $A_i = 0$ if the ith conformation is not a bend ($R > 7$ Å).

E. *Analysis of Globular Proteins.* The quantities $P_{X,b}$ and $\langle R\rangle_X$, determined theoretically by eq 3, 6, and 8, also can be determined empirically from an analysis of the conformations of dipeptide segments in the x-ray structures of globular proteins, using the equations

$$P_{E,b} = N_b/N \quad (10)$$

and

$$\langle R\rangle_E = \sum_{i=1}^{N} R_i/N \quad (11)$$

where the subscript E indicates that the values were determined empirically; N is the total number of occurrences of the particular dipeptide sequence, *excluding those in which both residues are in an α helix*, and N_b is the number of such occurrences which are bend conformations. Since helices are known to be formed by cooperative processes,[5] which include specific long-range interactions not present in the *N*-acetyl-*N'*-methylamide dipeptides, the helical regions of the proteins were excluded from the statistical analysis in order to be able to compare the empirical quantities in eq 10 and 11 with the theoretical quantities in eq 3, 6, and 8. Except when indicated otherwise, extended structures were included in the statistical analyses of proteins. All other data on dipeptide sequences in the 20 globular proteins were used in the analysis.

F. *Distribution Functions.* 1. *Probability Distribution Function.* The probability distribution function $P(R)$ is defined as the probability that a given dipeptide sequence has a value of R in the interval between R and $R + dR$. The function is defined such that

$$\int_{R=0}^{\infty} P(R)\, dR = 1 \tag{12}$$

$P(R)$ was evaluated by setting dR to a finite interval ΔR, and employing eq 8, where $\langle R \rangle_\Omega = P(R)$ and where $A_i = 1$ if the value of R falls within the particular interval between R and $R + \Delta R$; otherwise, $A_i = 0$. In this study, $P(R)$ was determined using a grid step size of 5, 10, or 30° over conformational space. The value of $\Delta R = 0.25$ Å was used when the step size was 5 or 10°, and $\Delta R = 0.5$ Å when the step size was 30°. The bend probabilities P_b and the average R values $\langle R \rangle$ can be determined from the probability distribution function using the equations

$$P_b = \int_{R=0}^{7} P(R)\, dR \tag{13}$$

and

$$\langle R \rangle = \int_{R=0}^{\infty} R\, P(R)\, dR \tag{14}$$

Since, in practice, $P(R)$ is calculated using the Boltzmann factors in eq 8 and 9, the evaluation of eq 13 and 14 is identical with the evaluations of eq 8, with $\langle A \rangle = P_{\Omega,b}$ and $\langle R \rangle_\Omega$, respectively, and hence, $P_b \equiv P_{\Omega,b}$, and $\langle R \rangle \equiv \langle R \rangle_\Omega$. Besides being useful for the calculation of probabilities over any range of values of R, the additional advantage of the function $P(R)$ is that the distribution plot of $P(R)$ vs. R gives a visual description of the distinctive conformational characteristics of the individual dipeptides.

2. *Conformational Volume Distribution Function.* The conformational hypervolume distribution function $V(R)$ is defined as the volume of conformational space which has a value of R in the interval between R and $R + dR$. The function is defined such that

$$\int_{R=0}^{\infty} V(R)\, dR = V = (2\pi)^k \tag{15}$$

where V is the total conformational volume and, as above, k is the number of variable dihedral angles. In this study, $V(R)$ was evaluated numerically at the same time as $P(R)$ (eq 8) by counting the number of points in conformational space which have a value of R between R and $R + \Delta R$. Since M is the total number of points taken in all of conformational space (see eq 8), each point corresponds to a conformational volume of V/M.

The volume of conformational space containing bend conformations is given by

$$V_b = \int_{R=0}^{7} V(R)\, dR \tag{16}$$

3. *Probability Density Distribution Function.* The mean probability density distribution function $\sigma(R)$ is defined as the probability per unit conformational volume that the value of R is in the interval between R and $R + dR$. Within each such interval

$$\sigma(R) = P(R)/V(R) \tag{17}$$

The mean probability density is given by

$$\sigma = \int_{R=0}^{\infty} P(R)\, dR / \int_{R=0}^{\infty} V(R)\, dR = 1/V \tag{18}$$

and the mean bend probability density is given by

$$\sigma_b = \int_{R=0}^{7} P(R)\, dR / \int_{R=0}^{7} V(R)\, dR = P_b/V_b \tag{19}$$

4. *Significance of $P(R)$, $V(R)$, and $\sigma(R)$.* According to eq 17, the probability distribution function $P(R)$ depends on two factorable quantities: (a) the molecular geometry (i.e., the bond lengths and bond angles), which determines the amount of conformational space within each interval between R and $R + dR$, and (b) the energetics, i.e., the conformational energies within each interval between R and $R + dR$. The conformational volume distribution function $V(R)$ depends only on the molecular geometry, but not on the energetics, and the probability density distribution function $\sigma(R)$ depends only on the energetics but not on the molecular geometry. Thus, the determination of $V(R)$ and $\sigma(R)$ gives new insights into the origin of the stabilities of bend conformations in peptides and proteins.

IV. Results and Discussion

The list of minimum-energy conformations for each of the nine dipeptides are given elsewhere;[20] therefore, conformational properties of individual minima will not be discussed here.

A. *Validity of Methods Used to Represent Conformational Space.* Table I gives the calculated values of $P_{X,b}$ and $\langle R \rangle_X$, where $X = Q$, Z, and Ω for the three methods of approximation (section III.D), and the corresponding values from the analysis of 20 x-ray structures of proteins, where $X = E$. Numerical integration (eq 8 and 9) gives exact results in the limit as the distance between each point on the conformational space grid becomes vanishingly small. Ideally, to determine if this grid step size is sufficiently small, evaluation of the integral should be repeated using successively smaller steps until the results do not change appreciably as the step size gets smaller. In practice, however, this requires far too much computer time. Therefore, values of dihedral angles were taken in 30° intervals for all dipeptides except Gly-Pro, Pro-Gly, and Pro-Pro, for which intervals of 10, 10, and 5°, respectively, were taken (in addition to 30° intervals).

Values of $P_{\Omega,b}$ and $\langle R \rangle_\Omega$ for Gly-Pro and Pro-Pro change as the step size is decreased (Table I), indicating that a step size of 30° is too large for these dipeptides. On the other hand, a decrease in step size did not affect the results for Pro-Gly significantly, indicating that a 30° interval is sufficiently small in this case. This is due to the fact[61] that the low-energy region of the conformational space of the X residue in X-Pro dipeptides is much smaller than that in Pro-X dipeptides (see Figure 5 of ref 61). When the step size is 30°, only a relatively small number of points falls in the low-energy regions of the conformational space of the X-Pro dipeptides. On the other hand, the conformational space of the X residue in Pro-X dipeptides is not restricted significantly by the Pro residue,[20,61] and therefore a grid step size of 30° is adequate. This can be generalized to include the dipeptides not containing Pro, since the

TABLE I: Bend Probabilities and Average $C^{\alpha}_{i} \cdots C^{\alpha}_{i+3}$ Distances[a]

Peptide[b]	n[c]	Grid step size, deg	N[d]	$P_{Q,b}$	$P_{Z,b}$	$P_{\Omega,b}$	$P_{E,b}$	$\langle R\rangle_Q$, Å	$\langle R\rangle_Z$, Å	$\langle R\rangle_\Omega$, Å	$\langle R\rangle_E$, Å
Ala-Ala	35	30	23	0.26	0.14	0.10	0.35	8.13	8.63	8.84	7.87
Ala-Gly	46	30	23	0.52	0.35	0.33	0.52	7.07	7.76	7.80	6.95
Ala-Pro[e]	10	30	8	0.0	0.0	0.0	0.13	9.29	9.38	9.39	8.35
Gly-Ala	42	30	17	0.48	0.28	0.30	0.06	7.05	7.75	7.88	8.80
Gly-Gly	55	30	22	0.53	0.37	0.33	0.09	6.97	7.47	7.82	9.04
Gly-Pro[e]	21	10	11	0.22	0.13	0.11	0.09	7.87	8.15	8.13	8.25
		30				0.04				8.38	
Pro-Ala	20	30	9	0.26	0.16	0.22	0.33	7.99	8.26	8.30	7.82
Pro-Gly	25	10	12	0.61	0.47	0.52	0.58	6.76	7.08	7.09	6.60
		30				0.51				7.15	
Pro-Pro[e]	5	5	2	0.0	0.0	0.0	0.0	8.31	8.45	8.46	8.43
		30				0.0				8.76	
Proteins[f]			2654				0.24				8.30

[a] Bend probabilities are dimensionless. [b] *N*-Acetyl-*N'*-methylamide dipeptides (for quantities with subscripts Q, Z, and Ω), or dipeptide sequences (excluding those in which both residues are in an α helix) in the x-ray structures of 20 globular proteins (for quantities with subscript E). [c] Number of minima for *N*-acetyl-*N'*-methylamide dipeptides. [d] Number of occurrences of dipeptide sequences (excluding helical ones) in 20 proteins. [e] The values of n, $P_{Q,b}$, and $P_{Z,b}$ for Ala-Pro, Gly-Pro, and Pro-Pro are slightly different from those in Table VI of ref 20a because, in the present study ω_{i+1} was held fixed at 180°, whereas in the other study it was allowed to vary during minimization from starting points at ω_{i+1} = 180° and 0° (see Table V, ref 61). [f] Data on this line are for all dipeptide sequences (excluding helical regions) in the 20 x-ray structures of globular proteins.

conformational space of each residue in those dipeptides is similarly unrestricted by the presence of its neighboring residue.[20] The results suggest that, for all of the dipeptides except those in which Pro is the second residue, $P_{\Omega,b}$ and $\langle R\rangle_\Omega$ are determined with sufficient accuracy by eq 8 if the grid step size is less than or equal to 30°.

Making the assumption that numerical integration by the Ω approximation (eq 8 and 9) is a valid approximation to $P_{W,b}$ and $\langle R\rangle_W$, the validity of the other methods of approximation (Q and Z) can be assessed. Table I shows that quantities determined by approximation Z (eq 6) for each dipeptide are very close to those determined by approximation Ω (eq 8), suggesting that the statistical weights evaluated by the method of Gō et al.[60] at each low-energy minimum provides a valid representation of the energetically important regions of conformational space. Approximation Q (eq 3), on the other hand, is obviously inadequate for determining the conformational properties of *isolated* dipeptides.

B. *Effect of Sequence on the Calculated Values of* $P_{Z,b}$ *and* $\langle R\rangle_Z$. The dipeptides fall roughly into three groups based on the values of their calculated bend probabilities $P_{Z,b}$: low values of $P_{Z,b}$ (<0.1), Ala-Pro and Pro-Pro; intermediate values of $P_{Z,b}$ (0.1–0.2), Ala-Ala, Gly-Pro, and Pro-Ala; high values of $P_{Z,b}$ (>0.2), Ala-Gly. Gly-Ala, Gly-Gly, and Pro-Gly. It is clear from this result, and from previous work[20a] on other proline-containing dipeptides, that X-Pro dipeptides have low bend probabilities, except when X = Gly. The results also indicate, in general, that X-Gly dipeptides (and Gly-Ala) have relatively high bend probabilities and that the other dipeptides have intermediate bend probabilities. Perhaps the most important conclusion is that occurrences of bend conformations in a particular dipeptide depend both on the amino acid composition and on the amino acid sequence.

Although certain dipeptides may be grouped into the same category because of similar values of $P_{Z,b}$, the overall conformational character of those dipeptides may be quite different. This is illustrated in Figure 2, where the probability distribution function P(R) is plotted against R for various dipeptide sequences. A comparison of the P(R) curves of Gly-Pro and Ala-Ala shows that, even though the relative areas under the curves in the region $R \leq 7$ Å are about the same (i.e., the values of $P_{\Omega,b}$ are approximately equal; see Table I), the shapes of the curves and locations of maxima are very different. One consequence of this is that the values of $\langle R\rangle_\Omega$ for Gly-Pro and Ala-Ala also are quite different (Table I).

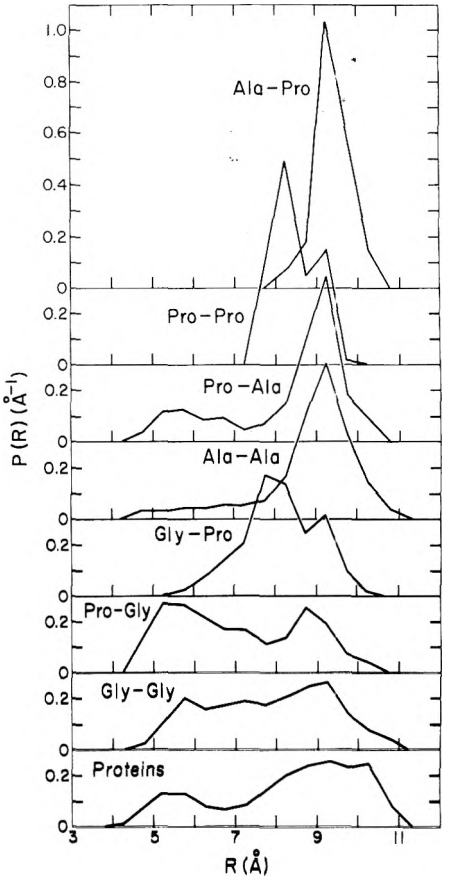

Figure 2. Plots of P(R) vs. R for seven *N*-acetyl-*N'*-methylamide dipeptides and for dipeptide sequences (excluding those in which both residues are in an α helix) of 20 globular proteins.

Figure 2 shows, in fact, that each dipeptide whose distribution function is plotted has a distinct conformational character. The P(R) vs. R curves of two dipeptides, Ala-Gly and Gly-Ala, are not shown in Figure 2 because their probability distribution functions are essentially the

TABLE II: Conformational Volumes and Mean Probability Densities

Peptide[a]	Grid step size, deg	k[b]	V, rad^k Å^{-1}	V_b, rad^k Å^{-1}	V_b/V	σ, rad^{-k}	σ_b, rad^{-k}	σ_b/σ
Ala-Ala	30	4	1559	461	0.30	0.000 64	0.000 20	0.32
Ala-Gly	30	4	1559	438	0.28	0.000 64	0.000 76	1.19
Ala-Pro	30	3	248	70	0.28	0.004 0	0.0	0.0
Gly-Ala	30	4	1559	437	0.28	0.000 64	0.000 70	1.08
Gly-Gly	30	4	1559	413	0.27	0.000 64	0.000 79	1.24
Gly-Pro	10	3	248	66	0.27	0.004 0	0.001 67	0.42
Pro-Ala	30	3	248	78	0.31	0.004 0	0.002 86	0.71
Pro-Gly[c]	10	3	248	73	0.30	0.004 0	0.007 13	1.77
Pro-Pro	5	2	39	11	0.29	0.025	0.0	0.0
Proteins						0.000 64[d]	0.000 56[e]	0.83
Proteins						0.000 64[d]	0.000 76[f]	1.19

[a] *N*-Acetyl-*N'*-methylamide dipeptides, or dipeptide sequences (excluding those in which both residues are in an α helix) in the x-ray structures of 20 globular proteins. [b] Number of variable dihedral angles in the dipeptide. [c] Compare with Figure 2. [d] The value of σ for the proteins is approximated by assuming that $k = 4$ for all dipeptide segments; hence the value of σ is the same as that for Ala-Ala, Ala-Gly, etc. [e] σ_b is approximated by $P_{E,b}/V_b$ (see eq 19), where $P_{E,b}$ is determined for all dipeptide sequences (excluding those in which both residues are in an α helix) in 20 x-ray structures of proteins, and V_b is taken as that for Ala-Gly. [f] Same as *e* except also exluding dipeptide sequences in which both residues are in an extended structure (defined in section IIIA).

same as that of Gly-Gly. For this reason, Ala-Gly, Gly-Ala, and Gly-Gly not only have similar values of $P_{\Omega,b}$ but also have similar values of $\langle R \rangle_\Omega$ (see Table I).

C. *Comparison of Theoretical and Empirical Results.* Table I gives the empirical bend probabilities $P_{E,b}$ and empirical average $C^\alpha_i \cdots C^\alpha_{i+3}$ distances $\langle R \rangle_E$ determined from the analysis of dipeptide sequences (excluding those in which both residues are in an α helix) in the x-ray structures of 20 globular proteins. These empirical quantities are compared with those calculated using the various approximations (Q, Z, and Ω) given above. Although the Q approximation was shown in section IVA to be inadequate for *isolated* dipeptides, there is no a priori reason why it should be any more or less valid than the Z or Ω approximation for representing conformational properties of dipeptide segments in a protein chain. This is because the relative librational entropy, which is calculated explicitly for an isolated dipeptide in the Z and Ω approximations but not in the Q approximation, may be very different when the dipeptide is incorporated into a relatively rigid globular protein.

Making the assumption that the theoretical results accurately represent the conformational behavior of *N*-acetyl-*N'*-methylamide dipeptides in the gas phase, and taking into consideration the statistical error due to the small sample, several important observations and conclusions ensue from a comparison of the theoretical and empirical results.

1. In each of the five dipeptides Ala-Ala, Ala-Gly, Pro-Ala, Pro-Gly, and Pro-Pro, the value of $P_{Q,b}$ is within 0.1 of the value of $P_{E,b}$ and, concomitantly, the value of $\langle R \rangle_Q$ is within 0.3 Å of the value of $\langle R \rangle_E$. Agreement between $P_{Z,b}$ and $P_{E,b}$ (or between $\langle R \rangle_Z$ and $\langle R \rangle_E$), however, is not as good. This suggests that, for these five dipeptides, (a) the librational entropy calculated for *isolated* dipeptides does not apply to the dipeptide segments of a protein chain, and (b) bends in proteins are stabilized mainly by local interactions (i.e., those within each residue or between adjacent residues) rather than long-range interactions (i.e., those between residues that are separated by at least one residue). If long-range interactions dominated, such correlation between $P_{Q,b}$ and $P_{E,b}$ would not be likely to occur.

2. In Gly-Pro, there is close agreement between $P_{Z,b}$ and $P_{E,b}$ (and between $\langle R \rangle_Z$ and $\langle R \rangle_E$) but not between $P_{Q,b}$ and $P_{E,b}$ (nor between $\langle R \rangle_Q$ and $\langle R \rangle_E$). It is reasonable to assume that the librational entropy of Gly-Pro in a protein chain is not very different from that in an isolated dipeptide since the conformational space of a Gly residue preceding Pro is so restricted[61] by interactions with the pyrrolidine ring. Hence, it can be concluded that bends in proteins of the sequence Gly-Pro also are stabilized primarily by local interactions.

3. In Ala-Pro, the observed bend probability $P_{E,b}$ (0.13) is somewhat higher than the calculated value (0.0), and $\langle R \rangle_E$ (8.35 Å) is much lower than $\langle R \rangle_Z$ (9.38 Å). The results of *earlier* calculations[20] on Ala-Pro, in which ω was allowed to vary and to assume the value of the cis form ($\omega \simeq 0°$), gave $P_{Z,b} = 0.01$ and $\langle R \rangle_Z = 9.26$ Å, not significantly different from the results obtained here in which ω was held fixed at 180°. The discrepancy between the calculated and observed bend probabilities seems to be due to the fact that the single occurrence of an Ala-Pro bend is found at residues 68–69 of thermolysin,[29] in the middle of a distorted α helix. Although this region of the protein is not an α helix by the definition used throughout this paper, it is an α helix on the basis of the dihedral angles given in Matthews et al,[29] which were determined by a method different from ours (see section IIB). If this particular bend *is* considered to be part of an α helix, the unexpected occurrence of an Ala-Pro bend logically may be ascribed to the long-range interactions which stabilize the α helix. This also could explain, to a large degree, the difference between $\langle R \rangle_E$ and $\langle R \rangle_Z$ of Ala-Pro.

4. The discrepancy between the calculated and observed bend probabilities in Gly-Ala and Gly-Gly is not easy to explain. The number of occurrences of these dipeptide sequences in the 20 proteins is significant ($N = 17$ and 22, respectively), so that the discrepancy cannot be attributed to statistical fluctuations. Moreover, the low fraction of occurrences in bends cannot be explained by a high occurrence of these sequences in β structure; even when regions of extended structure are omitted from the analysis, $P_{E,b}$ of Gly-Ala is 0.07 and $P_{E,b}$ of Gly-Gly is 0.12, only slightly greater than the values given in Table I. It may be that the relative conformational freedom of Gly makes it particularly susceptible to effects from long-range interactions. Further study will be required to resolve this problem.

D. *Bend Regions of Conformational Space.* For each of the nine dipeptides, Table II lists (a) the total conformational volume V, which depends only on the number of variable dihedral angles; (b) the volume V_b of conformational space in which the dipeptide is in a bend; and (c) the bend fraction V_b/V of conformational space. Interestingly, even though the number of variable dihedral

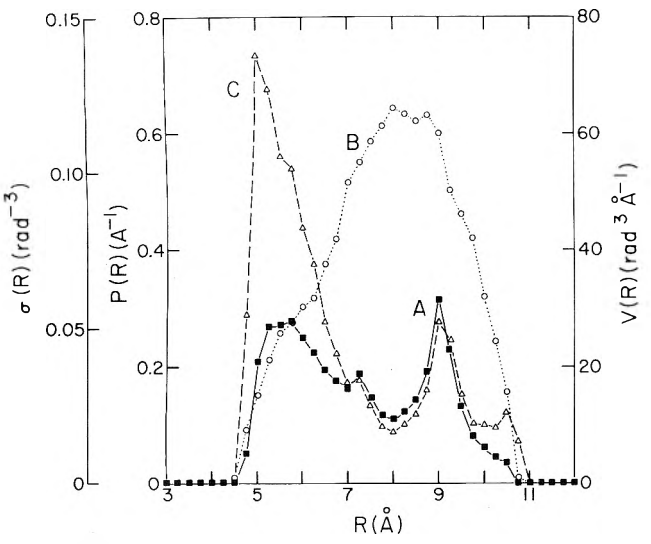

Figure 3. (A) P(R) vs. R, (B) V(R) vs. R, and (C) $\sigma(R)$ vs. R for *N*-acetyl-*N'*-methylprolylglycineamide, from a 10° map over all conformational space.

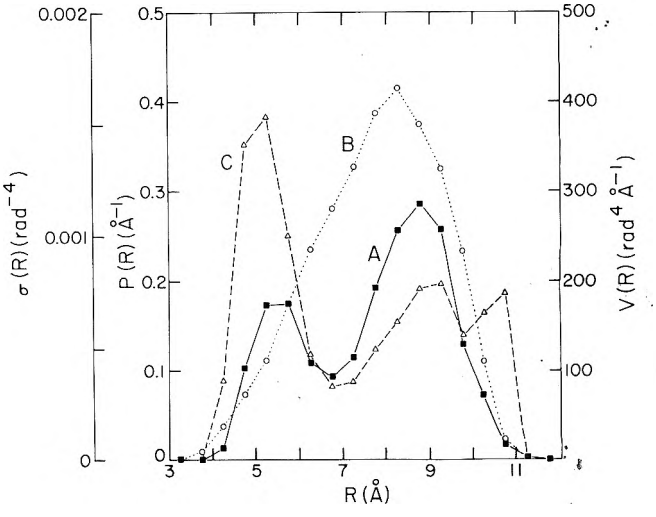

Figure 4. (A) P(R) vs. R for dipeptide sequences (excluding those in which both residues are in an α helix or in extended structure) in globular proteins. (B) V(R) vs. R for *N*-acetyl-*N'*-methylalanylalanineamide, from a 30° map over all conformational space. (C) $\sigma(R)$ vs. R obtained by dividing curve A by curve B at each point.

angles is not the same in all of these dipeptides, the fraction of the total conformational volume which is a bend conformation is approximately the same for all dipeptides (0.27–0.31). Table II also lists (d) the mean probability density σ (= $1/V$); (e) the mean bend probability density σ_b (= $P_{\Omega,b}/V_b$); and (f) the ratio of the mean bend probability density to the mean probability density σ_b/σ, which is equal to the ratio of the population fraction to the volume fraction of bends [i.e., $\sigma_b/\sigma \equiv (N_b/N)/(V_b/V)$]. A ratio of $\sigma_b/\sigma > 1$ implies that the interactions within bends are more favorable than the overall average, and $\sigma_b/\sigma < 1$ implies that the interactions in bends are less favorable than the average. Since the fraction V_b/V is relatively independent of amino acid sequence but the ratio σ_b/σ is strongly dependent upon sequence, the conclusion can be drawn that the particular bend probability $P_{\Omega,b}$ of each dipeptide sequence is due to certain energetically favorable (and/or unfavorable) interactions and not due simply to the relative amounts of bend and nonbend conformational space for the particular dipeptide.

This is illustrated graphically for Pro-Gly in Figure 3. The probability distribution (curve A) has approximately the same area under the curve in the bend region ($R \leq 7$ Å) as in the nonbend region ($R > 7$ Å), but the probability density distribution (curve C) has much more area under the curve in the bend region than in the nonbend region. The result is that $\sigma_b/\sigma = 1.77$ (Table II), indicating that the energetic interactions are, on the average, much more favorable in bends than in nonbends.

The analysis of dipeptide sequences (excluding helical ones) in globular proteins gives $\sigma_b/\sigma = 0.83$ (Table II) indicating that the interactions in bends are less favorable, on the average, than those in the other conformations (nonregular structure and β structure). On the other hand, if helical *and* extended structure are omitted[62] from the analysis (which causes all β structure to be omitted), the ratio σ_b/σ is 1.19. This suggests that bend conformations are stabilized by interactions which are more favorable, on the average, than those in other nonregular structures in proteins.

This is illustrated in Figure 4. Curve A gives the empirical probability distribution function as determined by considering nonregular structures (α helix and extended structure[62] were excluded in this analysis) in the 20 proteins. The volume distribution function (curve B) for the proteins was taken to be that of Ala-Ala, but V(R) of any of the dipeptides would give the same qualitative results since their shapes are similar (cf. curve B in Figure 3 and curve B in Figure 4). The probability density distribution function (curve C) is much greater in the region of $R \leq 7$ Å than in the region of $R > 7$ Å, as was found for Pro-Gly in Figure 3. The conclusion is that, in contrast to most other nonregular structures (i.e., the nonbend structures) in globular proteins, most bends arise from energetically favorable local interactions. Furthermore, curves A and C show, by the minimum at $R \sim 7$ Å, that there is a natural division between bends and nonbends with respect to their value of R. Thus, as with the α helix and β structure, bends are a distinguishable type of protein structure and not merely an arbitrarily defined type of nonregular conformation. Of course, bends differ from the α helix and β structure in that the dihedral angles in bends can take on a variety of values, whereas the dihedral angles in ordered conformations must, by definition, take on values within a specific range. In summary, bends are similar to the α helix and β structure in that (a) they have a naturally defined range of values of R and (b) they are stabilized by energetically favorable interactions.

V. Summary and Conclusions

The results and conclusions of the statistical mechanical analysis of the conformational space of the nine *N*-acetyl-*N'*-methylamide dipeptides containing Ala, Gly, and Pro, and the analysis of the x-ray structures of 20 globular proteins, can be summarized as follows.

1. Average conformational properties evaluated by numerical integration over all conformational space, which required relatively large amounts of computer time, and by summation of the statistical weights of all local low-energy minima, calculated by the method of Gō et al.,[60] which required much less computer time, yielded essentially the same results. It can be concluded, therefore, that the approximation of Gō et al.[60] is a valid and efficient method of determining statistical weights of minimum-energy conformations of dipeptides, and that approximation Z is a valid and efficient method of calculating conformational properties of *isolated* dipeptides.

2. Conformational properties of dipeptides [as reflected in the calculated probability distribution functions P(R), the bend probabilities P_b, and the average $C^{\alpha}_i \cdots C^{\alpha}_{i+3}$

distances R] are a function of amino acid composition and sequence. (See Figure 2 and Table I.)

3. For many dipeptide sequences, the calculated bend probabilities, using approximation Q, are very close to the observed fraction of occurrences of bends in globular proteins. This suggests that, for those particular sequences, bends are stabilized mainly by local interactions (i.e., those between atoms within the dipeptide) rather than by long-range interactions. For other sequences (e.g., Gly-X dipeptides), the calculated and observed bend probabilities are not in agreement, suggesting that interactions other than those within the isolated dipeptides (e.g., long-range interactions, solvent interactions, etc.) may be responsible for the conformational properties of these dipeptides in proteins.

4. The analysis of the 20 globular proteins shows that (a) the empirical probability distribution function $P(R)$ (see Figure 4) has two distinct peaks, separated by a minimum in the region of $R \sim 7$ Å, indicating the existence of a natural division between bend and nonbend regions of conformational space (when described by R), and (b) the probability density in the bend region is much greater than in the nonbend region, indicating that most bends are stabilized by energetically favorable interactions not present to the same degree in nonbends. In this sense, a bend can be considered to be a distinguishable type of structure (just as the α helix or β structure) rather than an arbitrarily defined type of nonregular conformation.

5. The three distribution functions—$P(R)$, which depends on molecular geometry and energetics, $V(R)$, which depends on geometry alone, and $\sigma(R)$, which depends on energetics alone—have been shown to be particularly useful for the characterization of bend and nonbend regions of conformational space.

Acknowledgment. We are indebted to Drs. A. W. Burgess, N. Gō, and G. Némethy for helpful discussions, and to Dr. T. F. Koetzle for providing us with the x-ray coordinates from the Protein Data Bank, Brookhaven National Laboratories, Upton, Long Island, N.Y.

References and Notes

(1) This work was supported by research grants from the National Institute of General Medical Sciences of the National Institutes of Health, U.S. Public Health Service (GM-14321), and from the National Science Foundation (PCM75-08691).
(2) A preliminary report of a portion of this work was presented at the 4th American Peptide Symposium, New York City, April 1975; see ref 3.
(3) S. S. Zimmerman and H. A. Scheraga in "Peptides: Chemistry, Structure and Biology", R. Walter and J. Meienhofer, Ed., Ann Arbor Publishing Co., Ann Arbor, Mich., 1975, p 263.
(4) (a) NIH Postdoctoral Fellow, 1974–1977. (b) Cornell University. (c) NIH Postdoctoral Fellow, 1972–1974. Present address: Chemistry Division, Argonne National Laboratory, Argonne, Ill. 60439. (d) Weizmann Institute. (e) To whom requests for reprints should be addressed, at Cornell University.
(5) See, for example, G. D. Fasman in "Poly-α-Amino Acids", G. D. Fasman, Ed., Marcel Dekker, New York, N.Y., 1967, p 499.
(6) Nonregular structures in proteins are sometimes called "random coil", but the latter name is inappropriate since no portion of the native conformation of a globular protein is ever random; the nonregular structures have *specific* conformations.
(7) Also called β bend, β turn, reverse turn, chain reversal, etc.
(8) C. M. Venkatachalam, *Biopolymers*, **6**, 1425 (1968).
(9) P. N. Lewis, F. A. Momany, and H. A. Scheraga, *Proc. Natl. Acad. Sci. USA*, **68**, 2293 (1971).
(10) I. D. Kuntz, *J. Am. Chem. Soc.*, **94**, 8568 (1972).
(11) J. L. Crawford, W. N. Lipscomb, and C. G. Schellman, *Proc. Natl. Acad. Sci. USA*, **70**, 538 (1973).
(12) P. N. Lewis, F. A. Momany, and H. A. Scheraga, *Biochim. Biophys. Acta*, **303**, 211 (1973).
(13) G. Némethy and M. P. Printz, *Macromolecules*, **5**, 755 (1972).
(14) R. Chandrasekaran, A. V. Lakshminarayanan, U. V. Pandya, and G. N. Ramachandran, *Biochim. Biophys. Acta*, **303**, 14 (1973).
(15) K. Nishikawa, F. A. Momany, and H. A. Scheraga, *Macromolecules*, **7**, 797 (1974).
(16) B. Maigret and B. Pullman, *Theor. Chim. Acta*, **35**, 113 (1974).
(17) V. Z. Pletnev, F. A. Kadymova, and E. M. Popov, *Biopolymers*, **13**, 1085 (1974).
(18) J. C. Howard, A. Ali, H. A. Scheraga, and F. A. Momany, *Macromolecules*, **8**, 607 (1975).
(19) S. Tanaka and H. A. Scheraga, *Macromolecules*, **9**, 812 (1976).
(20) (a) S. S. Zimmerman and H. A. Scheraga, *Biopolymers*, in press, (b) *ibid.*, to be submitted.
(21) D. W. Urry and T. Ohnishi in "Peptides, Polypeptides and Proteins", E. R. Blout, F. A. Bovey, M. Goodman, and N. Lotan, Ed., Wiley, New York, N.Y., 1974, p 230.
(22) E. R. Blout, C. M. Deber, and L. G. Pease in "Peptides, Polypeptides and Proteins", E. R. Blout, F. A. Bovey, M. Goodman, and N. Lotan, Ed., Wiley, New York, N.Y., 1974, p 266.
(23) K. D. Kopple and A. Go in "Peptides: Chemistry, Structure and Biology", R. Walter and J. Meienhofer, Ed., Ann Arbor Publishing Co., Ann Arbor, Mich., 1975, p 139.
(24) In this paper, the term "local interactions" will refer to interactions between atoms within an amino acid residue (i.e., "short-range interactions") plus interactions between adjacent residues (i.e., those within a particular dipeptide sequence). "Long-range interactions" will refer to those between atoms separated by one or more amino acid residues in the polypeptide chain.
(25) G. N. Ramachandran, C. Ramakrishnan, and V. Sasisekharan, *J. Mol. Biol.*, **7**, 95 (1963).
(26) The term "dipeptide" should not be confused here with the earlier usage of the term to refer to *N*-acetyl-*N'*-methylamides of single residues. As used here, the terms "single residue" and "dipeptide" refer to the structures $CH_3CO-X-NHCH_3$ and $CH_3CO-X-Y-NHCH_3$, respectively, where X and Y are amino acid residues.
(27) F. R. Maxfield and H. A. Scheraga, *Biochemistry*, **15**, 5138 (1976).
(28) H. C. Watson, *Prog. Stereochem.*, **4**, 299 (1969).
(29) B. W. Matthews, L. H. Weaver, and W. R. Kester, *J. Biol. Chem.*, **249**, 8030 (1974).
(30) F. S. Mathews, M. Levine, and P. Argos, *J. Mol. Biol.*, **64**, 449 (1972).
(31) (a) D. M. Shotton and H. C. Watson, *Nature (London)*, **225**, 811 (1970); (b) D. M. Shotton and B. S. Hartley, *Biochem. J.*, **131**, 643 (1973).
(32) J. J. Birktoft and D. M. Blow, *J. Mol. Biol.*, **68**, 187 (1972).
(33) F. A. Quiocho and W. N. Lipscomb, *Adv. Protein Chem.*, **25**, 1 (1971).
(34) J. Drenth, J. N. Jansonius, R. Koekoek, and B. G. Wolthers, *Adv. Protein Chem.*, **25**, 79 (1971).
(35) J. Deisenhofer and W. Steigemann, *Acta Crystallogr., Sect., B*, **31**, 238 (1975).
(36) G. M. Edelman, B. A. Cunningham, G. N. Reeke, Jr., J. W. Becker, M. J. Waxdal, and J. L. Wang, *Proc. Natl. Acad. Sci. USA*, **69**, 2580 (1972).
(37) (a) C. W. Carter, Jr., J. Kraut, S. T. Freer, Ng. H. Xuong, R. A. Alden, and R. G. Bartsch, *J. Biol. Chem.*, **249**, 4212 (1974); (b) S. T. Freer, R. A. Alden, C. W. Carter, Jr., and J. Kraut, *ibid.*, **250**, 46 (1975).
(38) R. Diamond, *J. Mol. Biol.*, **82**, 371 (1974).
(39) P. C. Mcews and R. H. Kretsinger, *J. Mol. Biol.*, **91**, 201 (1975).
(40) R. A. Alden, J. J. Birktoft, J. Kraut, J. D. Robertus, and C. S. Wright, *Biochem. Biophys. Res. Commun.*, **45**, 337 (1971).
(41) R. J. Fletterick and H. W. Wyckoff, *Acta Crystallogr., Sect. A*, **31**, 698 (1975).
(42) A. Arnone, C. J. Bier, F. A. Cotton, V. W. Day, E. E. Hazen, Jr., D. C. Richardson, J. S. Richardson, and A. Yonath, *J. Biol. Chem.*, **246**, 2302 (1971).
(43) (a) F. R. Salemme, S. T. Freer, Ng. H. Xuong, R. A. Alden, and J. Kraut, *J. Biol. Chem.*, **248**, 3910 (1973); (b) F. R. Salemme, S. T. Freer, R. A. Alden, and J. Kraut, *Biochem. Biophys. Res. Commun.*, **54**, 47 (1973).
(44) (a) M. Buehner, G. C. Ford, D. Moras, K. W. Olsen, and M. G. Rossmann, *J. Mol. Biol.*, **82**, 563 (1974); (b) *ibid.*, **90**, 25 (1974).
(45) R. M. Burnett, G. D. Darling, D. S. Kendall, M. E. LeQuesne, S. G. Mayhew, W. W. Smith, and M. L. Ludwig, *J. Biol. Chem.*, **249**, 4383 (1974).
(46) G. Fermi, *J. Mol. Biol.*, **97**, 237 (1975).
(47) (a) W. A. Hendrickson and W. E. Love, *Nature (London), New Biol.*, **232**, 197 (1971); (b) W. A. Hendrickson, W. E. Love, and J. Karle, *J. Mol. Biol.*, **74**, 331 (1973).
(48) IUPAC-IUB Commission on Biochemical Nomenclature, *Biochemistry*, **9**, 3471 (1970).
(49) A. W. Burgess, P. K. Ponnuswamy, and H. A. Scheraga, *Isr. J. Chem.*, **12**, 239 (1974).
(50) The Fortran computer program for ECEPP, its description, and all associated geometric and energy parameters are available on magnetic tape from the Quantum Chemistry Program Exchange. Write to QCPE, Chemistry Department, Room 204, Indiana University, Bloomington, Ind. 47401 for standard program request sheets, and then order No. QCPE 286.
(51) F. A. Momany, R. F. McGuire, A. W. Burgess, and H. A. Scheraga, *J. Phys. Chem.*, **79**, 2361 (1975).
(52) S. Tanaka and H. A. Scheraga, *Macromolecules*, **7**, 698 (1974).
(53) S. S. Zimmerman, M. S. Pottle, G. Némethy, and H. A. Scheraga, *Macromolecules*, **10**, 1 (1977).
(54) M. J. D. Powell, *Comput. J.*, **7**, 155 (1964).
(55) For example, see R. H. Pennington, "Introductory Computer Methods and Numerical Analysis", Macmillan, New York, N.Y., 1965, p 236.
(56) P. J. Flory, *Macromolecules*, **7**, 381 (1974).
(57) N. Gō and H. A. Scheraga, *Macromolecules*, **9**, 535 (1976).

(58) See, for example, N. Davidson, "Statistical Mechanics", McGraw-Hill, New York, N.Y., 1962, p 207.
(59) "Low-energy", as the term is used here, refers to conformational energies within 3 kcal/mol of the energy at the global minimum.
(60) (a) N. Gō and H. A. Scheraga, *J. Chem. Phys.*, **51**, 4751 (1969); (b) N. Gō, P. N. Lewis, and H. A. Scheraga, *Macromolecules*, **3**, 628 (1970); (c) N. Gō, M. Gō, and H. A. Scheraga, *ibid.*, **7**, 137 (1974).
(61) S. S. Zimmerman and H. A. Scheraga, *Macromolecules*, **9**, 408 (1976).
(62) In most of the analyses in this paper, extended structure is included since (a) specific long-range interactions (such as the hydrogen bonds observed in α helix and β structure) cannot be identified readily, and (b) there are no data to indicate that an extended structure (which lacks interstrand hydrogen bonds) is formed by cooperative interactions, such as those in an α helix (see section IIIE). Extended structure was not included, however, in determining the data in the last line of Table II and in curve A of Figure 4 for the sake of comparison. The results show that the *general* conclusions are the same whether or not extended structure is included in the analysis. (See Figure 1 of ref 3 for a similar plot in which extended structure was included.)

Study of Metal Oxide Catalysts by Temperature Programmed Desorption. 2. Chemisorption of Oxygen on Copper(II) Ion-Exchanged Y-Type Zeolites

Masakazu Iwamoto,[1] Kouji Maruyama, Noboru Yamazoe, and Tetsuro Seiyama*

Department of Materials Science and Technology, Faculty of Engineering, Kyushu University, Higashi-ku, Fukuoka, 812 Japan *(Received November 29, 1976)*

Publication costs assisted by Kyushu University

The adsorption of oxygen on Cu(II) ion-exchanged Y-type zeolites was studied over the temperature range 0–500 °C by means of a temperature programmed desorption (TPD) technique. At least five different states of adsorbed oxygen were indicated by the appearance of five TPD peaks, with maxima located at 40 (α), 80 (β), 320 (γ), 470 (δ), and >550 °C (ϵ), respectively. These peaks were not observed in the TPD chromatograms from NaY or HY, suggesting that the active sites for oxygen adsorption are created in the zeolite by substituting Cu(II) ions for Na(I) or H(I) ions. Taking into account the influences of adsorption method, adsorption temperature, and Cu(II) ion-exchange level on the amounts of α–ϵ oxygen, the corresponding oxygen adsorbates were assigned as follows: α and β are molecular oxygen adsorbing on the zeolite skeleton, γ and δ are molecular oxygen adsorbing on Cu(II) ions located at S_{II} and S_{III}, and ϵ is the extraframework oxygen atoms bound by the Cu(II) ions situated at S_I. The activation energies of desorption were 32.2 and 47.4 kcal/mol, respectively, for γ and δ oxygen. Oxygen adsorption was markedly affected by the coadsorption of water; not only a new desorption peak (ω) appeared at 390–400 °C instead of γ or δ, but the amount of oxygen adsorption increased on water preadsorption. These effects were interpreted to be related to the hydration and migration of Cu(II) ions in the zeolite framework. It is concluded that, in the presence of water, the coordination of an equimolar water and oxygen to the same Cu(II) ions results in the ω adsorption state and that the capacity for oxygen adsorption is enhanced due to the migration of Cu(II) ions at S_{II} toward the supercage. The above assignments for γ, δ, and ω adsorption enabled the estimation of the distribution of Cu(II) ions over each exchange site in dehydrated zeolite, which showed reasonable agreement with that from the x-ray data.

Introduction

Over the past few years numerous studies have been made of transition metal ion-exchanged zeolites. In particular, divalent copper-exchanged Y-type zeolite (CuNaY or CuKY) has been shown to exhibit catalytic activity in oxidation,[2-5] cracking,[6] and isomerization reactions[7] of hydrocarbons. We described high catalytic activity of metal ion-exchanged Y-type zeolites for the oxidation of olefins[2] and the oxidative dehydrogenation of cyclohexane.[5] For an understanding of these catalytic phenomena, it would be very important to know the adsorption state of the reactants. However, there is serious lack of basic knowledge on the adsorptive properties of zeolite catalysts, especially for oxygen adsorption. The very basic questions as to where and how oxygen molecules or atoms are adsorbed in the zeolite structure or how they are activated to react with reactants remain to be answered.

In a previous paper,[8] we studied oxygen adsorption on nickel oxide by means of a temperature programmed desorption (TPD) technique and obtained results showing the existence of several modes of oxygen adsorption. In the present paper, we tried to approach the above questions by applying the same technique to CuNaY–O_2 systems. CuNaY was chosen as a model system, since it is distinguished from other ion-exchanged zeolites in the catalytic activity[5] as well as in the adsorptive capacity for oxygen.[9]

Divalent copper-exchanged Y-type zeolites have been extensively studied by electron spin resonance spectroscopy[10-15] and x-ray diffraction analysis.[16,17] These studies have shown that Cu(II) cations are distributed over different sites within the zeolite framework and that the populations on these sites are markedly influenced by the presence of adsorbates such as water and ammonia. Still, little has been understood on the oxygen adsorption phenomena in a zeolite. This work sheds some light on such problems as the kinds and amounts of the oxygen adsorbates which form within the zeolite framework containing Cu(II) cations, and their interactions with water when water is coadsorbed.

Experimental Section

Materials. Five CuNaY samples with different Cu(II) contents were prepared from Linde NaY zeolite (SK-40) of composition $Na_{56}(AlO_2)_{56}(SiO_2)_{136}$. The zeolite was ion exchanged in aqueous cupric sulfate solutions with adequate concentrations, washed with water, and dried at 200

°C. The respective exchange levels of Cu(II) ions were analyzed to be 6, 15, 32, 47, and 62% by conventional analytical procedures. These samples are called CuNaY-6 etc. hereafter. Decationated Y-type zeolite (denoted HY) was prepared by degassing the NH_4^+ form of zeolite at 500 °C for several hours. All the powder samples obtained as above were sieved to 20–60 mesh for use in TPD experiments. The x-ray diffraction patterns of the samples before and after use were in complete agreement with one another, showing the stability of the zeolite structure within the limits of the present work.

Helium gas of ultra-high-purity grade (>99.995%) was supplied from Air Product & Chemical. Before use in TPD experiments, helium and oxygen were passed through a cold trap cooled to liquid nitrogen temperature for complete removal of moisture.

Methods and Procedures. The TPD apparatus used is the same as that reported previously.[8] After being mounted in the TPD cell, each zeolite sample was degassed at 500 °C for more than 2 h and then exposed to an oxygen atmosphere at the same temperature for more than 2 h. These pretreatments were always carried out for fresh samples in order to remove water and possible hydrocarbon impurities on the zeolite surface. Each run of TPD experiments consisted of three parts, i.e., sample conditioning at an elevated temperature, oxygen adsorption under specified condition, and controlled heating for oxygen desorption. Sample conditioning was achieved by a series of treatments at 500 °C: evacuation ($<10^{-5}$ Torr) for 2 h, exposure to oxygen (100 Torr) for 1 h, and reevacuation for 15 min. For oxygen adsorption and desorption either of the following two procedures was applied.

Procedure I. After the sample conditioning, the sample was cooled to a chosen temperature and exposed to an oxygen atmosphere (100 Torr) for 2 h for oxygen adsorption. Then, the sample was evacuated for 15 min, and cooled to 10 °C in vacuo within 30 min. At that temperature helium was diverted to flow through the reactor at a rate of 30 cm^3/min and the programmed heating was started. The heating rate was set at 5 K/min unless specified otherwise.

Procedure II. This procedure was applied in runs 1–3, 12–16, 18, and 19. After the sample conditioning 100 Torr of oxygen was first introduced at 500 °C, and then the system was immediately started to cool at a rate of 3.3 K/min under the same oxygen atmosphere to 10 or 250 °C. Oxygen adsorption in this case was thus attained not at a constant temperature but over a certain temperature range. At 10 or 250 °C, the sample was evacuated for 15 min before going to programmed heating, which was the same as in procedure I.

ESR spectra of Cu(II) ions were recorded in the X-band region at room temperature with a Hitachi 771 spectrometer equipped with a TE_{102} mode cavity. Before recording, zeolite samples were treated in the same way as above in a 4-mm o.d. pylex glass tube that was thin enough to be inserted into the microwave cavity.

Results

Temperature Programmed Desorption of Oxygen from CuNaY-62. Typical desorption chromatograms of oxygen from CuNaY-62, NaY, and HY are shown in Figure 1. In these experiments, oxygen was adsorbed by procedure II with cooling from 500 to 10 °C. In the case of CuNaY-62, at least five different states of adsorbed oxygen are indicated by the appearance of five TPD peaks with peak maxima located at 40, 80, 320, 470, and >550 °C. These are designated α, β, γ, δ, and ϵ, respectively. In contrast, NaY or HY shows a single, vanishingly small desorption

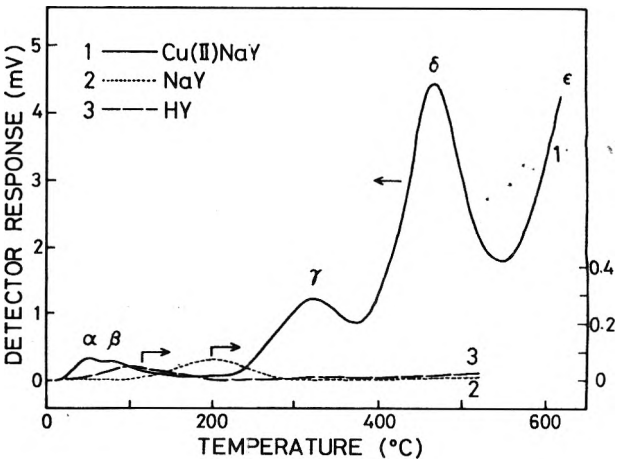

Figure 1. TPD chromatograms of oxygen from HY, NaY, and CuNaY-62.

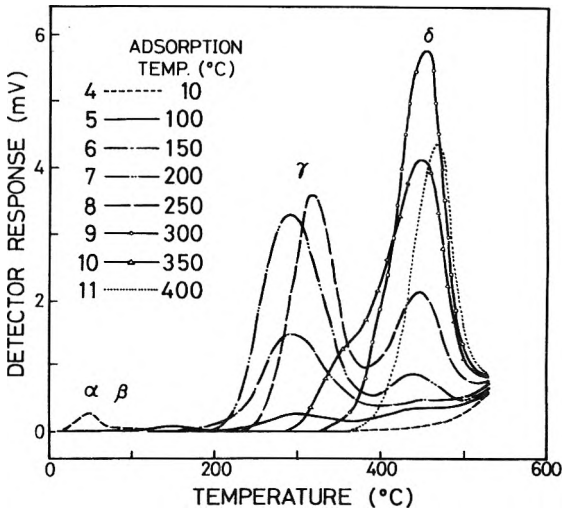

Figure 2. The variation of TPD chromatogram of oxygen from CuNaY-62 with adsorption temperature.

peak at 200 or 100 °C, respectively. These facts indicate that new active sites for oxygen adsorption are created in the zeolite by substituting Cu(II) ions for Na(I) or H(I) ions. In the following description, we use terms such as γ adsorbate, γ adsorption, or γ oxygen for brevity, which mean the oxygen adsorbate, the adsorption state, or the desorbed oxygen corresponding to the γ peak, respectively.

In order to characterize the above desorption peaks, the influence of the temperature of oxygen adsorption (T_{ad}) on the TPD chromatogram was examined. The activation energies of desorption were also determined for the γ and δ peaks. Figure 2 shows TPD chromatograms from CuNaY-62 samples on which oxygen has been adsorbed at various T_{ad}'s between 10 and 400 °C by procedure I. Four desorption peaks α, β, γ, and δ are seen to appear in the range 10–500 °C with their intensities markedly depending on T_{ad}. The amounts of desorbed oxygen for γ and δ were evaluated from respective peak areas and are plotted against T_{ad} in Figure 3. It is seen that γ and δ show marked dependence on T_{ad}, exhibiting bell-shaped correlations which possess maxima roughly at 200 and 350 °C, respectively. If one takes the sum of both (γ + δ), however, it shapes a broad peak with a plateau of ca. 1.3 cm^3/(gram of catalyst) at its top as shown in the same figure. The existence of the plateau suggests that γ and δ are complementary to one another, or in other words, the γ and δ adsorbates share a definite number of common adsorption sites. The complementary nature of γ and δ will be discussed later.

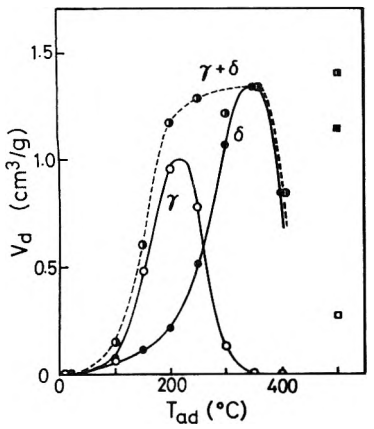

Figure 3. Dependence of the amounts of desorbed oxygen (V_d) on adsorption temperature (T_{ad}). Squares represent the values of run 1.

TABLE I: Temperature Programmed Desorption of γ and δ Oxygen[a]

γ oxygen			δ oxygen		
b, K/min	T_M, K	v_d,[b] cm³/g	b, K/min	T_M, K	v_d,[b] cm³/g
5.3	592.2	0.77	5.5	737.0	1.06
10.8	604.3	0.80	10.8	748.9	1.11
15.2	612.0	0.78	14.0	758.7	1.03
21.4	620.7	0.80	20.8	765.2	1.07

[a] Oxygen adsorption was carried out at 250 °C (for γ oxygen) or 380 °C (for δ oxygen). [b] v_d is the amount of desorbed oxygen.

Two comments are worth mentioning here. First, the chromatograms in Figure 2 assure that the interconversion of the oxygen adsorbates during TPD experiments is insignificant. For instance, run 10 which exhibited a single desorption peak, δ, indicates that none of the conversions of $\delta \rightarrow \gamma$, $\delta \rightarrow \beta$, and $\delta \rightarrow \alpha$ occurred during the cooling or heating procedure applied. Similar conclusions can be derived from the other runs. Second, the temperature of the γ peak maximum was found to shift slightly with T_{ad}; it was ca. 290 °C for $T_{ad} \leq 200$ °C (runs 6 and 7), while ca. 320 °C for $T_{ad} \geq 250$ °C (runs 1 and 8). Probably this means that the γ adsorption undergoes a slight modification depending on T_{ad}. In this paper, however, no further reference is made with respect to this phenomenon.

The activation energies of desorption (E_d) were determined. As mentioned in the previous paper,[8] when the sample temperature increases linearly with time and the desorption takes place from a homogeneous surface without appreciable readsorption, the peak temperature (T_M) of a desorption peak is correlated with E_d and the heating rate (b) by the following equation:

$$2 \ln T_M + \ln b = \frac{E_d}{RT_M} + \ln \frac{E_d v_m}{Rk_0}$$

where v_m is the amount of the corresponding adsorbate at full surface coverage, and k_0 and R are constants. This equation allows the determination of E_d if the T_M's are measured at different heating rates. Such analyses were applied to γ and δ. α and β were excluded because of the insufficient accuracy of their T_M's. For the analyses for γ and δ, the temperatures of oxygen adsorption (procedure I) were set to 250 and 380 °C, respectively, in order that the respective peaks should dominate in the TPD chromatograms. The results were summarized in Table I. For each of γ and δ, T_M increased with increasing heating rate, while the amount of desorbed oxygen (V_d) remained

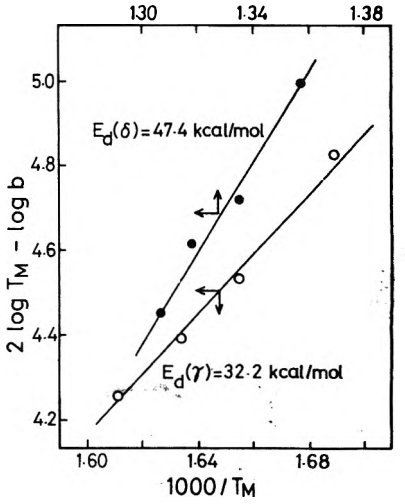

Figure 4. Activation energies of desorption of oxygen from CuNaY-62.

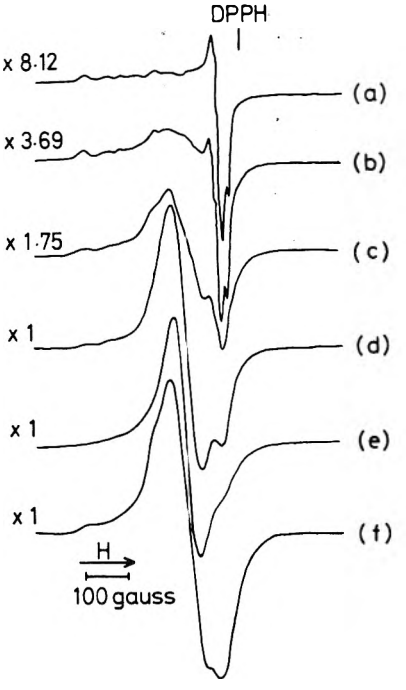

Figure 5. ESR spectra obtained at room temperature for CuNaY-6 (a), -12 (b), -32 (c), -47 (d), and -62 (e) all pretreated at 500 °C. Curve f is for CuNaY-62 hydrated at 250 °C as explained in the text.

unchanged. The plots gave straight lines in agreement with the above equation as shown in Figure 4. From the slopes, the activation energies were determined to be $E_d(\gamma)$ = 32.2 and $E_d(\delta)$ = 47.4 kcal/mol.

Influence of Cu(II) Ion-Exchange Level on Oxygen Adsorption. The influence of the Cu(II) ion-exchange level on the TPD chromatogram of oxygen was examined by using the five CuNaY samples with different Cu(II) content. Before examination, however, it was felt necessary to know the state of Cu(II) ions exchanged in zeolites. Figure 5 shows the ESR spectra of Cu(II) ions recorded for the five samples after the completion of the same pretreatments (dehydration and oxidation at 500 °C) as was performed in the TPD experiments. These spectra are similar to those previously reported by other researchers[10-15] and interpreted as follows. The spectra obtained for low exchanged CuNaY (<20% Cu(II) ion-exchanged) consist of at least two sets of g values ($g_{\|}^1$ = 2.38 and $g_{\|}^2$ = 2.30), which indicate that Cu(II) ions occupy two or more nonequivalent exchanged sites in the zeolite unit cell. As the Cu(II) ion concentration in the zeolite

TABLE II: Effect of Water on Oxygen Adsorption

	Run no.	Adsorption procedures		v_d,[a] cm³/g	
		Oxygen adsorption[b]	Water adsorption	Oxygen	Water
A	8	250 °C, 2 h		1.28 (γ + δ)	0
	17	250 °C, 2 h	250 °C, 10 μL pulse	1.25 (ω)	
	18	500 → 250 °C[c]		1.39 (γ + δ)	0
	19	500 → 250 °C[c]	250 °C, 10 μL pulse	1.37 (ω)	
		Water adsorption	Oxygen adsorption[b]		
B	20	250 °C, 10 μL pulse		0	1.96
	21	250 °C, 10 μL pulse	250 °C, 2 h	1.93 (ω)	
	22	250 °C, 10 μL pulse	250 °C, 2 h	(1.93)	2.03[d]

[a] v_d is the amount of oxygen or water desorbed. [b] Oxygen pressure was 100 Torr in all cases. [c] Oxygen adsorption was performed by cooling from 500 to 250 °C with procedure II. [d] This value was calculated by using the result of run 21.

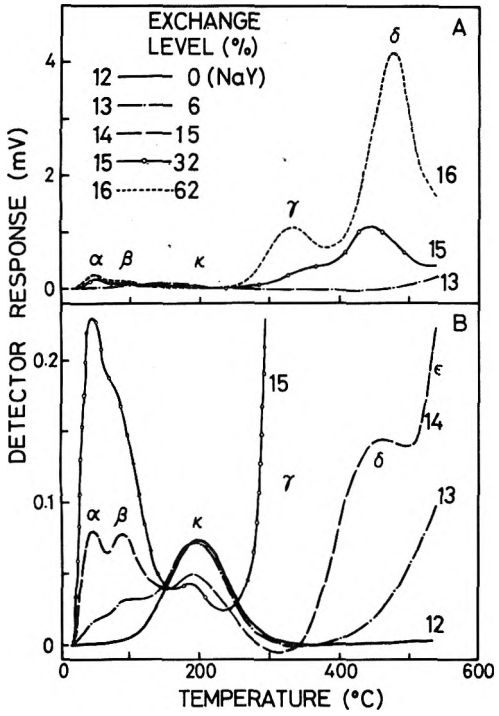

Figure 6. TPD chromatograms of oxygen from CuNaY samples with various ion-exchange levels. Parts of (A) are magnified in (B).

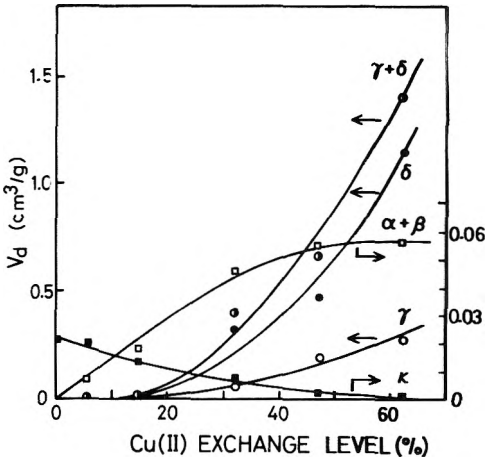

Figure 7. Correlation of the amounts of desorbed oxygen (V_d) with the Cu(II) ion-exchange level.

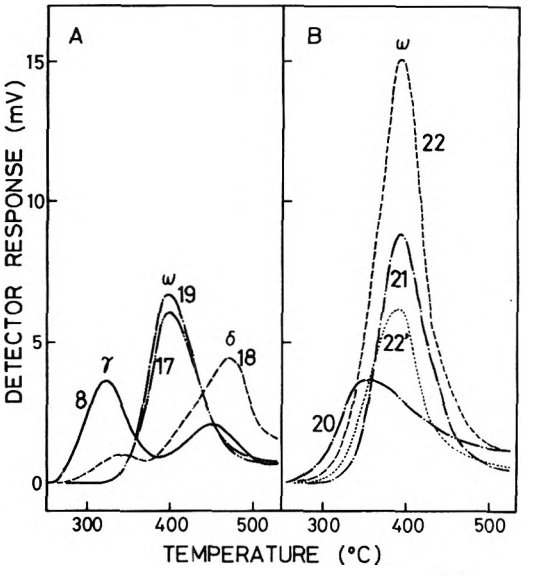

Figure 8. Effects of water on oxygen adsorption. The numbers correspond to those in Table II.

increases, the ESR spectrum changes due to other exchange sites being occupied and to spin interactions between copper ions. At sufficiently high Cu(II) ion-exchange level, more than one Cu(II) ion are located in each sodalite cage. The close proximity of these paramagnetic ions to one another results in spin-exchanged interactions that cause the ESR spectrum to collapse to one symmetric line.

The TPD chromatograms obtained for these samples are shown in Figure 6. In these experiments oxygen was adsorbed by cooling from 500 to 10 °C in an oxygen atmosphere (procedure II). Clearly, all the peaks α through ε become larger with the increase in the Cu(II) ion content. In addition, a new, small desorption peak (κ) appears at 190–200 °C. κ is the largest for Na(I)Y and decreases with increasing the exchange level, indicating the oxygen adsorption associated with Na(I) ions.

The influence of the Cu(II) ion-exchange level is quantitatively depicted in Figure 7. For α and β, only their sum is considered here. The oxygen amounts for α + β, γ, and δ increase with the exchange level, while that for κ behaves oppositely. Further it is recognized that α + β and γ + δ exhibit characteristic correlations with the exchange level, and the latter increases rapidly above ca. 20%. These facts reflect that the exchanged Cu(II) ions occupy certain specific cation sites in the zeolite unit cell in preference to others as discussed later.

Effect of Water on Oxygen Adsorption. In the foregoing paragraphs, the adsorption–desorption of oxygen was studied for dehydrated zeolite samples. This phenomenon was found to be markedly affected by the coadsorption of water, a new desorption peak being caused to appear instead of γ and δ peaks. In this paragraph, the effect of water was examined in relation to γ and δ adsorptions. Experiments were performed in two ways (A and B), and the results were summarized in Figure 8 and Table II together with the conditions applied for the adsorption of

TABLE III: Comparison of Siting of Cu(II) Ions in Dehydrated Cu(II) Ion-Exchanged Y-Type Zeolites

	Ref 16[a]		Ref 17[b]		This work[c]	
Inside the sodalite cage structure	I 3.2 I′ 11.1 } 14.3		I 1.5 I'_A 11.4 I'_B 2.8 } 15.7		I I′	} 16.3
			II′ 0.8		II′	0.3
Inside or on the periphery of supercage structure			II_A 3.8 II_B 1.5		II	0.8
Unidentified	1.7		3.3			
Total	16.0		25.1			17.4

[a] For a sample evacuated at 500 °C for 12 h. [b] For a sample evacuated at 150 °C for 20 h. [c] These values were estimated from the TPD spectra (see text).

oxygen and water. In all cases, fresh CuNaY-62 samples were used after the same pretreatment at 500 °C as mentioned in the previous paragraphs. In runs 17, 19, and 21, a liquid nitrogen trap was equipped between the TPD cell and the detector to separate off the water vapor desorbed during the TPD experiments.

First, the effect of water addition to oxygen preadsorbed systems was examined (Table IIA and Figure 8A). In run 8 or 18, oxygen alone was adsorbed at 250 °C for 2 h (procedure I), or during cooling from 500 to 250 °C (procedure II), respectively. The resulting chromatograms 8 and 18 show γ and δ peaks similar to those mentioned earlier. In runs 17 and 19, on the other hand, 10 μL of water was pulsed into the system by using a helium carrier (30 cm^3/min) after the completion of the above oxygen adsorption procedures. Ten minutes after the water pulse, the system was reevacuated for 10 min at the same temperature, followed by cooling to 10 °C for the start of the programmed heating. In the corresponding chromatograms 17 and 19, the γ and δ peaks were completely replaced by a new desorption peak (ω) appearing at 390–400 °C. It was confirmed in separate experiments that the increase of the water pulse up to 50 μL or the prolonged evacuation time after the water pulse up to 2 h gave no significant effects on the TPD chromatogram. It is notable that virtually the same chromatograms were obtained in runs 17 and 19 irrespective of the difference of the oxygen adsorption procedures. In addition, the amounts of oxygen in runs 17 and 19 are very close to those for $\gamma + \delta$ in runs 8 and 18, respectively. These indicate that both γ and δ are exclusively and completely converted to ω on the addition of water.

Next, the effect of water adsorption on the subsequent oxygen adsorption was examined (Table IIB and Figure 8B). Water was adsorbed in the same way as above. The adsorption of water alone gave rise to a broad peak of water desorption at 350 °C (run 20). Additional oxygen adsorption (run 21 or 22) resulted in chromatogram 21 or 22 when the response was recorded for desorbed oxygen alone or for both desorbed oxygen and water, respectively. Apparently, the difference between these chromatograms is attributable to the desorption of water. Curve 22′ is a difference chromatogram synthesized for the water desorption. Clearly the preadsorption of water causes the ω peak to appear similarly as in the previous experiments (A). Quantitatively, however, the amount of ω oxygen in run 21 is found to be a factor of 1.5 larger than that in run 8 (Table II). This indicates that the capacity of the exchanged zeolite for oxygen adsorption is increased by the preadsorption of water. At the same time, the shift of the desorption peak from 20 to 22′ indicates the adsorption state of water itself being also affected by the coadsorption of oxygen. In addition, runs 21 and 22 reveal an important fact that oxygen and water are coadsorbed in nearly equimolar quantities and are desorbed at the almost same temperature region. This fact strongly suggests the cooperative nature of the adsorptions of oxygen and water as will be discussed later.

The ESR spectrum of Cu(II) ions for a CuNaY-62 sample, hydrated through the same treatment as performed in run 20, is presented by curve f in Figure 5. The signal, less symmetric than curve e for the corresponding dehydrated sample, suggests that spin interactions decreases on hydration of the zeolite sample. However, no further change in ESR spectrum was observed with the coadsorption of oxygen.

Discussion

General Background for Y-Type Zeolite. Oxygen adsorbing (or desorbing) on CuNaY in the temperature range 10 to 600 °C exhibited five characteristic peaks in the TPD chromatograms. Of these peaks, four (α, β, γ, and δ) are clearly evident, whereas the remaining one (ϵ) is less evident being indicated by insufficient responses. These peaks change sensitively depending on the method and temperature of oxygen adsorption, the exchange level of Cu(II) ions, and the coexistence of water. Interpretation of these phenomena requires understanding of the structure of the adsorbent zeolite.

The crystal structures of faujasite type zeolites, including the synthetic Y zeolites, have been reviewed by Smith.[18] The sodalite unit has an internal diameter of 6.6 Å and the enclosed void space is called the sodalite cage. These units, which are connected by hexagonal prisms, embrace a larger void space which is called the supercage. An idealized projection and a cut-away view are given in Figure 9. It is now clear from x-ray diffraction data that the cations occupy five principal sites in the dehydrated faujasite-type structure. Site I (S_I) is in the center of the hexagonal prism. Site II (S_{II}) projects slightly outward into the supercage from the free six-ring. Site I′ ($S_{I'}$) and II′ ($S_{II'}$) project into the sodalite unit from shared and free six-ring, respectively. Site III (S_{III}) is at the four-ring, but the exact situation is still not established.[17,19] Gallezot et al.[16] and Maxwell and de Boer[17] determined the exact locations of copper cations in Cu(II) ion-exchanged zeolites dehydrated at 500 and 150 °C, respectively, by the x-ray diffraction method. Their results were summarized in Table III. In spite of the difference of the Cu(II) ion-exchange levels and the dehydration temperatures, the distributions of Cu(II) ions over S_I and $S_{I'}$ are surprisingly similar in these two works, and indicate that 14–16 Cu(II) ions per unit cell are located preferentially at S_I or $S_{I'}$.

The degree of the preference of divalent cations for sites S_I and $S_{I'}$ depends on the cationic species. Generally speaking, alkaline earth cations show a very strong tendency to occupy the interior sites (S_I or $S_{I'}$) in dehydrated zeolites; a large fraction of S_I and $S_{I'}$ is filled first

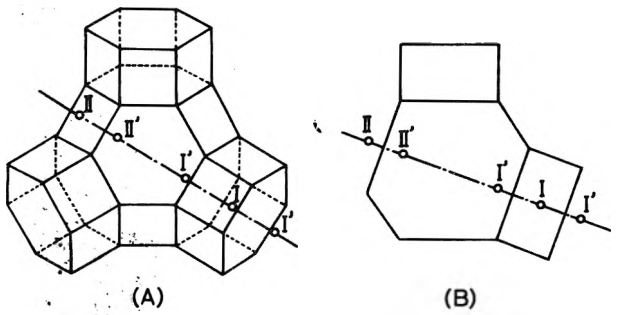

Figure 9. Idealized sodalite unit and hexagonal prisms: (A) projection, and (B) cut-away view. Positions of cation sites are designated I, I', II, and II'.

before sodium ions at S_{II} or S_{III} can be replaced.[20] On the other hand, transition metal cations exhibit less overwhelming preference for S_I or $S_{I'}$.[16,21,22] For example, Gallezot and Imelik[22] have shown that, when the exchange level arises above 12 Ni per unit cell, the additional nickel cations are sited outside the hexagonal prism and sodalite cage. Similar tendency is also observed for Cu(II)NaY zeolites as described before.[5]

In hydrated Cu(II) ion-exchanged zeolites, the exact locations of Cu(II) ions are smeared except for a few sited at S_I and $S_{I'}$. However, it is now accepted that various molecules such as water or ammonia coordinate Cu(II) ions in the zeolite structure and cause them to migrate from the sodalite cage toward the supercage. Especially, the change of ESR spectra of Cu(II) ions accompanied by hydration and dehydration of zeolite samples has been studied in detail. Naccache and Ben Taarit[12] reported that in entirely hydrated samples the Cu(II) ion is in the form of an hexaaquo complex localized in the center of the supercage. The effect of evacuation of the sample containing 16 Cu(II) ions per unit cell was studied by Turkevich et al.[13] The hyperfine structure particularly in the high-field band appears at 200 °C; however, this hyperfine structure disappears on evacuation at 300–400 °C. Taking into account the results by Krüerke and Jung,[14] most of the adsorbed water desorbs in the range 150–300 °C.

Exchanged Cations as Adsorption Sites for Oxygen. For comparison with the present data on CuNaY, the TPD chromatograms of oxygen from Mn(II)NaY, Co(II)NaY, and Ni(II)NaY[9] are shown in Figure 10. In contrast to the case for CuNaY, the responses are far weaker for these samples. Clearly, the chromatograms vary extensively with the samples used, being characteristic of the kinds of cations exchanged. This indicates a strong association of the exchanged cations in the oxygen adsorption involved.

It has been known that the superoxide ion O_2^- can be produced in the various cation forms of Y-type zeolites by x, γ, or UV irradiations.[23–26] Kasai[23] first reported the formation of the superoxide ions on NaY and BaY and concluded that the principal g values of the radicals depended on the positive charges of the cations. Wang and Lunsford[25] studied the superoxide ion produced on alkaline earth Y-type zeolites and found no significant trend in the change of g_z values with the alkaline earth cations. However, the hyperfine interaction between the cation and an unpaired electron of the superoxide ion occurred on HY, AlY, ScY, and LaY, indicating that the cation was part of the adsorption site.[24,26] Recently O_2^- radical formation on NaY[27] or Ti(III)Y[28] by a purely chemical reaction has been reported and the adsorption centers are supposed to be the cations.

Taking into account the above results, we conclude that the oxygen adsorbates responsible for TPD spectra are

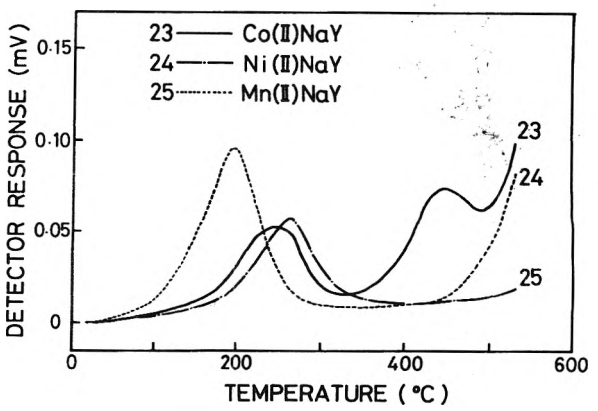

Figure 10. TPD chromatograms of oxygen from Co(II)NaY, Ni(II)NaY, and Mn(II)NaY[9] after oxygen adsorption by procedure II with the cooling from 500 to 10 °C.

bound by the exchanged cations directly or indirectly. In this connection, for CuNaY samples, it was attempted to detect the change of the state of Cu(II) ions accompanied by oxygen adsorption by ESR spectroscopy, but the ESR spectrum of Cu(II) ions was found to be little influenced by exposure to oxygen, in agreement with the result by Turkevich et al.[11] Jacobs et al.[29] recently observed oxygen desorption from CuNaY by means of gravimetric analysis, and proposed, in disagreement with our view, the desorption of lattice oxygen accompanied by the reduction of Cu(II) ions. The proposal, however, is unlikely to be consistent with the various phenomena observed in the present study.

Adsorption of γ and δ Oxygen. As pointed out previously, the plateau (ca. 1.3 cm^3/g) in the curve of the amount of γ + δ vs. T_{ad} in Figure 3 suggests that γ and δ share common adsorption sites. This suggestion is supported by the following facts. First, the sum (γ + δ) in run 1, 1.42 cm^3/g, is also nearly equal to the above plateau value irrespective of the different oxygen adsorption procedures applied. Second, it was shown that CuNaY samples which had preadsorbed 1.33 cm^3/g of δ oxygen at 350 °C could not adsorb γ oxygen any more at 250 °C. Third, while CuNaY-15 exhibited only the δ peak when oxygen had been adsorbed by procedure II (run 14), the same sample was found to exhibit γ desorption alone almost to the same amount when oxygen had been adsorbed at 250 °C by procedure I.

The amount of desorbed oxygen for γ + δ in run 1, 1.42 cm^3/g, corresponds to 0.047 oxygen molecules adsorbing per Cu(II) ion. Assuming a molecular adsorption, this means that only 0.8 Cu(II) ions in the unit cell of CuNaY-62 ($Cu_{17.4}Na_{21.2}Y$) are active for the adsorption. This value is too small to be compared with the total Cu(II) ions, and suggests only the Cu(II) ions located at specific sites being responsible for it. Important information concerning this is provided by the experiments on CuNaY samples with different cation-exchange levels. As in Figure 7, the amount of γ + δ is very small for low-exchanged CuNaY zeolites until it increases rapidly above 20% exchange. Considering that, as mentioned before, the Cu(II) ions at low exchange levels prefer the S_I and $S_{I'}$ sites in the zeolite unit cell though not so overwhelmingly as alkaline earth ions do, it is obvious that the above tendency of γ + δ well correlates to the occupancy of Cu(II) ions at sites other than S_I and $S_{I'}$. The strong interaction of the γ and δ adsorbates with water (Figure 8) also suggests that the responsible adsorption sites are inside or on the periphery of the supercage structure.

Based on the above consideration, we conclude that the γ and δ adsorbates are associated with the Cu(II) ions at

S_{II} (and S_{III} if it is occupied) in the supercage structure. The cations at $S_{II'}$ in the sodalite cage are excluded here because they are not likely to be accessible for the adsorbates which are considered to be molecular on the basis of the reasons described below. The importance of the cations at sites S_I, $S_{I'}$, and $S_{II'}$ will be discussed later with respect to the other types of oxygen adsorption. It is very interesting to note here that the above tendency of $\gamma + \delta$ vs. the exchange level of CuNaY is in fair agreement with that of the catalytic activity vs. the exchange level reported for the oxidative dehydrogenation of cyclohexane.[5] This fact reflects on the importance of these oxygen adsorbates in the catalytic oxidation reaction over CuNaY catalysts. In the catalysis, it has been proposed that the exchanged cations at exposing sites such as S_{II} and S_{III} should be potentially active, whereas the cations at hidden sites such as S_I or $S_{I'}$ should be inactive.

The γ and δ adsorbates were shown to share common adsorption sites, keeping their sum amounting to an almost constant value. This implies that both adsorbates should be either molecular or atomic. If one is molecular and another is atomic, for example, the atomic type requires adsorption sites twice as much as the molecular type does and this assures no longer the constancy of their sum. The fact that both γ and δ transformed into ω by the interaction with water indicates that they are not extremely different.

It was already mentioned that $\gamma + \delta$ amounts to 0.8 molecules per unit cell of CuNaY-62. Crystallographically, the x-ray data of Table III show that less than one Cu(II) ion is present in a single supercage at that exchange level (the unit cell contains eight supercages). This demonstrates the difficulty of such a dissociative adsorption that each oxygen atom should be adsorbed on the Cu(II) ions in the supercage, since it should require the migration of the dissociated oxygen atoms from a supercage into another. In addition, dissociative adsorption cannot explain why the atomic, and therefore penetrative, oxygen adsorbates prefer only exposed cations. Furthermore, it was experimentally shown that both γ and δ oxygen followed first-order desorption kinetics. Thus, we conclude that both γ and δ adsorbates are of molecular types coordinating to the Cu(II) ions located in the supercage. For these we postulate the following types of adsorption: an end-on type (γ) and a side-on type (δ). Further physi-

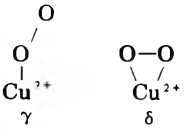

cochemical evidence should be collected to support this.

Effect of Water on Oxygen Adsorption. The presence of water was found to affect not only the state of adsorbed oxygen but also the amount of it. As for the former effect, water coadsorption caused the ω desorption to appear instead of γ and δ desorptions which were typical in the absence of water. For the latter, the amount of oxygen adsorption increased on water preadsorption.

The effects are related to the hydration and migration of Cu(II) ions in zeolite, as is suggested from the comparison of the ESR spectra of Cu(II) ions for a dehydrated and a hydrated CuNaY-62. Runs 20 and 21 in Table II assure that 2.0 cm^3/g of water still remains on CuNaY-62 even after evacuation at 250 °C. These water molecules are used for the hydration of Cu(II) ions and eventually show an effect of pulling out Cu(II) ions from sodalite cages toward more exposed sites. The increase in oxygen adsorption on water preadsorption is thus interpreted as resulting from the increase of the Cu(II) ions located at such exposed sites. Calculation shows that, in run 21, ω oxygen amounts to 1.1 oxygen molecules per unit cell of zeolite. Since ω adsorption is considered to be of molecular type as mentioned later, this means that 0.3 Cu(II) ions are newly activated by the hydration, the quantity being reasonably ascribed to the migration of the Cu(II) ions at $S_{II'}$ toward the supercage.

As mentioned above, it is proposed that, while in a dehydrated zeolite only the Cu(II) ions located at S_{II} (and S_{III}) are responsible for the oxygen adsorption in γ and δ, the Cu(II) ions at $S_{II'}$ are also activated for oxygen adsorption in the presence of water. Such a consideration enables the estimation of the distribution of Cu(II) ions over each exchangeable site in a dehydrated zeolite, as shown in Table III. The population of $S_I + S_{I'}$ was equated to the difference between the total number of the Cu(II) ions exchanged (17.4) and that responsible for ω adsorption (1.1). The values thus estimated are in reasonable agreement with the x-ray data.

Interesting facts were found concerning interactions between adsorbed oxygen and water. Of these, the most interesting is that oxygen and water were adsorbed in nearly equimolar quantities, as indicated from runs 20–22. Taking into consideration that the desorption state of water itself was also affected in the presence of oxygen and that oxygen and water were desorbed at the almost same temperature region, this strongly suggests that an equimolar water and oxygen coordinates to the same Cu(II) ions, giving rise to ω adsorption states. The ω state should not vary so extremely from the γ or δ state because the latter is converted to the former in the presence of water. The following may be presented as a plausible model for the ω state:

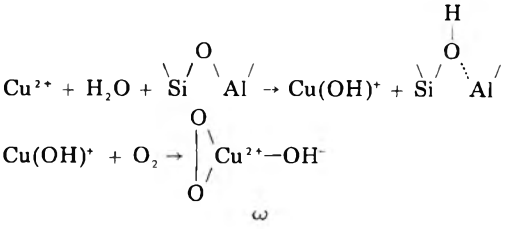

Here –Si–O–Al– represents the zeolite skeleton. The existence of the hydrated species $Cu(OH)^+$ has already been confirmed by IR spectroscopy.[30] Oxygen is considered to coordinate to this species nondissociatively.

Oxygen Adsorption in Other States. The correlation between the amount of $\alpha + \beta$ and the exchange level of CuNaY shown in Figure 7 suggests that α and β are related, at least in tendency, to the number of Cu(II) ions occupying S_I and $S_{I'}$. It is not likely, however, that the corresponding adsorbates, which desorb at such a low temperature as 40 or 80 °C, should directly coordinate to the Cu(II) ions. Rather, they are probably molecular adsorbates adsorbing on the periphery of the hexagonal prisms which contain Cu(II) ions at $S_{I'}$. Vedrine and Naccache[31] have identified, by ESR spectroscopy, the superoxide ion O_2^- adsorbing on the lattice oxygen of the zeolite framework, in line with this assignment. However, the amounts of α and β are too small to be simply compared with the amount of these Cu(II) ions. The exact nature of these adsorptions is still not established.

For NaY and low Cu(II) ion-exchanged samples, κ adsorption was observed. The corresponding adsorbate can be assigned to O_2^- adsorbing on Na(I), on the basis of the ESR data of other workers[23,27] that O_2^- was formed on Na(I) in zeolite at lower temperatures and that it was completely eliminated when heated above 150 or 300 °C.

The oxygen adsorbate desorbing at 100 °C from HY may also be the superoxide ion O_2^-.

Finally, oxygen adsorption in ϵ is discussed. ϵ is so stable as to desorb above 500 °C, and exists in fairly large quantities even at low Cu(II) ion-exchange levels in contrast to γ and δ as shown in Figure 6, though the exact amount was not measured considering the thermal stability of the zeolite structure. We assign this adsorbate to the extraframework oxygen atoms bound by Cu(II) ions situated at S_I'. The existence of extraframework oxygen atoms, located slightly off the center of the sodalite cage, has been well estimated in some metal ion-exchanged zeolites. It has been confirmed by ESR that the identical and nonlinear Cu(II) ion pairs in Y-type zeolites are formed through the mediation of extraframework oxygen atoms.[10] The number of extraframework oxygen atoms is 5 and 5.3, respectively, for $Cu_{16}Na_{24}Y$ dehydrated at 500 °C[16] and $Cu_{25.1}K_{5.8}Y$ dehydrated at 150 °C.[17] The agreement of these values indicates that the number of extraframework oxygen atoms is nearly constant at high exchange levels and that they are little desorbed by evacuation at 500 °C. Using Mössbauer spectroscopy[32] and IR spectroscopy,[33] Boudart et al. have reached the conclusion that, in a dehydrated Fe(II)NaY zeolite, ferrous ions which occupy predominantly S_I are pulled into the sodalite cage upon oxidation to form iron–oxygen–iron bridges and have made sure that the oxygen atoms involved do not desorb at 400 °C.

References and Notes

(1) Present Address: Department of Industrial Chemistry, Faculty of Engineering, Nagasaki University, Nagasaki, 852 Japan.
(2) I. Mochida, S. Hayata, A. Kato, and T. Seiyama, *J. Catal.*, **15**, 314 (1969); **23**, 31 (1971).
(3) C. Naccache and Y. Ben Taarit, *J. Catal.*, **22**, 171 (1971).
(4) S. Roginskii, I. L. Tsitovskaya, et al., *Dokl. Akad. Nauk SSSR*, **196**, 872 (1970).
(5) I. Mochida, T. Jitsumatsu, A. Kato, and T. Seiyama, *J. Catal.*, **36**, 361 (1975).
(6) K. Tsutsumi, S. Fujii, and H. Takahashi, *J. Catal.*, **24**, 146 (1972).
(7) C. Dimitrov and H. F. Leach, *J. Catal.*, **14**, 336 (1969).
(8) M. Iwamoto, Y. Yoda, M. Egashira, and T. Seiyama, *J. Phys. Chem.*, **80**, 1989 (1976).
(9) M. Iwamoto, K. Maruyama, N. Yamazoe, and T. Seiyama, *J. Chem. Soc., Chem. Commun.*, 615 (1976).
(10) C. C. Chao and J. H. Lunsford, *J. Chem. Phys.*, **57**, 2890 (1972).
(11) J. Turkevich, Y. Ono, and J. Soria, *J. Catal.*, **25**, 44 (1972).
(12) C. Naccache and Y. Ben Taarit, *Chem. Phys. Lett.*, **11**, 11 (1971).
(13) A. Nicul, D. Stamires, and J. Turkevich, *J. Chem. Phys.*, **42**, 3684 (1965).
(14) U. Krüerke and P. Jung, *Z. Phys. Chem.*, **58**, 53 (1968).
(15) R. G. Herman, J. H. Lunsford, H. Beyer, P. A. Jacobs, and J. B. Uytterhoeven, *J. Phys. Chem.*, **79**, 2388 (1975).
(16) P. Gallezot, Y. Ben Tarrit, and B. Imelik, *J. Catal.*, **26**, 295 (1972).
(17) I. E. Maxwell and J. J. de Boer, *J. Phys. Chem.*, **79**, 1874 (1975).
(18) J. V. Smith, Second International Conference on Molecular Sieve Zeolites, 1970, p 401, Worcester Polytechnic Institute, Worcester, Mass.
(19) J. V. Smith, *Adv. Chem. Ser.*, **No. 101**, 171 (1971).
(20) For example; T. A. Egerton and F. S. Stone, *Trans. Faraday Soc.*, **66**, 2364 (1970); J. W. Ward, *J. Phys. Chem.*, **74**, 3021 (1970); K. Tsutsumi and H. Takahashi, *J. Phys. Chem.*, **74**, 2710 (1970).
(21) For example; C. L. Angell and P. C. Schaffer, *J. Phys. Chem.*, **70**, 1413 (1966); D. H. Olson, *J. Phys. Chem.*, **72**, 4366 (1968); T. I. Barry and L. A. Lay, *J. Phys. Chem. Solids*, **27**, 1821 (1966).
(22) P. Gallezot and B. Imelik, *J. Phys. Chem.*, **77**, 652, 2556 (1973).
(23) P. H. Kasai, *J. Chem. Phys.*, **43**, 3322 (1965).
(24) K. M. Wang and J. H. Lunsford, *J. Phys. Chem.*, **73**, 2069 (1969).
(25) K. M. Wang and J. H. Lunsford, *J. Phys. Chem.*, **74**, 1512 (1970).
(26) K. M. Wang and J. H. Lunsford, *J. Phys. Chem.*, **75**, 1165 (1971).
(27) T. Imai and J. W. Habgood, *J. Phys. Chem.*, **77**, 925 (1973).
(28) Y. Ono, K. Suzuki, and T. Keii, *J. Phys. Chem.*, **78**, 214 (1974).
(29) P. A. Jacobs, W. Wilde, R. A. Scoonheydt, J. B. Uytterhoeven, and H. Beyer, *J. Chem. Soc., Faraday Trans. 1*, 1221 (1976).
(30) A. V. Kiselev and V. I. Lygin, "Infrared Spectra of Surface Compounds", Wiley, New York, N.Y., 1975, p 300.
(31) J. C. Vedrine and C. Naccache, *J. Phys. Chem.*, **77**, 1606 (1973).
(32) W. N. Delgass, R. L. Garten, and M. Boudart, *J. Chem. Phys.*, **50**, 4603 (1969); *J. Catal.*, **18**, 90 (1970).
(33) R. A. Dalla, R. L. Garten, and M. Boudart, *J. Catal.*, **41**, 40 (1976).

Measurement of "Free-Ligand" Optical Anisotropies in Solution and the Potential Use of Highly Anisotropic Ligands as Optical Probes in Laser Light Scattering Studies

N. Asting and W. H. Nelson*

Department of Chemistry, University of Rhode Island, Kingston, Rhode Island 02881

(Received June 4, 1976; Revised Manuscript Received December 17, 1976)

Optical anisotropies at 632.8 nm of the neutral ligands 2,4-pentanedione, 8-quinolinol, 1,3-diphenylpropanedione, and tropolone have been measured in cyclohexane or benzene at 20 °C. Aqueous solutions containing varying amounts of NaCl supporting electrolyte have been studied as well to determine the anisotropies of the simple anions HCO_3^-, NO_3^-, SCN^-, and N_3^-. Because anisotropies of certain of the organic ligands have been found to be extraordinarily large, complexes containing two of these ligands will have very large optical anisotropies the magnitudes of which will depend substantially on the relative positions of the ligands. It has been shown that highly anisotropic ligands can be used as structural probes of the complexes to which they are bound. Sample calculations have been made for a typical six-coordinate complex.

Introduction

Molecular optical anisotropies provide information which can be used to determine molecular geometry or electronic structure. Frequently, more than one method of determination is available. For example, in the gas phase anisotropies can be obtained either through Kerr effect studies or by means of depolarized Rayleigh-scattered-light intensity measurements.[1] Determinations for the solid state can be made if birefringence data are available for crystals of known structure. For the most part, applications for the determination of structure have centered on the study of small molecules in nonpolar solvents by means of the Kerr effect[2] or depolarized Rayleigh light scattering.[3-5] More recently, it has been demonstrated that relatively complex molecules can be investigated structurally by light scattering either in aqueous[6] or nonaqueous[7] solutions. Such efforts are especially worthwhile when the results of more conventional spectroscopic analysis cannot be interpreted unambiguously.

TABLE I: Calibration Data for the Plastic Standard Based on the Anisotropic Scattering of Benzene in Cyclohexane[a]

Benzene concn, M	n(6328 Å)	d_{20}	Solvfac	$I_{h,soln}/I_{h,std}$	$I_{h,c\text{-}hex}/I_{h,std}$	$I_{h,ben}/I_{h,std}$	$10^7 R_{90std}$
0.236	1.426 12	0.7806	0.9786	0.510	0.405	0.144	4.095
0.450	1.427 11	0.7822	0.9605	0.625	0.405	0.236	3.775
0.949	1.429 74	0.7867	0.9196	0.875	0.405	0.503	3.749
1.151	1.430 69	0.7885	0.9025	0.965	0.405	0.599	3.816

[a] Solvfac = $(c_0/d_0)[(n^2 + 2)/(n_0^2 + 2)]^2$. $d_{20} = 0.7804$ (pure cyclohexane).

Typically, if a system is to be studied effectively, bond polarizability data must be available. Then, if bond polarizability additivity[8] can be assumed, molecular optical anisotropies can be calculated.[9] If there are large differences between anisotropies of candidate structures, comparison of calculated and measured anisotropies allows structural assignments to be made. Alternately, if molecular structure is known, bond polarizability components can be inferred from molecular polarizability anisotropies.[8]

Measured polarizability components are available for a substantial number of bonds. Methods of bond polarizability component calculation have been proposed[10,11] and optical anisotropies calculated from them have been compared[12] with those experimentally determined by light scattering methods. Bond polarizability components can be calculated and used, with caution, to predict molecular optical anisotropies for molecules with localized bonds. Such studies are encouraging, but it must be recognized that uncertainties in calculated molecular anisotropies[12] can range from a very-likely 10% to an order of magnitude or more.

Uncertainties in predicting the intensities of depolarized Rayleigh scattering also involve more than just inaccuracies in experimentally determined bond polarizabilities. Collisional complex formation[13,14] and solvent dependent electrical field effects[15-18] also can lead to significantly increased values of the depolarized Rayleigh scattering intensity and the related apparent optical anisotropies. The importance of such effects tends to be proportionately large if molecular anisotropies concerned are small. For that reason, measurements of depolarized Rayleigh-scattered light for the purpose of molecular structural determination are most useful if molecular optical anisotropies are large and differences in anisotropies of candidate structures are relatively large also.

Thus far, most optical anisotropy measurements have involved simple organic systems possessing relatively small polarizability anisotropies. There are numerous examples of successful application of the Kerr effect and light scattering to structural analysis. However, there has been concern expressed over interpretation of results including measured values of the bond polarizability components. Uncertainties related to the calculation of bond polarizabilities and bond polarizability components remain a substantial problem.

This paper describes a simple experimental approach to the problem of structural analysis which substantially reduces the dependency upon bond polarizability data. Potentially, it could be used with considerable advantage to study coordination compounds especially. Instead of measuring bond polarizabilities and then using them as a basis for the calculation of molecular optical anisotropies, it is proposed that measurement of ligand polarizability anisotropies be made directly. The, anisotropies of complexes can be estimated on the basis of the additivity of ligand anisotropies alone if ligand anisotropies are large. It will be shown that anisotropies of several well-known ligands such as 1,3-diphenylpropanedione are very large, and, consequently, that complexes containing these ligands can exhibit even larger optical anisotropies which will be strongly a function of molecular structure.

In contrast, other ligands such as HCO_3^- or NO_3^- which possess much smaller anisotropy values may be of little use as structural probes. Certainly, SCN^- and N_3^- show much greater promise.

Experimental Section

The Light-Scattering Photometer. Intensities of horizontally and vertically polarized Rayleigh scattered light were measured using a specially constructed photometer described elsewhere.[20] The light source was a 3.0-mW Spectra Physics Model 122 CW He–Ne gas laser which provided a vertically polarized light source of wavelength 632.8 nm. All measurements were made with 30 × 30 mm glass cells purchased from the Virtus Company painted on the outside, except for entrance slits, with a flat black paint to minimize reflections. Depolarized scattering was checked for fluorescence and Raman contributions by means of an interference filter; a Perkin-Elmer 582-1218. All measurements were made in an air-conditioned room of temperature 20 ± 1 °C.

Photometer Calibration. The photometer was calibrated independently for the two solvent systems studied. Aqueous solution calibration was done by means of 12-tungstosilicic acid solutions as described earlier.[21] Calibration for cyclohexane-solution studies was done by measuring the anisotropic scattering of four relatively dilute solutions of benzene in cyclohexane. Turbidity increments due to the benzene were calculated by means of Bothorel's equation[3] assuming a γ^2 value of 28.0×10^{-48} cm^6 for benzene. Representative calibration data are presented in Table I and plotted in Figure 1.

A lucite block mounted on a microscope stage was used as a secondary standard. By careful mechanical adjustment it was possible to reproduce scattered-light intensities due to the block with a precision of 0.2–0.5%.

Solution Clarification. Dust-free solutions were obtained by using a Millipore stainless steel filter funnel Model xx4004700 in conjunction with Millipore filters of type VCWP04700 which have a uniform pore size of 1000 Å. Solutions were forced through the filter under a positive N_2 pressure of 1–2 psi adjusted to produce a flow rate of 1–2 ml/min. Solutions were judged to be dust-free when scattered-light intensities converged to a reproducible value varying only by 1–2%. Generally, three filtrations were enough to produce "clean solutions" but, as a general practice, five or six filtrations were performed and intensities were measured after each filtration.

Solution Densities and Refractive Indices. Specific gravities were measured at 20.0 °C using a Westphal-type balance. The refractive indices were measured at 20.0 °C as well by means of a Bausch and Lomb Model 33-45-03 Series 021 precision refractometer, estimated to be precise to $n = \pm 0.00003$ calibrated as outlined previously.[21]

Reagents. All chemicals except tropolone were of reagent grade and were used without further modification.

TABLE II: Light Scattering Data Obtained for Sodium Nitrate as a Function of Supporting Electrolyte Concentration[a]

Solution	n(6328 Å)	d_{20}	Solvfac	$I_{h,sol}/I_{h,std}$	$10^{48}\gamma^2$ cm^6
1.0 M $NaNO_3$ in H_2O	1.340 84	1.0586	0.9880	0.156	6.4
2.0 M $NaNO_3$ in H_2O	1.349 05	1.1131	0.9682	0.308	6.2
3.0 M $NaNO_3$ in H_2O	1.356 76	1.1652	0.9446	0.451	6.0
4.0 M $NaNO_3$ in H_2O	1.364 01	1.2130	0.9154	0.609	6.0
1.0 M $NaNO_3$ in 1.0 M NaCl	1.349 94	1.0975	0.9861	0.147	5.9
2.0 M $NaNO_3$ in 1.0 M NaCl	1.357 64	1.1470	0.9620	0.300	6.0
3.0 M $NaNO_3$ in 1.0 M NaCl	1.364 93	1.1991	0.9392	0.437	5.8
4.0 M $NaNO_3$ in 1.0 M NaCl	1.371 83	1.2524	0.9166	0.585	5.7
1.0 M $NaNO_3$ in 3.0 M NaCl	1.366 71	1.1649	0.9784	0.135	5.3
2.0 M $NaNO_3$ in 3.0 M NaCl	1.373 72	1.2157	0.9568	0.274	5.4
3.0 M $NaNO_3$ in 3.0 M NaCl	1.380 30	1.2647	0.9325	0.410	5.3

[a] Solvfac = $(c_0/d_0)[(n^2 + 2)/(n_0 + 2)]$. d_0 = solvent density, c_0 = grams of solvent per milliliter of solution, n_0 = solvent refractive index, n = solution refractive index.

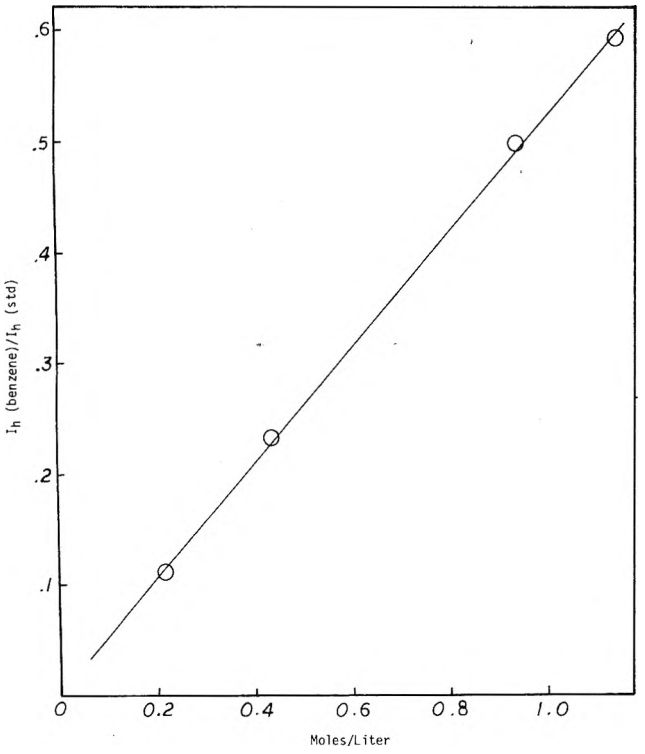

Figure 1. A plot of depolarized scattering intensity vs. concentration for benzene in cyclohexane.

Tropolone obtained from the Aldrich Chemical Co. was recrystallized once from ethanol before use. Purity and identity of organic ligands were checked by carbon–hydrogen elemental analysis, measurement of NMR spectra, and measurement of melting and boiling points. Solvents were distilled before use even though they were purchased as analytical reagent grade materials.

Calculation of the Molecular Polarizability Anisotropy, γ^2

The molecular polarizability anisotropy (optical anisotropy) of a solute molecule can be determined[3] by measurement of the intensity increments of depolarized Rayleigh-scattered light from solution as follows:

$$\gamma^2 = \frac{135\lambda^4}{16\pi^4 p(n^2+2)^2}\left[R_i(\text{soln}) - R_i(\text{solv})\frac{c_0}{d_0}\left(\frac{n^2+2}{n_0^2+2}\right)^2\right]$$

If the molecular polarizability tensor is diagonalized

$$\gamma^2 = 1/2[(\alpha_{xx} - \alpha_{yy})^2 + (\alpha_{xx} - \alpha_{zz})^2 + (\alpha_{yy} - \alpha_{zz})^2]$$

λ is the wavelength of incident radiation in centimeters, p is the number of solute molecules per milliliter, n is the refractive index of the solution, n_0 is the refractive index of the pure solvent, c_0 is the number of grams of solvent per milliliter of solution, and d_0 is the density of the pure solvent. R_i(soln) and R_i(solv) are, respectively, the Rayleigh constants of the solution and pure solvent which are proportional to corresponding depolarized scattered-light intensities measured 90° to the incident polarized laser beam.

Basically

$$R_i(\text{soln}) = \frac{I_h(\text{soln})}{I_h(\text{std})}R_i(\text{std})$$

I_h(soln) and I_h(std) are relative intensities of scattered light associated with the solution and the standard, respectively. It was assumed that R_i(soln) and R_i(solv) values contained a small and equal contribution from parasitic light which cancelled. Elimination of parasitic light was accomplished in standardization by taking advantage of that fact. That is, the increment R_i(soln) − R_i(solv) of standard solution scattering was used to calibrate the instrument rather than the scattering from a pure liquid which it was feared would contain an unknown amount of parasitic light.

Anisotropy data are summarized in Tables II–V. Figure 2 shows a typical plot of depolarized scattered-light intensity vs. concentration.

Discussion

It was expected that the simple inorganic anions would be only slightly anisotropic. Indeed, the bicarbonate and nitrate ions show only relatively small optical anisotropies. The measured solution values for nitrate compare well with those determined previously[22] from solid state birefringence data. Thiocyanate and azide ions exhibit somewhat larger values as expected. It is noteworthy, however, that the anisotropy of 22×10^{-48} cm^6 observed for azide is nearly as large as that of benzene. Such a large value associated with a simple triatomic molecule while hardly astonishing is not expected on the basis of simple calculations.[10,11]

Of course, one cannot ignore the possibility that anisotropies obtained from aqueous solution studies contain components due to solute–solute and solute–solvent interactions. Addition of supporting electrolyte produced no significant change in observed optical anisotropies of the solutes studied, however. Such an observation is not unexpected since a related study[21] involving simple water-soluble organic molecules produced similar results. It seems that solute–solute interactions are not contributing substantially to the observed anisotropy values of N_3^-. However, local electric fields may contribute to such apparent anisotropies. No attempt has been made here

TABLE III: Light Scattering Data Obtained for Sodium Thiocyanate as a Function of Supporting Electrolyte Concentration

Solution	n(6328 Å)	d_{20}	Solvfac	$I_{h,sol}/I_{h,std}$	$10^{48}\gamma^2$ cm^6
0.2 M NaSCN in H_2O	1.335 29	1.0086	0.9991	0.070	14.5
0.5 M NaSCN in H_2O	1.340 51	1.0261	0.9995	0.180	14.8
1.0 M NaSCN in H_2O	1.348 97	1.0429	0.9872	0.361	14.6
2.0 M NaSCN in H_2O	1.365 75	1.0802	0.9649	0.719	14.2
3.0 M NaSCN in H_2O	1.381 63	1.1196	0.9420	1.031	13.3
0.2 M NaSCN in 1.0 M NaCl	1.344 89	1.0498	0.9995	0.070	14.3
0.5 M NaSCN in 1.0 M NaCl	1.349 87	1.0598	0.9926	0.191	15.4
1.0 M NaSCN in 1.0 M NaCl	1.358 10	1.0799	0.9841	0.377	15.1
2.0 M NaSCN in 1.0 M NaCl	1.374 33	1.1182	0.9638	0.724	14.2
3.0 M NaSCN in 1.0 M NaCl	1.390 34	1.1560	0.9412	1.037	13.2
0.2 M NaSCN in 3.0 M NaCl	1.362 56	1.1239	0.9977	0.077	15.4
0.5 M NaSCN in 3.0 M NaCl	1.367 32	1.1352	0.9926	0.173	13.7
1.0 M NaSCN in 3.0 M NaCl	1.375 25	1.1510	0.9811	0.355	13.8
2.0 M NaSCN in 3.0 M NaCl	1.390 75	1.1891	0.9626	0.678	12.9
2.5 M NaSCN in 3.0 M NaCl	1.398 35	1.2054	0.9500	0.845	12.8

TABLE IV: Miscellaneous Light Scattering Data Obtained for Sodium Bicarbonate, Potassium Bicarbonate, and Sodium Azide

Solution	n(6328 Å)	d_{20}	Solvfac	$I_{h,sol}/I_{h,std}$	$10^{48}\gamma^2$ cm^6
0.5 M $NaHCO_3$ in H_2O	1.337 28	1.0285	0.9960	0.040	3.3
1.0 M $NaHCO_3$ in H_2O	1.342 29	1.0590	0.9913	0.096	3.9
0.5 M $KHCO_3$ in H_2O	1.337 27	1.0334	0.9927	0.041	3.4
1.0 M $KHCO_3$ in H_2O	1.342 28	1.0640	0.9800	0.092	3.8
0.5 M $KHCO_3$ in 1.0 M KCl	1.346 36	1.0783	0.9906	0.031	2.5
1.0 M $KHCO_3$ in 1.0 M KCl	1.350 97	1.1081	0.9774	0.073	2.9
0.5 M NaN_3 in H_2O	1.337 89	1.0208	0.9986	0.285	23.5
1.0 M NaN_3 in H_2O	1.343 63	1.0378	0.9910	0.561	23.0
2.0 M NaN_3 in H_2O	1.355 54	1.0766	0.9806	1.092	21.9
4.0 M NaN_3 in H_2O	1.377 54	1.1484	0.9494	2.180	21.2
1.0 M KCl	1.341 39	1.0453			

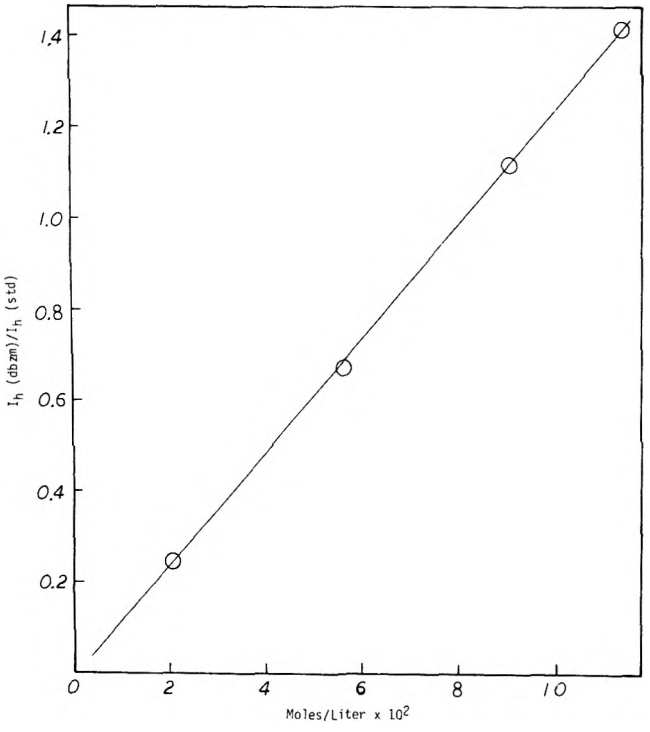

Figure 2. A plot of depolarized scattering intensity vs. concentration for dibenzoylmethane in cyclohexane.

to measure or calculate the magnitudes of such effects.

Studies involving nonaqueous nonpolar solvents are based upon much simpler theoretical foundations.[3] Cyclohexane and carbon tetrachloride are especially attractive media. They not only interact weakly with the solutes, but potentially produce only small contributions to the depolarized scattering due to solvent ordering or solvent–solute interactions, since the solvent molecules themselves are nearly isotropic. Besides, a very substantial amount of useful Kerr effect work has been done by LeFevre and co-workers using these solvents.

The large magnitudes of the molecular optical anisotropies of the neutral ligands 2,4-pentanedione, 1,3-diphenylpropanedione, and tropolone (Table V) are undoubtedly due to the fact that these molecules are planar in solution. Indeed, it has been known for some time that the enol form of 2,4-pentanedione predominates in hexane.[23] NMR studies[24] show that in cyclohexane solutions 91% of the 2,4-pentanedione exists in the enol form. If one assumes that the keto form has a very low anisotropy, as is likely, the calculated anisotropy of the enolic form should be approximately 40×10^{-48} cm^6. Such a value certainly is reasonable since it is similar to that of benzene, another planar, six-membered ring system. In the same vein, it is encouraging to note that the value determined for tropolone (130.2×10^{-48}) is similar to that determined previously[25] for azulene (148×10^{-48}). No direct comparison of 1,3-diphenylpropanedione light-scattering anisotropy data is possible at this time. It must be noted, however, that its very large experimental value requires that the two phenyl groups attached at the 1 and 3 positions of the diketone be coplanar with respect to one another and the ring formed by the enol moiety. That is, the entire carbon atom molecular skeleton must be essentially planar. Solutions of 1,3-diphenylpropanedione studied undoubtedly were composed of nearly 100% enolic form.[23]

The most significant observation that can be drawn from an examination of the molecular optical anisotropies of these ligands is simply that they are all highly anisotropic. It follows that a complex which contains one or possibly more of these ligands will also very likely be highly anisotropic, and will Rayleigh-scatter substantial amounts

TABLE V: Light Scattering Data Obtained for Neutral Ligands

Solution	n(6328 Å)	d_{20}	Solvfac	$I_{h,sol}/I_{h,std}$	$10^{48}\gamma^2$ cm^6
0.200 M 2,4-pentanedione in C_6H_{12}	1.424 75	0.7839	0.9805	0.138	37.8
0.342 M 2,4-pentanedione in C_6H_{12}	1.424 83	0.7861	0.9652	0.234	37.5
0.491 M 2,4-pentanedione in C_6H_{12}	1.424 89	0.7882	0.9488	0.310	34.6
0.731 M 2,4-pentanedione in C_6H_{12}	1.425 08	0.7932	0.9246	0.475	35.6
0.020 M 1,3-diphenylpropanedione in C_6H_{12}	1.425 04	0.7819	0.9983	0.241	659.2
0.055 M 1,3-diphenylpropanedione in C_6H_{12}	1.426 67	0.7844	0.9937	0.673	668.2
0.089 M 1,3-diphenylpropanedione in C_6H_{12}	1.428 82	0.7868	0.9900	1.124	688.1
0.112 M 1,3-diphenylpropanedione in C_6H_{12}	1.430 13	0.7887	0.9876	1.425	691.9
0.022 M tropolone in C_6H_{12}	1.424 65	0.7807	0.9985	0.051	126.1
0.039 M tropolone in C_6H_{12}	1.425 00	0.7818	0.9977	0.096	134.7
0.058 M tropolone in C_6H_{12}	1.425 43	0.7822	0.9959	0.142	133.7
0.081 M tropolone in C_6H_{12}	1.425 92	0.7833	0.9944	0.187	126.5
0.207 M 8-quinolinol in C_6H_6	1.501 72	0.8911	0.9792	0.711	168.9
0.276 M 8-quinolinol in C_6H_6	1.502 89	0.8939	0.9726	1.070	190.3
0.345 M 8-quinolinol in C_6H_6	1.504 11	0.8956	0.9648	1.400	198.7
0.414 M 8-quinolinol in C_6H_6	1.505 33	0.8982	0.9580	1.730	204.3
Cyclohexane (C_6H_{12})	1.424 19	0.7797			
Benzene (C_6H_6)	1.498 19	0.8837			

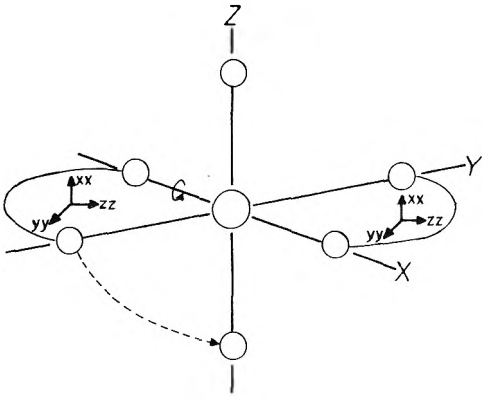

Figure 3. Conversion of trans (D_{2h}) to cis (C_2). *X*, *Y*, and *Z* are molecular axes; *xx*, *yy*, and *zz* are chelate ring polarizability semiaxes.

of depolarized light. Metal–oxygen bonds formed probably will enhance the effect but only very slightly. Furthermore, the intensity of depolarized Rayleigh scattering will be directly related to the geometrical arrangement of these ligand rings in complexes. It follows that highly anisotropic ligands may serve as very sensitive structural probes of the complex to which they are bound. A series of calculations based upon a simple model octahedral complex X_2MCh_2 follows which will show that expected anisotropies will be very large and very sensitive to angles between ligands.

Model Calculations

As shown in Figure 3 the polarizabilities of the ligands can be described in terms of three diagonal components, α_{xx}, α_{yy}, and α_{zz} of a diagonalized ligand polarizability tensor. If one assumes that α_{yy} and α_{zz} are equal and that they describe the ligand polarizability in the plane defined by the carbon atom skeleton it is simple to show that a molecule of the type trans-X_2MCh_2, which has coplanar bidentate ligands, Ch^-, and simple monodentate ligands, X^-, will have an anisotropy value four times that of a free ligand. Contributions to the anisotropy involving the six metal–ligand bonds cancel, it is assumed.

In short, to obtain the trans-complex value of γ^2 one simply adds[9] group polarizability components to give a resultant molecular anisotropy. For the molecule as a whole it can be seen by inspection that the diagonal elements of the diagonalized molecular polarizability tensor are respectively, $2\alpha_{xx}$, $2\alpha_{yy}$, and $2\alpha_{zz}$. Since for the free ligand, Ch, the anisotropy, $\gamma_{lig}^2 = {}^1/_2[(\alpha_{xx} - \alpha_{yy})^2 + (\alpha_{xx} - \alpha_{zz})^2] = (\alpha_{xx} - \alpha_{yy})^2$ it follows for the trans molecule that $\gamma_{mol}^2 = {}^1/_2[(2\alpha_{xx} - 2\alpha_{yy})^2 + (2\alpha_{xx} - 2\alpha_{zz})^2] = 4(\alpha_{xx} - \alpha_{yy})^2$.

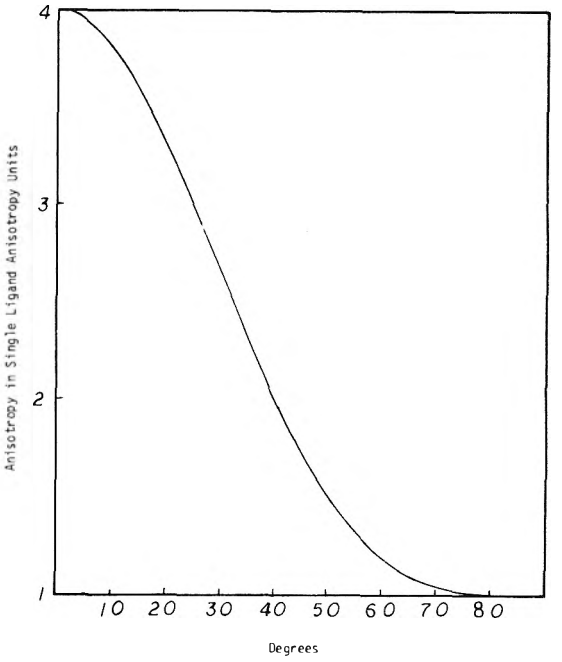

Figure 4. A plot of anisctropy vs. angle *XZA*.

TABLE VI: Theoretical Complex/Ligand Anisotropy Ratios Calculated as a Function of Angle *XZA*

XZA	γ^2 complex/γ^2 ligand	*XZA*	γ^2 complex/γ^2 ligand
0	4.000	50	1.512
10	3.822	60	1.187
20	3.339	70	1.041
30	2.687	80	1.003
40	2.033	90	1.000

That is, γ_2 for the molecule equals four times γ^2 for the free ligand.

Figure 3 also indicates the coordinates for the ligands and the whole molecule describing the transformation from D_{2h} (trans) to C_2 (cis). As this conversion takes place, the angle called XZA defined by the "*xx*" axis of the ligand undergoing transformation and the "*z*" coordinate axis of the complex passes from 0 to 90°, and, the molecular anisotropy changes from $4\gamma_{lig}^2$ to γ_{lig}^2. Figure 4 and Table VI show by means of standard calculations[9] the functional dependence of the complexes molecular anisotropy upon the ligand angle of rotation.

It is apparent from the figure and the table that the optical anisotropy will be a sensitive function of structure

as long as the ligand anisotropy is large. Hence, it is anticipated that ligands such as tropolone or 1,3-diphenylpropanedione should serve as excellent structural probes and that light scattering studies of such complexes should yield valuable structural information.

This tool appears to be an especially attractive means with which to probe the structures of labile systems in solution. Many such structures are difficult or impossible to study effectively by other means. For example, it should be relatively simple to determine the amounts of cis and trans isomers present in solution for octahedral complexes of the general type dialkylbis(1,3-diphenylpropanedionato)tin(IV), even though most NMR studies of such systems to date have been hampered by problems associated with very rapid rates of ligand exchange. It is anticipated that the structures of ion pairs can be studied in a similar fashion.

References and Notes

(1) Lord Rayleigh, *Phil. Mag.*, **35**, 373 (1918).
(2) C. G. LeFevre and R. J. W. LeFevre, *Rev. Pure Appl. Chem.*, **5**, 261 (1955); A. Weissberger, Ed., "Physical Methods of Organic Chemistry", Vol. 1, 3rd ed, Interscience, New York, N.Y., 1960, Chapter 36.
(3) C. Clement and P. Bothorel, *C. R. Acad. Sci.*, **251**, 2323 (1960).
(4) D. J. Coumou, E. L. Mackor, and J. Hijmans, *Trans. Faraday Soc.*, **60**, 1538 (1964).
(5) D. J. Coumou, *Trans. Faraday Soc.*, **65**, 2654 (1969).
(6) A. Gaglani, N. Asting, and W. H. Nelson, *Inorg. Chem.*, **13**, 1715 (1974).
(7) W. R. Russo and W. H. Nelson, *J. Am. Chem. Soc.*, **92**, 1521 (1970).
(8) K. G. Denbigh, *Trans. Faraday Soc.*, **36**, 936 (1940).
(9) R. S. Smith and E. Mortensen, *J. Chem. Phys.*, **32**, 503 (1960).
(10) E. R. Lippincott and J. M. Stutman, *J. Phys. Chem.*, **68**, 2926 (1964).
(11) T. V. Long and R. A. Plane, *J. Chem. Phys.*, **43**, 457 (1965).
(12) W. H. Nelson, *J. Phys. Chem.*, **76**, 1502 (1972).
(13) H. S. Gabelnick and H. J. Strauss, *J. Chem. Phys.*, **54**, 3846 (1971).
(14) G. R. Alms, T. D. Gierke, and W. H. Flygare, *J. Chem. Phys.*, **61**, 2083 (1974).
(15) R. Pecora and W. A. Steele, *J. Chem. Phys.*, **42**, 1872 (1965).
(16) J. Kielich, *J. Chem. Phys.*, **46**, 4090 (1967).
(17) M. Malmberg and E. R. Lippincott, *J. Colloid Interface Sci.*, **27**, 591 (1968).
(18) A. K. Burnham, G. R. Alms, and W. H. Flygare, *J. Chem. Phys.*, **62**, 3289 (1975).
(19) M. J. Aroney, R. J. W. LeFevre, and J. D. Saxby, *Aust. J. Chem.*, **18**, 1501 (1965).
(20) W. R. Russo and W. H. Nelson, *J. Am. Chem. Soc.*, **92**, 455 (1970).
(21) N. Asting, A. Gaglani, and W. H. Nelson, *J. Colloid Interface Sci.*, **45**, 170 (1973).
(22) B. Dzhuraev, V. I. Elfimov, and M. F. Vcks, *Vestn. Leningr. Univ., Fiz., Khim.*, **141** (1972).
(23) K. H. Myer, *Berichte*, **47**, 826 (1914).
(24) L. W. Reeves, *Can. J. Chem.*, **35**, 1351 (1957).
(25) J. R. LaLanne and P. Bothorel, *Mol. Phys.*, **19**, 227 (1970).

Infrared Spectroscopic Evidence for Matrix-Isolated SF_6^-

James E. Barefield, II, and William A. Guillory*

Department of Chemistry, University of Utah, Salt Lake City, Utah 84112 *(Received September 13, 1976)*

Publication costs assisted by the National Science Foundation

A new absorption at 594 cm^{-1}, generated by charge transfer processes involving the photoionization of NO, Na, and K in the presence of matrix-isolated SF_6, has been tentatively assigned to the SF_6^- ion. This absorption was also observed to result from the photolysis of SF_6 with the 1048- and 1066-Å resonance lines of argon. Attempts to generate this feature by electron impact and crossing a beam of metastable argon atoms with a SF_6 beam were unsuccessful.

Introduction

Sulfur hexafluoride, having O_h symmetry, has a ground state electronic term $^1A_{1g}$. The ground state electronic configuration of SF_6 is $a_{1g}^2 t_{1u}^6 e_g^4$, hence, the ground state of SF_6^- is expected to be a doublet with the configuration $a_{1g}^2 t_{1u}^6 e_g^4 a_{1g}^1$, and the corresponding term is $^2A_{1g}$. A great deal of effort has been devoted to the study of SF_6^-. The rate of attachment of thermal electrons to SF_6 has been studied by Hickam and Fox.[1] Compton et al. studied the nondissociative attachment of electrons to SF_6.[2] According to this study, the nondissociative attachment of electrons to SF_6 produces a long-lived SF_6^- ion. The long lifetime was accounted for by assuming equipartitioning of energy among the vibrational modes of the SF_6^- ion. Electron transfer from excited Rydberg states of rare gas atoms to SF_6 has been theoretically predicted by Matsuzawa to proceed with a large cross section.[3] This theoretical prediction has been experimentally confirmed by Hotop and Niehaus.[4]

Very little is known about the molecular structure of SF_6^-. According to the XY_6 Walsh diagram,[5] the addition of an electron to the next highest totally symmetric MO (a_{1g}) of SF_6 retains the O_h symmetry, but would be expected to reduce the average S–F bond energy. Depending upon the extent of this reduction in S–F bond energy, one would expect to observe two red-shifted infrared active vibrational frequencies due to SF_6^-.

In this manuscript, we report on several attempts to prepare the SF_6^- ion: (1) charge transfer from NO, Na, and K, (2) electron, and (3) metastable atom impact on SF_6. The photolysis products of the SF_6 molecule, using the 1066- and 1048-Å resonance lines of argon, are also reported.

Experimental Section

Sulfur hexafluoride was obtained from the Matheson Co. (purity, 99.99%) and was used without further purification. Nitric oxide, obtained from the Matheson Co., was further purified by trap-to-trap distillation at 77 K. The argon matrix gas was also obtained from the Matheson Co. (purity, 99.9999%). Traces of H_2O and CO_2 were removed from the gas by passing it through a column packed with P_2O_5 and ascarite. The alkali metals were vaporized from a cylindrical stainless steel metal oven enclosed in a quartz shield, which was resistively heated.

The cryostat and the photolysis sources used in these experiments have been described previously.[6] The spectra were recorded with a Perkin-Elmer 180 grating infrared

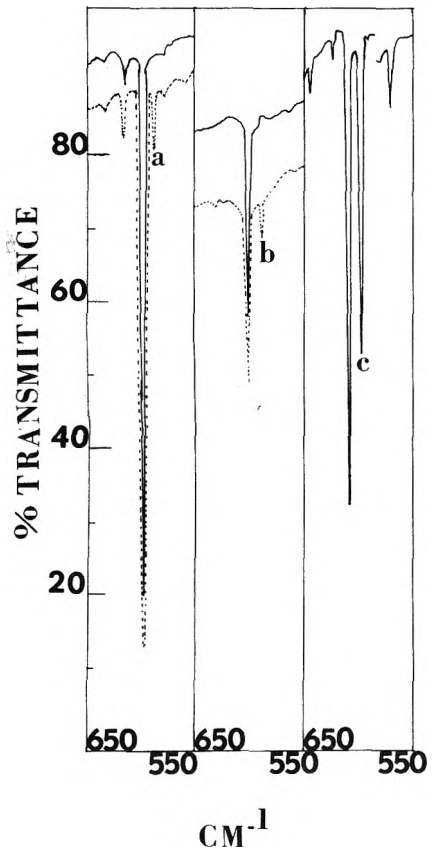

Figure 1. The infrared spectra of (a) SF_6:NO:Ar = 1:2:600, a total of 9.89 mmol of this sample was deposited over a 270-min period; (b) SF_6:Ar (1:500) + Na, a total of 9.36 mmol of this sample was deposited over a 300-min period; (c) SF_6:Ar = 1:1500, a total of 9.89 mmol of this sample was photolyzed with an Ar resonance lamp for 60 min. In both a and b above the solid trace is before and the dotted trace is after photolysis with an H_2 resonance lamp and a Xe–Hg lamp, respectively.

spectrophotometer. Under typical scanning conditions, the resolution and frequency accuracy was 1 cm^{-1} between 300 and 2000 cm^{-1} and 2 cm^{-1} between 2000 and 4000 cm^{-1}.

Results and Discussion

When a sample of SF_6:NO:Ar = 1:2:600 at 10 K was exposed to the 1215-Å resonance line resulting from a microwave powered discharge H_2/He mixture, new features were observed at 884, 858, 810, 705, and 594 cm^{-1}. The new features centered at 884, 858, and 705 cm^{-1} agree well with the gas and solid phase spectra of SF_4 reported by Redington.[7] Upon warming the photolyzed film to 30 K for 5 min and then recooling to 10 K, the intensity of the 810-cm^{-1} absorption decreased significantly, whereas the 594-cm^{-1} absorption disappeared completely. This behavior is indicative of highly reactive and unstable species. The 594-cm^{-1} absorption is shown in Figure 1a.

A typical spectrum of a sample of SF_6:Ar:Na at 10 K after photolysis appears in Figure 1b. The consistent new feature which was observed in all the alkali metal experiments (i.e., samples of SF_6:Ar:Na and SF_6:Ar:K) was centered at 594 or 595 cm^{-1}. This new feature was generated by depositing the SF_6:Ar:Na or SF_6:Ar:K sample at 10 K and then photolyzing the matrix film with a 1000 W ozone-free Xe–Hg lamp (Schoeffel Corp.). The samples were irradiated sequentially from an initial exposure time of 10 min to times as long as 3 h, with intermittant recording of the infrared spectrum. This method of photolysis was carried out because the negative ion which results from the charge transfer process can be both generated and destroyed (photoneutralized) with the same

TABLE I: Summary of the Absorptions (cm^{-1}) in the SF_6 Charge Transfer Experiments with NO, Na, and K[a]

	Before photolysis	After photolysis	Assignment[b]
NO	1871 (vs)		NO
	1862 (m)		
	1775 (s)		$(NO)_2$
		1588 (s)	
	1574 (m)		$SF_6(\nu_2 + \nu_3)$
	1270 (w)		
	1251 (w)		$SF_6(\nu_2 + \nu_4)$
	1178 (w)		
	989 (s)		$SF_6(\nu_2 + \nu_6)$
	937, 920 (vs)		$SF_6(\nu_3)$
		884 (m)	$SF_4(\nu_1)$
	869 (m)		$SF_6(\nu_5 + \nu_6)$
		858 (m)	$SF_4(\nu_6)$
		810 (s)	$^{32}SF_2$(?)
		705 (m)	$SF_4(\nu_8)$
	613 (vs)		$SF_6(\nu_4)$
		594 (w)	$SF_6^-(\nu_4)$
Na	989 (w)		$SF_6(\nu_2 + \nu_6)$
	937 (vs).		$^{32}SF_6(\nu_3)$
	920 (w)		$^{34}SF_6(\nu_3)$
	613 (s)		$SF_6(\nu_4)$
		595	$SF_6^-(\nu_4)$
K	937 (vs)		$^{32}SF_6(\nu_3)$
	920 (m)		$^{34}SF_6(\nu_3)$
	613 (s)		$SF_6(\nu_4)$
		594	$SF_6^-(\nu_4)$

[a] In the NO experiments, the radiation source was a hydrogen resonance lamp (1215 Å). The radiation source used in the alkali metal (i.e., sodium and potassium) experiments was a 1000-W xenon–mercury lamp. The abbreviations for the relative spectral intensities are: m = medium, vs = very strong, s = strong, w = weak, vw = very weak. [b] The SF_4 and SF_6 assignments are based on the works of ref 7 and ref 9, 10, and 11, respectively.

radiation source (i.e., the 1000-W Xe–Hg lamp). Indeed, this behavior was observed in these (SF_6–alkali metal) experiments. Initial exposure times of 10–45 min resulted in the appearance of the new feature at 594 or 595 cm^{-1}. However, upon extended exposure of the same sample to the radiation source, the new feature disappeared completely.

In order to determine whether or not the new feature (594 cm^{-1}) was the direct result of SF_6 photolysis with the Xe–Hg lamp, "in situ" photolysis of a sample of SF_6:Ar = 1:600 was carried out. In this experiment, no new features were observed. The implication then from the SF_6–alkali metal photolysis experiments is that the new feature observed at 594 or 595 cm^{-1} is due to the photoinduced charge transfer process

$$SF_6 + M \xrightarrow{h\nu} SF_6^-M^+ \quad (1)$$

where M is atomic sodium or potassium. A summary of the results and tentative assignments of the absorptions resulting from the charge transfer experiments between NO, K, Na, and SF_6 appears in Table I.

The absorption spectrum of SF_6 in the vacuum ultraviolet region has been investigated by Liu.[8] Four electronic transitions centered at 1053.9, 936.1, 872.0, and 830.2 Å were reported. We report here on the products which were generated via excitation into the band centered at 1053.0 Å. The new features along with corresponding spectral intensities are listed in Table II. The excitation source was an argon resonance lamp which has resonance lines at 1066 and 1048 Å. The major process occurring is the production of SF_4. The product features were intense enough that the sulfur 32 and 34 isotopic absorptions could

TABLE II: Summary of Absorptions (cm^{-1}) in the Photolysis of SF_6:Ar = 1:1500 with 1066- and 1048-Å Radiation

Before photolysis	After photolysis	Assignment[a]
1871 (m)		$SF_6(2\nu_2 + \nu_4)$
1571 (w)		$SF_6(\nu_2 + \nu_3)$
989 (w)		$SF_6(\nu_2 + \nu_6)$
937 (vs)		$^{32}SF_6(\nu_3)$
928 (w)		$^{33}SF_6(\nu_3)$
920 (s)		$^{34}SF_6(\nu_3)$
	884 (s)	$^{32}SF_4(\nu_1)$
	873 (vw)	$^{34}SF_4(\nu_1)$
	858 (s)	$^{32}SF_4(\nu_6)$
	846 (vw)	$^{34}SF_4(\nu_6)$
	808 (vs)	$^{32}SF_2(?)$
	798 (w)	$^{34}SF_2(?)$
	704 (vs)	$^{32}SF_4(\nu_8)$
	681 (w)	$^{34}SF_4(\nu_8)$
613		$SF_6(\nu_4)$
	594 (s)	SF_6^-
	551 (m)	$SF_4(\nu_3)$
	528 (m)	$SF_4(\nu_7)$

[a] For the SF_4 assignments, see ref 7. The $^{34}SF_4$ assignments are based on the results of these experiments.

be observed. The two new features which have not been previously observed were centered at 808 and 594 cm^{-1}, respectively. The feature at 808 cm^{-1} has a sulfur 34 isotopic counterpart at 798 cm^{-1}. The 594-cm^{-1} absorption has been tentatively assigned to the SF_6^- ion. The highest yield of the 594-cm^{-1} feature was observed in these vacuum UV photolysis experiments, as shown in Figure 1c.

The absorptions which occur as a result of 1215-Å photolysis of matrix-isolated SF_6 doped with NO at 810 cm^{-1} and 1066- and 1048-Å photolysis in pure argon at 808 cm^{-1}, appear to be due to the same species. Vacuum UV photolysis of SF_6 in argon doped CO matrices resulted in no production of FCO. Thus, atomic detachment from SF_6 or some other fragment does not appear to be a major process giving rise to the 810 (808) cm^{-1} absorption. Since the absorptions of SF_4 are known, the most plausible assumption is that this absorption might be a stretching motion of SF_2. Using the known SF_2 bond angle of 98.25° from microwave studies,[12] the calculated $^{34}SF_2$ ν_3 stretching mode is 796 cm^{-1}, as compared to the observed frequency of 798 cm^{-1}. Finally, a recent theoretical calculation[13] of the vibrational frequencies of $^{32}SF_2$, predicted ν_3 to be 830 ± 10 cm^{-1}, is in good agreement with our observed frequency of 810 cm^{-1}.

Attempts were also made to produce SF_6^- by crossing a beam of SF_6 with an electron beam in one case and a beam of metastable Ar atoms in another. These systems, having "free flight" from the reaction zone to the cold window, were subsequently analyzed using infrared spectroscopy. The cross sections for SF_6^- formation via argon metastable energy transfer[4] and nondissociative electron attachment[14] are 1.7×10^{-12} and 2×10^{-14} cm^2, respectively. Therefore, both processes would have been expected to produce a sufficient concentration of SF_6^- for infrared detection. However, the predicted lifetime for the vibrationally excited species, which is probably produced in both cases, is of the order of 1–10 μs, which is significantly shorter than the time traversed by the ion from the reaction zone to the cold window. Thus it is not totally surprising that we were not able to observe the 594-cm^{-1} absorption tentatively assigned to SF_6^-.

Although it is generally impossible to predict the extent to which the ν_3 mode would shift for SF_6^-, it is surprising that we do not observe this absorption red-shifted from ν_3 of SF_6; we assume therefore, that it is probably masked beneath ν_3 of SF_6, rather than assuming that its intensity is lower than the bending vibration.

Acknowledgment. We greatly acknowledge support of this work by the National Science Foundation through Grant No. GP-43745.

References and Notes

(1) W. M. Hickam and R. E. Fox, *J. Chem. Phys.*, **25**, 642 (1956).
(2) R. N. Compton, L. G. Christophorou, G. S. Hurst, and P. W. Reinhardt, *J. Chem. Phys.*, **45**, 4634 (1966).
(3) M. Matsuzawa, *J. Phys. Soc. Jpn.*, **32**, 1088 (1972).
(4) H. Hotop and A. Niehaus, *J. Chem. Phys.*, **47**, 2506 (1967).
(5) G. Herzberg, "Molecular Spectra and Molecular Structure, III. Electronic Spectra and Electronic Structure of Polyatomic Molecules", Van Nostrand, Princeton, N.J., 1967, p 323.
(6) G. R. Smith and W. A. Guillory, *J. Chem. Phys.*, **56**, 1423 (1972).
(7) R. L. Redington and C. V. Berney, *J. Chem. Phys.*, **43**, 2020 (1965).
(8) T. Liu, G. Moe, and A. B. F. Duncan, *J. Chem. Phys.*, **19**, 71 (1951).
(9) R. T. Lagemann and E. A. Jones, *J. Chem. Phys.*, **19**, 534 (1951).
(10) H. L. Classen et al., *J. Chem. Phys.*, **53**, 341 (1970).
(11) B. Weinstock and G. Goodman, *Adv. Chem. Phys.*, **9**, 169 (1965).
(12) D. R. Johnson and F. X. Powell, *Science*, **164**, 950 (1969).
(13) C. Bliefert and K. P. Wanczek, *Z. Naturforsch. A*, **25**, 1770 (1970).
(14) B. H. Mahan and C. E. Young, *J. Chem. Phys.*, **44**, 2192 (1966).

Infrared and Raman Spectra, Vibrational Assignment, and Barriers to Internal Rotation for Dimethylsilylamine

J. R. Durig* and P. J. Cooper[1]

Department of Chemistry, University of South Carolina, Columbia, South Carolina 29208 (Received September 13, 1976)

Publication costs assisted by the University of South Carolina

The infrared spectra of gaseous $(CH_3)_2NSiH_3$ and $CH_3CD_3NSiH_3$ have been recorded from 80 to 3800 cm^{-1}. The Raman spectra of $(CH_3)_2NSiH_3$ and $CH_3CD_3NSiH_3$ have been recorded to within 25 cm^{-1} of the exciting line in all three physical states. A vibrational assignment has been made, and the methyl and silyl torsional modes observed. A barrier to internal rotation of 3.23 kcal/mol has been calculated for the methyl groups, while a barrier of 1.51 kcal/mol was calculated for the silyl group. Upon consideration of all available data, it is concluded that an intramolecular d_π–p_π interaction in dimethylsilylamine is not very significant.

Introduction

Particular attention has been paid to the study of various silyl amines because of their tendency to form planar compounds. For example, previous studies of trisilylamine,[2-5] $(SiH_3)_3N$, have shown the vibrational spectra to be consistent with a planar heavy-atom skeleton. That trisilylamine adopts a planar configuration at the nitrogen atom has also been demonstrated by an electron diffraction investigation.[6] Vibrational[7,8] and electron diffraction[9] studies have both shown that methyldisilylamine, $CH_3N(SiH_3)_2$, also exhibits a planar heavy-atom configuration. In addition, a planar structure has also been indicated for disilylamine, $(SiH_3)_2NH$, in an electron diffraction study.[10] Of the silyl amine compounds studied to date, only dimethylsilylamine, $(CH_3)_2NSiH_3$, appears not to have a planar heavy-atom skeleton. Vibrational studies by Buttler and McKean[11] and by Goldfarb and Khare[8] have both implicated a nonplanar structure for dimethylsilylamine. A subsequent electron diffraction investigation[12] seemed to confirm this. However, discrepancies in certain vibrational assignments exist between the two vibrational studies, and the possibility that the molecule might be planar in the ground vibrational state is thought to exist.

In a continuing effort to elucidate the forces giving rise to the barriers to internal rotations, we are presently interested in the torsional barriers in compounds containing group 4A and group 5A elements. Currently, no information is available on the barriers to internal rotation in silyl amine compounds. Therefore, in the hope of clearing up the existing discrepancies in the vibrational assignment, conclusively establishing either the planarity or nonplanarity of the heavy-atom skeleton, and providing some information on the methyl and silyl torsional barriers, we have undertaken a reinvestigation of the vibrational data for dimethylsilylamine and have further expanded it to include Raman and far-infrared spectral data for both $(CH_3)_2NSiH_3$ and $CH_3CD_3NSiH_3$.

Experimental Section

The samples used in the present work were prepared by the methods of Aylett and Emsley[13] or Sujishi and Witz.[14] Iodosilane, SiH_3I, or bromosilane, SiH_3Br, was allowed to react with either dimethylamine, $(CH_3)_2NH$, or dimethylamine-d_3, CH_3CD_3NH, depending on whether the undeuterated or deuterated dimethylsilylamine was to be prepared. The iodosilane and bromosilane used in the above syntheses were both prepared according to the method of Ward.[15]

Raman spectra were recorded to 4000 cm^{-1} with a Cary Model 82 Raman spectrophotometer equipped with a Spectra-Physics Model 171 argon ion laser. The 5145-Å line was used and the laser power was varied from 0.5 to 5 W at the head depending on the physical state under investigation. A standard Cary gas cell with multipass optics was utilized to obtain the spectra of gaseous dimethylsilylamine and dimethylsilylamine-d_3. Spectra of the liquids were obtained from samples in sealed glass capillaries. The spectra of solid $(CH_3)_2NSiH_3$ and $CH_3CD_3NSiH_3$ were recorded by condensing the sample onto a brass plate maintained at ~77 K in a Cryogenics Technology Inc. Spectrim cryostat equipped with a Lake Shore Cryotronics Model DTL 500 high precision temperature controller. Under these conditions the samples condensed on the plate as a clear glass. The samples were annealed by allowing the temperature to increase to ~245 K, whereupon a white crystalline solid was observed to form, and then quickly lowered to ~100 K, at which temperature all Raman spectra of the solid phase were recorded. Polarization measurements were made using the standard Cary accessories. Frequencies measured for sharp, resolvable bands are expected to be accurate to at least ±2 cm^{-1}.

Infrared spectra were recorded with a Digilab FTS-15B Fourier transform interferometer. Mid-infrared spectra from 3800 to 450 cm^{-1} were obtained using a germanium beam splitter on a KBr substrate and a glower source, while far-infrared spectra from 450 to 80 cm^{-1} were obtained by using a 6.25-μm Mylar beam splitter and a high pressure Hg arc lamp source. Spectra of the gaseous phase were recorded by using a 10-cm cell with KBr windows and ~3 Torr of sample pressure in the mid-infrared, or polyethylene windows and ~600 Torr of sample pressure in the far-infrared. Atmospheric water vapor was removed from the spectrometer housing by purging with dry nitrogen. Mid-infrared spectra were recorded at an effective resolution of better than 1.0 cm^{-1} and far-infrared spectra at an effective resolution of better than 0.5 cm^{-1} using a modified "boxcar" apodization function for photometric accuracy. As a result, measured frequencies are expected to be accurate to better than ±1 cm^{-1} in the mid-infrared region and approximately ±0.2 cm^{-1} in the far-infrared region.

Vibrational Assignment

The Raman spectra of gaseous, liquid, and solid $(CH_3)_2NSiH_3$ and $CH_3CD_3NSiH_3$ are shown in Figures 1 and 2, respectively. The mid-infrared spectra of gaseous

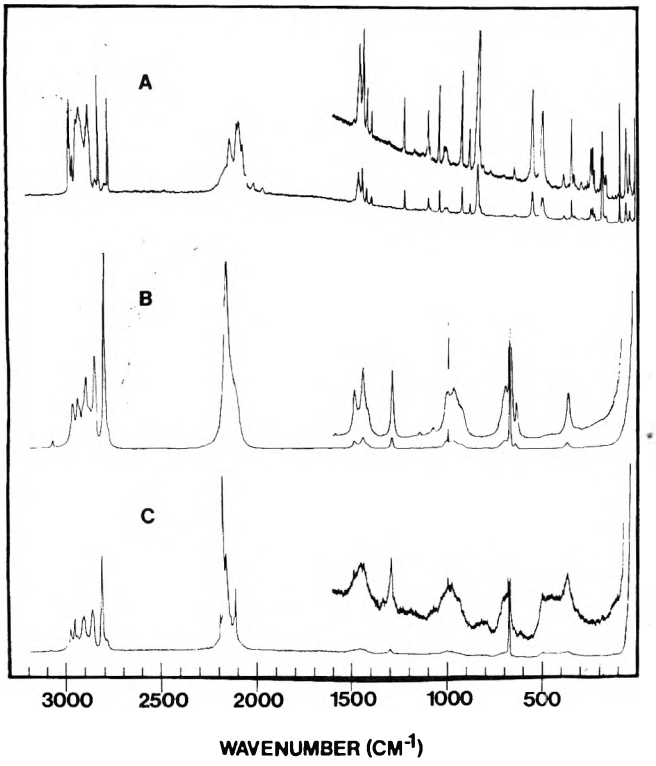

Figure 1. Raman spectra of $(CH_3)_2NSiH_3$: (A) annealed solid, spectral bandwidth 2 cm^{-1}; (B) liquid, spectral bandwidth 1 cm^{-1}; (C) gas, spectral bandwidth 2 cm^{-1}.

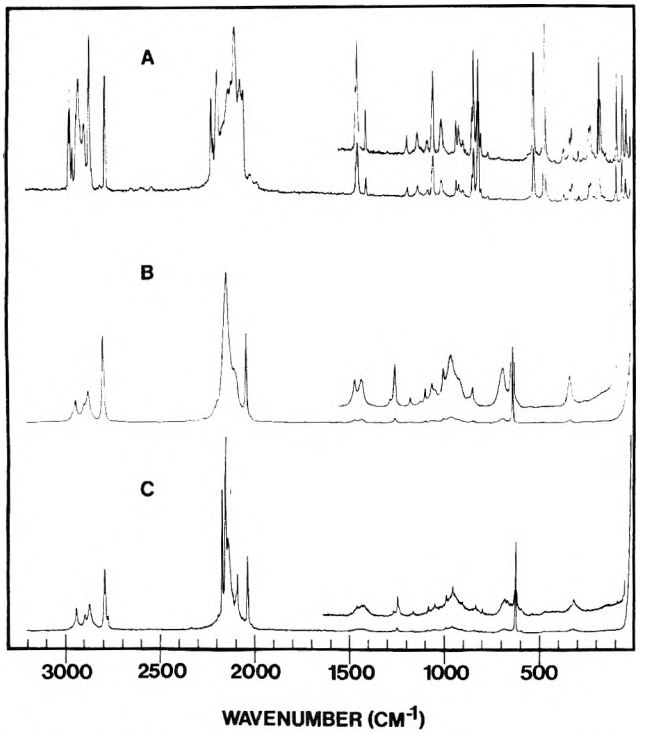

Figure 2. Raman spectra of $CH_3CD_3NSiH_3$: (A) annealed solid, spectral bandwidth 3 cm^{-1}; (B) liquid, spectral bandwidth 1 cm^{-1}; (C) gas, spectral bandwidth 2 cm^{-1}.

$(CH_3)_2NSiH_3$ and $CH_3CD_3NSiH_3$ are both presented in Figure 3, while the far-infrared spectra are shown in Figure 4. It was not possible to conclusively establish either the planarity or nonplanarity of the heavy-atom skeleton solely on the basis of C_s and C_{2v} selection rules. However, it will be shown in the section on torsional assignments that the heavy-atom skeleton is nonplanar for both molecules, and $(CH_3)_2NSiH_3$ will belong to the symmetry group C_s, with

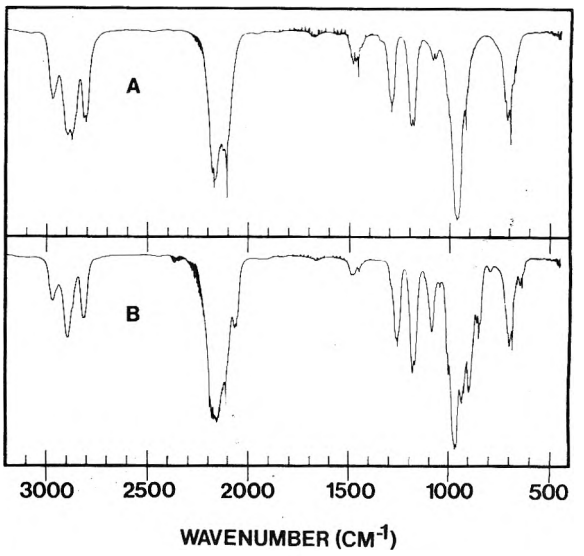

Figure 3. Infrared spectra of gaseous dimethylsilylamine: (A) $(CH_3)_2NSiH_3$; (B) $CH_3CD_3NSiH_3$.

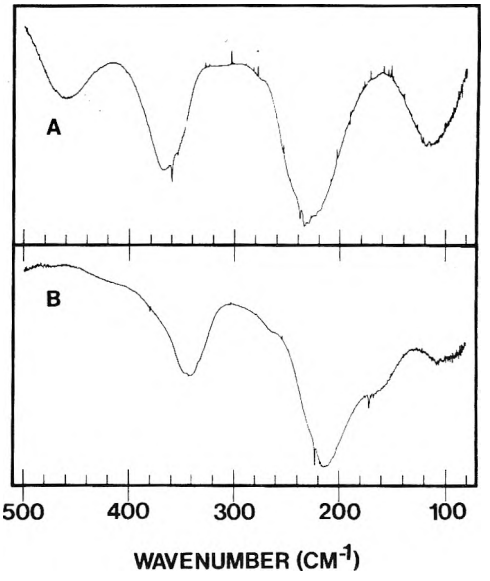

Figure 4. Far-infrared spectra of gaseous dimethylsilylamine: (A) $(CH_3)_2NSiH_3$; (B) $CH_3CD_3NSiH_3$.

18 A′ and 15 A″ modes predicted, while $CH_3CD_3NSiH_3$ will then belong to the symmetry group C_1. In either case, all 33 normal vibrational modes will be both infrared and Raman active.

The observed frequencies and assignments for $(CH_3)_2NSiH_3$ and $CH_3CD_3NSiH_3$ are given in Tables I and II, together with approximate descriptions of the normal modes. As in the previous vibrational study[11] of $(CH_3)_2NSiH_3$, we too were unable to assign all of the CH_3 stretching fundamentals. However, in addition to the A′ and A″ CH_3 symmetric stretches previously assigned, we also assigned the two CH_3 antisymmetric stretches, ν_1 and ν_{19}, to the band at 2970 cm^{-1} in the gas and 2957 cm^{-1} in the liquid, since the frequency was considered too high to be due to an overtone of one of the CH_3 deformations. This assignment is consistent with the observation of a band at the same frequency in $CH_3CD_3NSiH_3$, corresponding to one of the CH_3 antisymmetric stretches. The assignment of the other two CH_3 antisymmetric stretches, ν_2 and ν_{20}, however, still proves too elusive due to the abundance in the CH_3 stretching region of what must be overtones and combination bands of the CH_3 deformations.

The two SiH_3 antisymmetric stretches and the SiH_3 symmetric stretch are assigned to the bands near 2170 and 2106 cm^{-1}, respectively, in both the light and heavy compounds. The fine structure appearing on the high frequency side of the SiH_3 stretches, as well as on the low frequency side of the SiH_3 deformations, in the mid-infrared spectra of both compounds is attributed to the presence of SiH_3Br. The closely spaced series of bands centered at 2350 cm^{-1} in the mid-infrared spectrum of $CH_3CD_3NSiH_3$ is due to atmospheric CO_2. The CH_3 deformations, which all occur in the 1400–1500-cm^{-1} region, were assigned on the basis of the Raman polarization data and the results of a previous vibrational assignment[16] of the corresponding modes in dimethylamine.

Assignment of the spectra in the region below 1300 cm^{-1} proved difficult. As first pointed out by Buttler and McKean,[11] not only is there significant coupling between several of the vibrational modes in this region, but the differences between the spectra of the gas and solid phases are considerable. The assignments presented in this study for the gas and liquid phase frequencies are in fairly good agreement with those reported previously.[11] The two A′ CH_3 rocking modes are assigned to the infrared A–C hybrid-type bands at 1293 and 1149 cm^{-1}, while the two A″ CH_3 rocking modes are assigned to the infrared B-type bands at 1189 and 1074 cm^{-1}. The C–N antisymmetric stretch in $(CH_3)_2NSiH_3$ is assigned to the weak shoulder at 1030 cm^{-1} in the Raman spectrum of the liquid. The SiH_3 symmetric and antisymmetric deformations are assigned to the infrared bands near 971 and 922 cm^{-1}, respectively, in both the heavy and light compounds. The A′ SiH_3 rocking mode is assigned to the infrared A–C hybrid-type band at 695 cm^{-1}, and the A″ SiH_3 rocking mode is then assigned to the shoulder at 715 cm^{-1} which appears to be of B-type contour.

Buttler and McKean,[11] in their study of $(CH_3)_2NSiH_3$, assigned the C–N symmetric stretch to a band at 1003 cm^{-1}, and the Si–N stretch to an ill-defined, weak band at 670 cm^{-1}. In a subsequent investigation of the matrix-isolated solid by Goldfarb and Khare,[8] it was argued that the band at 1003 cm^{-1} corresponded to the Si–N stretching frequency, while a band near 900 cm^{-1} in the matrix spectrum was assigned to the C–N symmetric stretch. The observation of a sharp, medium-intense polarized line at 670 cm^{-1} in the Raman spectra of the gas and liquid phases, and of an A–C hybrid-type band at 670 cm^{-1} in the infrared spectrum of $(CH_3)_2NSiH_3$, confirms the initial assignment of Buttler and McKean.[11] The Raman line at 670 cm^{-1} is too intense for an SiH_3 rock and too high in frequency for a skeletal bend. The polarized lines near 1003 cm^{-1} in the Raman spectra of gaseous and liquid $(CH_3)_2NSiH_3$, and the corresponding band of A–C type contour at 1005 cm^{-1} in the infrared spectrum, must, therefore, be assigned to the C–N symmetric stretch. Further evidence for the correctness of this assignment is demonstrated by the occurrence of bands near 642 cm^{-1} and near 1005 cm^{-1} in both infrared and Raman spectra of $CH_3CD_3NSiH_3$. The 642-cm^{-1} band is obviously the analogue of the band at 670 cm^{-1} in the light compound, which is ascribed to the Si–N stretch. The small decrease in frequency can best be attributed to coupling of the Si–N stretch with the C–N stretch, which is already coupled with the highest frequency CH_3 rocking mode. The (H_3)C–N stretch in the heavy compound is assigned to the infrared and Raman bands near 1006 cm^{-1}, which are little shifted from the bands near 1003 cm^{-1} assigned to the C–N symmetric stretch in the light compound. This is in agreement with the assignments of the C–N symmetric stretch in dimethylamine-d_0[16] and the (H_3)C–N stretch in dimethylamine-d_3[17] to bands at 924 and 925 cm^{-1}, respectively. The differences in the C–N stretching frequencies between the dimethylamines and dimethylsilylamines is, of course, due to the introduction of coupling between the C–N stretch and the Si–N stretch in the dimethylsilylamines. The (D_3)C–N stretch in the heavy compound is assigned to the infrared and Raman bands at 855 cm^{-1}, shifted from the frequency of 820 cm^{-1} assigned to the (D_3)C–N stretch in dimethylamine-d_3,[17] as a result of coupling with the Si–N stretch.

The A′ C–N–C skeletal deformation in $(CH_3)_2NSiH_3$ is assigned to the far-infrared band at 359.7 cm^{-1}. The Q-branch observed at 354.2 cm^{-1} is thought to be due to the deformation in an excited torsional state. The C–N–C deformation is observed at 342.4 cm^{-1} in the infrared spectrum of the deuterated compound. The broad band occurring at 459 cm^{-1} in the far-infrared spectrum of the light compound is considered to be the result of an impurity on the cell windows, as evidenced by its lack of any recognizable band contour and the absence of any counterpart in the spectrum of the heavy compound. The C–N–Si out-of-plane skeletal deformation is assigned to the band at 268 cm^{-1} in the far-infrared spectrum, shifting to 256 cm^{-1} upon deuteration. The C–N–Si in-plane skeletal deformation, although not directly observed, is estimated to occur at approximately 234 and 215 cm^{-1} in the light and heavy compounds, respectively. The reasoning behind this assignment will be made apparent in the following section of this paper.

That a specific intermolecular association such as that first proposed by Sujishi and Witz[14] occurs in dimethylsilylamine has been conclusively confirmed by the two previous vibrational studies,[8,11] and the greater disparity between the gas and condensed phase spectra in the region below 1300 cm^{-1} shown to be indicative of involvement of the nitrogen and silicon atoms in the interaction leading to association. The major point of disagreement in those two investigations occurred over the assignments of the C–N symmetric stretch and the Si–N stretch. Since we have already shown the gas phase assignment of Buttler and McKean[11] to be correct, we conclude on the basis of our Raman spectra of the solid that at least one, and possibly both, of the bands observed at 505 and 465 cm^{-1} by Buttler and McKean[11] must correspond to the Si–N stretch. Since no bands of comparable intensity are to be found anywhere nearer the gas phase frequency of 670 cm^{-1} for the Si–N stretch, we assign the bands at 550 and 498 cm^{-1} in the solid phase Raman spectra to the Si–N stretch in the light compound and at 524 and 468 cm^{-1} in the heavy compound. On the basis of their assignment of the Si–N stretch to a much higher frequency, Goldfarb and Khare[8] assigned these bands to deformations of the rigid skeletal framework of the polymerized species. We have assigned the C–N symmetric stretch in the light compound and the (H_3)C–N stretch in the heavy compound to bands at 919 cm^{-1} in the solid phase Raman spectra of both compounds. The downward shift in frequency from the gas phase value is in keeping with the decrease in frequency of the Si–N stretch upon condensation, since both modes have already been shown to be coupled in the gas phase molecules. The assignments suggested in this work for the solid phase frequencies are, in most cases, in fair agreement with those proposed by Buttler and McKean.[11]

An X-ray diffraction study by Rudman et al.[18] has shown that crystalline dimethylsilylamine forms cyclic pentamers which consist of ten-membered, slightly skewed rings formed by alternating silicon and nitrogen atoms. Each

TABLE I: Observed Infrared and Raman Frequencies (cm^{-1}) and Assignments for $(CH_3)_2NSiH_3$[a,b]

Raman				
Gas	Liquid	Solid	Infrared gas	Assignment
	3062 w,p		3077 vw	
		2972 s		
2970 m	2957 m		2970 m	$\nu_1(A')$, $\nu_{19}(A'')$ CH_3 antisymmetric stretches
		2966 s		
		2953 m		
2946 m	2931 m			
2930 m	2923 m,sh			
		2929 s		
		2915 s		$\nu_2(A') + \nu_{20}(A'')$ and overtones and combination
		2904 s,sh		bands due to CH_3 deformations
	2901 m,sh			
2901 m	2890 m		2983 s	
		2877 s,sh		
	2870 m			
			2873 s	
		2867 s		
2856 m	2843 m			
		2836 w		$2 \times \nu_8$
		2818 s		
2807 s	2794 s	2769 s	2803 m	$\nu_3(A')$, $\nu_{21}(A'')$ CH_3 symmetric stretches
		2789 w		$2 \times \nu_{25}$
	2763 w,sh			
2187 m			2189 s	Impurity ?
		2180 w,sh		
2169 vs	2158 s,p	2140 s	2170 s	$\nu_4(A')$, $\nu_{22}(A'')$ SiH_3 antisymmetric stretches
	2158 w,sh			
2156 s				
2108 m	2105 m,sh,p	2102 s	2106 s	$\nu_5(A')$ SiH_3 symmetric stretch
		2091 s		
		2074 s		$2 \times \nu_{12}$
		2053 w		$\nu_{12} + \nu_{13}$ or $\nu_{12} + \nu_{29}$
		2015 w		$\nu_{13} + \nu_{29}$
		1967 w		
		1485 vw		
1485 w,dp	1483, w,dp	1467 m,sh		$\nu_6(A')$, $\nu_{23}(A'')$ CH_3 antisymmetric deformations
		1460 m		
1471 w,dp		1454 m	1473 w	$\nu_{24}(A'')$ CH_3 antisymmetric deformation
1453 w,p		1440 m	1455 m	$\nu_7(A')$ CH_3 antisymmetric deformation
1440 w,p ?	1440 w,p ?	1417 m		$\nu_8(A')$ CH_3 symmetric deformation
	1419 w,sh,dp?	1392 m		$\nu_{25}(A'')$ CH_3 symmetric deformation
			1342 w	$2 \times \nu_{15}$
1333 vw				
1306 vw,sh				
		1298 vw		
1293 w,p	1289 w,p	1220 m	1293 m	$\nu_9(A')$ CH_3 rock
		1164 vw	1189 m	$\nu_{26}(A'')$ CH_3 rock
	1142 vw	1122 vw	1149 w	$\nu_{10}(A')$ CH_3 rock
1073 vw	1073 vw,dp	1087 vw	1075 w	$\nu_{27}(A'')$ CH_3 rock
	1030 vw,sh	1096 w		$\nu_{28}(A'')$ C-N antisymmetric stretch
1004 w,p	1002 w,sh,p	919 m	1005 m	$\nu_{11}(A')$ C-N symmetric stretch
992 w,p	992 w,p			Impurity ?
972 w,p	965 w,sh,p	1039 m	971 vs	$\nu_{12}(A')$ SiH_3 symmetric deformation
927 w,p	923 w,p	1011 w	922 m	$\nu_{13}(A')$, $_{29}(A'')$ SiH_3 antisymmetric deformations
		1000 w		
		995 w,sh		
		985 vw		
		878 w	715 m	$\nu_{30}(A'')$ SiH_3 rock
696 w,p	695 w,p	834 m	695 s	$\nu_{14}(A')$ SiH_3 rock
		803 vw		
		768 vw		
		696 vw		
670 m,p	670 m,p	550 m	670 m	$\nu_{15}(A')$ Si-N stretch
		498 m?		
		642 vw		
640 vw	638 w,p			
			459 m	Impurity
360 w,p	364 w,p	385 w	359.7 m	$\nu_{16}(A')$ C-N-C deformation
			354.2 m	
		344 m	268 w,sh	$\nu_{31}(A'')$ C-N-Si out-of-plane deformation
			238.5 s	$\nu_{17}(A')$ CH_3 torsion
			~240[b]	$\nu_{32}(A'')$ CH_3 torsion
		241 w	~234[b]	$\nu_{18}(A')$ C-N-Si in-plane deformation
			115	$\nu_{33}(A'')$ SiH_3 torsion
		328 w		
		290 vw		

TABLE I (*Continued*)

Raman				
Gas	Liquid	Solid	Infrared gas	Assignment
		257 vw		
		232 w		
		222 w		
		204 vw		
		182 s		Lattice mode
		163 w		
		130 vw		
		104 w		
		99 vw		
		92 m		Lattice mode
		60 m		Lattice mode
		41 m		Lattice mode
		34 vw, sh		Lattice mode
		30 vw, sh		
		18 vw		Lattice mode

[a] Abbreviations used: w, weak, m, medium; s, strong; v, very; sh, shoulder; p, polarized; dp, depolarized. [b] See text for discussion.

nitrogen atom is tetrahedrally bonded, while each silicon atom is five-coordinated in a trigonal bipyramidal arrangement. Therefore, a detailed assignment of the infrared and Raman spectra of solid $(CH_3)_2NSiH_3$ and $CH_3CD_3NSiH_3$ does not seem possible due to the large number of active fundamental vibrational frequencies of the pentamer unit. For the sake of simplicity, we have assigned the solid phase frequencies on the basis of the symmetry of the unassociated molecule.

Because of the coplanarity of the three Si–H bonds around each silicon in the crystalline state, a large disparity between the SiH_3 stretching regions in the gas and solid spectra is expected. However, due to the profuseness of bands in this region, especially in that of the solid, any definitive assignment is impossible. One of the more notable differences in the spectrum of dimethylsilylamine upon condensation is the upward shift in frequency of the SiH_3 deformations, contrary to the usually observed downward shift (e.g., the silyl halides[19]). This unusual upward shift is obviously the result of the trigonal bipyramidal arrangement about the silicon atoms in the solid phase. We observed several bands in the Raman spectrum of the solid phase of the light compound which appeared to have counterparts sufficiently shifted in the deuterated compound so as to be attributable to skeletal deformations of the C_2–N moiety. Therefore, on this basis, the C–N–C deformation and the C_2–N in-plane wag are assigned to the bands at 385 and 344 cm^{-1}, respectively, shifting to 367 and 323 cm^{-1} upon deuteration. The C_2–N out-of-plane rock is assigned to the band at 241 cm^{-1} in the spectrum of the light compound, but its counterpart is not observed in the spectrum of the heavy compound as it is quite possibly obscured by the pair of bands at 232 and 223 cm^{-1}.

Rudman et al.[18] have suggested that the two low frequency bands previously assigned as Si–N stretches are due to in-plane and out-of-plane ring deformational modes. We consider these frequencies, 550 and 498 cm^{-1} in the spectrum of the light compound and 524 and 468 cm^{-1} in the spectrum of the heavy compound, to be too high to be due to such deformational modes. We believe that our assignment of these bands to the Si–N stretch is correct, and the fact that there are two bands is attributable to the existence of in-phase and out-of-phase motions.

Torsional Assignments and Barriers to Internal Rotations

For a molecule such as dimethylsilylamine three torsional vibrations are expected. In the case of $(CH_3)_2NSiH_3$, the torsional oscillations of the two methyl groups will give rise to one A′ and one A″ mode, while the SiH_3 torsion will account for another A″ mode. A–C hybrid band contours are expected for A′ modes, while B-type band contours should result from A″ modes. For $CH_3CD_3NSiH_3$, bands due to the CH_3 and CD_3 torsions should exhibit A–C hybrid band contours, while bands arising from the SiH_3 torsion should be of primarily B-type contour.

The sharp Q branch at 238.5 cm^{-1} in the spectrum of the light compound is assigned as the $1 \leftarrow 0$ transition of the A′ methyl torsion. The Q branches between 210 and 235 cm^{-1} are expected to be the torsional hot-band series for this mode. In the heavy compound, the sharp bands at 223.3 and 171.3 cm^{-1} are assigned to the $1 \leftarrow 0$ transitions of the CH_3 and CD_3 tops, respectively. Once again, the bands immediately following on the low frequency side of these transitions are expected to be the torsional hot-band series of the respective torsions. Qualitatively, one would predict the $1 \leftarrow 0$ transition to be the most intense. However, we observed that several of the torsional hot-band transitions for the CH_3 torsions in both the light and heavy molecules were more intense than the $1 \leftarrow 0$ transitions. This indicates the existence of a band due to an additional vibrational mode lying beneath these torsional transitions. From the contours of the bands resulting from the CH_3 torsions, we estimate these bands at 234 and 215 cm^{-1} in the light and heavy compounds, respectively, and assign them to the C–N–Si in-plane skeletal deformation. We were unable to observe the A″ CH_3 torsion in the spectrum of the light compound, but based on the small F' value in dimethylsilylamine and the fairly small value of the coefficient of the sine–sine coupling term found for dimethylamine,[17] which should be close to the value for the corresponding quantity in dimethylsilylamine, we can predict that it should occur at a frequency very close to that of the A′ torsion.

An attempt was made to fit the data for the CH_3 and CD_3 tops in both the light and heavy compounds to a two-dimensional potential function based on a new theoretical treatment by Groner and Durig[20] of the torsional vibrations in $(CH_3)_2X$-type molecules having C_s symmetry. All such endeavors, however, met with failure for both the deuterated and undeuterated compounds. In the case of $(CH_3)_2NSiH_3$, the kinetic top–top interactions between the two methyl groups is expected to be moderately large and the coefficient of at least the cosine–cosine coupling term should be significant. We were severely limited though in the amount of data available for the light compound as we were only able to unambiguously assign the $1 \leftarrow 0$ transition of the A′ CH_3 torsion and were unable to observe

TABLE II: Observed Infrared and Raman Frequencies (cm^{-1}) and Assignments for $CH_3CD_3NSiH_3$[a,b]

Raman				
Gas	Liquid	Solid	Infrared gas	Assignment
		2973 s		
2967 w,sh	2957 m,sh		2971 m	ν_1 CH_3 antisymmetric stretch
		2966 s		
2957 m	2943 m			$2 \times \nu_{11}$ or ν_2 CH_3 antisymmetric stretch ?
		2954 m		
		2933 s		
		2922 s		
2909 m	2899 m			
		2891 s		
2886 m	2877 m		2890 m	$2 \times \nu_{12}$
		2865 vs		
		2807 vw		
2805 m	2797 s	2782 s	2805 m	ν_3 CH_3 symmetric stretch
2791 m				
	2728 vw			
		2638 vw		
		2590 vw		
		2536 vw		
	2343 vw			
		2220 s		
	2216 w			
		2212 m		
2208 w	2200 w			$2 \times \nu_{15}$
		2190 s		
2184 m	2172 m,sh		2189 s	Impurity?
2168 s	2155 vs	2133 s	2170 s	ν_6, ν_7 SiH_3 antisymmetric stretches
2155 m				
		2119 s		
2107 m	2106 m,sh	2098 vs	2105 s	ν_8 SiH_3 symmetric stretch
		2073 s		
		2055 s		
2054 m	2047 s		2054 m	ν_9 CD_3 symmetric stretch
2033 w	2025 w			
		2017 w		
		1982 w		
	1490 vw,sh	1459 m,sh		ν_{10} CH_3 antisymmetric deformation
1450 w,bd	1472 w	1452 m	1480 w,bd	ν_{11} CH_3 antisymmetric deformation
	1438 w	1407 w	1448 w	ν_{12} CH_3 symmetric deformation
1284 w	1284 vw		1290 m	$2 \times \nu_{27}$
1263 w	1260 w	1188 w	1264 m	ν_{13} CH_3 rock
1182 vw	1177 vw	1121 vw	1185 s	ν_{14} CH_3 rock
			1160 w	
	1124 vw			
1104 w	1100 vw	1133 w	1104 m	ν_{15} CD_3 deformation
1067 w	1065 vw	1082 w		ν_{16} CD_3 deformation
	1049 vw		1053 w	ν_{17} CD_3 deformation
1008 w	1004 w	919 w	1007 s	ν_{18} (H_3) C-N stretch
973 w	968 w	1057 m,sh	974 vs	ν_{19} SiH_3 symmetric deformation
		1053 m		
930 w		933 w		ν_{20} CD_3 rock
922 w	924 w,sh	1010 w	923 s	ν_{21}, ν_{22} SiH_3 antisymmetric deformations
	875 vw,sh	896 w		ν_{23} CD_3 rock
855 w	852 vw	816 vs	855 m	ν_{24} (D_3) C-N stretch
819 w				
			801 w	
		801 w		
		765 vw		
		706 vw		
703 w		848 w	711 m	ν_{25} SiH_3 rock
686 w	693 w	839 m	693 m	ν_{26} SiH_3 rock
	669 vw		668 w	
641 m	642 s	524 m	643 w	ν_{27} Si-N stretch
		468 m?		
612 vw	612 vw,sh			
586 vw				
560 vw	560 vw			
	539 vw			
	360 vw,sh			
337 w	340 w	367 w	342.4 m	ν_{28} C-N-C deformation
			333.0 m,sh	
	260 vw,bd	323 w	256 w,sh	ν_{29} C-N-Si deformation
			223.3 s	ν_{30} CH_3 torsion
			~215[b]	ν_{31} C-N-Si deformation
			171.3 m	ν_{32} CD_3 torsion
			103 m,bd	ν_{33} SiH_3 torsion

TABLE II (*Continued*)

Raman				
Gas	Liquid	Solid	Infrared gas	Assignment
		332 w		
		287 w		
		256 vw		
		232 w		
		223 w		
		205 vw		
		179 vs		Lattice mode
		160 vw		
		123 vw		
		105 w		
		94 w		
		89 m		Lattice mode
		58 m		Lattice mode
		40 w		Lattice mode
		34 w,sh		
		30 w,sh		
		18 w		Lattice mode

[a] Abbreviations used: w, weak; m, medium; s, strong; v, very; sh, shoulder. [b] See text for discussion.

any of the torsional double jumps in the Raman spectrum of the gas phase. In $CH_3CD_3NSiH_3$, we expect the kinetic top–top interaction between the CH_3 and CD_3 tops to be fairly small and, hence, on the basis of the results for dimethylamine-d_3,[17] the coefficient of the cosine–cosine coupling term to be somewhat smaller than that for the light compound and the coefficient of the sine–sine coupling term to be negligible. Here too we were hampered in obtaining the necessary data by not being able to observe the torsional double jumps in the Raman spectrum of the gas. Also, the possibility that the CD_3 torsion is significantly coupled to the SiH_3 torsion must be examined.

The bands at 115 and 103 cm^{-1} in the light and heavy compounds, respectively, both have contours attributable to a series of overlapping B-type bands and are, thus, assigned to the SiH_3 torsion. To the best of the authors' knowledge this is the first observation of a torsional frequency of a silyl group bonded to nitrogen. Taking into consideration the experimental uncertainty in frequency measurement due to the broadness of the bands and the difference in F numbers in the light and heavy compounds, we conclude that this difference between the SiH_3 torsional frequencies in the light and heavy compounds is real and that, more specifically, it is a result of coupling between the SiH_3 top and the CD_3 top in the heavy compound. In the light compound it is expected that coupling of the SiH_3 top with the two methyl tops is insignificant. Such coupling would, of course, invalidate any results obtained by using a two-dimensional potential function to fit the CH_3 and CD_3 top data in the heavy compound.

Therefore, all torsional data were fit by neglecting all top–top interactions and using a one-dimensional periodic potential function. The torsional assignments together with the results of all calculations are summarized in Table III. Since coupling between the CH_3 and SiH_3 tops is expected to be almost nonexistent in the light compound and since coupling between the CH_3 and CD_3 tops is expected to be small in the heavy compound, we consider the barrier to internal rotation of 1.51 kcal/mol calculated for the SiH_3 top in the light compound as best approximating the actual silyl barrier and the value of 3.23 kcal/mol calculated for the CH_3 top in the heavy compound as best approximating the actual methyl barrier.

If the heavy-atom skeleton were indeed planar, then the internal rotational barrier about the Si–N bond would be sixfold and we would expect the silyl top to be essentially freely rotating. Also, we would predict rotational fine structure in the form of bands of alternating strong–weak–weak intensity to be exhibited on the antisymmetric SiH_3 stretch. The fact that we observed the SiH_3 torsion and found the barrier to internal rotation to be appreciable, and were unable to observe any fine structure on the antisymmetric SiH_3 stretch, is clearly evidence of the nonplanarity of the heavy-atom skeleton.

TABLE III: Observed Torsional Frequencies and Potential Constants for Dimethylsilylamine

	$(CH_3)_2NSiH_3$	$CH_3CD_3NSiH_3$
Methyl torsions		
ν, cm^{-1} (CH_3 τ)	238.5	223.3
ν, cm^{-1} (CD_3 τ)		171.3
F,[a] cm^{-1} (CH_3 top)	5.531	5.503
F',[a] cm^{-1}	−0.0183	−0.0230
F,[a] cm^{-1} (CD_3 top)		2.863
V_3, kcal/mol (CH_3 top)	3.65	3.23
V_3, kcal/mol (CD_3 top)		3.52
	$(CH_3)_2NSiH_3$	$CH_3CD_3NSiH_3$
Silyl torsions		
ν, cm^{-1}	115	103
F,[a] cm^{-1}	3.155	3.113
V_3, kcal/mol	1.51	1.25

[a] All F numbers calculated from the structural parameters presented in ref 12.

Discussion

Of particular interest in the silyl amine compounds is the possibility of a d_π–p_π interaction between the lone pair electrons on the nitrogen and the d orbitals of the silicon atom. Certain controversy exists concerning the strength of such an interaction in dimethylsilylamine. Glidewell et al.[12] reported the Si–N bond distance in methyldisilylamine to be shorter by 0.010 ± 0.007 Å than that in trisilylamine, and the Si–N bond distance in dimethylsilylamine to be shorter by 0.011 ± 0.005 Å than that in methyldisilylamine. The authors speculated that these differences might reflect the enhancement of (p → d)π bonding between nitrogen and silicon as the number of silyl groups decreases. While we feel that such an explanation is reasonable for trisilylamine and methyldisilylamine, which are both planar, we do not think it valid to extend it to a molecule such as dimethylsilylamine whose structure is nonplanar. We tend to believe that the nonplanarity of the heavy-atom skeleton in dimethylsilylamine would not be very agreeable to sufficient p and d orbital overlap for a strong d_π–p_π interaction. Also, any significant amount of (p → d)π bonding should manifest itself in a change in

the hybridization of the nitrogen atom with a resultant change in the C–N–C bond angle. That these angles are almost identical in dimethylsilylamine[12] and dimethylamine[21,22] argues against any appreciable d_π–p_π interaction. We are thus inclined to attribute the differences in the Si–N bond distance between methyldisilylamine and dimethylsilylamine to the difference in electronegativity of the nitrogen atom in the two molecules.

Goldfarb and Khare,[8] assuming a strong d_π–p_π interaction (i.e., greater double bond character, hence a greater force constant), erroneously placed the Si–N stretching frequency over 300 cm^{-1} higher than it actually occurs. We have confirmed the relatively low Si–N stretching frequency of 670 cm^{-1}, although coupling of the Si–N stretch with the C–N stretch has definitely been shown to exist in this molecule. Such a low frequency, even considering the effect of coupling, is consistent with the lack of any significant d_π–p_π interaction.

One of our major concerns is the interplay of bonded and nonbonded interactions on barriers to internal rotations. If the extent of (p → d)π bonding were considerable in dimethylsilylamine, then the silyl barrier would be expected to be fairly large. The silyl barrier calculated for dimethylsilylamine (1.51 kcal/mol) is within experimental error of that calculated for silylphosphine (1.512 ± 0.026 kcal/mol).[23] Such a low value for the silyl barrier in dimethylsilylamine essentially rules out the possibility of any extensive double bond character in the Si–N bond. Although one might expect a higher barrier in dimethylsilylamine than in silylphosphine due to the fact that the Si–P distance (2.249 Å)[23] is longer than the Si–N distance (1.715 Å),[12] the result is not unreasonable when the rather large C–N–Si bond angle in dimethylsilylamine (120.0°)[12] and the small H–P–Si angle in silylphosphine (92.8°)[23] are considered. The methyl barrier calculated in dimethylsilylamine (3.23 kcal/mol) is comparable to that in dimethylamine (3.007 ± 0.035 kcal/mol).[17] This is to be expected since the structural parameters of the dimethylamino moiety are nearly identical in both compounds. Also, the methyl hydrogens in dimethylsilylamine approach the silyl hydrogens to approximately the same distance that the methyl hydrogens in dimethylamine approach the hydrogen bonded to the nitrogen, 2.34 Å vs. 2.23 Å.

It is interesting to note that the apparent lack of any appreciable intramolecular d_π–p_π interaction can help account for the strong intermolecular d_π–p_π interaction observed for dimethylsilylamine in the solid phase.

Glidewell[24,25] has recently discussed the structural trends in the silyl amines in terms of steric factors. Thus, the increase in bond angles and Si–N bond distances in the series $(CH_3)_2NSiH_3$, $(SiH_3)_2NCH_3$, and $(SiH_3)_3N$ is interpreted on the basis of increasing nonbonded interactions with increasing SiH_3 substitution. While our results are in agreement with the steric model presented by Glidewell,[24,25] we by no means preclude the possibility of perhaps a very weak d_π–p_π interaction in dimethylsilylamine.

Acknowledgment. The authors gratefully acknowledge the financial support given this work by the National Aeronautics and Space Administration through Grant NGL-41-002-003. Acknowledgment is also given to the National Science Foundation for funds to purchase the Digilab FTS-15B interferometer by Grant MPS-75-06296.

References and Notes

(1) Taken in part from the thesis of P. J. Cooper, to be submitted to the Department of Chemistry in partial fulfillment of the requirements for the Ph.D. degree.
(2) D. W. Robinson, *J. Am. Chem. Soc.*, **80**, 5924 (1958).
(3) E. A. V. Ebsworth, J. R. Hall, M. J. Mackillop, D. C. McKean, N. Sheppard, and L. A. Woodward, *Spectrochim. Acta*, **13**, 202 (1958).
(4) V. H. Kriegsmann and W. Forster, *Z. Anorg. Allg. Chem.*, **298**, 212 (1959).
(5) T. D. Goldfarb and B. N. Khare, *J. Chem. Phys.*, **46**, 3379 (1967).
(6) K. Hedberg, *J. Am. Chem. Soc.*, **77**, 6491 (1955).
(7) M. J. Buttler, D. C. McKean, R. Taylor, and L. A. Woodward, *Spectrochim. Acta*, **21**, 1379 (1965).
(8) T. D. Goldfarb and B. N. Khare, *J. Chem. Phys.*, **46**, 3384 (1967).
(9) C. Glidewell, D. W. H. Rankin, A. G. Robiette, and G. M. Sheldrick, *J. Mol. Struct.*, **4**, 215 (1969).
(10) D. W. H. Rankin, A. G. Robiette, G. M. Sheldrick, W. S. Sheldrick, B. J. Aylett, I. A. Ellis, and J. J. Monaghan, *J. Chem. Soc. A*, 1224 (1969).
(11) M. J. Buttler and D. C. McKean, *Spectrochim. Acta*, **21**, 485 (1965).
(12) C. Glidewell, D. W. H. Rankin, A. G. Robiette, and G. M. Sheldrick, *J. Mol. Struct.*, **6**, 231 (1970).
(13) B. J. Aylett and J. Emsley, *J. Chem. Soc. A*, 652 (1967).
(14) S. Sujishi and S. Witz, *J. Am. Chem. Soc.*, **76**, 4631 (1954).
(15) G. L. Ward, *Inorg. Syn.*, **11**, 159 (1968).
(16) G. Gamer and H. Wolff, *Spectrochim. Acta, Part A*, **29**, 129 (1973).
(17) J. R. Durig, M. Griffin, and P. Groner, *J. Chem. Phys.*, in press.
(18) R. Rudman, W. C. Hamilton, S. Novick, and T. D. Goldfarb, *J. Am. Chem. Soc.*, **89**, 5157 (1967).
(19) D. F. Ball, M. J. Buttler, and D. C. McKean, *Spectrochim. Acta*, **21**, 451 (1965).
(20) P. Groner and J. R. Durig, *J. Chem. Phys.*, submitted for publication.
(21) J. E. Wollrab and V. W. Laurie, *J. Chem. Phys.*, **48**, 5058 (1968).
(22) B. Beagley and T. G. Hewitt, *Trans. Faraday Soc.*, **64**, 2561 (1968).
(23) J. R. Durig, Y. S. Li, M. M. Chen, and J. D. Odom, *J. Mol. Spectrosc.*, **59**, 74 (1976).
(24) C. Glidewell, *Inorg. Chim. Acta Rev.*, **7**, 69 (1973).
(25) C. Glidewell, *Inorg. Chim. Acta*, **12**, 219 (1975).

Resonance Raman Spectra of Monolayers of a Surface-Active Dye Adsorbed at the Oil–Water Interface

Taisuke Nakanaga[1] and Tohru Takenaka*

Institute for Chemical Research, Kyoto University, Uji, Kyoto-Fu, 611, Japan *(Received August 13, 1976; Revised Manuscript Received January 17, 1977)*

Publication costs assisted by Kyoto University

Resonance Raman spectra have been recorded for a monolayer of a surface-active dye, Suminol Milling Brilliant Red BS (abbreviated as BRBS), adsorbed at the interface between carbon tetrachloride and an aqueous solution by using a previously proposed method of total reflection of the exciting light at the interface. Theoretical considerations of the Raman scattering activity due to an evanescent wave in the total reflection have been made with a model of uniaxial orientation suitable for the BRBS molecule at the interface. From polarization measurements of the resonance Raman spectra at various concentrations of BRBS in the aqueous solution, the changes in intensity ratios of polarized Raman bands were found to have some correspondence to the change in the interfacial pressure. It was therefore concluded that the BRBS molecules were almost freely oriented in the monolayer at lower interfacial pressure, while the planes of the molecules showed a tendency to subtend an angle with the interface at higher interfacial pressure.

Introduction

Vibrational spectroscopic studies of molecular orientation in monolayers adsorbed at the liquid–gas or liquid–liquid interface have been a subject of much interest in the field of surface chemistry. In the previous paper,[2] we have reported the resonance Raman spectra of a monolayer of complexes of a cationic surfactant (cetyltrimethylammonium bromide) and an anionic azo dye (methyl orange) adsorbed at the interface between carbon tetrachloride and an aqueous solution, and have discussed the orientation of the dye molecule in the monolayer. For the purpose of studying the molecular orientation of a surfactant, the present paper deals with the Raman spectra of monolayers of a surface-active anionic azo dye, Suminol Milling Brilliant Red BS (BRBS) adsorbed at the interface

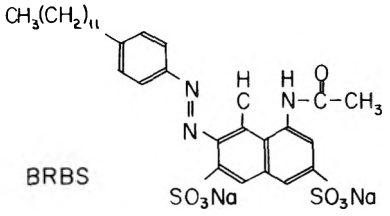

between carbon tetrachloride and an aqueous solution. Since BRBS has an electronic absorption doublet at 510 and 550 nm, the resonance enhancement of Raman intensity is expected for the exciting wavelength of 488.0 and 514.5 nm of the Ar^+ laser. Under the assumption of uniaxial orientation suitable for BRBS, the change in the molecular orientation with the amount of the adsorbed molecules is studied.

Experimental Section

A sample of BRBS was supplied by Sumitomo Chemical Industry Co. Ltd. After application of the salting-out technique, it was recrystallized twice from water–ethanol solution. Results of the elementary analysis showed that each BRBS molecule contained three water molecules in it. Carbon tetrachloride was the specially prepared reagent for spectroscopy by Nakarai Chemicals, Ltd. and used without further purification. Pure water was prepared by redistillation of distilled water which had been passed through an ion-exchange resin column.

Measurements of the interfacial tension between carbon tetrachloride and the aqueous solution were carried out at room temperature by the Wilhelmy method using a Teflon plate.

For measurements of the resonance Raman spectra of the adsorbed monolayers, the previously proposed method of total reflection of the exciting light at the interface was used (Figure 1). Details of the measurements have been described in the previous paper.[2] The angle of incidence of the exciting light at the interface was 84°. The penetration depth of the evanescent wave in the aqueous solution was 1390 Å for the 488.0-nm light of an Ar^+ laser. The Raman spectra were recorded on a Japan Electron Optics Laboratory Model JRS-S1 laser Raman spectrophotometer with a Spectra-Physics Model 164 Ar^+ laser (4 W). The output power of the exciting light was kept less than 100 mW to protect the interface from thermal agitation.

The resonance Raman spectra of a bulk solution were obtained by using a 1-mm capillary tube.

Results and Discussion

Interfacial Tension. In Figure 2, the interfacial tension γ between carbon tetrachloride and the aqueous solution is plotted as a function of the logarithm of the concentration C of BRBS. From the tangent to the curve at the concentration 5×10^{-4} M, at which the amount of the adsorbed molecules seems to be saturated, the surface excess of BRBS is obtained as $\Gamma = 2.8 \times 10^{-10}$ mol cm^{-2} by the use of the Gibbs adsorption isotherm. This means that the surface area A occupied by each molecule is 60 Å^2, in good agreement with the calculated molecular area[3] 65 Å^2. It is therefore concluded that the adsorbed BRBS molecules form the condensed monolayer at this concentration.

Resonance Raman Spectra of the Bulk Solution and the Adsorbed Monolayer. Resonance Raman spectra of the bulk aqueous solution of BRBS (2×10^{-4} M) are shown in Figure 3A, where $I_\parallel$ and $I_\perp$ denote the intensities of Raman scattering with the electric vectors parallel and perpendicular to that of the exciting light, respectively. The depolarization ratios ($\rho_l = I_\perp/I_\parallel$) measured for the strong and medium intensity bands were found to be approximately 1/3 irrespective of the exciting wavelength of the Ar^+ laser. Thus it can be said for these bands that only one diagonal element of the Raman scattering tensor is resonance enhanced.[4]

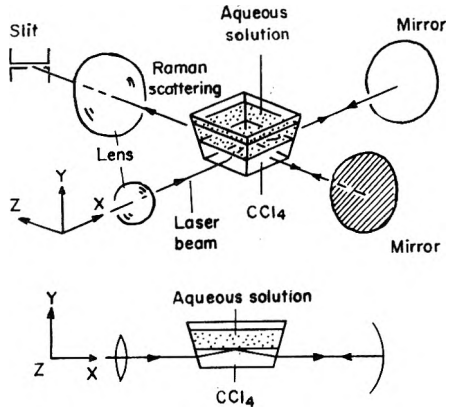

Figure 1. Total reflection method for Raman measurements of monolayers adsorbed at the interface between carbon tetrachloride and aqueous solutions.

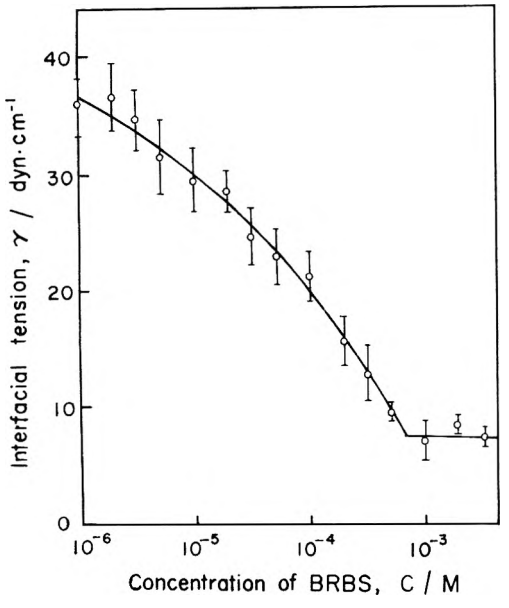

Figure 2. Interfacial tension γ between carbon tetrachloride and aqueous solution of BRBS as a function of logarithm of concentration C of BRBS.

Figure 3B represents the resonance Raman spectrum of BRBS in the monolayer adsorbed at the interface between carbon tetrachloride and the 2×10^{-4} M aqueous solution recorded by the total reflection method of Figure 1. Although the signal-to-noise ratio is low, the Raman spectrum which resembles that of the bulk solution can be obtained on the background due to Raman bands of carbon tetrachloride. Frequency shift of the BRBS bands cannot be seen on the transition from the aqueous solution to the monolayer.

From polarization measurements of the resonance Raman spectra, we will discuss the orientation of the BRBS molecules in the adsorbed monolayer in the next section.

Orientation of the BRBS Molecules in the Monolayer. Let us define the space-fixed axes X, Y, and Z as shown in Figure 1. Y is the axis normal to the interface XZ, and XY is the plane of incidence of the exciting light. As was discussed in the previous paper,[2] when the Raman radiation emitted by the interaction between the monolayers and the evanescent wave is observed along the Z axis, there are four possible geometries of polarization measurements as a consequence of the combination of two polarization directions of the excitation (parallel and perpendicular to the plane of incidence) and two polarization directions of

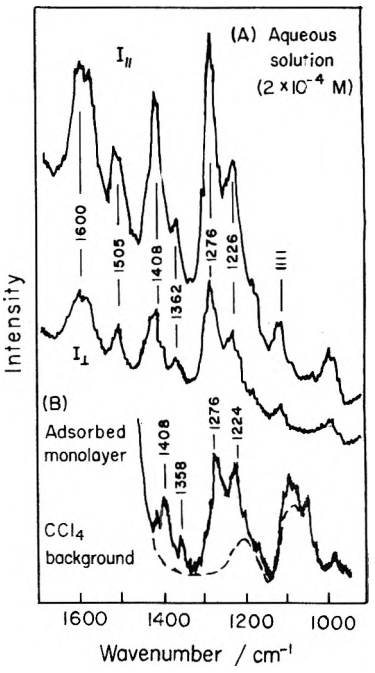

Figure 3. Resonance Raman spectra of BRBS: (A) aqueous solution of BRBS (2×10^{-4} M); (B) monolayer adsorbed at the interface between carbon tetrachloride and the aqueous solution. For $I_{\parallel}$ and $I_{\perp}$, see text.

the Raman radiation (parallel to the X and Y axes). Under the assumption of the uniaxial orientation which will be mentioned below, the Raman intensities observed by these polarization measurements is proportional to[5]

$$I_{\perp X} = \alpha_{ZX}^2 |E_Z|^2 \tag{1}$$

$$I_{\perp Y} = \alpha_{ZY}^2 |E_Z|^2 \tag{2}$$

$$I_{\parallel X} = \alpha_{XX}^2 |E_X|^2 + \alpha_{YX}^2 |E_Y|^2 \tag{3}$$

and

$$I_{\parallel Y} = \alpha_{XY}^2 |E_X|^2 + \alpha_{YY}^2 |E_Y|^2 \tag{4}$$

Here the first subscript of I refers to the excitation polarization and the second to that of Raman radiation, and α_{XY} etc. are the elements of the Raman scattering tensor based on the space-fixed axes. E_X, E_Y, and E_Z are the respective components of the electric field amplitudes in the monolayer and are given by[6]

$$E_X = \frac{2(\sin^2 \psi - n_{31}^2)^{1/2} \cos \psi}{(1 - n_{31}^2)^{1/2} \{(1 + n_{31}^2) \sin^2 \psi - n_{31}^2\}^{1/2}} E_{\parallel}^0 \tag{5}$$

$$E_Y = \frac{2n_{32}^2 \sin \psi \cos \psi}{(1 - n_{31}^2)^{1/2} \{(1 + n_{31}^2) \sin^2 \psi - n_{31}^2\}^{1/2}} E_{\parallel}^0 \tag{6}$$

and

$$E_Z = \frac{2 \cos \psi}{(1 - n_{31}^2)^{1/2}} E_{\perp}^0 \tag{7}$$

where n_{31} is the ratio of the refractive index of the aqueous solution n_3 to that of carbon tetrachloride n_1, n_{32} the ratio of n_3 and the refractive index of the monolayer n_2, ψ the angle of incidence, and $E_{\parallel}^0$ and $E_{\perp}^0$ are the amplitudes of the incident light with the electric vectors parallel and perpendicular to the plane of incidence, respectively. Since the adsorbed monolayer is much thinner than the penetration depth, the electric field can be assumed constant over the monolayer thickness.

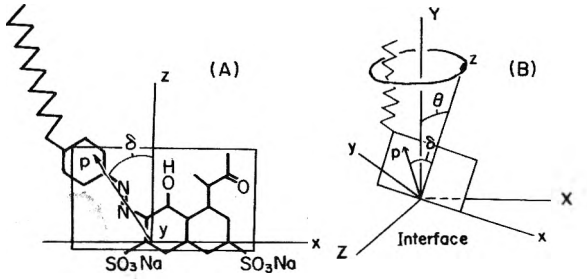

Figure 4. Schematic drawings of (A) the BRBS molecule and of (B) the uniaxial orientation of BRBS in the monolayer.

In order to express the elements α_{XY} etc. in terms of the elements α_{xy} etc. which are based on the molecular-fixed axes, it is convenient to assume a type of orientation of the BRBS molecule in the monolayer. If we represent the chromophore of the BRBS molecule as a rectangle, as shown in Figure 4A, two sulfonate groups are located at the base of the rectangle and the dodecyl group is at one end of the upside. The molecular-fixed axes x, y, and z are defined as shown in Figure 4A. Since it has been known from the measurements of the depolarization ratio in the bulk aqueous solution that only one diagonal element of the Raman scattering tensor is exceptionally enhanced, we assume that the corresponding principal axis p lies on the plane of the chromophore and forms an angle δ with the z axis. The adsorbed BRBS molecules may be oriented at the interface placing the two sulfonate groups into water and the dodecyl group into carbon tetrachloride (Figure 4B). It is therefore reasonable to assume that the z axis of the molecules is uniaxially oriented with respect to the Y axis with an angle θ, holding the x axis parallel to the interface (the XZ plane). Under this assumption, α_{XY}^2 etc. are given by

$$\alpha_{XX}^2 = 3\alpha_{ZX}^2 = (3/8)(\sin^2\delta + \sin^2\theta\cos^2\delta)^2\alpha_p^2 \quad (8)$$

$$\alpha_{YY}^2 = \cos^4\theta\cos^4\delta\alpha_p^2 \quad (9)$$

and

$$\alpha_{XY}^2 = \alpha_{YX}^2 = \alpha_{ZY}^2 = (1/2)\cos^2\theta\cos^2\delta \times (\sin^2\theta\cos^2\delta + \sin^2\delta)\alpha_p^2 \quad (10)$$

through the averaging process over the angle referring to the rotation of the z axis around the Y axis.[2,7] Here, α_p is the above-mentioned diagonal element of the Raman scattering tensor based on the molecular-fixed axes.

Further, we make an assumption about θ that the planes of the chromophore are uniformly distributed between $\theta = 0°$ and $\theta = \theta_0°$. Thus the distribution function can be defined as

$$F(\theta) = 1 \quad (0° \leqslant \theta \leqslant \theta_0°)$$
$$= 0 \quad (\theta_0° \leqslant \theta \leqslant 180°)$$

Multiplying eq 8–10 by $F(\theta)\sin\theta$ and integrating the product with respect to θ, we have

$$\alpha_{XX}^2 = 3\alpha_{ZX}^2 = (3/8)[A_1 - (2/3)A_2 + (1/5)A_3]\alpha_p^2 \quad (11)$$

$$\alpha_{YY}^2 = (1/5)A_3\alpha_p^2 \quad (12)$$

and

$$\alpha_{XY}^2 = \alpha_{YX}^2 = \alpha_{ZY}^2 = (1/2)[(1/3)A_2 - (1/5)A_3]\alpha_p^2 \quad (13)$$

where

$$A_1 = 1 - \cos\theta_0, A_2 = (1 - \cos^3\theta_0)\cos^2\delta, \quad A_3 = (1 - \cos^5\theta_0)\cos^4\delta \quad (14)$$

Substituting eq 5–7 and eq 11–13 into eq 1–4 and using

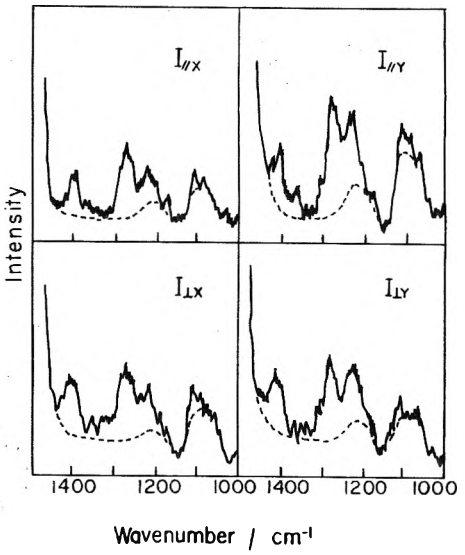

Figure 5. Resonance Raman spectra of BRBS in the adsorbed monolayer recorded at four polarization geometries. Broken lines represent the backgrounds due to Raman bands of carbon tetrachloride. $C = 2 \times 10^{-4}$ M.

proper values $n_1 = 1.46$, $n_2 = 1.43$, $n_3 = 1.34$, and $\psi = 84°$, we have the Raman intensity ratios

$$\frac{I_{\parallel X}}{I_{\parallel Y}} = \frac{0.72A_1 + 1.2A_2 - 0.86A_3}{0.32A_2 + 1.8A_3} \quad (15)$$

and

$$\frac{I_{\perp X}}{I_{\perp Y}} = \frac{3A_1 - 2A_2 + 0.6A_3}{4A_2 - 2.4A_3} \quad (16)$$

Experimentally, each ratio is obtained by measuring the intensities of the Raman bands recorded by changing the polarization of the Raman radiation in turn from the X to Y directions at a fixed polarization direction of the exciting light (either parallel or perpendicular to the plane of incidence). It is apparent from eq 15 and 16 that the angles δ and θ_0 can be determined from measurements of the two intensity ratios.

Figure 5 represents the polarized Raman spectra of BRBS in the adsorbed monolayer recorded at four polarization geometries mentioned above. For the all polarization geometries, the Raman spectra of BRBS can apparently be observed on the background due to carbon tetrachloride. The two intensity ratios $I_{\parallel X}/I_{\parallel Y}$ and $I_{\perp X}/I_{\perp Y}$ were obtained for each Raman band at various concentrations of BRBS in the aqueous solution. Since the number of molecules in the monolayer is so small that the Raman intensity is weak even being enormously enhanced by the resonance effect, the accuracy of the measurements is fairly low. Therefore, the ratio measurements were repeated more than 20 times for each band. Figure 6 shows the results obtained for the 1276-cm^{-1} band. Other bands with relatively strong and medium intensity gave rise to similar results. It is seen from Figure 6 that the ratio $I_{\parallel X}/I_{\parallel Y}$ gives a nearly constant value of about 0.9 in the lower concentration region and about 0.6 in the concentration region greater than 1×10^{-4} M. The ratio $I_{\perp X}/I_{\perp Y}$, on the other hand, gives a nearly constant value of about 1.0 over the whole region except around 1×10^{-4} M, where a little smaller value is obtained.

In Figure 7, the changes of the intensity ratios are compared with the change of the interfacial pressure π obtained from the interfacial tension γ of Figure 2 by $\pi = \gamma_0 - \gamma$, where γ_0 is the interfacial tension (43.8 dyn cm^{-1}) between pure water and carbon tetrachloride. The abscissa

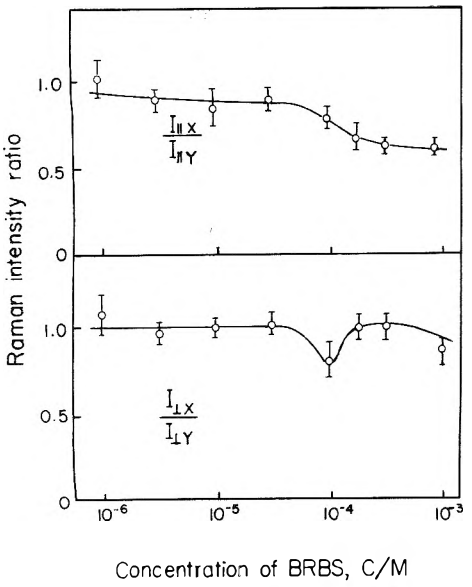

Figure 6. Raman intensity ratios $I_{\parallel X}/I_{\parallel Y}$ and $I_{\perp X}/I_{\perp Y}$ for 1276-cm^{-1} band as a function of concentration C of BRBS in aqueous solution.

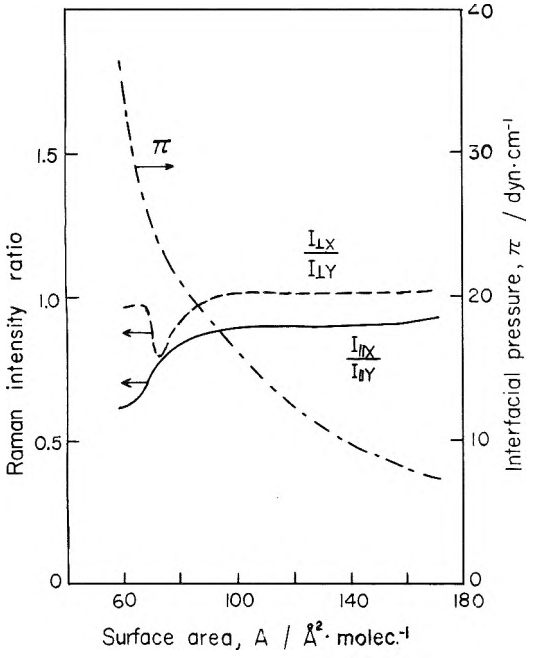

Figure 7. Raman intensity ratios $I_{\parallel X}/I_{\parallel Y}$ and $I_{\perp X}/I_{\perp Y}$ and the interfacial pressure π as a function of surface area A occupied by each BRBS molecule at the interface.

of the figure is the surface area A occupied by each BRBS molecule obtained from the tangents to the γ–log C curve (Figure 2) at respective concentrations using the Gibbs adsorption isotherm. It is to be noted that there is some correspondence between the π–A curve and the intensity ratio–A curves. The slope of the π–A curve is relatively low at surface areas larger than about 80 Å^2 and becomes steep at smaller surface areas. This may suggest that the monolayer is in the liquid expanded film state at large surface areas and in the condensed film state at small surface areas. Correspondingly, the two intensity ratios show a constant value in the region of the liquid expanded film and start to decrease at about 100 Å^2 where the monolayer starts to change from the liquid expanded film to the condensed film. Since, as was discussed above, the two intensity ratios reflect the molecular orientation, the correspondence between the π–A curve and the intensity ratio–A curves suggests that there is a correspondence

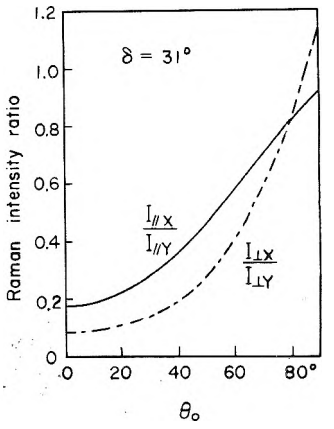

Figure 8. Raman intensity ratios $I_{\parallel X}/I_{\parallel Y}$ and $I_{\perp X}/I_{\perp Y}$ expressed by eq 15 and 16 as a function of θ_0. δ is fixed at 31°.

between the physical state of the monolayer and the molecular orientation.

Substituting the constant values of $I_{\parallel X}/I_{\parallel Y} = 0.9$ and $I_{\perp X}/I_{\perp Y} = 1.0$ at the large surface area into eq 15 and 16, we have the results $\delta = 31°$ and $\theta_0 = 86°$. The value of δ is thought to be reasonable if we consider that the direction of the transition moment of the electronic absorption band of BRBS is analogous to that of the corresponding band of *trans*-azobenzene.[8] The value of θ_0, on the other band, means that the planes of the chromophore have the uniform distribution between vertical orientation and almost horizontal orientation at the interface. This is convincing as the state of the liquid expanded film.

The decreases of the two intensity ratios with decreasing the surface area from 100 to 70 Å^2 can also be interpreted by eq 15 and 16. Plotting the two intensity ratios of eq 15 and 16 as a function of θ_0 with the fixed value of $\delta = 31°$, we have the results of Figure 8. Decreases of the two intensity ratios with decreasing θ_0 values from 86 to 80° in Figure 8 quantitatively reproduce the decreases of the ratios in Figure 7. This is indicative of the fact that the decreases of the two ratios in Figure 7 are interpreted by the decrease of θ_0. In other words, the planes of the chromophore show a tendency to subtend an angle with the interface with decreasing surface area. This may be mainly due to the increase of the intermolecular interaction with increasing amount of the adsorbed molecules, which accompanies the transition of the physical state of the monolayer from the liquid expanded film to the condensed film.

The change in the two intensity ratios at surface areas smaller than 70 Å^2 cannot be interpreted by the orientation model of Figure 4. In this region of the condensed film where the higher order of regularity in the molecular orientation is expected, the other model should be taken into account.

Additional Note. After completing this manuscript a paper was published by Ohnishi and Tsubomura,[9] who have studied the visible absorption spectra of a monolayer of BRBS (SMBR in their paper) adsorbed at the interface between carbon tetrachloride and the aqueous solution by using the total reflection method. They have concluded from dichroic measurements of absorption bands that the axis of the conjugation chain of the molecule is strongly inclined to the interface. Their conclusion is not in conflict with ours, although closer comparison is difficult because of differences of the assumptions adopted and of the extent of discussions.

Acknowledgment. The authors are indebted to Dr. N. Ohi of Sumitomo Chemical Industry Co. Ltd. for a gift of

the BRBS sample. The research was supported in part by a Grant for Scientific Research from the Ministry of Education, Japan.

References and Notes

(1) Present address: National Chemical Laboratory for Industry, Honmachi, Shibuya-Ku, Tokyo, 151, Japan.
(2) T. Takenaka and T. Nakanaga, *J. Phys. Chem.*, **80**, 475 (1976).
(3) C. H. Giles, "Proceedings of the 2nd International Congress of Surface Activity", Butterworths, London, 1957, p 92.
(4) O. S. Mortensen, *Chem. Phys. Lett.*, **3**, 4 (1969).
(5) P. R. Monson and W. M. McClain, *J. Chem. Phys.*, **53**, 29 (1970).
(6) N. J. Harrick, "Internal Reflection Spectroscopy", Interscience, New York, N.Y., 1967, Chapter II.
(7) In case of $\delta = 0°$, eq 8–10 coincide with expressions of case 1 in Table II in the previous paper.[2]
(8) D. L. Beveridge and H. H. Jaffé, *J. Am. Chem. Soc.*, **88**, 1948 (1966).
(9) T. Ohnishi and H. Tsubomura, *Chem. Phys. Lett.*, **41**, 77 (1976).

An Investigation of the Digitized Raman Band Profiles of Aqueous Indium(III) Chloride Solutions

Toomas Jarv, J. Timothy Bulmer,† and Donald E. Irish*

Guelph-Waterloo Centre for Graduate Work in Chemistry, Waterloo Campus, University of Waterloo, Waterloo, Ontario, Canada, N2L 3G1

(Received September 15, 1976)

Publication costs assisted by the National Research Council of Canada

The chloro complexes of indium(III) generate closely spaced, polarized Raman lines (stretching vibrations of indium–chloride bonds) which are observed as a single, broad, band profile. The band maximum shifts from 311 to 279 cm^{-1} as the chloride-to-indium ratio is increased from 0.48 to 15.9. Several numerical procedures have been applied to the digitized band profiles in order to investigate their usefulness for extracting the hidden information concerning the number of lines and their parameters. These were asymmetry analysis, including finding the centroid, the lower and upper semi-half-band width and the third moments, factor analysis, numerical band fitting, and stability constant modeling. For the compositions studied evidence for four species is presented: $[InCl(H_2O)_5]^{2+}$, $[InCl_2(H_2O)_4]^{+}$, $[InCl_3(H_2O)_3]$, and $[InCl_4(H_2O)_2]^{-}$. All methods failed to give reproducible stability constants.

Introduction

The indium(III) cation is aquated by six molecules of water in the presence of noncoordinating anions such as perchlorate and nitrate.[1-3] On addition of chloride ion the hexaaquoindium(III) cation undergoes successive substitution to give species of the type $[In(H_2O)_{6-n}Cl_n]^{(3-n)+}$. Many studies of the stability constants of these complexes have been reported.[4] Ferri[5] recently carried out a thorough emf study with $[In^{3+}] \leq 0.015$ M; his data were adequately accounted for in terms of three complexes, viz. $n = 1$, 2, and 3. The stability constants were in good agreement with those obtained from cation exchange studies by Carleson and Irving[6] and Busev and Kanaev.[7] Reports of species with $n = 4$, 5, or 6 are based on meagre evidence, although it is well established that solvent extraction of indium from aqueous hydrohalic acid solutions with oxygenated solvents gives an organic phase containing InX_4^- anions, usually in the form of an associated ion pair.[8,9] Raman spectra are consistent with tetrahedral geometry for this species.[10-13] Hanson and Plane[14] provided evidence for the existence of $InCl_4^-$ in water/methanol solutions, the Raman spectrum of which is different from the only species in aqueous solution which may have the 1:4 ratio of In^{3+}:Cl^-.

The principal feature in the Raman spectrum of aqueous indium chloride solutions is a somewhat asymmetrical, polarized band which shifts from about 311 to 279 cm^{-1} as the chloride-to-indium ratio is increased. Hanson and Plane[14] assigned the contour to $InCl^{2+}$(aq), $InCl_2^+$(aq), and $InCl_4^-$(aq). Woodward and Taylor[12] even suggested $InCl_5^{2-}$ and $InCl_6^{3-}$ ions were being formed but knowledge of the system was then at a rudimentary stage. A variety of thermodynamic and conductance data have recently been published for the aqueous indium chloride system.[15-18] Campbell[15] found that the conductance of a concentrated (13.37 equiv L^{-1}) solution of indium chloride is almost negligible ($\Lambda = 1.04\ \Omega^{-1}\ cm^2\ equiv^{-1}$) and suggested that the highly concentrated solution consists almost entirely of uncharged species such as $InCl_3$.

The qualitative and inconclusive aspects of previous Raman spectral studies and the uncertainties in species identification have motivated the present study.

Powerful new techniques have become available in Raman spectroscopy. Spectral data, recorded in digital format and stored on magnetic tape, can be quantitatively analyzed by a number of procedures. In this study we explore the potential of asymmetry analysis, factor analysis, numerical band fitting, and equilibrium constant fitting to extract information contained in the band envelope concerning the number of species present and their concentrations.

Experimental Section

Thirty-one solutions were prepared in accordance with the mole ratio method;[19] Cl^-/In^{3+} ratios, R, spanned the range 0.48 to 15.9. Stock solutions of concentrated $In(ClO_4)_3 \cdot 11H_2O$ (G. Frederick Smith Chemical Co.) or $InCl_3$ (Cominco Ltd. or J. T. Baker, Analyzed Reagent Grade) were prepared and analyzed for indium by the EDTA titration procedure.[20] Chloride was determined by gravimetric analysis.[21] The specified Cl^-/In^{3+} ratios, R, were obtained by mixing weighed amounts of the stock solutions and standardized HCl and/or $HClO_4$ (the internal intensity standard). Two mole ratio series were prepared: 18 solutions with $[In^{3+}] = 0.635$ M and 13

† Present address: Syncrude Canada Ltd. Research, P.O. Box 5790, Edmonton, Alberta, Canada, T6C 4G3.

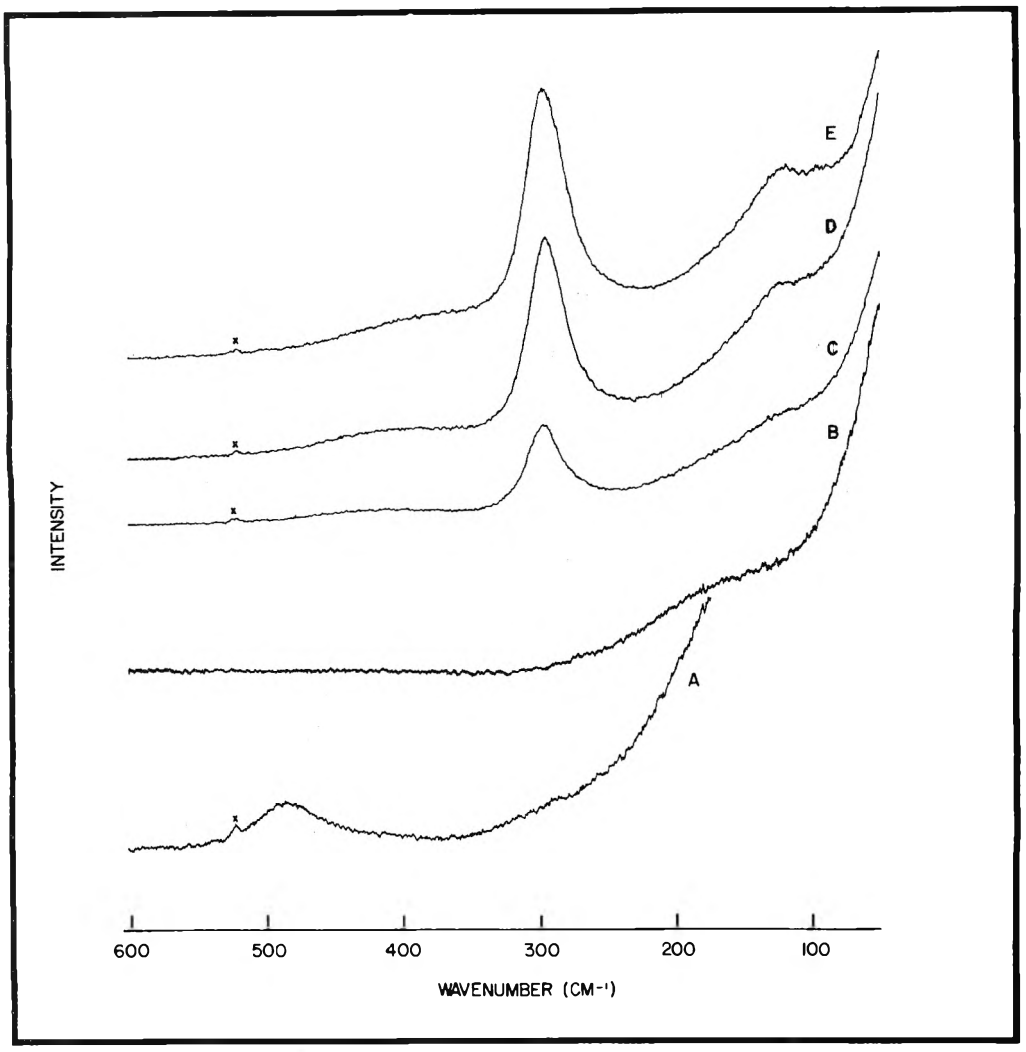

Figure 1. Raman spectra of aqueous $InCl_3$ solutions: (A) Raman spectrum of 1.17 M hexaaquoindium(III) cation in nitric acid media; (B) Raman spectrum of water under the same conditions, the intermolecular band of liquid water is evident; (C) 1.00 M $InCl_3$; (D) 1.96 M $InCl_3$; (E) 3.99 M $InCl_3$. × designates a plasma line.

solutions with $[In^{3+}] = 1.00$ M. Some acidified stoichiometric solutions of $InCl_3/H_2O$ were also studied. Solutions were filtered through Millipore FHLPO 1300 0.100 μm filters prior to spectral measurements.

Raman spectra, excited by the 514.5-nm line of a Spectra-Physics Model 165 argon ion laser, were recorded with a computerized Jarrell-Ash Raman facility described elsewhere.[22] Typically data were collected at 481 points between 170 and 410 cm^{-1} using a 6-cm^{-1} spectral slit width and 1.5 W of laser power. Samples were contained in a glass cell[23] which fits snugly in a copper housing maintained at 25 ± 0.2 °C by means of a Haake water circulator. All samples were allowed approximately 30 min to reach thermal equilibrium before spectra were run. Data were collected in the following sequence: intensity of the 980-cm^{-1} line of ClO_4^- scanned from 870 to 990 cm^{-1}; intensity from the chloro complexes of indium scanned from 170 to 410 cm^{-1}; intensity of the 980-cm^{-1} line of ClO_4^- repeated. A relative intensity $I(\bar{\nu})$ was obtained at each $\bar{\nu}$ from the relation

$$I(\bar{\nu}) = \frac{\text{counts}(\bar{\nu})_{\text{sam}} \times P_{\text{std}}}{\text{mean integrated intensity}_{\text{std}}} \times \frac{[ClO_4^-]}{P_{\text{sam}}}$$

where P is the selected counting period, std refers to the standard, and sam to the sample. Data, stored on magnetic tape, could be plotted for visual inspection.[22] The spectral background, consisting of the Rayleigh wing broadened by scatter from the medium, was fitted with an exponential quadratic function[22] (see Figure 5 of ref 22). This procedure proved to be superior to subtracting scaled intensity from a blank because the Rayleigh wing shape is dependent on solvent structure and this is not identical in blank and sample because solution components cannot be identical. Other procedures used in the quantitative analysis of the baseline-corrected, digitized spectra will be described when they are discussed.

Results and Numerical Analyses

Spectral Features. Typical spectra which illustrate the concentration dependence of Raman bands of acidified, aqueous $InCl_3$ solutions are shown in Figure 1. The hexaaquoindium(III) ion, observed in aqueous solutions of indium nitrate, gives rise to a band at 484 cm^{-1}, Figure 1A. (The bands of the nitrate ion indicate that no inner-sphere indium–nitrate binding occurs under these conditions.) This band is absent from the spectra of the solutions of indium chloride, Figure 1C–E. For the latter, the major features are an intense polarized band at 295 cm^{-1}, a diffuse, polarized band which shifts from about 434 to 378 cm^{-1}, and depolarized intensity centered at about 126 cm^{-1}. To assist in the identification of the constituents which generate these bands, digitized spectra were obtained for 31 solutions with varied Cl^-/In^{3+} ratios. Five of the baseline-corrected spectra for $[In^{3+}] = 1.00$ M and chloride concentrations increasing from 0.50 to 9.80 M are

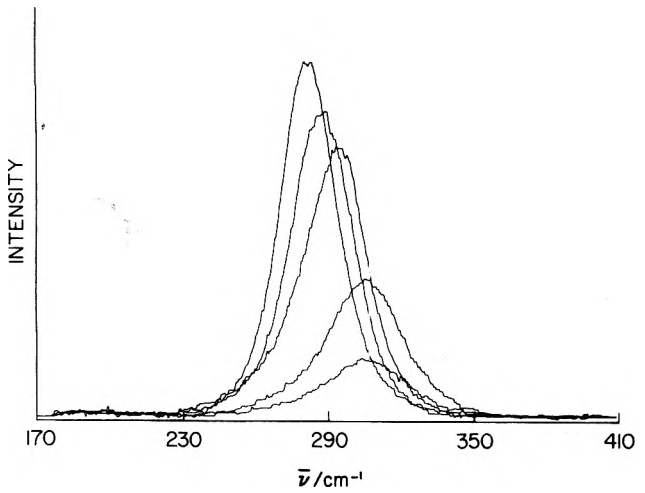

Figure 2. Spectra of solutions with $[In^{3+}] = 1.00$ M and chloride concentration varied from 0.50 to 9.80 M. $[Cl^-]/[In^{3+}]$ of curves (left to right) are 9.75, 7.04, 4.12, 1.02, and 0.50.

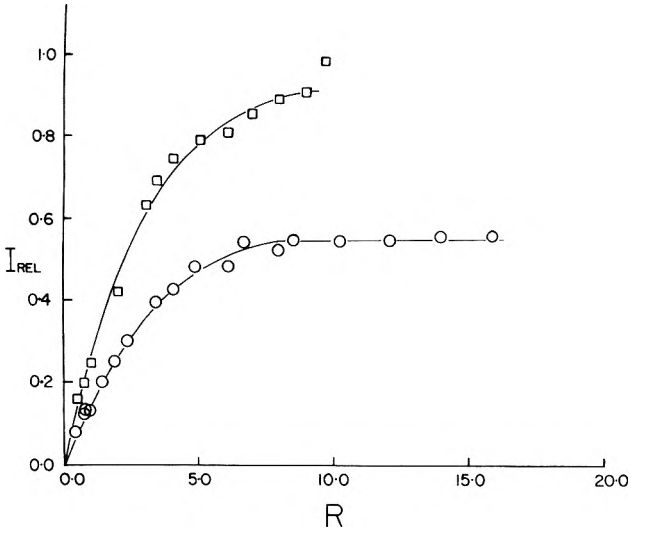

Figure 3. Mole ratio plot of relative intensities against R, the ratio of concentrations of total chloride-to-indium: (O) $[In^{3+}] = 0.635$ M; (□) $[In^{3+}] = 1.00$ M.

shown in Figure 2. Relative integrated band intensities, I_{rel}, obtained with the trapezoidal band area calculation feature of the baseline computer program, are plotted against R in Figure 3 for the two mole ratio series. The intensity change is consistent with the stepwise formation of chloroindium(III) complexes but leveling, which may be consistent with essentially complete conversion to the complex with the highest ligand number, does not occur until $R \simeq 10$. As the ratio R increases the peak maximum $\bar{\nu}_0$ changes from about 311 to 279 cm^{-1} without displaying distinct shoulders (Figure 4). Clearly it is impossible to deduce from a perfunctory examination of these spectra either the number of complexes or their identities. Because asymmetry arises from band overlap the quantification of band asymmetry was considered as one possibly useful method of extracting information hidden in the Raman contours.

Asymmetry Analysis. A computer program developed by Jones et al.[24] was modified to extract the following information: the peak maximum $\bar{\nu}_0$, the centroid $\bar{\nu}_\mu$, the lower and upper semi-half-band widths SHBW ($^1/_2(\Delta\bar{\nu}_{1/2})_L$ and $^1/_2(\Delta\bar{\nu}_{1/2})_U$), the asymmetry ratio, AR, defined as the ratio of the lower to upper SHBW, the difference between peak maximum and centroid, the average SHBW which is equal to one-half of the full width at half-height ($^1/_2$ FWHH), and the incomplete third moments $\mu_3(j)$ at j equal to 2, 3, and 4 average semi-half-band widths from the peak maximum. The data are collected in Table IM.[25] The location of the centroid $\bar{\nu}_\mu$ shown in Figure 4 and plots of $\bar{\nu}_0 - \bar{\nu}_\mu$ against R clearly indicate asymmetry on the low wavenumber side which gives way to asymmetry on the high wavenumber side when $R > 10$ (for $[In^{3+}] = 0.635$ M) or $R > 7.5$ (for $[In^{3+}] = 1$ M). For the 0.635 M series the difference $\bar{\nu}_0 - \bar{\nu}_\mu$ decreases until $R = 1$, then increases to $R = 5$, and decreases thereafter, becoming negative but $\bar{\nu}_0$ does not attain a constant value as anticipated if an ultimate chloro complex is formed. The difference is very sensitive to data quality and the data exhibit scatter. Plots of AR against R exhibit the same general trend, viz. asymmetry alternating from the lower to the upper and back to the lower wavenumber side of $\bar{\nu}_0$. The average semi-half-band width is less sensitive to data quality and for both series of solutions the contour is observed to sharpen until $R \simeq 3.5$, broaden until $R \simeq 5$ to 6, and then continually sharpen (Figure 5). This plot has no absolute reference point to aid interpretation. For this reason the asymmetry quantification was extended to the consideration of incomplete third moments.

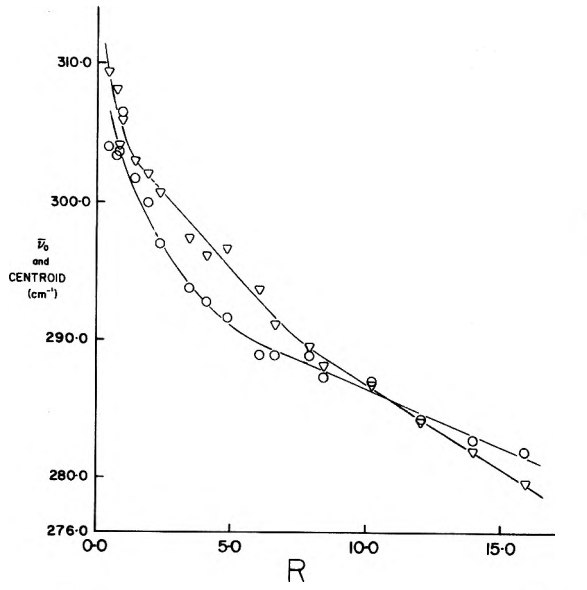

Figure 4. $\bar{\nu}_0$ and $\bar{\nu}_\mu$ vs. R for $[In^{3+}] = 0.635$ M: (O) centroid ($\bar{\nu}_\mu$); (▽) peak maximum ($\bar{\nu}_0$).

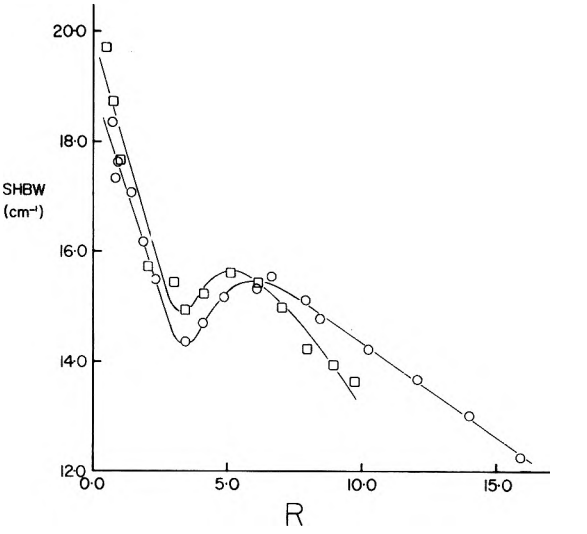

Figure 5. Semi-half-band width vs. R. (O) $[In^{3+}] = 0.635$ M; (□) $[In^{3+}] = 1.00$ M.

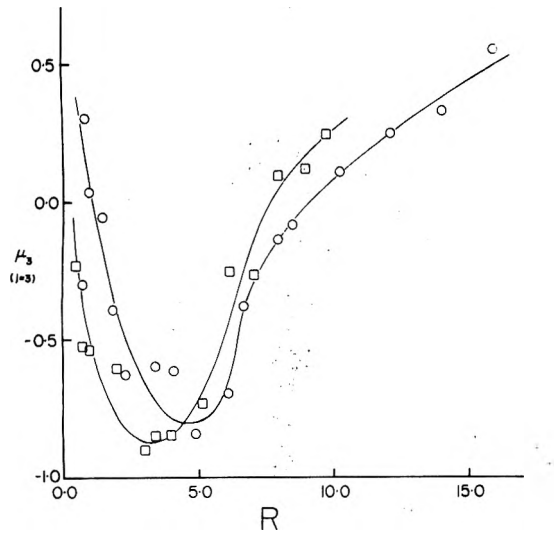

Figure 6. Third moment $\mu_3(j = 3)$ vs. R: (O) $[In^{3+}] = 0.635$ M; (□) $[In^{3+}] = 1.00$ M.

The third moment[24] provides a measure of band asymmetry. Symmetric bands have zero incomplete third moments while asymmetry to high or low wavenumber yields positive or negative incomplete third moments. A plot of $\mu_3(3)$ against R is presented in Figure 6 and is very similar to that of $\mu_3(4)$ against R. The incomplete third moment appears to quantify band asymmetry with sufficient reliability to provide viable assistance in chemical interpretation.

The primary parameter required to understand the above data and the chemistry is the number of constituents (NC) contributing intensity significantly to the overall contour. One method of determining NC is by band resolution. In this method[26] a band shape is selected and NC is taken as the number of bands required to fit the spectrum. As long as the positions of the peaks and the half-band widths do not change appreciably and the overlap is not too severe, this fitting method is successful. However specification of a band shape may create an unnecessary or undesirable dependence in (NC). A separate method is therefore needed for the determination of NC.

Factor Analysis. Factor analysis or principal component analysis (PCA) provides the number of scattering constituents (NC) for a series of spectra by an independent method. Rather than assuming a band shape, factor analysis is based upon standard theorems of linear algebra. When a set of constitutive properties is measured for each of a series of solutions, PCA is applicable to solve for NC.[27,28]

For Raman spectral measurements an expression analogous to Beer's law is assumed to have the form

$$I_{ij} = \sum_{k}^{NC} J_{ik} C_{kj} \qquad (1)$$

where I_{ij} is the Raman intensity at the ith wavenumber in the jth solution, J_{ik} is the molar intensity of the kth species at the ith wavenumber, and C_{kj} is the concentration of the kth species in the jth solution. In matrix notation, eq 1 becomes

$$\mathbf{I} = \mathbf{JC} \qquad (2)$$

where the dimensions are as follows: **I** is NW × NS for the Raman intensity matrix; **J** is NW × NC for the molar intensity matrix; and **C** is NC × NS for the concentration matrix. NW is the number of wavenumbers digitized, NS is the number of solutions studied, and NC is the number of scattering species. Under the experimental conditions NW > NC and NS > NC, and provided both the spectrum of one of the individual constituents is not a linear combination of the spectra of the other constituents and the concentration of one or more species cannot be expressed as a linear combination of the concentrations of the other constituents for all experiments performed, then rank (**I**) = NC. Thus the number of scattering components is given by the rank of the matrix **I**.

TABLE I: PCA Results for In^{3+}-Cl^- Solutions

$[Cl^-]/[In^{3+}]$ range	No. of bands inferred	No. of samples in range
$[In^{3+}] = 0.635$ M		
0 → 2.36	2	7
0 → 4.89	3	11
3.46 → 15.91	3	11
0 → 15.91	4	18
$[In^{3+}] = 1.00$ M		
0 → 2.05	2	4
0 → 5.13	3	8
3.46 → 9.75	3	8
0 → 9.75	4	13
Combined data		
0 → 15.91	4	31
6.68 → 15.91	3	11
7.95 → 15.91	2(3?)	9

Currently the method of determining the rank of **I** is to examine the eigenvalues and eigenvectors of the second moment matrix,[29] $\mathbf{Q} = \bar{\mathbf{I}}\mathbf{I}$, where $\bar{\mathbf{I}}$ is the transpose of **I** and the matrix **Q** has the same rank as **I**. The number of statistically nonzero eigenvalues equals NC. Four statistical criteria have been described[27] for selecting the eigenvalues which do not arise from experimental error and computational procedures.

Factor analysis applied to all 31 spectra indicated the existence of four species. The first four eigenvalues are much larger than the square root of the variance[30] and the fifth is comparable in magnitude (Table IIM[25]). The square root of the number of photon counts was used for the uncertainty in Raman intensity for each digitized point. Comparison of the residual standard deviations[31,32] support the conclusion that NC is 4. Table IIIM[25] summarizes the results of a calculation using from 1 up to 31 of the eigenvectors of **Q** to regenerate the intensity matrix **I**. Each row of this table records χ_m^2 and the distribution of misfits between the experimental and regenerated Raman intensity data as a function of the estimated error in each of the 7781 data points of the intensity matrix.[27,30] For four eigenvectors, only 441 data points are outside of four standard deviations and thus four appears to be the minimum number for NC. Factor analysis was next used to isolate possible ranges of R where there are less than four components. The results are summarized in Table I. These results now permit further interpretation of the SHBW and third moment plots.

Interpretation of SHBW and Third Moment Plots. The average SHBW will be smallest if one component predominates but will increase when a second or third component band is overlapping it. Similar arguments may be advanced to rationalize the incomplete third moment changes with concentration ratio. The third moment plots provide a valuable absolute reference point which the SHBW plots do not have, namely, the symmetric shape condition $\mu_3 = 0.0$.

The SHBW plot (Figure 5) has three slopes and each slope can be attributed to contributions from at least two

species so the whole R range could encompass six species. However these slope changes are linked by maxima and minima and consequently there must be species common to slopes 1 and 2 as well as 2 and 3. Therefore the minimum number of components to rationalize the SHBW trends is four. This conclusion agrees with the PCA results discussed earlier.

The third moment plot (Figure 6) can also be used to argue for the presence of four species. To have positive μ_3 as for $R < 1.5$, two species must exist and as μ_3 changes sign after $R = 1.5$, the second species becomes the more prominent; possibly a third species is appearing as the curve begins to minimize about $R = 2.5$. At about $R = 5.0$ μ_3 begins to become less negative indicating the increasing contribution from a third species.

The contribution from the third species increases up to $R = 9.0$ where essentially a symmetric band exists with possible minor contributions from the second and forth species. The third moment becomes positive indicating the appearance of a fourth component. This positive μ_3 increases as R increases; one would expect this indication of asymmetry to plateau and eventually return to zero (i.e., one species) if the R range were increased past the limits studied here, unless a fifth species is formed.

Estimates of the positions of the peak maxima for the first three species may be obtained using the third moment plot (Figure 6, which gives the ranges in which each species predominates) and the peak maximum plot (Figure 4) for the series with $[In^{3+}] = 0.635$ M. For the first species a value of 311 ± 2 cm^{-1} is obtained by taking the peak maximum plot to infinite dilution. The position for the second species is found to be 300 ± 2 cm^{-1} using the R range of 1.0–2.5. Similarly for the third species, a frequency of 289 ± 2 cm^{-1} was obtained using an R range of 7–10. The band position for the fourth species is indeterminant at present as no symmetric band profile was observed for $10 < R < 15.9$. For the series with more concentrated indium, similar positions were estimated.

There exists one disagreement between the conclusions from the PCA method and the earlier conclusions. The PCA method suggests two components below $R = 2.36$ while the trends in band parameters, discussed heretofore, predicted three. This discrepancy is possibly due to an accidental linearity in the intensities between two of the species in this region. PCA cannot distinguish species whose concentrations are directly proportional. The rest of the PCA results agree with the interpretations given for previous plots.

Numerical Band Fitting. Visual-aided curve fitting with the program CURVER[26] using the additional information provided by PCA and asymmetry analysis gave unsatisfactory results because of severe band overlap. Numerical band fitting was applied in an attempt to obtain meaningful trends; the program used is an adaptation of the one developed by Pitha and Jones[33] and subsequently modified by Murphy and Bernstein[34] to permit constraint relationships among the band parameters. In the fitting procedure a mathematical product function, 50% Gaussian and 50% Lorentzian, was used as the model curve.[24] Positions of the first three bands were fixed at values given above and the fourth band was found to occur consistently around 279 ± 2 cm^{-1}. This position of the fourth band is consistent with the approximation of equal intervals between the bands of successive complexes: cf. thallium chloride.[35]

Fixing the band positions in the computer program BNDFT gave lines with consistent half-band widths of 40 ± 2, 23 ± 2, 32 ± 2, and 22 ± 2 cm^{-1} for the 311-, 300-, 289-, and 279-cm^{-1} bands, respectively.

A two band fit was reasonable for R values from 4.90 to 15.91. Below this range, difficulty in maintaining the 300-cm^{-1} FWHH at 23 cm^{-1} indicated the possibility that a two band fit was insufficient. Subsequently a three band fit was attempted on all samples with $R < 8.48$, holding the positions and half-band widths fixed. Over the whole composition range and for particular subranges the numbers of components utilized in BNDFT agree reasonably well with the number of components predicted by PCA. These BNDFT intensities are presented in Table IVM[25] and illustrated in Figures 7 and 8. Figure 7 displays the goodness of fit obtained from BNDFT and ERROREST[36] computer programs for a few of the spectra with $[In^{3+}] = 0.635$ M. For plots b and c of Figure 7 the misfit is probably a function of the model curve chosen and of the least-squares method of fitting used in BNDFT. Figure 8 displays the contribution from each species, the summation of the contributions, and the original total relative intensity taken from Figure 3. It can be seen that the total intensity is adequately described in terms of the sum of the intensities of the component bands.

A Model for the Significant Equilibria. Before stability constant programs can be applied to the information derived from BNDFT, asymmetry, and PCA analyses a specific model must be chosen to account for the data. For indium and chloride in water, a stepwise equilibrium is presumed to occur:

$$In(H_2O)_6^{3+} + xCl^- = InCl_x(H_2O)_{6-x}^{(3-x)+} + xH_2O$$

Evidence for the hexaaquoindium(III) cation and mixed haloaquoindium(III) species was presented in the Introduction. There is little chance of nonaquated species being formed in the aqueous media as In^{3+} has a high affinity for hard donor atoms such as the oxygen of H_2O.[9] Four species that could account for Figure 8 are $[InCl(H_2O)_5]^{2+}$, $[InCl_2(H_2O)_4]^+$, $[InCl_3(H_2O)_3]$, and $[InCl_4(H_2O)_2]^-$. From the literature, the evidence for the first three species is strong. The stepwise progression of band positions is similar to that observed from analogous species in thallium chloride solutions.[35] If species such as $[InCl_5H_2O]^{2-}$ and $[InCl_6]^{3-}$ are formed in lieu of $[InCl_4(H_2O)_2]^-$ one would expect a greater band shift between $InCl_3(H_2O)_3$ and the subsequent species than is observed in this study (cf. ref 35).

Referring to Figure 8, the mole ratio curve begins to level after about $R = 10$. The plateau could imply that the total number of bonds formed is remaining constant. However the fourth equilibrium

$$InCl_3(H_2O)_3 + Cl^- = [InCl_4(H_2O)_2]^- + H_2O$$

indicates that one more In–Cl bond is formed and thus one would expect the fourth species to generate more intensity than the third. The third species, however, has a FWHH = 32 ± 2 cm^{-1} whereas the fourth species has a FWHH = 22 ± 2 cm^{-1}. The intensity expected from the formation of the additional In–Cl bond is offset by the narrowness of the band of the new species. This fortuitous cancellation is probably the main cause of the leveling of the relative intensity plot.

Stability Constant Calculations. In principle it should be possible to apply to Raman intensity data programs such as KEQUIL,[31] SCOGS,[37] SQUAD,[38] and KSEEK[39] which have been developed to handle absorbance measurements. These programs are capable of evaluating stability constants, molar intensities, and concentrations of all species. Attempts to apply these programs to the data described above failed. The correlation coefficients between suc-

TABLE II: GAUSSZ Results Obtained from BNDFT Data

Model	J_3	$J_3:J_2:J_1$	K_1	K_2	K_3	Variance
1	0.84	3:2:1	27.40	0.16	12.55	0.059 21
2	0.84	3:1.8:0.9	139.84	3.05	10.61	0.068 94
3	0.84	3:2.2:1.1	11.64	0.083	17.49	0.055 93
4[a]	0.84	3:2:1	27.39	0.16	12.54	0.059 20
5	0.90	3:2:1	12.10	0.65	1.87	0.062 48
6	0.90	3:1.8:0.9	38.06	0.79	2.23	0.102 83
7	0.90	3:2.2:1.1	6.57	0.48	1.90	0.050 15
8[b]			380.19	18.20	2.29	

[a] Different set of guesses chosen for input β's. [b] Reference 5.

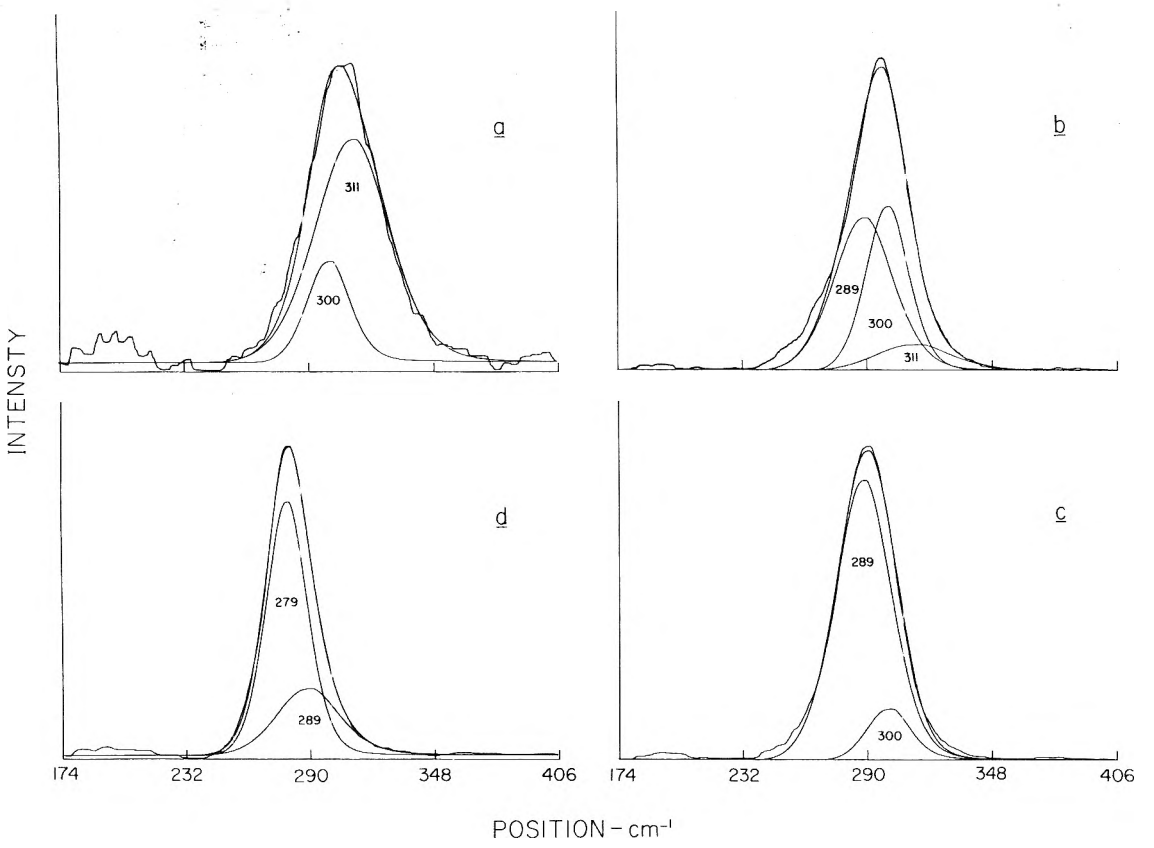

Figure 7. Display of the goodness of the fit as obtained from BNDFT for $[In^{3+}] = 0.635$ M. R values for the spectra are (a) 0.48, (b) 3.46, (c) 7.95, and (d) 15.91.

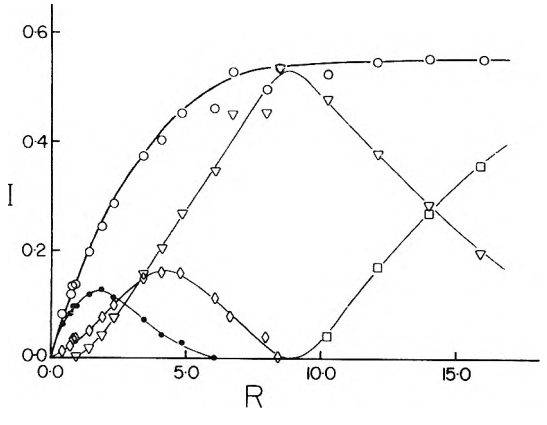

Figure 8. BNDFT integrated intensities vs. R: (O) total band intensity from BNDFT; (—) total experimental band intensity; (●) 311-cm^{-1} band intensity; (◇) 300-cm^{-1} band intensity; (▽) 289-cm^{-1} band intensity; (□) 279-cm^{-1} band intensity.

cessive equilibrium constants were large. Various composition regions were utilized in the hope of isolating the stability constants for specific species but reasonable values were not generated. The limited accuracy of the data and the very severe band overlap are probably the major factors responsible for the failure of the computer programs to give reproducible stability constants.

The above programs use peak heights in the calculations. In a final attempt to obtain stability constants, the band areas from BNDFT were used to generate $\bar{n}$ (average number of ligands bound) and C_F (free ligand) data for the computer program GAUSSZ.[40] The molar scattering coefficient (J) must be determined before the calculation can proceed. At about $R = 8.5$ of Figure 8, only one species appears to contribute intensity and this is the third. Its molar intensity, J_3, must have a minimum value given by I_3/C_3 where I_3 is considered to be the integrated intensity of the band when $R = 8.5$ and C_3 is the concentration of the third species which must be less than the total indium concentration ($C_3 \leq 0.635$ M); thus $J_3 \geq 0.84$. If the In^{3+}–Cl^- equilibria are stepwise then one can assume J_1 and J_2 are simple multiples of J_3 ±10%. The $\bar{n}$, C_F, and J_i values were placed in the GAUSSZ program to obtain equilibrium constants. The program converged with reasonable variance but the different estimates of J gave significantly different values of K_i, as listed in Table II. In contrast to the constants obtained by Ferri[5] the BNDFT/GAUSSZ results are not stepwise and are much

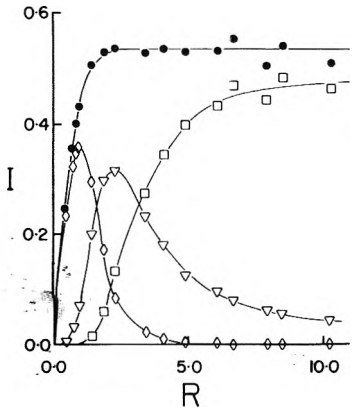

Figure 9. Calculated Raman intensities vs. R, as obtained from SQUAD using log β_1 = 2.54, log β_2 = 3.84, and log β_3 = 4.20: (●) total intensity; (◇) $InCl^{2+}$ species intensity; (▽) $InCl_2^+$ species intensity; (□) $InCl_3$ species intensity.

smaller. With J_3 = 0.90 a comparable K_3 value is obained but the K_1 and K_2 values are an order of magnitude smaller. Inability of GAUSSZ to generate stepwise β's for the assumed values of J indicates that this method is also unsuccessful in giving reliable stability constants.

To ascertain the consequences of constants with magnitudes equal to those of Ferri's β's[5] a back calculation was performed with the Raman intensity version of SQUAD.[38] SQUAD provided individual species concentrations at each R value as well as the peak height scattering coefficients at each wavenumber (J_h). These J_h values were converted to an area by a trapazoidal area calculation to give an integrated J for each species. The J_i values obtained from the back calculation are 0.22, 0.32, and 0.83 for i = 1, 2, and 3, respectively. The value 0.83 agrees well with the estimate referred to earlier. The other values are much lower than the 1:2:3 ratio assumed. The relative intensity for each species was calculated using the relation $I = JC$. The results are displayed by Figure 9. The total intensity curve of Figure 8 clearly requires smaller stability constants than the total intensity curve of Figure 9. The constants obtained by Ferri cannot reproduce the Raman observations. They were obtained by experiments performed with much more dilute solutions. It is probable that they do not describe the equilibria existing in more concentrated solutions of low water activity, especially when activity coefficients are neglected in the calculations, although agreement between Raman and emf measured β's was observed for the Cd^{2+}/NO_2^- system.[41] Constancy of concentration quotients determined by Raman intensity analyses was noted by Nixon and Plane[42] and has been observed many times since then (e.g., ref 40 and 41). Uncertainty in J_i also contributes significantly to the uncertainty in the constituent concentrations, C_1, C_2, C_3, but it should be noted that the total intensity profile is independent of these assumed values.

Discussion

In this study, factor analysis indicated that four species exist in the R range 0.48–15.91. Asymmetry analysis and third moment data also predicted four components. Numerical band fitting required four Gaussian–Lorentzian bands to fit the recorded contours. Thus qualitatively, the spectra are adequately assigned to four species. The numerical procedures have indeed been an aid in interpreting the band profile but this particular system taxes the capabilities of these to their limit. It remains a disappointment that stability constants could not be calculated from the data. It appears that in any future Raman study of this system the effect of controlling the ionic strength should be investigated. From the experience gained in this study a word of caution is in order for those who, after obtaining a Raman spectrum as in Figure 1, feel they have obtained the evidence for proposing the existence of a single species and its identity.

The $\bar{\nu}_s$ (In–Cl stretch) bands of the complexes identified in this study are now compared with results from previous studies. For both $[InCl(H_2O)_5]^{2+}$ and $[InCl_2(H_2O)_4]^+$ we anticipate only one Raman active vibration (neglecting the water molecules). Values of 311 and 300 cm^{-1} for these species are in accord with the results of Hanson and Plane.[14] Values of 289 and 279 cm^{-1} for $InCl_3(H_2O)_3$ and $[InCl_4(H_2O)_2]^-$, respectively, are a reasonable progression of frequencies for a reasonable progression of species. Indium appears to preserve its octahedral coordination in the aqueous medium. For the tetrahedral species $InCl_4^-$, characterized in ether,[12] molten salts,[43,44] and solid,[45] $\bar{\nu}_s$ occurs at about 319 cm^{-1} and thus it is not present in the aqueous medium. In the solid phase $[InCl_4(H_2O)_2]^-$ has two water molecules adjacent to each other.[46] Infrared lines reported for this crystal do not correspond with the Raman frequencies reported above. Possibly the D_{4h} symmetry is adopted in aqueous solution.

The alternative species In_2Cl_6 for our fourth complex would be consistent with the plateau of Figures 2 and 6. However a strong 354-cm^{-1} line has been ascribed to it in melts[43] and 368 cm^{-1} in the gas phase.[47] Thus we consider the assignment to $[InCl_4(H_2O)_2]^-$ to be more plausible in aqueous media. In the solid state $[InCl_5]^{2-}$ vibrates at 294 cm^{-1} [48,49] but this frequency is lowered by addition of water to the coordination sphere to 280 cm^{-1} for $[InCl_5(H_2O)]^{2-}$.[49] We anticipate that in an aqueous medium this frequency would be still lower. We do not rule out the possible existence of this species in aqueous solutions of very high R value. As can be seen in Figures 4–6 the band parameters have not attained constant values at the highest R values of this study but our PCA results indicate that the probability that another species exists in this composition range is marginally outside of our confidence limits. Woodward and Taylor observed a frequency of 275 cm^{-1} from an indium chloride solution saturated with HCl;[12] they assigned it to $InCl_6^{3-}$. In the solid state this species is thought to generate a 275-cm^{-1} line.[50,51] Clearly the possible close spacing of the lines from the several species with coordination number >4 prevents a clear resolution of the problem of identification by vibrational spectroscopy.

With this background an interpretation of the stoichiometric solutions (Figure 1) is suggested. The position of the most intense band (295 cm^{-1}) falls between the positions attributed to $[InCl_2(H_2O)_4]^+$ and $[InCl_3(H_2O)_3]$ and its lower SHBW is greater than the upper SHBW. Thus we conclude that these solutions contain the first three complexes and that as the activity of water decreases the higher complexes are favored. The presence of water in the first coordination sphere is clearly revealed by the broad polarized band at ca. 378 cm^{-1}. The downward shift (from 484 cm^{-1} for no Cl^- in the first coordination sphere to 378 cm^{-1} for three Cl^- ions) is consistent with a weakening of the In^{3+}–H_2O bonds concomitant with the formation of In^{3+}–Cl^- bonds and the increasing FWHH (60 to 118 cm^{-1}) is indicative of an increasing exchange rate with bulk water. The 126-cm^{-1} intensity, which has an estimated 48 cm^{-1} FWHH, is attributed to one or more deformation modes of the highest complex. This interpretation adequately accounts for the low conductance observed by Campbell[15] for a solution of composition similar to that which generates Figure 1E. At this high

concentration the stoichiometric solution essentially contains $[InCl_3(H_2O)_3]$ molecules and only a low population of charged species. Recently Campbell[18] calculated a K value for:

$$InCl_2^+ + Cl^- = InCl_3$$

of about 100 from conductance data. In comparison to the literature and our estimates his K value is too large. The derivation of the K from consideration of only one equilibrium and the use of conductance data for concentrated solutions, for which there is still no adequate theoretical link to stability constants, makes his K value unacceptable.

Acknowledgment. This work was supported by the National Research Council of Canada. The authors express thanks to Professor A. N. Campbell, who first suggested a reinvestigation of the $InCl_3$ system, for helpful discussion, Mr. H. E. Hirsch, Cominco Ltd., Trail, B.C. for providing a sample of $InCl_3$, and R. N. Jones, W. F. Murphy, and H. J. Berstein for providing copies of their computer programs.

Supplementary Material Available: Tables IM, IIM, IIIM, and IVM containing asymmetry analysis data, results of factor analysis, a table of intensity misfits, and normalized intensity BNDFT results (5 pages). Ordering information is available on any current masthead page.

References and Notes

(1) A. Fratiello, R. E. Lee, V. M. Nishida, and R. E. Schuster, *J. Chem. Phys.*, **48**, 3705 (1968).
(2) T. H. Cannon and R. E. Richards, *Trans. Faraday Soc.*, **62**, 1378 (1966).
(3) A. Fratiello, D. D. Davis, S. Peak, and R. R. Schuster, *Incrg. Chem.*, **10**, 1627 (1971).
(4) L. G. Sillen and A. E. Martell, *Chem. Soc., Spec. Publ.*, **No. 17** (1964); **No. 25** (1971).
(5) D. Ferri, *Acta Chem. Scand.*, **26**, 733 (1972).
(6) B. G. F. Carleson and H. Irving, *J. Chem. Soc.*, 4390 (1954).
(7) A. I. Busev and N. A. Kanaev, *Vestn. Mosk. Univ., Ser. Mat.*, **1**, 135 (1959).
(8) H. M. Irving and F. J. C. Rossotti, *J. Chem. Soc.*, 1927, 1938, 1956 (1955).
(9) A. J. Carty and D. G. Tuck, *Prog. Inorg. Chem.*, **19**, 243 (1975).
(10) L. A. Woodward and P. T. Bill, *J. Chem. Soc.*, 1699 (1955).
(11) L. A. Woodward and G. H. Singer, *J. Chem. Soc.*, 716 (1958).
(12) L. A. Woodward and M. J. Taylor, *J. Chem. Soc.*, 4473 (1960).
(13) P. Dobud, D. Sutton, and D. G. Tuck, *Can. J. Chem.*, **48**, 2290 (1970).
(14) M. P. Hanson and R. A. Plane, *Inorg. Chem.*, **8**, 746 (1969).
(15) A. N. Campbell, *Can. J. Chem.*, **51**, 3006 (1973).
(16) A. N. Campbell, E. M. Kartzmark, and O. N. Bhatnagar, *Can. J. Chem.*, **52**, 1954 (1974).
(17) E. M. Kartzmark, *Can. J. Chem.*, **52**, 3459 (1974).
(18) A. N. Campbell, *Can. J. Chem.*, **53**, 1761 (1975).
(19) M. T. Beck, "Chemistry of Complex Equilibria", Van Nostrand-Reinhold, London, England, 1970, p 86 *ff.*
(20) J. Kinnumen and B. Wennerstrand, *Chem. Anal.*, **46**, 92 (1957).
(21) R. B. Fisher and D. G. Peters, "Quantitative Chemical Analysis", 3rd ed, W. B. Saunders, Philadelphia, Pa., 1968, pp 195–197.
(22) J. T. Bulmer, D. E. Irish, F. Grossman, G. Herriot, M. Tseng, and A. J. Weerheim, *Appl. Spectrosc.*, **29**, 506 (1975).
(23) D. E. Irish, T. Jarv, and O. Puzic, *Appl. Spectrosc.*, in press.
(24) R. N. Jones, K. S. Seshadri, N. B. W. Jonathan, and J. W. Hopkins, *Can. J. Chem.*, **41**, 750 (1963).
(25) See paragraph at end of text regarding supplementary material.
(26) A. R. Davis, D. E. Irish, R. B. Roden, and A. J. Weerheim, *Appl. Spectrosc.*, **36**, 384 (1972).
(27) J. T. Bulmer and H. F. Shurvell, *J. Phys. Chem.*, **77**, 256 (1973).
(28) J. T. Bulmer and H. F. Shurvell, *J. Phys. Chem.*, **77**, 2085 (1973).
(29) J. L. Simmonds, *J. Opt. Soc. Am.*, **53**, 968 (1963).
(30) Z. Z. Hugus and A. A. El-Awady, *J. Phys. Chem.*, **75**, 2954 (1971).
(31) J. J. Kankare, *Anal. Chem.*, **42**, 1322 (1970).
(32) G. Wernimont, *Anal. Chem.*, **39**, 554 (1967).
(33) J. Pitha and R. N. Jones, *Can. J. Chem.*, **44**, 3031 (1966); **45**, 2347 (1967); "Optimization Methods for Fitting Curves to Infrared Band Envelopes", NRC Bulletin No. 12, National Research Council of Canada, Ottawa, 1968.
(34) W. F. Murphy and H. J. Bernstein, *J. Phys. Chem.*, **76**, 1147 (1972).
(35) T. G. Spiro, *Inorg. Chem.*, **4**, 731 (1965).
(36) J. T. Bulmer, Ph.D. Thesis, Queen's University, Kingston, Ontario, Canada, 1973.
(37) I. G. Sayce, *Talanta*, **15**, 1397 (1968).
(38) D. J. Leggett and W. A. E. McBryde, *Anal. Chem.*, **47**, 1065 (1975).
(39) P. J. Burchill and J. A. McRae, *Aust. J. Chem.*, **24**, 187 (1971).
(40) D. E. Irish, T. G. Chang, J. T. Bulmer, and P. J. Gleeson, *J. Solution Chem.*, **4**, 969 (1975).
(41) D. E. Irish and R. V. Thorpe, *Can. J. Chem.*, **53**, 1414 (1975).
(42) J. Nixon and R. A. Plane, *J. Am. Chem. Soc.*, **84**, 4445 (1962).
(43) H. A. Oye, E. Rytter, and P. Klaeboe, *J. Inorg. Nucl. Chem.*, **36**, 1925 (1974).
(44) J. H. R. Clarke and R. E. Hester, *J. Chem. Phys.*, **50**, 3106 (1969).
(45) J. Trotter, F. W. B. Einstein, and D. G. Tuck, *Acta Crystallogr., Sect. B*, **25**, 603 (1969).
(46) M. L. Ziegler, H. U. Schlimper, B. Nuber, J. Weiss, and G. Ertel, *Z. Anorg. Allg. Chem.*, **415**, 193 (1975).
(47) I. R. Beattie and J. R. Horder, *J. Chem. Soc. A*, 2655 (1969).
(48) I. Wharf and D. F. Shiver, *Chem. Commun.*, 526 (1968).
(49) D. M. Adams and D. C. Newton, *J. Chem. Soc., Dalton Trans.*, 681 (1972).
(50) T. Barrowcliffe, I. R. Beattie, P. Day, and K. Livingston, *J. Chem. Soc. A*, 1810 (1967).
(51) D. M. Adams and D. M. Morris, *J. Chem. Soc. A*, 694 (1968).

Spectroelectrochemical Investigations of the Reduction of Benzaldehyde and *p*-Cyano- and *p*-Phenylbenzaldehyde in Sulfolane

N. R. Armstrong,* Rod K. Quinn,

Sandia Laboratories, Albuquerque, New Mexico 87115

and N. E. Vanderborgh†

Department of Chemistry, University of New Mexico, Albuquerque, New Mexico 87131 *(Received October 25, 1976)*

Publication costs assisted by Sandia Laboratories

Spectroelectrochemical investigations are presented for the reduction of benzaldehyde and *p*-cyano- and *p*-phenylbenzaldehyde in the solvent sulfolane. Two reduction intermediates were observed for the *p*-cyanobenzaldehyde reduction. One intermediate was the radical anion which was consumed in a dimerization reaction, $k_2 = 85$–$88\ M^{-1}\ s^{-1}$. The other intermediate was the electrochemically inactive complex between the radical anion and the unreduced parent. The verification of this complexation clarifies previous voltammetric studies of this type of reduction mechanism.

We report spectroelectrochemical studies recently completed for the reduction of benzaldehyde and *p*-phenyl- and *p*-cyanobenzaldehyde in the solvent sulfolane. These studies complement recently reported spectroelectrochemical studies of nitrobenzene and *p*-nitrobenzaldehyde reductions in this solvent.[1] Cyclic voltammetric and ring-disk voltammetric studies of benzaldehyde and para-substituted benzaldehyde reductions in sulfolane have also been reported.[2,3] A distinct retardation of the dimerization of the radical anion species in sulfolane as compared to other solvents was demonstrated.[4,5] The dimerization follows the initial one-electron reduction step of most benzaldehydes in an aprotic environment.[1-3]

$$\mathrm{Ph{-}CHO} \underset{-e^-}{\overset{+e^-}{\rightleftharpoons}} \mathrm{Ph{-}CHO^{-}\cdot} \xrightarrow{k_2} \mathrm{Ph{-}\underset{OH}{CH}{-}\underset{OH}{CH}{-}Ph}$$

The spectroelectrochemical technique was well suited to the study of the decay of the radical anions of several para-substituted benzaldehyde compounds. Strong visible absorbances were observed for the radical anion species. Certain mechanistic information was also observed by this technique which was not apparent in other electrochemical experiments. Digital simulation techniqes were applied to the spectroelectrochemical data to yield rate coefficients for decay of the *p*-cyanobenzaldehyde and *p*-phenylbenzaldehyde reduction intermediates.

Experimental Section

Main experimental details have been described previously.[1-3] Chemicals were purified using either column chromatography and distillation or by recrystallization.[1-3]

The Teflon spectroelectrochemical cell had a total volume of 2 mL. Geometric area of the electrode was 0.308 cm^2. Electrodes were 30 nm, semitransparent, vapor deposited platinum films on quartz substrates (OTE). The cell was positioned, along with a matching reference cell, in the sample and reference compartments of a spectrophotometer where the spectra of the reduction intermediates were recorded.[1] Selected wavelength regions of the visible spectrum were monitored following the application of a potential step applied to the working electrode to promote diffusion-controlled electrolysis of the parent species. Point-by-point spectra were reconstructed by repeating these measurements at different wavelengths.

Various potential perturbations were applied to the working electrode while the absorbance at a single wavelength was monitored. In the cyclic voltammetric experiments slowly varying triangular waveforms were applied ($dV/dt = 33.8$ mV/s). Potential-step experiments were also conducted. Here the potential of the working electrode was stepped beyond the cyclic voltammetric peak potential and the absorbance monitored as a function of time. In certain experiments the potentiostat was disconnected after a known electrolysis time, and the optical signal after this open circuit relaxation monitored.

Results and Discussion

The absorbance spectra for the one-electron reduction intermediates of *p*-cyanobenzaldehyde (PCNB) and *p*-phenylbenzaldehyde (PPhB) are shown in Figure 1. These spectra were taken 15 s after initiation of electrolysis, and are similar to those observed at shorter electrolysis times, differing only in absolute magnitude. For *p*-cyanobenzaldehyde, two sets of doublet bands were observed at 360, 370 nm and 500, 530 nm. For *p*-phenylbenzaldehyde, a broad doublet centered at 369 and 403 nm was observed. A weak absorbance was observed for the reduction intermediate of benzaldehyde at wavelengths below 350 nm. The intensity of this absorbance, however, was not sufficient, even at high benzaldehyde concentrations, to positively identify an absorbance maximum.

Absorbance vs. (electrolysis time)$^{1/2}$ plots were obtained for each wavelength maxima of $PCNB^{-}\cdot$ and $PPhB^{-}\cdot$ by stepping the OTE potential beyond the reduction peak potential.[6] For $PCNB^{-}\cdot$ the $A/t^{1/2}$ plots of both band maxima were nonlinear for electrolysis times up to 15 s, confirming the presence of a following chemical step consuming the $PCNB^{-}\cdot$ species. Previous voltammetric studies in sulfolane have indicated that this following chemical step consists of dimerization of the radical anion with a rate coefficient, k_2, of between 0.5–$1.5 \times 10^2\ M^{-1}\ s^{-1}$.[2,3] An extinction coefficient for each $PCNB^{-}\cdot$ doublet was estimated from the zero time extrapolation of the $A/t^{1/2}$ plots adjusted for the digital simulation conditions below.[6] These were $\epsilon_{360,370} = 2.1$–$2.7 \times 10^4\ M^{-1}\ cm^{-1}$ and

* Author to whom correspondence should be addressed. Present address: Department of Chemistry, Michigan State University, East Lansing, Mich. 48824.

† Present address: Los Alamos Scientific Laboratories, Los Alamos, N. Mex. 87544.

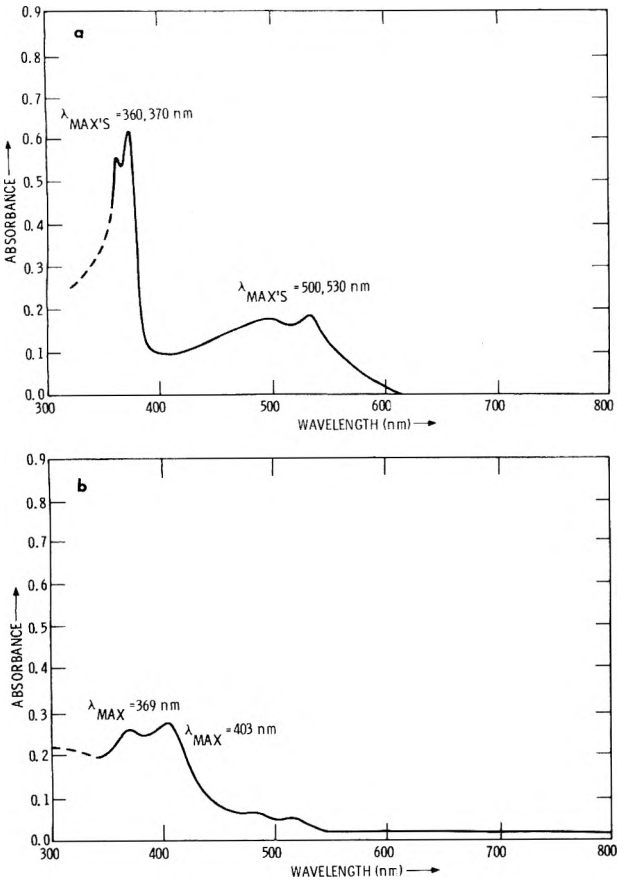

Figure 1. (a) Absorption spectrum of the *p*-cyanobenzaldehyde reduction intermediate. (b) Absorption spectrum of the *p*-phenylbenzaldehyde reduction intermediate. The potential of the OTE was stepped past the reduction peak potential and the absorbances were measured 15 s after initiation of electrolysis.

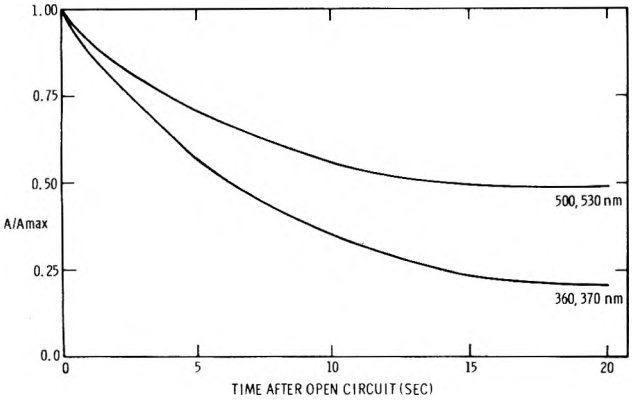

Figure 2. A/A_{max} vs. time for the species responsible for the 500,530 nm and 360,370 nm bands. The potential of the OTE was stepped past the reduction peak potential, electrolysis proceeded for 20 s, and then the flow of current ceased. Absorbances are plotted as a function of time after cessation of current and are normalized to their maximum values.

$\epsilon_{500,530} = 5.6\text{–}6.9 \times 10^3\ M^{-1}\ cm^{-1}$.

Potential step followed by open-circuit-relaxation experiments (6.7) were conducted for the PCNB reduction. The absorbance of each doublet was observed to decay as a function of time after ceasing electrolysis. The normalized absorbance behavior (A/A_{max}) following open circuit for the 500, 530 nm and 360–370 nm doublets was quite different (Figure 2). Differing stabilities of the species representing the two major absorbance bands seem to be indicated. If the two absorbance bands were from the same species, then the rates at which the normalized absorbance decayed should have been equal.

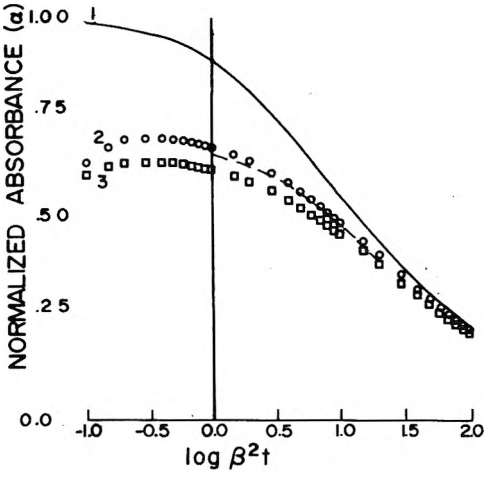

Figure 3. Digitally simulated working curves for the intermediate involved in dimerization. Normalized absorbance function (α) plotted vs. the logarithm of the dimensionless kinetic parameter (log $\beta^2 t$): case 1, no complexation, $K_{eq}'C_{bulk} = 0$; case 2, parent-ion complexation, $K_{eq}'C_{bulk} = 5$; case 3, parent-ion complexation, $K_{eq}'C_{bulk} = 10$. The dotted line indicates back calculated values of α vs. log $\beta^2 t$ using average, $k_2 = 85 \pm 8\ M^{-1}\ s^{-1}$, for PCNB.

Similar observations were made for the $A/t^{1/2}$ plots of the absorbance maxima of PPhB. Nonlinearity was observed, consistent with the previously reported dimerization of the radical anion ($k_2 = 2\text{–}9 \times 10^2\ M^{-1}\ s^{-1}$).[2] An estimate of the extinction coefficient was made, $\epsilon_{369,403} = 6.3\text{–}7.0 \times 10^3\ M^{-1}\ cm^{-1}$.

Digital simulation techniques were applied to the spectroelectrochemical data of PCNB and PPhB.[1,6,7] Working curves of normalized absorbance, α, vs. log $\beta^2 t$ (Figure 3) were prepared by methods previously described.[1,6] $\beta^2 t$ represents the dimensionless form of the rate parameters, $k_2 C^{bulk} t_k$, where k_2 is the second-order dimerization rate coefficient, C^{bulk} is the parent benzaldehyde concentration, and t_k is the electrolysis time. Case 1 in Figure 3 shows the behavior expected for an uncomplicated dimerization reaction. The PCNB absorbance/time data did not fit this working curve well over the range of log $\beta^2 t$ values from 0 to 1.5. Values of k_2 determined in this manner were much less than previously reported, and were not constant with each value of $\beta^2 t$ (i.e., each electrolysis time).

Because of the different decay rates of the two $PCNB^{-}\cdot$ absorbance bands (Figure 2), it was assumed that the 500,530 nm band could be due to a complexed form of the radical anion with the unreduced parent species. A similar complex was proposed for the one-electron reduction intermediate of *p*-nitrobenzaldehyde.[1] Charge transfer type complexes have been proposed for the radical anions of benzaldehyde.[5] New working curves were generated for the $PCNB^{-}\cdot$ intermediate (360,370 nm species) which assumed various magnitudes of complexation.

$$PCNB^{-}\cdot + PCNB \underset{}{\overset{K_{eq}'}{\rightleftharpoons}} (PCNB^{-}\cdot\ldots PCNB)$$

As a first assumption, the dimensionless equilibrium coefficient $K_{eq}'C^{bulk}$ ($K_{eq}' = 500$), determined for the *p*-nitrobenzaldehyde complexation, was used.[1] New working curves are shown as cases 2 and 3 in Figure 3 for various values of $k_{eq}'C^{bulk}$. Similar working curves were constructed for the absorbance/time data of the complex (500,530 nm bands), assuming its decay product was also the PCNB dimer. Values of k_2 determined from these curves were more constant with varying $\beta^2 t$ ($k_{2_{500,530}} = 88 \pm 19\ M^{-1}\ s^{-1}$ and $k_{2_{360,370}} = 85 \pm 8\ M^{-1}\ s^{-1}$). Back calculated values of log $\beta^2 t$, using the above k_2 values, are also plotted in Figure

3. These values of k_2 are in reasonable agreement with previous voltammetric determinations of k_2.[1-3]

Digital simulation techniques were also applied to the spectroelectrochemical data for the PPhB reduction. A reduction mechanism uncomplicated by parent-ion complexation was assumed, since the spectral data did not clearly indicate the presence of more than one reduction intermediate. Using the case 1 working curve (Figure 3) a dimerization rate coefficient $k_2 = 2.2\text{–}2.8 \times 10^2\ M^{-1}\ s^{-1}$ was determined. It is conceivable that the observed absorbance bands for the $PPhB^-\cdot$ species represent a parent-ion complex similar to the one proposed for PCNB. The uncomplexed species might have an absorbance in the UV and therefore be undetectable by normal spectroelectrochemical techniques.

The spectroelectrochemical technique has insufficient sensitivity at wavelengths below 350 nm to obtain a realistic extinction coefficient for the benzaldehyde radical anion species.[6] Nevertheless, the absorbance just below 350 nm was clearly due to a transient, electrochemically produced species, with an extinction coefficient of greater than $1000\ M^{-1}\ cm^{-1}$. The absorbance at 350 nm appeared with the onset of reduction of benzaldehyde and disappeared when the intermediate was electrochemically reoxidized (double potential step experiments). When left to decay in solution, the decay rate appeared to be proportional to the bulk concentration of benzaldehyde.

Nekrasov and co-workers have reported an absorbance in the near UV which was apparently for the $Ph\text{-}CHO^-\cdot$ species in aqueous ethanol.[5] The absorbance maxima shifted to longer wavelengths with decreasing acidity of the solvent. If this same species were being produced in sulfolane, we would expect to be able to easily observe its presence. This discrepancy in results may be due to mechanistic differences in the reduction pathways between the two solvents.[1-3,5]

The data presented here for the PCNB reduction clarifies the previous voltammetric data.[2,3] The ring-disk voltammetric results indicated that the decay of the reduction intermediate by dimerization was complicated by consumption of the $PCNB\cdot$ intermediate by another reaction. We have confirmed that this reaction is probably due to the complexation of the radical anion with the unreduced parent molecule producing a spectrally distinct species (500, 530 nm band). The parent-ion complex represents a more stable form of the reduction intermediate and appears to compete favorably for consumption of the radical anion at low solution concentrations of the radical anion. This is indicated in the digital simulation results presented here and in previous ring-disk voltammetric experiments.[3] A variation of ring-disk collection efficiency with PCNB radical anion concentration was noted. At low concentrations of radical anion, complexation with the parent molecule was favored, while at higher concentrations of radical anion, dimerization was the predominate reaction pathway ($k_2 = 45.2\ M^{-1}\ s^{-1}$). The complex may also undergo further polymerization or decay to an electroinactive species, but no evidence to support this conclusion was observed. The voltammetric results clearly indicate that only one electroactive intermediate is formed.[2,3]

These spectroelectrochemical investigations have expanded our understanding of the *p*-cyanobenzaldehyde reduction and that of other benzaldehydes. Previous studies of the chemical and electrochemical reduction of this compound have shown only that the radical anion species was produced.[3,8-12] The decay of the para-substituted intermediates by dimerization is greatly retarded compared to unsubstituted benzaldehyde (k_2(sulfolane) = $2.0\text{–}2.4 \times 10^3\ M^{-1}\ s^{-1}$).[2,3] Complexation of the radical anion of the type demonstrated here may explain part of this enhanced stability.

Acknowledgment. One of us (N.R.A.) acknowledges the Associated Western Universities for financial support through an AWU/AEC Graduate Fellowship at Sandia Laboratories. This work was supported by the U.S. Energy Research and Development Administration.

References and Notes

(1) N. R. Armstrong, R. K. Quinn, and N. E. Vanderborgh, *J. Phys. Chem.*, **80**, 2740 (1976).
(2) N. R. Armstrong, R. K. Quinn, and N. E. Vanderborgh, *Anal. Chem.*, **46**, 1759 (1974).
(3) N. R. Armstrong, R. K. Quinn, and N. E. Vanderborgh, *J. Electrochem. Soc.*, **122**, 615 (1975).
(4) C. N. R. Rao, V. Kalyanaraman, and M. V. George, *Appl. Spectrosc. Rev.*, **3**, 154 (1970).
(5) A. D. Korsun and L. N. Nekrasov, *Electrokhimiya*, **5**, 212 (1969).
(6) T. Kuwana and N. Winograd in "Electroanalytical Chemistry", Vol. 7, A. J. Bard, Ed., Marcel Dekker, New York, N.Y., 1974, pp 1–78, and references therein.
(7) J. Strojek, T. Kuwana, and S. Feldberg, *J. Am. Chem. Soc.*, **90**, 1355 (1968).
(8) D. Geske and A. Maki, *J. Am. Chem. Soc.*, **82**, 2671 (1960).
(9) A. Maki and D. Geske, *J. Am. Chem. Soc.*, **83**, 1852 (1961).
(10) P. Rieger and G. Fraenkel, *J. Chem. Phys.*, **37**, 2811 (1962).
(11) P. Rieger and G. Fraenkel, *J. Chem. Phys.*, **39**, 609 (1963).
(12) N. Steinberger and G. Fraenkel, *J. Chem. Phys.*, **40**, 723 (1964).

Electronic Spectroscopy of Phenyldiazene and Isoelectronic Monosubstituted Benzenes

Carl J. Seliskar

Chemistry Department, University of Cincinnati, Cincinnati, Ohio 45221 *(Received July 19, 1976; Revised Manuscript Received January 17, 1977)*

The systematics of the electronic spectra of seven monosubstituted benzenes, isoelectronic with and including phenyldiazene, are presented. New interpretations made from literature data and new data presented reveal that correlations of spectral properties obtained from experiment and CNDO/s-CI calculations are excellent. Inferences drawn from correlation of quantum chemical results and solvent polarity sensitivity data suggest that prior assignments of intramolecular charge transfer character to the $3^1A' \leftarrow 1^1A'$ ($\pi^* \leftarrow \pi$) transition in neutral species are in error. Specific comments are presented where new results add to, or conflict with, current literature attitudes on specific molecules in the phenyldiazene series.

Introduction

Phenyldiazene, benzylimine, benzaldehyde, styrene, and derived monoprotonated cations are 40 valence-electron monosubstituted benzenes (C_6H_5–X). Phenyldiazene (X = –N=N–H) has recently been synthesized and exhibits an interestingly new chemistry.[1-3] Benzylimines (X = –CH=N–R; R = H, CH_3, etc.) are of continuing interest because of the role arylaldimines play in biochemical systems[4,5] and in photochemical isomerization reactions.[6] Benzaldehyde (X = –CHO) and styrene (X = –CH=CH_2) spectroscopy[7] and photochemistry[8] occupy a significant portion of the chemical literature of the last 2 decades. Very little experimental work has been reported on the monoprotonated cations of these molecules. Further, it is now well established[9] that correlations of state energies and chemical properties can give valuable new insights into the photophysics of isoelectronic series of molecules.

The purpose of this communication is, first, to report interpretations of new experimental data and quantum chemical calculations and, secondly, to relate our results to several current literature attitudes concerning the phenyldiazene isoelectronic series of molecules.

Experimental Section

N-Methylbenzylimine was synthesized according to the method reported by El-Aasser et al.[4] and purified by vacuum distillation. Benzaldehyde, solvents, acids, and bases were used as commercially available spectroquality reagents or purified by distillation.

Solution spectra were measured at 300 K with a Cary 14 spectrophotometer. Monoprotonation of exocyclic groups of compounds were carried out reversibly and resulting spectra showed well-defined isobestic points. Gas-phase molecular spectra were measured at 300 K in a 10-cm pathlength gas cell especially adapted to the Cary 14 instrument.

Oscillator strengths were measured by planimetering the area under molar extinction vs. wavenumber absorption spectra for those transitions where reliable (±10%) deconvolution of bands could be made.

Computational Details

All valence-electron CNDO/s-CI calculations[10] were done assuming planar C_s point group structures with hexagonal benzene (r_{CH} = 1.085 Å; r_{CC} = 1.390 Å) as the fundamental cyclic unit. Exocyclic (X group) atoms were kept at fixed bond distances taken from crystallographic data on similar molecules and these values are given in Table I. Small variations (±10°) of ∠CNH, ∠COH, and ∠NNH cis and trans isomer angles from 120° resulted in very small changes in calculated transition energies and oscillator strengths (compare results for 110 and 120° in Figure 2, for example). Results reported are for an angular value of 110° which we feel is more in accord with crystal data and theoretical calculations on similar molecules (see, for example, ref 11 and 12). Computational results for cis and trans isomers of benzaldehyde and benzylimine (R = H) monocations show no significant energy or oscillator strength differences. However, cis and trans forms of phenyldiazene show quite significant changes (vide infra, Figure 2). Configuration interaction was limited to the first 60 monoexcited configurations for calculations reported. Two center electron repulsion integrals were taken according to the Mataga approximation.[13]

TABLE I: Exocyclic Group (X) Geometry Parameters for Phenyldiazene Isoelectronic Series

Exocyclic group (X)	Fixed geometric parameter
–N=N–H	r(CN) = 1.460 Å
	r(NN) = 1.250 Å
	r(NH) = 1.021 Å
	∠CNN = 120°
–CH=N–H	r(CC) = 1.350 Å
	r(CN) = 1.300 Å
	r(CH) = 1.071 Å
	r(NH) = 1.014 Å
	∠CCH = ∠CCN = 120°
–CHO	r(CC) = 1.400 Å
	r(CH) = 1.071 Å
	r(CO) = 1.210 Å
	∠CCH = ∠CCO = 120°
–CH=CH_2	r(CC) = 1.467 Å
	r(C=C) = 1.344 Å
	r(CH) = 1.058 Å
	∠CCC = ∠CCH = 120°

Assumption of planar structures for all molecules results in correlability of electronic states of all isoelectronic molecules within the C_s point group. Given σ/π separability, all low-energy electric dipole allowed electronic transitions emanating from the ground state (= $1^1A'$) are $^1A'' \leftarrow 1^1A'$ ($\pi^* \leftarrow \sigma$(n)) and $^1A' \leftarrow 1^1A'$ ($\pi^* \leftarrow \pi$). Definitions of molecule-fixed Cartesian axes are x = short and y = long in-plane axes for C_6H_5–X. Thus, $A'(\pi\pi^*)$ states correlate with $B_2(x)$ and $A_1(z)$ and $A''(\sigma\pi^*)$ states correlate with A_2 and $B_1(y)$ states of the C_{2v} ring unit C_6H_5–X. Atom numbering of phenyl carbons is from 1 to 6 beginning at the carbon attached to group X and proceeding in counterclockwise fashion. Exocyclic second row atoms are designated 7 and 8 in order of increasing distance from phenyl carbon 1. Calculated results are always given for the right-handed rotomer of the exocyclic group,

TABLE II: Comparison of Calculated and Experimental Spectral Data for Phenyldiazene Isoelectronic Series

Computation				Experiment			
Transn	Energy, eV	f_{calcd}	Polarzn	Transn	Energy, eV	f_{expt}	Polarzn
trans-Phenyldiazene							
$1^1A'' \leftarrow 1^1A'$	2.20	0.000	z	$\pi^* \leftarrow \sigma(n)$	2.6-3.5[a]	$\epsilon m \simeq 160$[a]	
$2^1A' \leftarrow 1^1A'$	4.58	0.010	x,y	$\pi^* \leftarrow \pi$	3.5-5.2[a]	0.22[a,b]	
$3^1A' \leftarrow 1^1A'$	4.98	0.487	y	$\pi^* \leftarrow \pi$	5.2-6.2[a]	$\epsilon m \simeq 10400$[a]	
$4^1A' \leftarrow 1^1A'$	5.85	0.184	x,y				
trans-Benzylimine[c]							
$1^1A'' \leftarrow 1^1A'$	4.26	0.006	z				
$2^1A' \leftarrow 1^1A'$	4.60	0.007	x,y	$\pi^* \leftarrow \pi$	4.37-4.79[b]	0.02[b]	
$3^1A' \leftarrow 1^1A'$	5.13	0.614	y	$\pi^* \leftarrow \pi$	4.79-5.74[b]	0.25[b]	
$4^1A' \leftarrow 1^1A'$	6.17	0.489	x,y	$\pi^* \leftarrow \pi$	5.74-6.5[b]	$\epsilon m \simeq 21900$[b]	
$5^1A' \leftarrow 1^1A'$	6.42	0.563	x,y				
Benzylimine cation[c]							
$2^1A' \leftarrow 1^1A'$	3.96	0.070	x	$\pi^* \leftarrow \pi$	3.94-5.61[b]	0.20[b]	
$3^1A' \leftarrow 1^1A'$	4.57	0.676	y				
$4^1A' \leftarrow 1^1A'$	5.72	0.005	x,y	$\pi^* \leftarrow \pi$	5.61->5.8[b]	$\epsilon m \simeq 12000$[b]	
$5^1A' \leftarrow 1^1A'$	6.42	0.451	x,y				
Benzaldehyde							
$1^1A'' \leftarrow 1^1A'$	3.25	0.000	z	$\pi^* \leftarrow n$	3.34[d]	5.5×10^{-4}[e]	z[f]
$2^1A' \leftarrow 1^1A'$	4.70	0.014	x	$\pi^* \leftarrow \pi$	4.51[g]	0.02[g]	x[f]
$3^1A' \leftarrow 1^1A'$	5.60	0.395	y	$\pi^* \leftarrow \pi$	5.34[g]	0.26[g]	y[f]
$4^1A' \leftarrow 1^1A'$	6.47	0.626	x	$\pi^* \leftarrow \pi$	5.8-6.7[b,g]		
$5^1A' \leftarrow 1^1A'$	6.56	0.993	y				
$6^1A' \leftarrow 1^1A'$	7.45	0.236	x	$\pi^* \leftarrow \pi$	6.7-7.2[b,g]		
trans-Benzaldehyde cation							
$2^1A' \leftarrow 1^1A'$	3.94	0.079	x	$\pi^* \leftarrow \pi$	3.18-3.87[b]	0.042[b,h]	
$3^1A' \leftarrow 1^1A'$	4.80	0.628	y	$\pi^* \leftarrow \pi$	3.87-5.06[b]	0.35[b,h]	
$4^1A' \leftarrow 1^1A'$	5.76	0.000	x,y	$\pi^* \leftarrow \pi$	5.06->6.2[b]	$\epsilon m \simeq 970$[b]	
$5^1A' \leftarrow 1^1A'$	6.48	0.565	x,y				
Styrene							
$2^1A' \leftarrow 1^1A'$	4.58	0.002	x	$\pi^* \leftarrow \pi$	4.43[g]	0.02[g]	x[i]
$3^1A' \leftarrow 1^1A'$	5.10	0.584	y	$\pi^* \leftarrow \pi$	5.21[g]	0.24[g]	y[i]
$4^1A' \leftarrow 1^1A'$	6.17	0.435	x	$\pi^* \leftarrow \pi$			
$5^1A' \leftarrow 1^1A'$	6.35	0.525	y	$\pi^* \leftarrow \pi$	5.7-6.7[b,g]		
$6^1A' \leftarrow 1^1A'$	6.62	0.295	y	$\pi^* \leftarrow \pi$			
$7^1A' \leftarrow 1^1A'$	7.20	0.062	x	$\pi^* \leftarrow \pi$	6.2-7.2[b,g]		
$8^1A' \leftarrow 1^1A'$	7.51	0.143	x,y	$\pi^* \leftarrow \pi$	>7.2[b,g]		

[a] References 1-3. [b] Results of this work. [c] Computational results are for benzylimine (R = H); experiment is for *N*-methylbenzylimine (R = CH_3). See ref 12 for similar comparison and discussion of alkyl substitution effects. [d] Reference 15 and works cited therein. [e] Y. Kanda, H. Kaseda, and T. Matumura, *Spectrochim. Acta*, 20, 1387 (1964). [f] R. Shimada and L. Goodman, *J. Chem. Phys.*, 43, 2027 (1965). [g] Reference 13. [h] K. Yates and B. F. Scott, *Can. J. Chem.*, 41, 2320 (1963). [i] Reference 19.

i.e., center 8 closest to ring carbon 6. Calculated results given in Table II (vide infra) represent intense transitions and the lowest (weak) $1^1A'' \leftarrow 1^1A'$ transition where correlation with experiment may be possible. Other transition (principally $\pi^* \leftarrow \sigma$) data may be obtained from the author on request.

Results and Discussion

Analyses of experimental and computational results for each of seven of the phenyldiazene isoelectronic series result in general conclusions which fall into two areas.

1. *Transition Energies and Oscillator Strengths.* A comparison of experimental energies and transition types is shown in Figure 1. Examination reveals that agreement for energies is excellent, i.e., within 0.5 eV for transitions falling at <6 eV. For higher energy transitions, assignments by correlation are not unambiguous because of the increased number of transitions expected and found at >6 eV. Although $\pi^* \leftarrow \sigma$ ($A'' \leftarrow 1^1A'$) transitions are calculated for >5 eV in the phenyldiazene series, none to date have been experimentally located (nor is it likely that they will be separable from adjacent strong transitions by current conventional spectroscopic techniques). For benzaldehyde, phenyldiazene, and, possibly, (*N*-methyl)benzylimine, experimental identification of the $1^1A'' \leftarrow 1^1A'$ transition can be compared quite favorably with computation. In the case of the (*N*-methyl)benzylimine cation, it appears that the first observed strong absorption band contains two $\pi^* \leftarrow \pi$ electronic transitions, i.e., $2,3^1A' \leftarrow 1^1A'$. No polarization data appear to be available to test this hypothesis but such measurements would provide a test of our results.

Comparisons of measured and calculated oscillator strengths for $2,3^1A' \leftarrow 1^1A'$ ($\pi^* \leftarrow \pi$) transitions are given in Table II and indicate that calculation overestimates the intensity by approximately a factor of 2. This conclusion is consistent with our previous experience with such analogies.[5,9,14]

2. *Intramolecular Charge Transfer Character in Low-Energy Transitions.* In cases where the calculated $1^1A'' \leftarrow 1^1A'$ transition involves, in an approximate sense, promotion of a localized nonbonding "n" molecular orbital electron (i.e., benzaldehyde, benzylimine, and, possibly, phenyldiazene), calculated intramolecular charge transfer character is found. Electron transfer is dominantly from exocyclic atom 8 to the phenyl ring as expected. However, in *trans*-phenyldiazene, the transfer is from center 7 to the ring in character. In the cases of styrene, *cis*-phenyldiazene, and all cationic isoelectronic species, the calculated $1^1A'' \leftarrow 1^1A'$ transition is from a very delocalized σ mo-

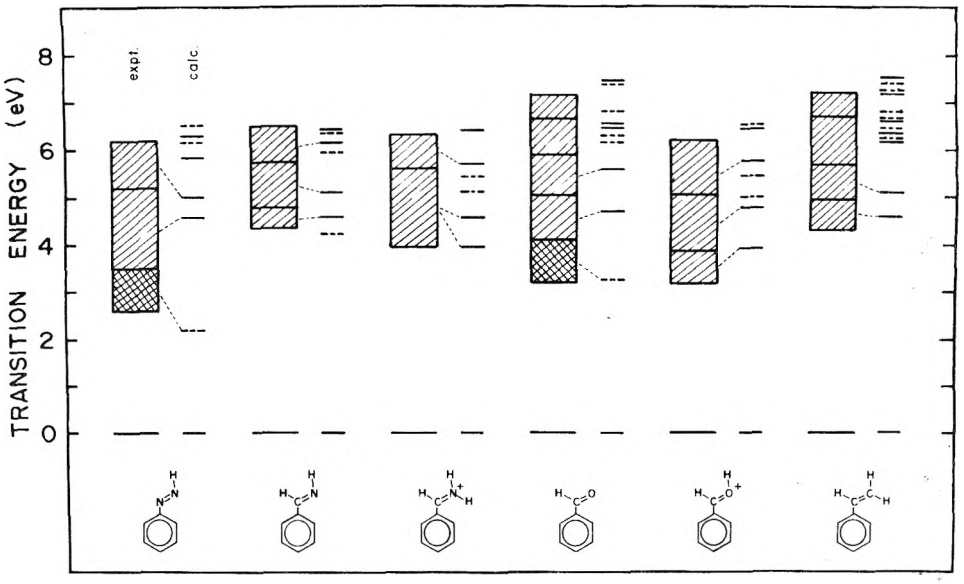

Figure 1. Comparison of transition energies and types for the phenyldiazene isoelectronic series. Experimental data: $\pi^* \leftarrow \sigma(n)$ transitions, double cross-hatched area; $\pi^* \leftarrow \pi$ transitions, single cross-hatched area. Calculated data: $\pi^* \leftarrow \sigma(n)$ transitions, heavy dashed bars; $\pi^* \leftarrow \pi$ transitions, heavy solid bars.

TABLE III: State Valence Shell Electron Densities for *trans*-Phenyldiazene

	State valence shell electron density				
Atom	1A′	1A″	2A′	3A′	4A′
1(C)	3.93	3.94	3.89	3.72	3.91
2(C)	4.01	4.05	3.94	4.02	3.94
3(C)	4.03	4.03	3.94	3.96	3.96
4(C)	4.01	4.14	4.01	3.86	4.02
5(C)	4.03	4.02	3.93	4.00	3.95
6(C)	4.00	4.00	3.95	3.99	3.94
7(N)	5.10	4.98	5.28	5.36	5.26
8(N)	5.18	5.22	5.34	5.38	5.30

lecular orbital and the resulting charge transfer character is in an opposite vectorial sense relative to, e.g., benzaldehyde. *cis*-Phenyldiazene is somewhat peculiar in that valence electron densities on exocyclic centers 7 and 8 change very slightly (<0.1 e), which is to be contrasted with the trans isomer (vide supra). The interplay of molecular orbital localization and effective exocyclic group electron-withdrawing power clearly provides the reversal of charge transfer sense.

Excited $2,3^1A'$ ($\pi\pi^*$) states of neutral species, except phenyldiazene, are calculated to be relatively nonpolar. Thus, in the main, our computational conclusions differ markedly from the dominant literature attitude[4,7,15] which ascribes overwhelming intramolecular charge transfer character to the $2,3^1A' \leftarrow 1^1A'$ transitions in these molecules. Again, *cis*- and *trans*-phenyldiazenes are peculiar in that $2,3^1A' \leftarrow 1^1A'$ transitions are calculated to have a significant charge transfer component (vide infra, Table III). In contrast to neutral isoelectronic molecules, all cationic species' $2,3^1A' \leftarrow 1^1A'$ calculated transitions have relatively large charge transfer components. As an example, the change in valence electron density on exocyclic atoms 7 and 8 is ~0.5 e for both $2,3^1A'$ states relative to $1^1A'$ state values.

While experimental solvent polarity data for low energy transitions of phenyldiazene series molecules are sparse, what is available is in excellent agreement with calculations: the measured $1^1A'' \leftarrow 1^1A'$ ($\pi^* \leftarrow$ n) transition in benzaldehyde is known[16] to involve a large change in molecular dipole moment. Observed solvent polarity sensitivity for $2,3^1A' \leftarrow 1^1A'$ transitions in benzaldehyde,[17] styrene,[18] and (*N*-methyl)benzylimine[4,19,20] is slight. Thus, experimental results agree qualitatively with theoretical inferences drawn above. The solvent sensitivity of the $2,3^1A' \leftarrow 1^1A'$ transitions in *trans*-phenyldiazene[1-3] show shifts of ~1400 cm^{-1} compared to ~150 cm^{-1} for (*N*-methyl)benzylimine.[19] It is clear that the charge transfer components in these $\pi^* \leftarrow \pi$ transitions in *trans*-phenyldiazene are significantly greater than for other neutral molecules in the series. In this regard, our inferences from calculations given above are shown to be correct.

In summary, although absolute values of calculated valence electron rearrangement in the low energy transitions in the phenyldiazene isoelectronic series are to be questioned, correlation of calculated changes within and between molecules appear to be experimentally borne out. If more solvent polarity data were available, comparison of spectral shifts within this series of isoelectronic molecules with our calculations could provide a more consistent test of our results.

In addition to the correlative aspects of our experimental and quantum chemical results, we find other new conclusions which relate to current literature attitudes for selected members of the phenyldiazene isoelectronic series.

Phenyldiazenes. Although our general results on phenyldiazenes confirm conclusions of Huang and Kosower,[1-3] we find apparent disagreement on two points. First, the antibonding combination of two nonbonding azo nitrogen orbitals (i.e., "η_+") referred to by Huang and Kosower obtains for *cis*- and *trans*-phenyldiazene in only a very approximate sense. Reduced molecular symmetry (C_s) in phenyldiazenes results in diffusion of the η_N molecular orbital amplitude throughout the σ framework of the molecule. Thus, extended analogies[3] with *cis*- and *trans*-diazene (C_{2v} and C_{2h}) molecular orbitals are of questionable value even in the absence of experiment. Secondly, the calculated $1^1A'' \leftarrow 1^1A'$ transition in *cis*-phenyldiazene is blue-shifted some 6000 cm^{-1} from that in the trans isomer. This result is opposite to a red shift argued for by Huang and Kosower[3] by analogy with diazenes. Measurements of the electronic absorption spectra of the cis and trans isomers of phenyldiazene would resolve this matter.

Calculated state valence-shell electron densities for low energy singlets in *trans*-phenyldiazene (Table III) indicate that the distal nitrogen atom gains charge in all transitions relative to the $1^1A'$ ground state. This suggests that

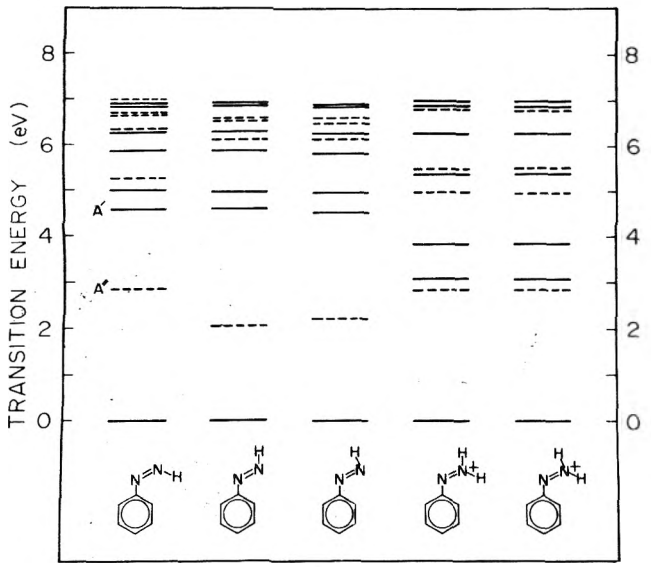

Figure 2. Comparison of calculated transition energies and types for phenyldiazene and derived cation geometric variants. Transitions types are given as follows: $(A'')\pi^* \leftarrow \sigma(n)$ states, heavy dashed bars; $(A')\pi^* \leftarrow \pi$ states, heavy solid bars. Angular variants of ∠NNH are for 120 and 110° as shown.

position 8 is the preferred center for protonation reactions in all low energy singlets including the ground state. No experimental data appear to be available to test this hypothesis. If protonated phenyldiazene in solution is sufficiently stable, measurements of infrared and/or Raman spectra of this species could give information about the position of protonation.

The interestingly new chemistry[1-3] and structural variation available to phenyldiazene makes the spectroscopy of this molecule important. As shown in Figure 2, isomerization or protonation of the outermost nitrogen atom results in large calculated spectral variations. Cis/trans isomerization of phenyldiazene results in a large change in the $1^1A'' \leftarrow 1^1A'$ transition energy (vide supra) and relatively smaller changes in the intense $2,3^1A' \leftarrow 1^1A'$ transitions. Protonation at nitrogen atom 8 (Figure 2) results in a relatively small blue shift of the $1^1A'' \leftarrow 1^1A'$ transition (for comparison see Figure 1) and a reasonable red shift for the $2,3^1A' \leftarrow 1^1A'$ transitions (compare Figures 1 and 2). The first effect is due to the presence of two near-identical azo centers and the second to reasons outlined in a prior section of this report. Unfortunately no electronic absorption spectra appear to be available to test these calculated trends.

Benzylimines. We have measured the spectrum of the gas phase molecule and a summary of our results is given in Table II and Figure 1. The absorption spectrum of (*N*-methyl)benzylimine in the gas phase and in concentrated solution shows no evidence of a distinctive weak transition on the long wavelength side of the first $\pi^* \leftarrow \pi$ transition. In short, our experimental work indicates that the $1^1A'' \leftarrow 1^1A'$ transition is embedded in the high intensity of the $2^1A' \leftarrow 1^1A'$ transition which begins at $\lambda \sim 2835$ Å.

Our calculations suggest that the electronic absorption spectra of *cis*- and *trans*-benzylimines are very nearly identical. Reports[4,19,20] of the spectra of benzylimines do not clearly identify the solution structure of the molecule. Combined infrared and electronic spectral measurements could possibly test the validity of our conclusions as to the spectral similarity of the two isomers. Protonation of *N*-methylbenzylimine in anhydrous ethanol/HCl is a reversible reaction and we find isosbestic points at 2120, 2210, and 2580 Å. A previous report[20] suggested that protonation might not be reversible in solution.

Benzaldehydes and Styrene. Comparison of experimental and calculated transition energies and oscillator strengths for these molecules (Table II and Figure 1) shows that general agreement is excellent. In the case of the neutral molecules our assignments may be seen to differ significantly from those of Kimura and Nagakura.[15] There are two reasons for differing: first, we interpret the shape of their published spectra differently (cf. Table II) and, secondly, we find our interpretation to agree better with CNDO/s–CI transition energies. Our computational results on styrene are very similar to those of King and van Putten[21] who have used a slightly different version of our program. We refer the reader to their work[21] for further detail.

Acknowledgment. We thank Professor H. H. Jaffé for his continued interest and for valuable discussions.

References and Notes

(1) P. C. Huang and E. M. Kosower, *J. Am. Chem. Soc.*, **90**, 2354 (1968).
(2) P. C. Huang and E. M. Kosower, *J. Am. Chem. Soc.*, **90**, 2362 (1968).
(3) P. C. Huang and E. M. Kosower, *J. Am. Chem. Soc.*, **90**, 2367 (1968).
(4) M. El-Aasser, F. Abdel-Halim, and M. A. El-Bayoumi, *J. Am. Chem. Soc.*, **93**, 590 (1971).
(5) C. J. Seliskar, *J. Mol. Spectrosc.*, **53**, 140 (1974).
(6) M. A. El-Bayoumi, M. El-Aasser, and F. Abdel-Halim, *J. Am. Chem. Soc.*, **93**, 586 (1971).
(7) See, for example, A. J. Duben, L. Goodman, and M. Koyanagi in "Excited States", Vol. I, E. C. Lim, Ed., Academic Press, New York, N.Y., 1974, pp 295–329.
(8) See, for example, M. H. Hui and S. A. Rice, *J. Chem. Phys.*, **61**, 833 (1974).
(9) C. J. Seliskar, O. S. Khalil, and S. P. McGlynn in ref 7, pp 231–294.
(10) J. Del Bene and H. H. Jaffé, *J. Chem. Phys.*, **48**, 1807 (1968).
(11) M. Martinez-Ripoll and H. P. Lorenz, *Acta Crystallogr., Sect. B*, **32**, 2322 (1976).
(12) J. M. Howell and L. J. Kirschenbaum, *J. Am. Chem. Soc.*, **98**, 877 (1976).
(13) R. L. Ellis, G. Kuehnlenz, and H. H. Jaffé, *Theor. Chim. Acta (Berl.)*, **26**, 131 (1972).
(14) C. J. Seliskar and S. P. McGlynn, *J. Chem. Phys.*, **56**, 1417 (1972).
(15) K. Kimura and S. Nagakura, *Theor. Chim. Acta (Berl.)*, **3**, 164 (1965).
(16) W. Liptay in ref 7, pp 129–229.
(17) L. Goodman and M. Koyanagi, *Mol. Photochem.*, **4**, 369 (1972).
(18) A. E. Lutskii and A. F. Soldatova, *Zh. Obshch. Khim.*, **35**, 2088 (1965).
(19) D. Pitea, D. Grasso, and G. Favini, *J. Mol. Struct.*, **10**, 101 (1971).
(20) T. Kubota and M. Yamakawa, *Bull. Chem. Soc. Jpn.*, **36**, 1564 (1963).
(21) G. W. King and A. A. G. van Putten, *J. Mol. Spectrosc.*, **44**, 286 (1972).

An Electron Spin Resonance Study of Fremy's Salt in a Dilute Polycrystalline Environment

M. T. Jones,* S. A. Trugman,† V. Rapini,‡ and R. Hameed

Department of Chemistry, University of Missouri—St. Louis, St. Louis, Missouri 63121 *(Received June 24, 1976; Revised Manuscript Received January 5, 1977)*

The ESR spectrum of Fremy's salt, $(KSO_3)_2NO$, in a dilute polycrystalline matrix has been recorded. The matrix used is the usual diamagnetic, yellow-orange form of Fremy's salt. The spectrum has been analyzed and the anisotropic magnetic resonance parameters which describe it have been measured. The value of the parameters so obtained are as follows: $g_1 = 2.00832$ (±0.00002); $g_2 = 2.00589$ (±0.00005); $g_3 = 2.00259$ (±0.00005); $A_1 = 5.5$ (±0.1); $A_2 = 5.5$ (±0.1); $A_3 = 28.9$ (±0.2). Not surprisingly, it is found that these parameters depend upon the matrix in which the Fremy's salt is found.

Introduction

While attempting to prepare the paramagnetic, triclinic, orange-brown form of Fremy's salt,[1,2] we found that we were able to prepare polycrystalline samples which were essentially the diamagnetic yellow-orange form and which contained a small amount of the paramagnetic monomer. The concentration of the latter is estimated to be approximately 1–2% and, thus, allowed the accurate measurement of the associate anisotropic g factors and hyperfine splittings (hfs) constants. The existence of this spectrum has been previously noted[3,4] but both groups of workers were interested in an accompanying triplet spectrum and made no attempt to analyze it. Their spectra were not as well resolved as those described here.

The anisotropic ESR parameters for Fremy's salt have been measured previously in dilute, rigid water solutions[5,6] and in the single crystal host $(KSO_3)_2NOH$.[7,8] However, there have been no studies reported in which the host was the diamagnetic yellow-orange form of $(KSO_3)_2NO$. Therefore, it was of interest to study the effect of host lattice upon the anisotropic ESR parameters. In addition, studies in our laboratory of the effect of various counterions upon the g factor of $(SO_3)_2NO^{2-}$ suggested that the structure of the $(SO_3)_2NO^{2-}$ ion in solution might be somewhat altered from that found in the solid state.[9] Therefore, it was of considerable interest to compare the anisotropic ESR parameters derived from water solutions and the polycrystalline samples under study here.

Experimental Section

Sample Preparation. The diamagnetic yellow-orange form of Fremy's salt was prepared according to the procedure of Moser and co-workers.[1,2] Polycrystalline samples prepared in this manner yielded no ESR spectra at room temperature. However, samples which were prepared by crystallization from water solutions which were intermediate in temperature between those used to prepare the yellow-orange and orange-brown forms gave ESR spectra similar to that shown in Figure 1. The crystals obtained were essentially yellow-orange in color. If these crystals were placed in the ESR spectrometer before they were completely dry, an isotropic ESR spectrum was observed to be superimposed upon the polycrystalline anisotropic spectrum. The g factor and hfs of this isotropic spectrum were identical with those observed for dilute water solutions of Fremy's salt. Thorough drying of the above samples caused the isotropic spectra to disappear with no changes in the anisotropic spectrum.

ESR Spectrometer. The ESR spectra were obtained with a Varian E-12 ESR spectrometer equipped with a dual cavity. The g factor and field calibration measurements were made by previously described techniques.[9,10] In addition, the superimposed isotropic spectra were quite useful. Water solutions of Fremy's salt were used as reference samples also. The hfs was taken to be 13.05 G[11] and the g value which was measured in our laboratory against that of lithium tetracyanoethylene in tetrahydrofuran is 2.005560 (±0.000004). No second-order shift corrections have been made.

Results

The polycrystalline ESR spectrum is shown in Figure 1. The anisotropic parameters were obtained, initially, through the use of the method described by Kneubühl.[12] The parameters were then refined through the use of a polycrystalline ESR spectrum simulation program written in our laboratory. The important feature of the method outlined by Kneubühl is that certain turning points in the polycrystalline spectra can be used to evaluate the anisotropic hfs or g value parameters. From spectra such as that shown in Figure 1, it is possible to fairly accurately obtain values for g_1, g_2, g_3, and A_3. The field positions associated with g_1, g_2, and A_3 were unambiguous. The field position associated with g_3 was obtained from the midpoint (corrected for second-order effects) between the A_3 extrema. One of the A_2 extrema was well enough resolved to make an estimate of its value. Finally, based on the assumption that $A(\text{solution}) = (A_1 + A_2 + A_3)/3$ it is possible to estimate the value of A_1. As will be demonstrated shortly this assumption leads to some error.

The results initially obtained from Kneubühl's method were refined by the use of computer spectral simulation techniques. The computer simulation program, which was written in our laboratory, took into account the important points discussed by Lefebvre and Maruani.[13] Initially, we used a minimization routine which compared some approximately 30 points uniformly selected along the experimental spectrum with the same points of the computed spectrum. While reasonable fits were obtained by this method, it is our opinion that better fits between calculated and experimental spectra were obtained by paying particular attention to the turning points in the spectrum. This was done visually for the data reported here but it

† UMSL Research Assistant; Harvard University Undergraduate. Present address: Department of Physics, Stanford University, Palo Alto, Calif.

‡ UMSL-NSF Undergraduate Research Participant, 1975. Present address: School of Dentistry, University of Missouri—Kansas City, Kansas City, Mo.

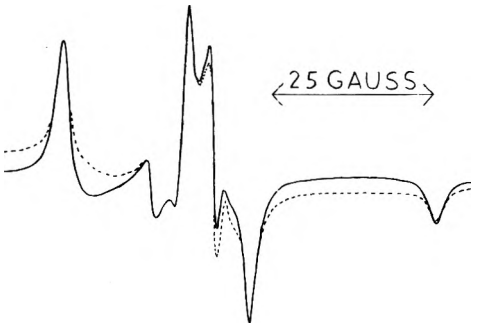

Figure 1. The solid line is the spectrum simulated with the parameters given in Table I. The dashed line represents the experimental spectrum which was recorded at room temperature.

TABLE I: Magnetic Parameters

	$(KSO_3)_2NOH^{a,c}$	Frozen $D_2O^{b\ c}$	$((KSO_3)_2NO)_2{}^{c,d}$
g_1	2.0094 (±4)	2.0081 (±2)	2.00832 (±2)
g_2	2.0055 (±4)	2.0057 (±2)	2.00589 (±5)
g_3	2.0026 (±4)	2.0025 (±2)	2.00259 (±5)
$\langle g \rangle$	2.0058 (±4)	2.0054 (±2)	2.00560 (±4)
A_1	5.5	5.5 (±0.5)	5.5 (±0.1)
A_2	7.7	4.0 (±0.5)	5.5 (±0.1)
A_3	27.5	29.8 (±0.3)	28.9 (±0.2)
$\langle A \rangle$	13.56	13.10 (±0.4)	13.3 (±0.2)
α^e		1.1	0.8
β		0.4	0.6

[a] Reference 8. [b] Reference 6. [c] The uncertainties represent the error in the last significent figure. [d] The uncertainties are obtained as the rms deviation of measurement from five separate spectra. [e] The line width $= \alpha + \beta \cos^2 \theta$, where θ is the polar angle. The units of α and β are in gauss.

could easily have been incorporated in the above minimization routine.

Finally, we found (in agreement with Freed et al.[6]) that an improved fit between experimental and simulated spectra was obtained if the line width associated with various angular orientations was represented in the following form:

$$\text{line width} = \alpha + \beta \cos^2 \theta$$

The angle θ is the polar angle, α is the line width when $\theta = 90°$, and β is the angular dependence parameter.

The data in Table I represent the anisotropic parameters which give the best overall fit between the experimental and simulated spectra with particular attention being paid to the turning points of the spectral envelope. Figure 1 shows a typical comparison between the two spectra. The data in Table I represent the average of five different spectral fits of computed and simulated spectra, where each experimental spectrum represents data taken on a different sample. Therefore, the uncertainties listed in Table I represent the precision of the data. We estimate the accuracy to be of the order of ±0.1 G. This is due to the very narrow line spectra which we were able to observe and the fact that upon some of the polycrystalline spectra there were superimposed solution spectra of Fremy's salt which allowed very accurate field calibrations to be made.

Discussion and Conclusions

An additional reason for wishing to simulate the ESR spectra was, we were concerned that perhaps the reason why different anisotropic parameters in different matrices were obtained was primarily due to the differences in resolution observed in the various matrices. However, this does not appear to be the case. For example, when the anisotropic parameters which are reported here are used to simulate spectra under conditions of poorer resolution, the simulated spectra so obtained do not agree well with the previously reported experimental spectra and vice versa. Therefore, we have concluded that the differences listed in Table I are real and are a consequence of the different radical environments and different radical structures.

Recall that one of the concerns expressed in the Introduction was whether or not the structure of Fremy's salt in aqueous solution might be different from its structure in the solid state which has been reported by Moser et al.[1,2] On the basis of the information presented in Table I, we believe that the structures are different. We are interested in learning more about the structure of Fremy's salt in aqueous solutions and are attempting to move toward that goal, in our laboratory, through the use of molecular orbital calculations of the g values and hfs.

One final point should be made regarding the average g and A values listed in Table I. We are confident that these values are not equal to the isotropic values which can be measured in aqueous solutions. All attempts at spectral simulation which required either that $\langle g \rangle$ or $\langle A \rangle$ (or both) be equal to their isotropic values in aqueous solution gave poorer fits than the values in Table I.

Acknowledgment. The partial support of this research by the National Science Foundation through Grant GP-28436 and through its Undergraduate Research Participation Grant EPP75-04388 is gratefully acknowledged. The hospitality of the University of Sheffield while the final details of the computer fit were worked out is also gratefully acknowledged.

References and Notes

(1) W. Moser and R. A. Howie, *J. Chem. Soc. A*, 3039 (1968).
(2) R. A. Howie, L. S. D. Glasser, and W. Moser, *J. Chem. Soc. A*, 3043 (1968).
(3) B. D. Perlson and D. B. Russell, *J. Chem. Soc., Chem. Commun.*, 69 (1972).
(4) M. Decorps, F. Genound, and M-C. Schouler, *Mol. Phys.*, **26**, 237 (1973).
(5) B. L. Bates, *Chem. Phys. Lett.*, **10**, 361 (1971).
(6) S. A. Goldman, G. V. Bruno, C. F. Polnazek, and J. H. Freed, *J. Chem. Phys.*, **56**, 716 (1972).
(7) S. I. Weissman and D. Banfill, *J. Am. Chem. Soc.*, **75**, 2534 (1953).
(8) P. J. Hamrick, H. Shields, and T. Gangiver, *J. Chem. Phys.*, **57**, 5029 (1972).
(9) M. T. Jones, R. Hameed, R. Kastrup, and V. Rapini, unpublished results.
(10) M. T. Jones, T. C. Kuechler, and S. Metz, *J. Magn. Reson.*, **10**, 149 (1973).
(11) M. T. Jones, *J. Chem. Phys.*, **38**, 2892 (1963).
(12) F. K. Kneubül, *J. Chem. Phys.*, **33**, 1074 (1960).
(13) R. Lefebvre and J. Maruani, *J. Chem. Phys.*, **42**, 1480 (1965).

Electron Spin Resonance Investigation of the Soluble Blue Copper(II) Hydroxide Complex

Yen-Yau H. Chao and David R. Kearns*

Department of Chemistry, University of California—San Diego, La Jolla, California 92093 *(Received July 26, 1976; Revised Manuscript Received December 20, 1976)*

Publication costs assisted by the U.S. Public Health Service

In basic (pH >12) solutions, copper(II) forms a soluble, paramagnetic type complex. From an investigation of the ESR properties of this and other structurally similar complexes, we conclude that the soluble complex is $Cu(OH)_4^{2-}$ with an approximately square-planar structure.

Introduction

While investigating the effect of pH on the formation of copper complexes with mononucleotides, we observed that the copper hydroxide precipitate dissolves in very basic aqueous solutions. This phenomenon has been known for some time and is often mentioned in standard inorganic texts.[1] In 1923 Müller[2] proposed that the soluble copper complex is CuO_2^{2-} but there have been no further studies to either prove or disprove the structure originally proposed by Müller.[3,4] Since Cu(II) has a d^9 electronic configuration, electron spin resonance (ESR) techniques have been widely used to study various properties of Cu(II) complexes. Maki and McGarvey[5] have developed a theory to analyze the ESR spectra in terms of the bonding property of some square-planar Cu(II) complexes. In the present study ESR is used along with the Maki–McGarvey theory to investigate the structure of the high pH soluble copper complex.

Experimental Section

Chemicals. All reagents used in this study were of reagent grade or higher. The dimethyl sulfoxide (Me_2SO) (spectro grade) and ethylene glycol (reagent grade) were purchased from Mallinkrodt Chemical works. Reagent grade $CuCl_2$ from Baker and Adamson was used throughout this study. Solutions for the ESR measurements were prepared by slowly adding concentrated NaOH (15 N) to a solution of $CuCl_2$ until a clear blue solution was formed. With the initial addition of hydroxide, a precipitate forms which subsequently dissolved upon the addition of more hydroxide. If NaOH is added very fast and in large excess without stirring (instead of slow dropwise addition with vigorous stirring), the dark brown CuO precipitate reported by Müller[2] is observed and this precipitate is insoluble, even in the presence of excess base.

ESR Measurements. A Varian E-3 spectrometer (x-band) was used for the ESR measurements. Since most of the ESR measurements were carried out at 77 K, the copper complexes were all prepared in a solvent containing 50% H_2O and 50% Me_2SO by volume. With this solvent mixture we obtained solutions which produced rigid glasses at 77 K with no evidence of aggregation of the copper.

Results

In acidic aqueous solutions (pH <7), Cu(II) has the structure $Cu(H_2O)_6^{2+}$,[6,7] and the room temperature ESR spectrum contains only a single broad line with a line width of >100 G. Around neutral pH, the ESR signal disappears and a light blue precipitate of $Cu(OH)_2$ forms.[8] Between pH 7 and 11 no ESR signal is detected and the solution remains cloudy. Above pH 12, however, the precipitate gradually dissolves and a clear, deep blue solution forms. Concommitantly, an ESR signal with resolved hyperfine splittings (Figure 1C) is observed (the line widths of the hyperfine lines are 20–30 G at room temperature). The ESR spectrum remains unchanged upon addition of excess base, indicating that only one paramagnetic species is formed in the basic solutions. This spectrum is quite different from that of $Cu(H_2O)_6^{2+}$ which shows only a single broad line (line width >100 G) with no hyperfine splitting. The effect of temperature on the ESR spectrum of the soluble blue copper species in D_2O is shown in Figure 1. If the copper complexes are axially symmetric and second-order perturbation terms are neglected (quadrupolar and nuclear Zeeman terms), the spin Hamiltonian for the system can be written as[9]

$$\mathcal{H} = \beta[g_{\parallel}H_zS_z + g_{\perp}(H_xS_x + H_yS_y)] + AS_zI_z + B(S_xI_x + S_yI_y) \quad (1)$$

where β is the Bohr magneton, $g_{\parallel}$ and A are the g value and hyperfine components, respectively, parallel to the molecular symmetry axis, $g_{\perp}$ and B are the g value and hyperfine components, respectively, perpendicular to the molecular symmetry axis, S's are the electron spins and I's are the nuclear spins.

Experimentally (see Figure 2), the ESR spectrum of the soluble blue copper hydroxide complex (I) shows that g_x and g_y are only slightly different (2.046 vs. 2.050) so that the assumption of square-planar geometry is only approximately correct. Nonequivalence of g_x and g_y has also been observed in $CuCl_4^{2-}$ by Sharnoff,[10] who attributed it to the presence of a rhombic term in the Coulomb Hamiltonian. Since g_x is very close to g_y in complexes I and III, the average value of g (2.048) was used in calculations of the bonding coefficients. The ESR parameters for I are listed in Table I, along with those previously reported for the $Cu(H_2O)_6^{2+}$ complex (complex II in Figure 3).[6]

The room temperature optical absorption spectrum of the blue, clear copper hydroxide solution exhibits a broad absorption band (centered at 15 700 cm^{-1}) in the visible range with no appreciable absorption band between 20 000 and 30 000 cm^{-1} (Figure 4).

Discussion

1. *Evidence that the Soluble Blue Copper(II) Hydroxide Complex is $Cu(OH)_4^{2-}$.* The ESR spectrum of the soluble copper complex formed in basic (pH >12) aqueous solutions is shown in Figure 1, and the relevant ESR parameters are given in Table I. The fact that this solution exhibits a strong ESR signal (comparable in intensity with that observed in acidic solutions) eliminates a polymeric

TABLE I: ESR Parameters and Orbital Coefficients[b] for Copper(II) Complexes I,[c] II,[d] and III[e]

	ΔE_{xy} ($\approx \Delta E_{xz}$), cm^{-1}	A, cm^{-1}	B, cm^{-1}	$g_\parallel$	$g_\perp$	α^{2b}	β^{2b}	β'^{2b}	r, Å
I[c]	15 700	0.0186	0.002 96	2.252	2.048	0.80	0.57	0.77	3.3 ± 0.3
II[d]	12 600[a]	0.128[a]	0.001 26[a]	2.400[a]	2.099[a]	0.82[a]	0.95[a]	0.98[a]	3.2[a]
III[e]	*15 700*	*0.0185*	*0.002 96*	*2.235*	*2.048*	*0.79*	*0.57*	*0.73*	*4.0 ± 0.3*

[a] Data from ref 6. [b] Refer to Maki and McGarvey's paper[5] for the definition of various orbital coefficients; smaller α^2 means larger σ bonding, smaller β^2 indicates larger out-of-plane π bonding, smaller β^2 means larger in-plane bonding. Lewis et al.[6] and La Mar (*Acta Chem. Scand.*, 20, 1359 (1966)) have pointed out the sp^2 hybridization scheme (for oxygen ligand) used in Maki and McGarvey's method is inappropriate. The terms (overlap integral and $T(n)$[5]) involved are small in the orbital coefficient calculations so no correction for the hybridization has been done for the computed results listed in this table. [c] I is $Cu(OH)_4^{2-}$. [d] II is $Cu(H_2O)_6^{2+}$. [e] III is $Cu((-O)CH_2(-O)CH_2)_2^{2-}$. [f] The optical absorption of $Cu(OH)_4^{2-}$ exhibits a broad band at 15 700 cm^{-1} and there is no other band in the region 20 000–30 000 cm^{-1} (see *Experimental Section*), so in the orbital bonding coefficient calculations[5] we assume ΔE_{xy} ($= E_{xy} - E_{x^2-y^2}$) $\approx \Delta E_{xz}{}^g$ ($E_{xz} - E_{x^2-y^2}$) = 15 700 cm^{-1}. [g] The orbital coefficients calculated from ESR data have been found to be insensitive to the small variation of transition energies.

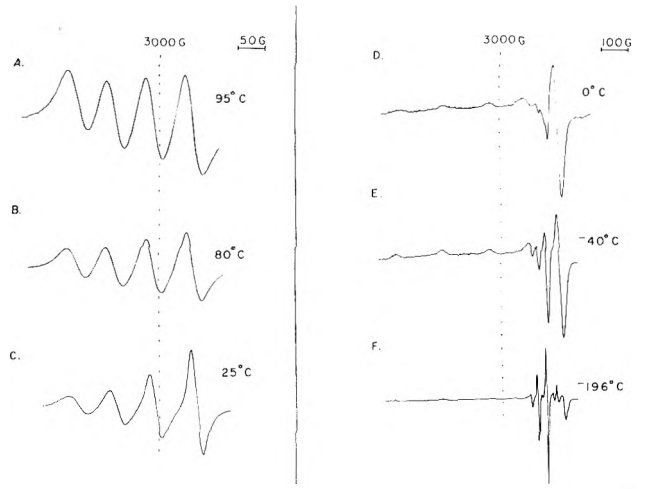

Figure 1. The temperature dependence of the ESR spectra of $Cu(OD)_4^{2-}$ in aqueous medium (100% D_2O for A–C, 50% Me_2SO–50% D_2O for D–F).

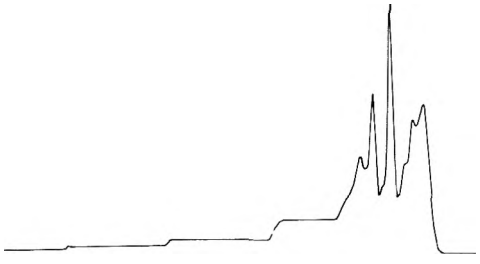

Figure 2. The experimental ESR spectrum, in absorption mode, of $Cu(OD)_4^{2-}$ at −196 °C.

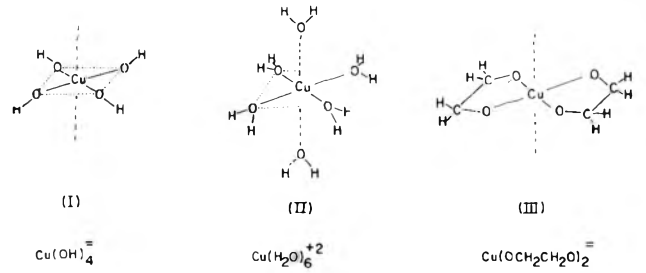

Figure 3. Proposed structures for several copper(II) complexes.

structure which would either have been diamagnetic or had an ESR spectrum differing from that observed due to spin–spin dipolar interactions. The fact that well resolved hyperfine structure is observed at room temperature (Figure 1C) also indicates that the complex is small (vida infra). Since $g_x \sim g_y \sim g_\perp < g_\parallel$ and $B = C < A$ for this

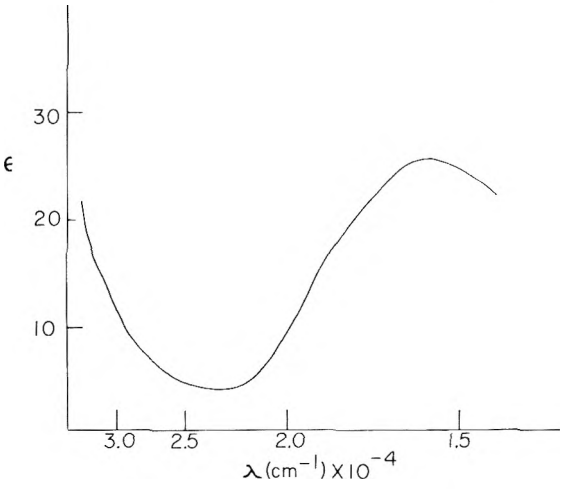

Figure 4. Optical absorption spectrum of $Cu(OH)_4^{2-}$ in H_2O (pH > 12).

complex, it must have an approximately square-planar geometry and this eliminates $Cu(OH)_3^-$ as a candidate.

By comparing the ESR properties of related copper complexes, it is possible to obtain additional information about the nature of the soluble copper hydroxide complex. The ESR properties of the aqueous copper complex formed in acidic solutions (structure II in Figure 3) have already been reported,[6] and these results are given in Table I. Copper also forms complexes at high pH (>12–13) with ethylene glycol (see structure III, Figure 3) and other diols[11] which have ESR properties that are quite similar to but not identical with the copper hydroxide complex (see Figure 4, Table I). (At lower pH (~10), Cu(II) reacts with ethylene glycol to form a green, soluble diamagnetic copper dimer complex (Chao and Kearns, unpublished).)

To account for the fact that complexes exhibiting nearly identical ESR properties at 77 K are formed between copper and several diols, including ribose, ribonucleosides, 5′ ribonucleotides, and fructose[11] (see Table I) but not with 2′ or 3′ ribonucleotides or with deoxynucleotides and with $g_x = g_y < g_\parallel$, we propose that the soluble copper hydroxide complex has an approximate square-planar structure (I), as shown in Figure 3. This would also account for the fact that the ESR properties of $Cu(OH)_4^{2-}$ and $Cu(H_2O)_6^{2+}$ (structure II) are rather different.

A calculation of the molecular orbital coefficients indicates that I and III have nearly identical binding properties, whereas those for II are rather different. These molecular orbital coefficients were calculated using the method of Maki and McGarvey[5] as modified by Kivelson and Nieman,[12,16] and the results are given in Table I. CuO_2^{2-} is expected to have structural and bonding

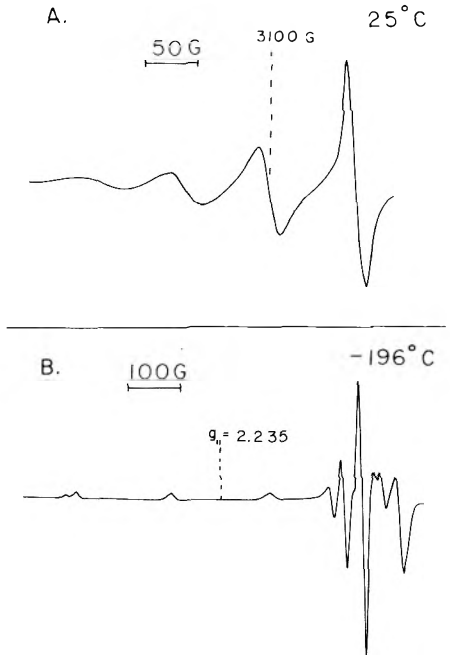

Figure 5. ESR spectra of the copper(II)–ethylene glycol complex; [ethylene glycol] = 1 M, [Cu(II)] = 10 mM, pH 12: (A) room temperature spectrum in 100% H_2O; (B) low temperature (−196 °C) spectrum in 50% Me_2SO–50% H_2O.

properties differing from $Cu(OH)_4^{2-}$ (I) and $Cu(OCH_2CH_2O)_2^{2-}$ (III). Table I shows that (except for the slight difference in β'^2 value) I and III have similar structural and bonding properties. Thus, the structure proposed by Müller[2] for the soluble blue copper complex, CuO_2, is incorrect.

The bonding coefficients in Table I indicate that the Cu–O bond in $Cu(OH)_4^{2-}$ is covalent and consequently unpaired electron density from copper will be found on the hydrogen nuclei (as found in the copper(II) bis-salicylaldehydeimine system)[13] and give rise to a hyperfine interaction. The nuclear magnetic moment of a proton is about three times larger than that of deuterium. Thus, if structure I is correct, substitution of deuterium for the protons in $Cu(OH)_4^{2-}$ will considerably sharpen the ESR spectrum. The spectra shown in Figure 6 confirm this prediction and at the same time provide additional evidence that the soluble Cu(II) species at high pH is not CuO_2^{2-}.[2] By way of contrast, proton hyperfine interactions in diol complexes (III) are expected to be much smaller. Experimentally, a slight sharpening of the lines in the low temperature ESR spectrum of glycerol (from about 12 to 10 G) is observed on converting from water to D_2O, but this may be due to water molecules bound in axial positions.

2. *Temperature Dependence of the ESR Spectrum of $Cu(OH)_4^{2-}$.* From a study of the anisotropy of the line widths and the temperature dependence of the ESR spectra we obtained additional information about the nature of the copper complex. As shown in Figure 1, the ESR spectrum of the soluble hydroxide complex is temperature dependent. As the temperature increases, the increased molecular tumbling rate of $Cu(OH)_4^{2-}$ (or decreased rotational correlation time τ_c[14]) averages out the anisotropic part (anisotropic g and hyperfine tensors) of the ESR spectrum. This is the well known phenomenon of motional narrowing. Consequently, as the temperature increases, the line width differences between the copper hyperfine components tend to vanish (Figure 1C, 1B, and 1A). This effect has been described by McConnell.[15]

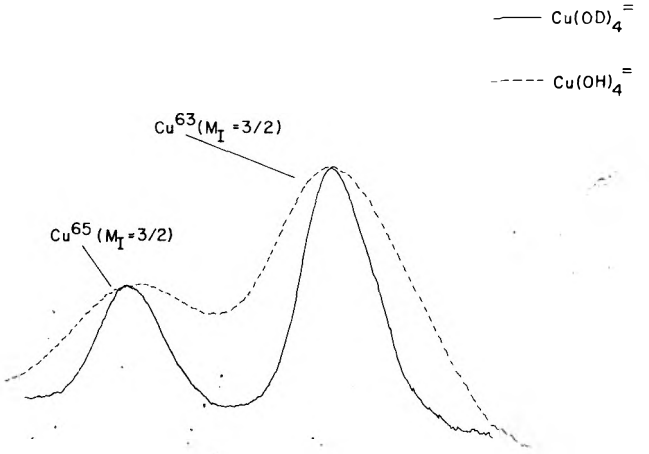

Figure 6. The $M_I = 3/2$ hyperfine component of $Cu(OH)_4^{2-}$ (or $Cu(OD)_4^{2-}$) in 50% Me_2SO–50% H_2O (or 50% Me_2SO–50% D_2O), $T = -196$ °C.

According to McConnell's theory, the anisotropic behavior (line width difference between hyperfine lines) at a given temperature is proportional to r^3 where r is the hydrodynamic radius of the molecule. Thus, the ESR results (Figure 1C and Figure 5A) indicate that III is larger than I and the hydrodynamic radii, r, calculated from the spectra[15] are 3.3 ± 0.3 Å for I and 4 ± 0.3 Å for III (Table I).[17] This agrees quite well with structures I and III shown in Figure 4. The hydrodynamic radius of II $Cu(H_2O)_6^{2-}$ (calculated by Lewis et al.[6] to be r = 3.3 Å) is the same as for I $Cu(OH)_4^{2-}$. The low temperature ESR spectrum of III (Figure 3B) is quite similar to that of I (Figure 1F), as expected from their structural similarities, although the ESR parameters are not exactly the same ($g_{\|}$ = 2.252 and I, and $g_{\|}$ = 2.235 for III).

Summary

The ESR results which we have described here support the notion that the soluble blue copper complex which is formed in basic (pH >12) aqueous solutions is $Cu(OH)_4^{2-}$. Other species which have been, or might plausibly be proposed, are shown to be inconsistent with experimental observations.

Acknowledgment. The support of the U.S. Public Health Service (GM 22969) is gratefully acknowledged.

References and Notes

(1) F. A. Cotton and G. W. Wilkinson, "Advanced Inorganic Chemistry", 3rd ed, Interscience, New York, N.Y., 1972, p 916.
(2) E. Müller, *Z. Phys. Chem.*, **105**, 73 (1923).
(3) J. W. Mellor, "Comprehensive Treatise on Inorganic and Theoretical Chemistry", Vol. 24, Longmans, Green and Co., New York, N.Y., 1960, p 144.
(4) A. Seidel, "Solubilities of Inorganic and Metal-organic Compounds", 4th ed, Vol. 1, New York, N.Y., 1958, p 959.
(5) A. H. Maki and B. R. McGarvey, *J. Chem. Phys.*, **29**, 31 (1958).
(6) W. B. Lewis, M. Alei, Jr., and L. O. Morgan, *J. Chem. Phys.*, **44**, 2409 (1966).
(7) B. R. McGarvey, *J. Phys. Chem.*, **61**, 1232 (1957).
(8) R. Näsänen and V. Tamminen, *J. Am. Chem. Soc.*, **71**, 1994 (1949).
(9) N. M. Atherton, "Electron Spin Resonance, Theory and Applications", Halsted Press, New York, N.Y., 1973.
(10) M. Sharnoff, *J. Chem. Phys.*, **42**, 3383 (1965).
(11) R. Aasa, B. Malmström, P. Saltman, and T. Vänngård, *Biochim. Biophys. Acta*, **80**, 430 (1964).
(12) D. Kivelson and R. Neiman, *J. Chem. Phys.*, **35**, 149 (1961).
(13) A. H. Maki and B. R. McGarvey, *J. Chem. Phys.*, **29**, 35 (1958).
(14) A. Abragam, "The Principles of Nuclear Magnetic Resonance", Oxford University Press, London, 1961.
(15) H. M. McConnell, *J. Chem. Phys.*, **25**, 709 (1956).
(16) β'^2 has been found[13] to be a better indication of covalent character than α^2 in a series of square-planar Cu(II) complexes.
(17) Although the system contains both copper isotopes 63 and 65, the hyperfine component ratio $A(^{65}Cu)/A(^{63}Cu)$ is close to 1 (1.07); the contribution to the uncertainty of r is thus small.

Effect of Exchanged Cations upon the Electron Spin Resonance Hyperfine Splitting of Chlorine Dioxide Adsorbed on X-Type Zeolites

H. Sugihara,* K. Shimokoshi, and I. Yasumori

Department of Chemistry, Tokyo Institute of Technology, Ookayama, Meguro-ku, Tokyo 152 *(Received July 26, 1976; Revised Manuscript Received December 30, 1976)*

Publication costs assisted by the Tokyo Institute of Technology

ESR spectra of ClO_2 adsorbed on X-type zeolites have been investigated. A systematic change in the chlorine hyperfine splitting was observed in the series of alkali metal zeolites LiX, NaX, KX, RbX, and CsX. This splitting has been well correlated with the ionic potential of the cations and also with the calculated field strength on the adsorption sites. On the other hand, the splittings observed for alkaline earth zeolites MgX, CaX, SrX, and BaX were smaller than those for the alkali metal zeolites and changed inversely relative to the ionic potential of the cations. The CNDO–MO calculation on ClO_2–cation system and the evaluation of the electrostatic field due to the exchanged cation indicates that the change in the splitting could be attributed to the perturbation of electronic states of the radical by the field. The results for the alkaline earth zeolites suggest that the metal hydroxide ion MOH^+, rather than M^{2+}, is the adsorption site. It has been concluded that the hydration of the exchanged cation increases with an increase in the ionic potential of the cations and that the dissociation of a water molecule also occurs to produce an acidic proton.

Introduction

The nature of active sites on cation-exchanged zeolites for acid-catalyzed reactions such as isomerization, cracking of hydrocarbons, and dehydration of alcohols has been the subject of a number of investigations. Rabo et al.[1] have proposed that the strong electrostatic field associated with the cation polarizes the adsorbed hydrocarbon molecules to cause catalytic activity through the formation of carbonium ion intermediates. Dempsey[2] has evaluated the strength of this electrostatic field by assuming a full ionic model of zeolites. On the other hand, Hilschler[3] has suggested that the polarizing action of the field due to the cation makes the proton of a structural hydroxyl group, or of an adsorbed water molecule on the cation, acidic. It has been proposed for a rare earth zeolite by Venuto et al.[4] and for a magnesium zeolite by Hall[5] that the proton released from an adsorbed water is transferred to the zeolite lattice so as to form an acidic hydroxyl group. Ward[6] has performed IR studies on the basis of this thought and clarified the acidic properties of zeolites. He concluded that the electrostatic potential or field due to the divalent cation dissociates an adsorbed water to produce an ion of the MOH^+ type.

Recently the importance of the effect of the surface field upon the electronic state of adsorbed radicals has been recognized, due to the fact that the field causes shifts in g values and/or in hyperfine splittings of their ESR spectra.[7-13] Gardner et al.[10] have obtained the value of the field strength on a silica gel, 6×10^7 V/cm, from a theoretical analysis of the shift in the isotropic hyperfine splitting of adsorbed atomic silver. We have reported a preliminary study on the systematic change in the anisotropic hyperfine splitting of the ClO_2 radical adsorbed on a series of alkali metal X-type zeolites.[13] In the present paper the results of extended work on zeolites exchanged by divalent alkaline earth cations are reported. The observed hyperfine shifts are complementary discussed in three ways. First, the dependence of the shifts on the ionic potential of the zeolite cation is examined. Secondly, the field strength at the position of adsorbed ClO_2 in equilibrium is evaluated for various kinds of cation sites in order to see the correlation with the observed shifts. Finally, the CNDO–MO calculation on various ClO_2–cation systems are carried out by taking into consideration the orientation of ClO_2 molecules on the cations and the role of adsorbed water. On the basis of this knowledge, the origin of the shift is interpreted in terms of the electronic state of ClO_2 interacting with exchanged cations.

Experimental Section

X-type zeolites exchanged with alkaline earth cations were prepared conventionally by immersing Linde 13X into aqueous solutions of the relevant salts such as nitrates and chlorides. This ion-exchange procedure was repeated until the ESR spectra of adsorbed ClO_2 became steady. The analysis using EDTA chelatometric titration showed that 66, 87, 98, and 100% of Na^+ in the starting 13X zeolite were exchanged by Mg^{2+}, Ca^{2+}, Sr^{2+}, and Ba^{2+}, respectively, for each final state. Seven CaX zeolites containing exchanged Ca^{2+} were prepared in a range from 10 to 87%.

The ClO_2 was generated by dropping concentrated H_2SO_4 onto solid mixture of $KClO_3$ and $H_2C_2O_4 \cdot 2H_2O$. Water in the evolved gas was removed by passing the gas over P_2O_5 and CO_2 was pumped off after the gas was frozen at 175 K.

The zeolite samples evacuated at various temperatures were then brought into contact with about 0.1 Torr of ClO_2 at room temperature. The ESR spectra were recorded at 77 K or at room temperature using a JES 3BSX X-band spectrometer.

Results and Discussion

Alkali Metal X Zeolites. The ESR spectra of ClO_2 adsorbed on NaX and KX zeolites were shown in our preceding communication.[13] Figure 1 illustrates the spectrum on KX at 77 K. The magnetic parameters determined experimentally are $A_{xx} = 79.9$ G, $A_{yy} = -18.4$ G, $A_{zz} = -8.3$ G, $A_{iso} = 17.7$ G (for ^{35}Cl nucleus), $g_{xx} = 2.002$, $g_{yy} = 2.017$, and $g_{zz} = 2.012$ where the z axis is chosen to bisect the O–Cl–O angle in the molecular plane and the x axis to be perpendicular to the plane. The hyperfine structure due to ^{37}Cl was observed separately. By making use of the differences in magnetic moments and natural abundance between ^{35}Cl and ^{37}Cl,[14] straightforward analysis of the spectrum was possible. The largest splitting, A_{xx}, decreases with increasing cation radius, i.e., in the

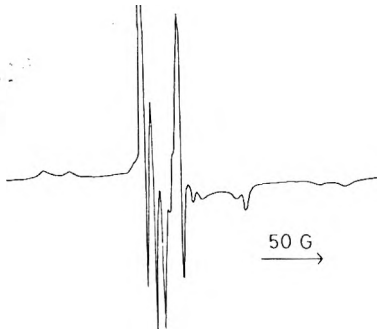

Figure 1. ESR spectrum of ClO_2 adsorbed on KX zeolite evacuated at 600 °C. The spectrum was recorded at 77 K.

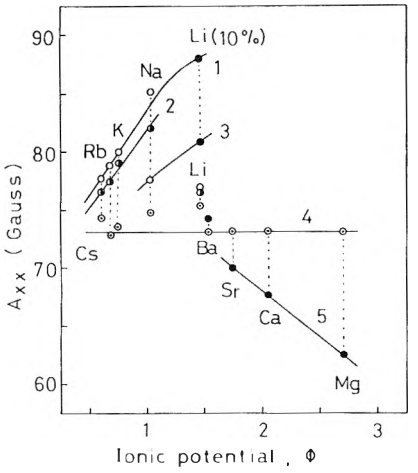

Figure 2. Dependence of hyperfine splitting A_{xx} of ClO_2 on the ionic potential ϕ of cations in X-type zeolites. Zeolites were pretreated at 25 (○), 200 (◑), 350 (⊖), and 600 °C (●). Observed values are classified into lines 1–5.

order K^+, Rb^+, and Cs^+. The spectrum of ClO_2 on NaX zeolite shows the presence of two kinds of species. As has been reported by Coope et al.,[11] this spectrum may be due to the species adsorbed on the surface cations at SII and SIII sites. The effects of exchanged cations upon the hyperfine splittings, A_{xx}, are summarized in Figure 2 together with the results for divalent-cation-exchanged X-type zeolites. In this figure A_{xx} values are plotted against the ionic potential ϕ of the cation, which has been proposed by Cartledge[15] and defined as the ratio of charge to radius, $\phi = z/r$.

Alkaline Earth X Zeolites. The ESR spectra of ClO_2 adsorbed on alkaline earth zeolites were measured at 77 K. All zeolites degassed at room temperature gave identical ClO_2 spectra with an A_{xx} value of 73.1 G. Marked changes in the spectra occurred when the zeolites were evacuated above 200 °C. Figure 3 shows the spectra of the radical adsorbed on MgX (66%), CaX (83%), SrX (98%), and BaX (100%) evacuated at 600 °C. BaX zeolite provided a well-resolved spectrum and an A_{xx} value of 74.0 G, which was slightly larger than that for the sample degassed at room temperature. Apart from a slight line broadening and a decrease in A_{xx} to 69.8 G, the spectrum obtained on SrX zeolite was typical of the single species. In the cases of CaX and MgX zeolites, the lines due to isotopes were poorly discernible and the extra lines appeared at positions shown by arrows in Figure 3a and b. Contrary to the case of alkali metal zeolites, the hyperfine splitting in the spectra on alkaline earth zeolites decreased with increasing size of the cations as is shown in Figure 2.

Figure 4 shows the spectra of adsorbed ClO_2 on CaX zeolites with varying degrees of ion exchange. Spectra due

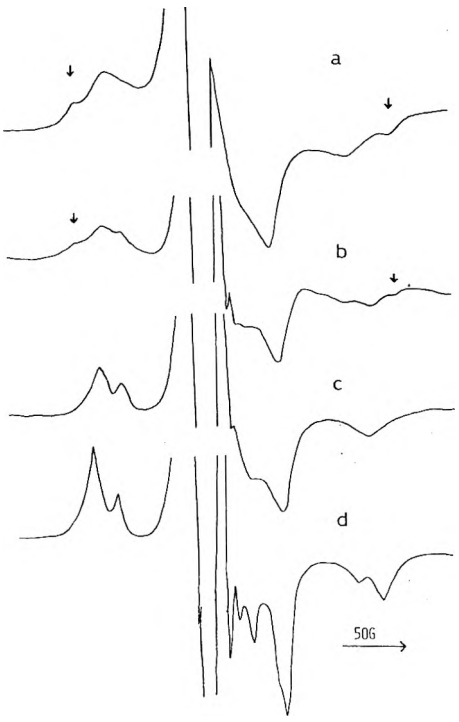

Figure 3. ESR spectra of ClO_2 adsorbed on alkaline earth X zeolites evacuated at 600 °C: (a) MgX (66%), (b) CaX (83%), (c) SrX (98%), and (d) BaX (100%). The spectra were recorded at 77 K. Arrows show the extra lines described in text.

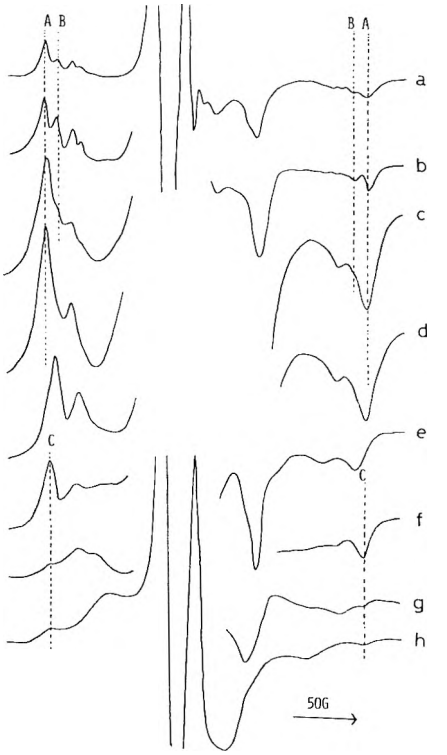

Figure 4. ESR spectra of ClO_2 adsorbed on CaX zeolites with various degree of exchange: (a) 0% (Na 100%), (b) 10%, (c) 23%, (d) 42%, (e) 59%, (f) 75%, (g) 83%, and (h) 87%. The spectra were recorded at 77 K. A and B indicate the outermost hyperfine components ($M_I = \pm 3/2$) of ^{35}Cl nuclei under different circumstances. C corresponds to the extra lines shown by arrows in Figure 3a and b.

to species A and B were observed when Ca^{2+} ions partially displaced Na^+ ions in zeolite (Figure 4b,c). Species B, which gave a smaller splitting, decreased in intensity with an increase in the degree of ion exchange. The spectrum of CaX (42%) showed species A only (Figure 4d). From a comparison with the spectrum on NaX (Figure 4a), both

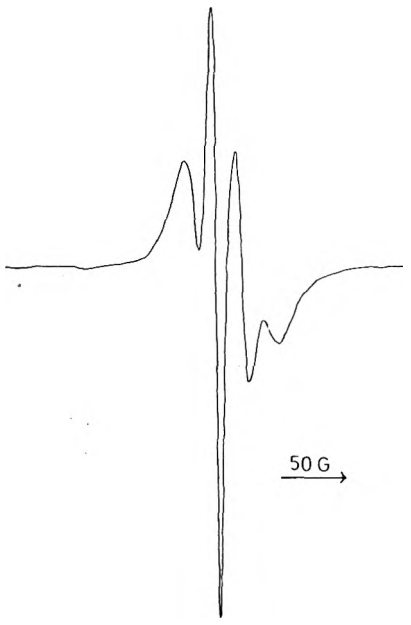

Figure 5. ESR spectrum of ClO_2 adsorbed on CaX (83%) zeolite evacuated at 600 °C. The spectrum was recorded at 25 °C.

species A and B were assigned as ClO_2 radicals interacting with Na^+ ions indicating that Ca^{2+} occupies preferentially interior sites (SI) to which ClO_2 is not accessible. From the studies of CaY[16] and AgX zeolites,[17] such a site preference occurs at low degrees of ion exchange. The A_{xx} value on CaX (59%), 78.6 G, is different from those of species A and B (Figure 4e). At higher degrees of ion exchange the spectra showed smaller hyperfine splitting accompanied by the extra lines C (Figure 4f,g,h). This could possibly be attributed to ClO_2 on Na^+, since its intensity decreases with increasing fraction of exchanged Ca^{2+} in the range from 75 to 87%. The ClO_2 spectrum on CaX (87%) markedly shrunk the splitting in comparison with those on CaX (75%) and CaX (83%).

The spectra of ClO_2 adsorbed on CaX (83%) and NaX were also recorded at room temperature as shown in Figures 5 and 6, respectively. The spectrum of ClO_2 on CaX (83%) was more isotropic than that on NaX, suggesting that the ClO_2 radical seems to be freely rotating on the surface. The spectrum on NaX shows that the rotation of ClO_2 on NaX seems to still be hindered.

In addition CaX (83%) evacuated above 700 °C was examined. This sample provided a similar spectrum at room temperature but different one at 77 K from that obtained on the CaX treated at 600 °C. This may suggest the change of the nature of the adsorption site as has been pointed out by Rabo et al.[1] in their IR study.

Correlation of A_{xx} to Ionic Potential and Field Strength at Adsorbed Sites. It is reasonable to suppose that the ClO_2 radical interacts with the exchanged cation in zeolites to change its electronic state, since the hyperfine splitting of ClO_2 depends on the kind of cation. Therefore, the ionic potential will be a usefull measure of the effect of the cation, as has been reported by Ward.[6] The linear relationship between the x component of the hyperfine tensor A_{xx} and the ionic potential ϕ holds for Na^+, K^+, Rb^+, and Cs^+ exchanged zeolites, as is seen in Figure 2. It seems significant that an A_{xx} of about 69 G is obtained when line 1 is extrapolated to zero potential. This is compatible with the value reported by McDowell et al.[18] for ClO_2 in rare gas matrices. The result for the LiX zeolite is somewhat peculiar. The two-species spectrum of ClO_2 was obtained with larger hyperfine splittings for NaX partially exchanged by Li^+ pretreated at high temperature such as 600 °C. The larger of two splittings falls on the straight line 1 in Figure 2 when the ionic potential of Li^+ is corrected by using the effective shielding constant.[13,19]

Figure 6. ESR spectrum of ClO_2 adsorbed on NaX zeolite evacuated at 600 °C. The spectrum was recorded at 25 °C.

The correlation between A_{xx} and ϕ discussed previously gives a reasonable explanation for the effect of the cationic field upon the radicals, provided that the radicals are located at similar sites on the zeolite surface. However, ClO_2 may be affected not only by the cation itself but also by the environment in which the cation is located. A tentative evaluation of the electrostatic field near the exchanged cations was thus performed on two kinds of surface sites: SII on the hexagonal faces and SIII on the square faces of the sodalite units, both facing toward the zeolite supercage. It is assumed that a unit negative charge is associated with each AlO_2 group of the zeolite lattice and is compensated by the positive charge of the exchanged cation.[2] In order to determine the equilibrium position of adsorbed ClO_2, the energy of electrostatic interaction between the radical and the zeolite lattice was calculated as a function of distance from the cations. A ClO_2 radical approaches with its negative oxygen end closer to the zeolite cation because of a Coulomb attractive force. A repulsive force becomes operative when they come closer together. Making use of the Born expression of a repulsive force, the energy of electrostatic interaction between two ions i and j is expressed as[20]

$$V_{ij} = \frac{z_i z_j e^2}{r_{ij}} + \frac{b_{ij} e^2}{r_{ij}^n}$$

For simplicity, the Born exponent n was taken to be 9 for all pairs of ion and the repulsive coefficient b_{ij} was chosen so that the equilibrium intermolecular distance equals the sum of the respective van der Waals radii of ions i and j. A charge distribution in the ClO_2 radical with a positive charge, $+\delta$, localized on the chlorine atom and a negative charge, -0.5δ, on each oxygen atom has been assumed. By summing directly over all pairs of these nominal ions the total electrostatic energy was estimated. In spite of the use of this simplified model, the calculated positions of ClO_2 on Li^+ and Na^+ are similar to those obtained from the CNDO–MO calculation as will be described below. Subsequently, the strength of electrostatic field was evaluated at the expected position of ClO_2 adsorbed on Li^+, Na^+, K^+, Rb^+, and Cs^+ at both SII and SIII sites. The result is shown on the abscissa in Figure 7. The circles in Figure 7 correspond to the cases where the site occu-

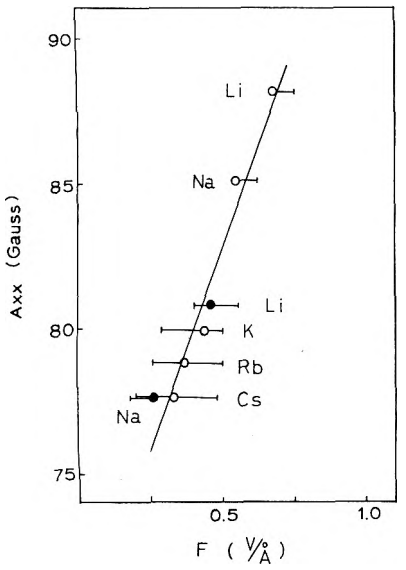

Figure 7. Dependence of hyperfine splitting A_{xx} of adsorbed ClO_2 upon the strength of electrostatic field F associated with cations at SII (●) and at SIII sites (O).

pancies of both SI (the center of hexagonal prism) and SI′ (in the sodalite cage) are 0.5 and those of both SII and SIII are 0.77. The values obtained are strongly dependent on the distribution of cations. Maximum deviations of the evaluated field strength due to the variation in cation distribution between SII and SIII sites are also illustrated in Figure 7. The figure evidently shows a linear hyperfine shift induced by the electric field in this region.[11] The two-species spectra of ClO_2 adsorbed on NaX and LiX (10%) can be attributed to the different field strength at SII and SIII sites. Absence of a second species in the spectra of ClO_2 on KX, RbX, and CsX may be explained as follows: The ClO_2 radical is adsorbed preferentially on the SIII cations because of its stronger interaction with the cation compared with the SII cation. The second ClO_2 radical can approach Li^+ or Na^+ at SII sites in the same supercage, whereas the smaller radius of the cage for the zeolites with larger cations does not allow two radicals to enter the same cage.

It was found that in the case of alkali metal zeolites, the ClO_2 spectra changed stepwise after heat treatments at 25, 200, and 350 °C. Physically adsorbed water molecules may shield the influence of each cation upon ClO_2 and give approximately the same hyperfine splitting. Most of these water molecules are removed by heating at 200 °C and the residual water associated with the cation may propagate the effect of the cation through the polarization of the water molecule. Since all the water molecules are removed above 350 °C, the cation itself is expected to be effectively exposed to ClO_2 in the case of alkali metal zeolites (except LiX) evacuated at such a high temperature. The lithium ion behaves rather abnormally; the observed hyperfine splitting deviates largely from the positive correlation of A_{xx} vs. ϕ as is seen in Figure 2. The effect of bare Li^+ is only observed when NaX is partially replaced by Li^+ and is evacuated above 600 °C. Such a treatment at high temperature is also necessary to remove water from LiY zeolite.[21]

In the alkaline earth zeolites the cations hold water more strongly than the alkali metal cations. Further, as has been proposed by Ward,[21] the strong field due to the divalent cation dissociates an adsorbed water to produce an ion of the MOH^+ type. Therefore, alkaline earth cations may give quite different adsorption sites for ClO_2 than alkali metal cations.

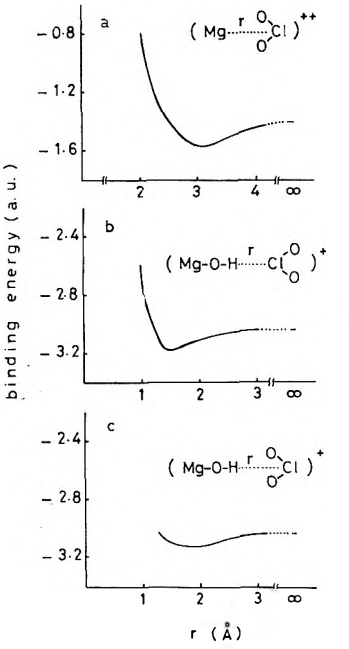

Figure 8. Variation of total binding energies of Mg^{2+}–ClO_2 and $MgOH^+$–ClO_2 systems with the distances between two components in these systems.

TABLE I: Results of CNDO-MO Calculation on M^{n+}–ClO_2 and $MOH^{(n-1)+}$–ClO_2 Systems

System	r^*_{M-Cl},[a] Å	q_{Cl}	$\rho_{Cl(p_x)}$	$\rho_{O(p_x)}$
ClO_2		0.3723	0.5313	0.2502
ClO_2–Li^+	3.0	0.4999	0.5805	0.2198
ClO_2–Na^+	3.8	0.4620	0.5614	0.2324
ClO_2–Mg^{2+}	3.0	0.6294	0.6081	0.2063

System	r^*_{Cl-H}, Å	$\rho_{Cl(p_x)}$	$\rho_{O(p_x)}$	Binding energy au
$LiOH$–ClO_2	1.5	0.5353	0.2472	−0.2550
$LiOH$–O_2Cl	1.9	0.5488	0.2393	−0.1991
$MgOH^+$–ClO_2	1.5	0.5219	0.2565	−3.1679
$MgOH^+$–O_2Cl	1.9	0.5616	0.2307	−3.1330

[a] r^*_{A-B} represents the equilibrium distance between A and B.

In order to ascertain the effective state of cations which interact with ClO_2 radical, a CNDO–MO calculation[22] on the radical–cation and radical–metal hydroxide systems was carried out. The basis set taken in the calculation was 2s, 2p Slater-type orbitals for oxygen and 3s, 3p, 3d ones for chlorine. The Cl–O bond length and the O–Cl–O angle were fixed at their equilibrium values, 1.491 Å and 116.5°, respectively.[23] The result of calculation on free ClO_2 shows that an unpaired electron distributes over atomic orbitals, i.e., 0.5313 on $Cl(p_x)$, 0.0519 on $Cl(d_{zx})$, −0.0835 on $Cl(d_{xy})$, and 0.2502 on $O(p_x)$. The anisotropic hyperfine coupling estimated from these densities (53.2, −26.6, −26.6 G) is fairly consistent with the observed splittings when the value of isotropic splitting obtained in an argon matrix is used.[18] Therefore, this calculation seems to be adequate for the present purpose.

In M^{n+}–ClO_2 and $MOH^{(n-1)+}$–ClO_2 (M^{n+} = Li^+, Na^+, and Mg^{2+}) systems, the bond lengths were fixed at R(Mg–O) = 2.10 Å, R(O–H) = 0.98 Å, and R(Li–O) = 2.04 Å, and the calculation was performed by changing the distance between M and Cl. In Figure 8 is shown the total binding energies of Mg^{2+}–ClO_2 and $MgOH^+$–ClO_2 systems as a function of the distance (r) between two components.

Table I summarizes the unpaired electron densities on $Cl(p_x)$ and $O(p_x)$ at their optimum configuration.

The comparison of the results for Li^+–ClO_2 with those for Na^+–ClO_2 shows that the density of unpaired electrons on $Cl(p_x)$ orbital, $\rho_{Cl(p_x)}$, increases with increasing total electron density on the chlorine atom. This result indicates that the increase in the chlorine hyperfine splitting of ClO_2 on alkali metal zeolites is due to the perturbation of electronic state of the radical by the cation.

The $\rho_{Cl(p_x)}$ value for Mg^{2+}–ClO_2 is largest of all systems calculated. The experimental splitting is, however, smaller than that of even free ClO_2, 69 G. The calculation of an alternative conformation of the $MgOH^+$–ClO_2 system, as is shown in Figure 8b,c, shows that the orientation of ClO_2 with the positive chlorine end close to the hydroxyl group is favorable in terms of binding energy. This orientation results in a decrease in the density of unpaired electrons on $Cl(p_x)$, which conforms with the observed trend. This result suggests that MOH^+, rather than M^{2+}, is the adsorption site for ClO_2 in the case of alkaline earth zeolites evacuated at 600 °C.

On the basis of these results the relationship between A_{xx} and ϕ shown in Figure 2 can be classified into the following groups in terms of the state and site of the cation: line 1, M^+ at SIII; line 2, $M(OH_2)_n^+$ at SIII; line 3, M^+ at SII; line 4, $M(OH_2)_n^+$ and $M(OH_2)_n^{2+}$ at SII; and line 5, MOH^+ at SII.

The present study shows that when the ionic potential of cation is sufficiently large, not only will the hydration of the cation proceed markedly, but the heterolytic dissociation of bound water into the proton and the hydroxyl ion may also occur as has already been described.[15] This scheme gives a reasonable explanation for the appearance of acidic properties; alkali metal zeolites lack acid sites because of the rather small ionic potential of the cations. The physically adsorbed water, except for the case of LiX zeolite, is easily removed by heating at 350 °C. On the other hand, in the alkaline earth zeolites hydrated cations exist even after evacuation at higher temperatures. The dissociation of the bound water increases with increasing field strength of ionic potential of the cations along the order from strontium to magnesium, producing an acidic proton. The properties of lithium and barium zeolites are intermediate between the two groups and most of the water will remain undissociated.

The present conclusion is also compatible with the results of kinetic investigation.[24] The catalytic activities of alkaline earth X-type zeolites for 1-butene isomerization were studied at temperatures ranging from 100 to 160 °C after partial hydration. The activities of MgX, CaX, and SrX zeolites were much enhanced by adding small amounts of water, nearly one molecule per divalent cation, whereas that of the BaX zeolite was not. The addition of excess water, however, caused the poisoning of catalytic activity and an increase in the activation energy for the reaction.

References and Notes

(1) J. A. Rabo, C. L. Angell, P. H. Kasai, and V. Schomaker, *Discuss. Faraday Soc.*, **41**, 328 (1966).
(2) E. Dempsey, "Molecular Sieves", Society of Chemical Industry, London, 1968, p 293.
(3) A. E. Hilschler, *J. Catal.*, **2**, 428 (1963).
(4) P. B. Venuto, L. A. Hamilton, and P. S. Landis, *J. Catal.*, 5, 484 (1966).
(5) W. K. Hall, *Chem. Eng. Prog. Symp. Ser.*, **63**(73), 68 (1967).
(6) J. W. Ward, *J. Catal.*, **10**, 34 (1968); **14**, 365 (1969).
(7) P. H. Kasai, *J. Chem. Phys.*, **43**, 3322 (1965).
(8) K. M. Wang and J. H. Lunsford, *J. Phys. Chem.*, **74**, 1512 (1970).
(9) J. H. Lunsford, *J. Phys. Chem.*, **74**, 1518 (1970).
(10) C. L. Gardner, E. L. Casey, and C. W. Grant, *J. Phys. Chem.*, **74**, 3273 (1970).
(11) J. A. R. Coope, C. L. Gardner, C. A. McDowell, and A. I. Pelman, *Mol. Phys.*, **21**, 1043 (1971).
(12) K. Sogabe, A. Hasegawa, Y. Yamada, and M. Miura, *Bull. Chem. Soc. Jpn.*, **45**, 3362 (1972).
(13) K. Shimokoshi, H. Sugihara, and I. Yasumori, *J. Phys. Chem.*, **78**, 1770 (1974).
(14) "Handbook of Chemistry and Physics", 48th ed, Chemical Rubber Co., Cleveland, Ohio, p E69.
(15) G. H. Cartledge, *J. Am. Chem. Soc.*, **50**, 2855. 2863 (1928).
(16) E.g., K. Tsutsumi and H. Takahashi, *J. Phys. Chem.*, **74**, 2710 (1970).
(17) E.g., H. Sugihara, L. Y. Chen, and I. Yasumori, *Bull. Chem. Soc. Jpn.*, **47**, 2089 (1974).
(18) C. A. McDowell, P. Raghunathan, and J. C. Tait, *J. Chem. Phys.*, **59**, 5858 (1973).
(19) M. H. Brooker and M. A. Bredig, *J. Chem. Phys.*, **58**, 5319 (1973).
(20) L. Pauling, "The Nature of the Chemical Bond", 3rd ed, Cornell University Press, Ithaca, N.Y., 1960, p 507.
(21) J. W. Ward, *J. Phys. Chem.*, **72**, 4211 (1968).
(22) J. A. Pople and D. L. Beveridge, "Approximate Molecular Orbital Theory", McGraw-Hill, New York, N.Y., 1970.
(23) J. D. Dunitz and K. Hedberg, *J. Am. Chem. Soc.*, **72**, 3103 (1950).
(24) H. Sugihara and I. Yasumori, to be published.

Free Energy Changes and Structural Consequences for the Transfer of Urea from Water and Ribonuclease A from Dilute Buffer to Aqueous Salt Solutions

Martha Y. Schrier, Alice H. C. Ying, Margaret E. Ross, and Eugene E. Schrier*

Department of Chemistry, State University of New York at Binghamton, Binghamton, New York 13901 *(Received June 28, 1976; Revised Manuscript Received January 17, 1977)*

Publication costs assisted by the U.S. Public Health Serviee

The free energies of transfer of urea from water to $CaCl_2$ and LiCl solutions and of ribonuclease A from dilute buffer to $CaCl_2$, LiCl, and NaCl solutions were obtained at 25 °C using the isopiestic vapor pressure equilibration technique. Salt molalities in these studies ranged up to 5.5 *m* $CaCl_2$, 8.9 *m* LiCl, and 5.7 *m* NaCl. The isothermal unfolding transitions of the protein at 25 °C in $CaCl_2$ and in LiCl solutions were followed by ultraviolet difference spectrophotometry. A change in slope toward more favorable solute–solute interaction is observed in the plots of the free energy of transfer vs. molality for both urea and ribonuclease A in the region 2.3–3.2 *m* $CaCl_2$ and 4.0–8.0 *m* LiCl. These molality ranges bracket the position of the unfolding transitions observed for ribonuclease A in the respective salt solutions. In NaCl solutions, the free energy changes for the protein are consistently unfavorable. Evidence is presented to show that urea adequately models the behavior of a peptide backbone unit in these salt solutions. On this basis, the number of peptide backbone units which are newly exposed to the solution in the native-to-unfolded transition of the protein is estimated. A change in the mutual solvation of both the cations and the peptide backbone unit is suggested as one possible cause of the more favorable solute–solute interaction as the $CaCl_2$ or LiCl molality is increased.

Introduction

Despite considerable effort in recent years,[1-5] there has as yet been no measure devised which differentiates quantitatively between salts with respect to their ability to unfold proteins in aqueous solutions. Moreover, the unfolding properties of individual salts vary markedly with their concentration. For example, LiCl has almost no effect on the transition temperature of ribonuclease A at concentrations up to 2 M but is able to unfold the protein at room temperature at higher salt concentrations.[3] A similar enhancement of the salt effect on protein conformation at high salt concentrations is seen in the case of calcium chloride solutions.[6] On the other hand, NaCl has relatively little effect on the conformation of the protein over the entire salt solubility range.

Recently,[7] we examined the limiting interaction parameters derived for several salt + urea + water systems and suggested that they were not helpful in correlating the order of effectiveness of salts in destabilizing protein structure. What was potentially important, however, was the acceleration of the decrease in the free energy of transfer of urea from water to LiCl solutions as the LiCl molality was increased in the system. A decreasing free energy of transfer implies favorable solute–solute interaction. This decrease contrasted with the behavior of the free energy of transfer of urea with other salts such as NaCl or Na_2SO_4. In these cases, the change of the free energy of transfer with increasing salt molality was positive. A relationship was implied between the enhanced solute–solute interaction in the LiCl + urea + water system and the ability of LiCl to unfold proteins.

The present study was initiated to elaborate this relationship. As will be shown, a complete investigation of the LiCl + urea + water system provides more compelling evidence for the shift toward more favorable solute–solute interaction as the salt molality is increased. Moreover, an entirely similar type of enhancement but of greater magnitude is shown to appear with increasing $CaCl_2$ molalities in the $CaCl_2$ + urea + water system. Striking changes in the plots of the free energy of transfer of ribonuclease A with increasing salt molality for the same salts suggest the possibility that enhancement of solute–solute interaction with increasing salt molality is a feature of the protein systems as well. The implications of this finding for the mechanism of protein unfolding by electrolytes will be considered.

Experimental Section

Materials. Urea (Fisher) was twice recrystallized from anhydrous methanol and dried under vacuum for 72 h at room temperature. Ribonuclease A (Types IIA and XIIA) was purchased from Sigma Chemical Co. Solutions of the protein were passed through a mixed-bed ion-exchange column (Rohm and Haas Amberlite MB-1). The pH of the protein solution as it came off the column was found to be between 9.6 and 9.7 in agreement with the value of 9.6 reported previously.[8] The protein solutions were lyophilized at concentrations below 1% to avoid aggregation. Dry weight measurements were used to establish final protein molalities. Calcium chloride dihydrate (Fisher) was used without further purification.

Lithium chloride (Fisher) was stored over P_2O_5 and heated under vacuum at 200 °C immediately before use. All operations involving it were done in a drybox. Doubly distilled water was used throughout the work. Solutions were made up using the molality scale—moles of each solute per 1000 g of water.

Isopiestic Measurements. The apparatus and technique for the isopiestic measurements have been described previously.[9,10] $CaCl_2$, LiCl, or NaCl were used almost exclusively as the reference solute for the solutions containing the respective salts except for a few runs involving the LiCl + urea + water systems where urea solutions were used as the reference. Generally, solutions were equilibrated at 25.0 ± 0.1 °C for about 1 week. In runs with urea, the experimental results consisted of the average value of the molality of the reference salt and average values of the molalities of salt and urea in the various mixtures. In runs involving the protein, the average molality of the reference salt and the average molalities

TABLE I: Number of Data Points and the Solute Molality Ranges for the Systems Studied

System	No. of data points	Solute molality ranges m_1, mol kg^{-1}	m_2, mol kg^{-1}
$CaCl_2$ + urea + H_2O	34	0.15-7.14	0.28-19.52
LiCl + urea + H_2O	58	0.12-10.90	0.23-16.50
$CaCl_2$ + ribonuclease A + H_2O	19	0.50-5.51	0.0003-0.0032
LiCl + ribonuclease A + H_2O	16	0.80-8.90	0.0006-0.0031
NaCl + ribonuclease A + H_2O	8	0.97-5.70	0.0010

of ribonuclease A and $CaCl_2$, LiCl, or NaCl in the solution in isopiestic equilibrium with the reference comprised the data set.

Spectrophotometric Measurements. The isothermal unfolding of ribonuclease A in $CaCl_2$ or LiCl solutions was followed at 25.0 ± 0.2 °C by ultraviolet difference spectroscopy using a Cary 14 spectrophotometer equipped with controlled temperature jackets for the sample and reference cells. The concentration of ribonuclease A was maintained at 3.0×10^{-5} m in all experiments while the molality of the salt was varied over a wide range. The pH values of all solutions employed in the spectrophotometric measurements were maintained at 7 using a tris buffer (0.005 M) also containing 0.12 M NaCl.

Cylindrical tandem double cells were used. A solution containing ribonuclease A, buffer, water, and $CaCl_2$ was placed in one compartment of one of the tandem double cells while water was added to the second compartment. In the other cell, a $CaCl_2$ solution of the same molality was added to one compartment and a solution of ribonuclease A, buffer, and water was added to the other compartment. In this way, the same components were in front of the sample and reference light beams at the same time ensuring compensation of extraneous optical effects but allowing the effect of the salt on ribonuclease A to be observed. When the temperature of both cells reached 25 °C, the absorbance was measured at 287 nm. A zero balance point was established by measurement at 325 nm.

The reversibility of the transition was investigated by preparing solutions of the protein at $CaCl_2$ or LiCl molalities higher than the range in which the transition was observed. These solutions were then diluted and the absorbance measured.

Results

Isopiestic Measurements. Tables 1M[11] and 2M[11] give the solute molalities of solutions in isopiestic equilibrium and the values of $-\Delta/(m_1m_2)$[9,10] for the systems, $CaCl_2$ + urea + water and LiCl + urea + water while Tables 3M,[11] 4M,[11] and 5M[11] give $-\Delta/(m_1m_2)$ for the systems, MCl_y + ribonuclease A + water where MCl_y is $CaCl_2$, LiCl, or NaCl, respectively. In these latter systems, protein molalities were sufficiently low, usually near 0.001 m, that there was no dependence of $-\Delta/(m_1m_2)$ on ribonuclease A molality. Experimental data bearing on this point are given in Tables 3M and 4M. In some runs with $CaCl_2$ or LiCl and protein in the molality region after the midpoint of the unfolding transition, precipitates were observed in the dishes containing protein at the conclusion of an isopiestic run. The significance of this observation will be discussed later on.

The osmotic coefficients for MCl_y + water, and urea + water solutions required for the calculation of $-\Delta/(m_1m_2)$ were obtained from the literature.[12-15] The value of the osmotic coefficient of ribonuclease A in dilute buffer was estimated as previously described.[10]

The values of $-\Delta/(m_1m_2)$ were correlated for the $CaCl_2$ + urea + water system and the three systems containing protein by an equation of the form

$$-\Delta/(m_1m_2) = g_{21}^{(0)} + g_{21}^{(1)}m_1 + g_{21}^{(2)}m_1^2 + g_{21}^{(3)}m_1^3 + g_{21}^{(4)}m_1^4 + g_{21}^{(5)}m_1^5 + g_{21}^{(6)}m_2 \quad (1)$$

while for the LiCl + urea + water system the following equation was used

$$-\Delta/(m_1m_2) = g_{21}^{(0)} + g_{21}^{(1)}m_1^{1/2} + g_{21}^{(2)}m_1 + g_{21}^{(3)}m_2 + g_{21}^{(4)}m_2^2 + g_{21}^{(5)}m_1^{1/2}m_2 + g_{21}^{(6)}m_1m_2 \quad (2)$$

In these equations, the subscript 1 represents the salt and 2 urea or ribonuclease A depending on the system considered. The various $g_{21}^{(i)}$ are coefficients which are determined by a least-squares fit of the values of $-\Delta/(m_1m_2)$ as a function of m_1 and m_2. Table I gives the molality range in which data were obtained and the number of values of $-\Delta/(m_1m_2)$ recorded for each system investigated. Table II gives the values of the coefficients and their standard deviations for the four systems which are correlated by eq 1 while Table III gives the values of the coefficients and their standard deviations for the LiCl + urea + water for which eq 2 was used. It should be noted that some of the coefficients have zero values in these equations.

The large uncertainties associated with the coefficients of eq 1 for the $CaCl_2$ or LiCl + ribonuclease + water systems deserve further comment. The shape of the curve

TABLE II: Coefficients and Their Standard Deviations for the Representation of $-\Delta/(m_1m_2)$ by Eq 1

System	$g_{21}^{(0)}$, kg mol^{-1}	$g_{21}^{(1)}$, kg^2 mol^{-2}	$g_{21}^{(2)}$, kg^3 mol^{-3}	$g_{21}^{(3)}$, kg^4 mol^{-4}	$g_{21}^{(4)}$, kg^5 mol^{-5}	$g_{21}^{(5)}$, kg^6 mol^{-6}	$g_{21}^{(6)}$, kg^2 mol^{-2}
$CaCl_2$ + urea + H_2O	0.2387	−0.031 94	0.026 61	−0 002 627			−0.007 616
(± standard deviation)	(0.0076)	(0.011)	(0.003 6)	(0 000 33)			(0.000 48)
$CaCl_2$ + ribonuclease A + H_2O	3.904	14.82	−28.49	17.71	−3.88	0.286	
(± standard deviation)	(8.7)	(23.6)	(21.4)	(8.5)	(1.5)	(0.10)	
LiCl + ribonuclease A + H_2O	−1.144	1.935	−2.838	1.142	−0.156 3	0.007 261	
(± standard deviation)	(6.7)	(12)	(6.7)	(1.7)	(0.19)	(0.007 8)	
NaCl + ribonuclease A + H_2O	−5.111	−0.3406					
(± standard deviation)	(0.39)	(0.11)					

TABLE III: Coefficients and Their Standard Deviations for the Representation of $-\Delta/(m_1m_2)$ by Eq 2

System	$g_{21}^{(0)}$, kg mol^{-1}	$g_{21}^{(1)}$, kg$^{3/2}$ mol$^{-3/2}$	$g_{21}^{(2)}$, kg^2 mol^{-2}	$g_{21}^{(3)}$, kg^2 mol^{-2}	$g_{21}^{(4)}$, kg^3 mol^{-3}	$g_{21}^{(5)}$, kg$^{5/2}$ mol$^{-5/2}$	$g_{21}^{(6)}$, kg^3 mol^{-3}
LiCl + urea + H_2O	0.1436	−0.077 89	0.032 72	−0.011 67	0.000 1696	0.007 005	−0.001 850
(± standard deviation)	(0.0047)	(0.006 7)	(0.001 9)	(0.001 3)	(0.000 039)	(0.001 3)	(0.000 31)

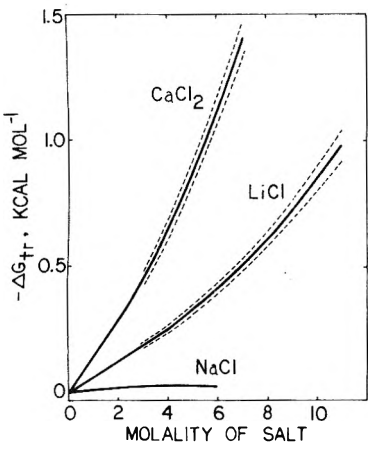

Figure 1. The quantity, $-\Delta G_{tr}$, for the transfer of urea from water to aqueous $CaCl_2$, LiCl, and NaCl[15] solutions as a function of salt molality at 25.0 °C. The dotted lines for $CaCl_2$ and LiCl are maximum and minimum values of $-\Delta G_{tr}$ based on the standard deviations of the respective fits of the experimental data.

of $-\Delta/(m_1m_2)$ vs. $CaCl_2$ or LiCl molality makes it difficult to find a single function capable of reproducing the results over the whole molality range. That the function given is adequate in spite of the uncertainties was shown by the fact that graphical integration of plots of $-\Delta/(m_1m_2)$ vs. $CaCl_2$ or LiCl molality gave values of the trace free energies of transfer nearly identical with those obtained by integration of the analytical expression (see eq 3).

Equation 1 can be integrated[9] to yield

$$-\ln \gamma_2(\text{trace}) = m_1\left\{g_{21}^{(0)} + \frac{1}{2}g_{21}^{(1)}m_1 + \frac{1}{3}g_{21}^{(2)}m_1^2 + \frac{1}{4}g_{21}^{(3)}m_1^3 + \frac{1}{5}g_{21}^{(4)}m_1^4 + \frac{1}{6}g_{21}^{(5)}m_1^5\right\} \quad (3)$$

where γ_2(trace) is the activity coefficient of either urea in $CaCl_2$ solution or ribonuclease A in $CaCl_2$, LiCl, or NaCl solutions under the condition that the molality of the nonelectrolyte, m_2, is zero. The negative of the trace free energy of transfer, $-\Delta G_{tr}$, at any salt molality, m_1, is given by multiplying eq 3 by RT. This is the negative of the free energy change when a solution of urea at infinite dilution in water or ribonuclease A at infinite dilution in dilute buffer solutions is transferred to a salt solution at a specified molality. A similar integration of eq 2 and multiplication of the result by RT leads to an expression for the negative of the trace free energy of transfer of urea from water to aqueous LiCl solutions. In further discussion, the quantity, $-\Delta G_{tr}$, or the expression, the free energy of transfer, will be taken to imply the trace quantity.

The quantity, $-\Delta G_{tr}$, for urea is plotted in Figure 1 as a function of the molalities of $CaCl_2$ and LiCl. The data of Bower and Robinson[15] have been used to obtain the same quantity for urea in NaCl solutions. The line representing $-\Delta G_{tr}$ as a function of NaCl molality is also shown in Figure 1. Figure 2 gives plots of $-\Delta G_{tr}$ vs. salt molality for the transfer of ribonuclease A from dilute buffer to $CaCl_2$, LiCl, and NaCl solutions. In both Figures 1 and 2, the dotted lines indicate the maximum spread of the results considering the standard deviation of the fit of the experimental data to be added to or subtracted from the calculated value.

Difference Spectra of Ribonuclease A in Aqueous Calcium Chloride or Lithium Chloride Solutions. The difference spectrum of ribonuclease A at 287 nm and 25 °C is plotted as a function of $CaCl_2$ and LiCl molalities

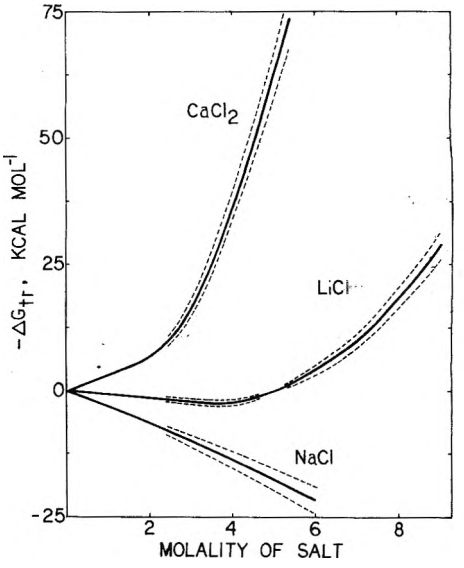

Figure 2. The quantity, $-\Delta G_{tr}$, for the transfer of ribonuclease A from dilute buffer to aqueous $CaCl_2$, LiCl, and NaCl solutions as a function of salt molality at 25.0 °C. The dotted lines are maximum and minimum values of $-\Delta G_{tr}$ for each salt based on the standard deviations of the respective fits of the experimental data.

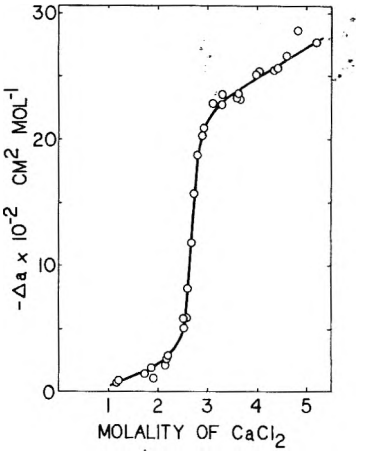

Figure 3. The molar differential absorptivity, Δa, for ribonuclease A at 287 nm as a function of $CaCl_2$ molality at 25.0 °C.

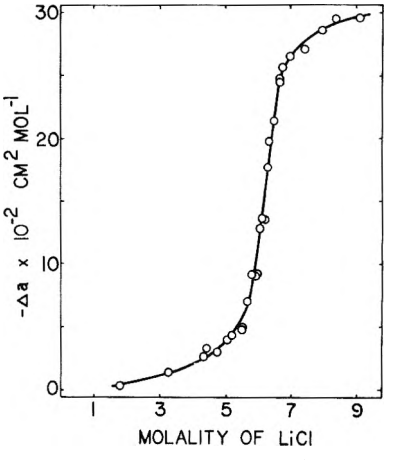

Figure 4. The molar differential absorptivity, Δa, for ribonuclease A at 287 nm as a function of LiCl molality at 25.0 °C.

in Figures 3 and 4, respectively. The sigmoidal shape of the curves is characteristic of the native-to-unfolded transition which has been observed for a number of protein + cosolute + water systems.[16] The salt molality at the

midpoint of the transition region is 2.7 *m* for $CaCl_2$ and 6.2 *m* for LiCl. Reversibility was demonstrated by the concordance of results starting with either native or unfolded protein.

Discussion

In what follows, the assumption is made that the interaction of salts with urea provides a fairly accurate indication of the effect of those salts in the peptide backbone unit, >CHCONH–, in a protein. The use of urea as a model compound for the peptide backbone unit deserves some comment. The free energies of transfer of urea from water to 2 *m* $CaCl_2$, 2 *m* LiCl, and 2 *m* NaCl are -280 ± 15, -125 ± 10, and -30 ± 10 cal/mol, respectively. Nandi and Robinson[4] have determined comparable values for the transfer of a group of related glycyl esters containing different numbers of peptide backbone units from water to these salt solutions. By taking differences between these free energies, they were able to establish approximate transfer values for the peptide backbone unit. Their values were -190 ± 60, -80 ± 60, and -50 ± 60 cal/mol. It can be seen that two of the values agree with those for urea within the large experimental error and that the third is just outside. We conclude from this comparison that urea is an acceptable model for the peptide backbone unit.

Nandi and Robison also showed that the free energy of transfer values for the peptide backbone unit did not depend on the number of these units (up to four) in the compound for the salt concentrations they investigated. Although it is a long extrapolation to go from small peptides to proteins, we infer from this result that there is an independent contribution of each accessible peptide backbone unit to the thermodynamic properties of the protein in a particular salt solution.

In order to derive any further information from the results shown in Figure 2, we require some hypothesis regarding the degree of exposure of various groups of the protein before and after unfolding. While $CaCl_2$ and LiCl interact favorably with peptide backbone units as suggested by the results above, they are well known[2] to salt out nonpolar residues. In aqueous solution in the absence of added salt, the protein is folded in a way which minimizes contact of the majority of the nonpolar side chains from the solution. Peptide backbone units are for the most part also out of contact with the solution. Polar side chains are largely exposed to the solution in all conformations which the protein assumes. As salt is added, the situation persists with minor changes in conformation until the transition region is reached. The protein unfolds in this region but the unfolding must be a restricted one. The conformation changes to allow maximum contact of the peptide backbone units with the ionic solution and to maintain minimum contact with nonpolar groups. On the basis of this picture, there should be a large positive change in the accessibility of peptide backbone units to the solvent in the unfolded vs. the native state while the accessibility of the nonpolar groups will be little changed. In the numerical calculations below, we will account for changes in the degree of exposure of peptide backbone units only.

It should be noted that in ribonuclease A + guanidine hydrochloride + water solutions, more exposure of the nonpolar groups is expected based on the negative free energy of transfer of model nonpolar side chains from water to guanidine hydrochloride solutions. Guanidine hydrochloride is known to unfold ribonuclease A to a greater extent than either $CaCl_2$ or LiCl.[17]

The number of peptide backbone units which become accessible to $CaCl_2$ and LiCl solutions in the unfolding process can be estimated in the following way. We extend the linear portion of plots of $-\Delta G_{tr}$ for ribonuclease A to $CaCl_2$ and LiCl solutions given in Figure 2 to salt molalities above the unfolding transition. Values of the free energy along that line crudely represent the contribution of constituent exposed groups of the *native* protein to $-\Delta G_{tr}$ at high salt molalities. Subtracting the value of this hypothetical $-\Delta G_{tr}$ for the native protein from the actual $-\Delta G_{tr}$ at a given salt molality yields the $-\Delta G_{tr}$ attributable to the interaction of salt with the newly exposed peptide backbone units of the protein.

The $-\Delta G_{tr}$ values for the newly exposed peptide backbone units obtained in this way are 7.5, 21.8, and 45.0 kcal/mol in 3, 4, and 5 *m* $CaCl_2$ solutions, respectively. Similarly, we obtain 15.8, 24.4, and 34.8 kcal/mol in 7, 8, and 9 *m* LiCl solutions. Dividing these values by the free energies of transfer of urea from water to the corresponding salt solutions we obtain 17, 35, and 54 peptide backbone units exposed in 3, 4, and 5 *m* $CaCl_2$ solutions, respectively, and 32, 40, and 49 in 7, 8, and 9 *m* LiCl, respectively.

Let us consider the first value in each series, 17 and 32. Examination of Figures 3 and 4 suggests that 3 *m* $CaCl_2$ and 7 *m* LiCl produce about the same extent of unfolding of ribonuclease A, i.e., the transition is virtually complete in both these salt molalities. We might expect the number of peptide backbone units which are exposed in the transition in the two salt solutions to be the same. Unfortunately the percentage change in the exposure of peptide backbone units is greatest in the transition region and the greatest demand is placed on the reliability of the estimation procedure. Even though the numbers are disparate, we will utilize their average value, 25 ± 8, in further discussion. It can be seen that there is correspondence between the number of peptide backbone units exposed in each salt solution at the higher molality values, i.e., at one molality unit from the end of the transition 35 is comparable to 40 and at two molality units from the end of the transition 54 agrees with 49.

The value of 25 peptide backbone units exposed to the solution in the unfolding of ribonuclease A by $CaCl_2$ or LiCl is comparable to another estimate we have made[10] of this quantity using a different procedure. In that case, we studied the unfolding of ribonuclease A by guanidine hydrochloride or urea. We estimated an increase of the accessibility of all groups of 25% upon unfolding. Applying this value to the peptide backbone units, an increase of 31 peptide backbone units exposed to the solution in the unfolding process is predicted. For reasons mentioned above, we would expect the value of the accessibility of peptide backbone units in guanidine hydrochloride solutions to be larger than that in $CaCl_2$ or LiCl solutions.

If we accept the estimate of less than one quarter of the peptide backbone units being newly exposed to the solution in the unfolding transition, how do we account for the much larger number of units which are estimated to be exposed in the post-transition region? Some uncertainty is likely in the estimation procedure due to the possibility of curvature in the extrapolation of the free energy of transfer of the native protein to the post-transition region. However, even a large error in this procedure would not account for the substantial apparent increase in exposed groups. Only one other explanation is forthcoming. The protein requires more flexibility in order to maximize favorable interactions of the peptide backbone units and minimize nonpolar group interactions with the solution. Under these circumstances, cleavage of one or more of the disulfide linkages could result. Such breakage allowed more groups to be exposed and accounts

in part for the striking post-transition changes seen in Figure 2.

Support for the notion of a further irreversible alteration of the protein conformation after the initial reversible unfolding comes from a study of the enzymatic activity of ribonuclease A after exposure to salts for 6 days or more in the isopiestic experiments. We found that the enzyme is fully active at all NaCl molalities up to saturation and at $CaCl_2$ and LiCl molalities up to the transition. The enzyme becomes progressively less active throughout the transition region and is essentially inactive at salt molalities higher than those necessary to bring about the transition. Dilution of samples of ribonuclease A at these high salt concentrations does not restore enzymatic activity. The seeming paradox between this experiment and the experimental demonstration of the reversibility of the difference spectroscopic transitions mentioned previously is a function of the different time scales involved in the two experiments. Apparently, the irreversible cleavage of the disulfide bonds is slow relative to the reversible unfolding step.

Some speculation is possible regarding the mechanism of the unfolding of ribonuclease A by these salts. Referring again to Figures 1 and 2 we see that a change in slope, small in the case of urea, pronounced in the case of the protein, is evident in the plots of $-\Delta G_{tr}$ for both urea and ribonuclease A in the region 2.3–3.2 *m* $CaCl_2$ and 4.0–6.0 *m* LiCl. These ranges bracket the salt molalities which produce the unfolding of ribonuclease A. This increase in the favorable interaction of the cosolute with the protein in the transition region has been observed previously by Noelken[18] in his studies of the interaction of lithium salts with serum albumen.

One may question whether these changes in slope particularly the relatively small ones in the urea systems are real or perhaps arise from the use of molality rather than molarity as the concentration scale. We answered this question to our satisfaction as follows. We converted the free energy data to a molarity basis and plotted it against salt molarity. For both $CaCl_2$ and LiCl systems with urea and protein systems the change in slope became more pronounced while for the sodium chloride system with protein linear behavior persisted. We also made plots of $-\Delta G_{tr}$ against the activity of the different salts. The information derived from their behavior will be discussed below.

The interaction of LiCl with urea and with ribonuclease A presents a marked contrast to the behavior of these compounds in NaCl solution. Whereas the favorable transfer free energy of urea increases regularly with increasing LiCl molality, there is almost no change in $-\Delta G_{tr}$ for urea in sodium chloride solution. Even though the interaction of ribonuclease A with LiCl solution is initially unfavorable at 25 °C, at higher molalities, the interaction eventually changes sign. On the other hand, the protein undergoes a consistently unfavorable interaction in sodium chloride solution.

If one accepts urea as a model for the behavior of the peptide backbone unit in aqueous salt solutions, then the small change of slope observed in the plot of $-\Delta G_{tr}$ of urea vs. $CaCl_2$ or LiCl molality is indicative of what happens to one of approximately 25 peptide backbone units in ribonuclease A at the salt molalities which produce the transition.

An interesting feature of the data for urea is that if one plots $-\Delta G_{tr}$ vs. the activity of $CaCl_2$ or LiCl rather than the molality the plots become linear. This suggests that the change in the nature of the interaction of the salts with water as the salt molality increases is correlated to the change in their interaction with urea. The following mechanism is consistent with these empirical findings. We envision that up to a certain salt molality the first solvation shell of the calcium or lithium ion is comprised entirely of water molecules. An attractive interaction is possible between the urea molecule and either of these ions but it must take place through the water molecules which solvate both entities. In the critical molality region, insufficient water is available to provide this intermediate solvation layer. The activity of the ions thereby increases. The larger urea molecule can then effectively compete with water in solvating the Ca^{2+} or Li^+ ions. Since the process is one of exchange of a water molecule for a urea molecule, a favorable entropy term should help drive the process. This term arises from access of the ions to both water and urea molecules. In effect, a previously excluded portion of the solution comprised of the urea molecules becomes available to ions. By extension, this argument applies to the peptide backbone units of the protein molecule as well.

As pointed out previously, precipitates were observed in some isopiestic runs involving $CaCl_2$ or LiCl + ribonuclease A + water but only at salt molalities in the region past the transition midpoint. In all cases, the results of the runs containing precipitates fell on the same line as data obtained when they were absent. The implication from this finding is that a given precipitate has a composition identical with the solution from which it was derived. Since it is known that lithium salts form complexes with model amides and with polyproline in the solid state,[5] we infer that the solution species in equilibrium with the precipitate has the same macromolecule–cosolute distribution. Therefore, this observation supports the hypothesis previously advanced by others[5] of the direct site binding of lithium and, by inference, calcium ions to proteins or, putting it in the terms used above, the entrance of the amide linkage into the solvation shell of the ions. An important adjunct of this conclusion is that such site binding occurs only at lithium chloride molalities greater than 4 *m* or $CaCl_2$ molalities greater than 2 *m*. In addition, we interpret the thermodynamic results obtained with NaCl solutions as giving no indication of the kind of interaction proposed for the LiCl system.

The unfolding propensities of LiCl and $CaCl_2$ deserve comparison. Calcium chloride is approximately twice as effective as LiCl as an unfolding agent. Again, this result is in keeping with the thermodynamic properties of urea in the salt solution. The values of both $-\Delta G_{tr}$ and $-\Delta H_{tr}$[7] for the transfer of urea to $CaCl_2$ solutions are two to three times the values for the transfer to LiCl solutions at intermediate salt molalities. We also have free energy of transfer data for four ribonuclease A + cosolute systems[10] in which the protein undergoes unfolding. In all of these systems, $-\Delta G_{tr}$ at the onset of unfolding is 5–8 kcal/mol while unfolding is complete at a $-\Delta G_{tr}$ value of 15–20 kcal/mol. Since the cosolutes are as diverse as urea and $CaCl_2$ this regularity is of interest and possible importance. While it is too early to speculate on the significance of the values themselves or the difference between them, it is worth noting that the substantial initial value implies that some preunfolding has already ensued before the major transition takes place. Further work on all the thermodynamic properties of these transitions is required before the generality of the proposals made here can be assured.

Acknowledgment. We wish to point out the specific contribution of M.E.R. to the isopiestic study of the $CaCl_2$ + ribonuclease A system and to A.H.C.Y. to the experimental determination of the isothermal transition curves

for ribonuclease A. This research was supported in part by Grant No. GM 11762 from the Institute of General Medical Sciences, U.S. Public Health Service.

Supplementary Material Available: Tables 1M–5M (7 pages). Ordering information is available on any current masthead page.

References and Notes

(1) D. R. Robinson and W. P. Jencks, *J. Am. Chem. Soc.*, **87**, 2470 (1965).
(2) E. E. Schrier and E. B. Schrier, *J. Phys. Chem.*, **71**, 1851 (1967).
(3) P. H. von Hippel and T. Schleich in "Structure and Stability of Biological Macromolecules", S. Timasheff and G. Fasman, Ed., Marcel Dekker, New York, N.Y. 1969.
(4) P. K. Nandi and D. R. Robinson, *J. Am. Chem. Soc.*, **94**, 1299 (1972).
(5) P. H. von Hippel, V. Peticolas, L. Schack, and L. Karlson, *Biochemistry*, **12**, 1256 (1973).
(6) D. Talbot, Ph.D. Dissertation, Dartmouth College, 1968.
(7) M. Y. Schrier, P. J. Turner, and E. E. Schrier, *J. Phys. Chem.*, **79**, 1391 (1975).
(8) C. Tanford and J. D. Hauenstein, *J. Am. Chem. Soc.*, **78**, 5287 (1956).
(9) E. E. Schrier and R. A. Robinson, *J. Biol. Chem.*, **245**, 2432 (1970).
(10) M. Y. Schrier and E. E. Schrier, *Biochemistry*, **15**, 2607 (1976).
(11) See paragraph at end of text regarding supplementary material.
(12) H. F. Gibbard and G. Scatchard, *J. Chem. Eng. Data*, **18**, 293 (1973).
(13) H. D. Ellerton and P. J. Dunlop, *J. Phys. Chem.*, **70**, 1831 (1966).
(14) R. A. Robinson and R. H. Stokes, "Electrolyte Solutions", 2nd ed, Butterworths, London, p 478.
(15) V. E. Bower and R. A. Robinson, *J. Phys. Chem.*, **67**, 1524 (1963).
(16) C. N. Pace, *CRC Crit. Rev. Biochem.*, **3**, 1 (1975).
(17) C. Tanford, *Adv. Protein Chem.*, **23**, 121 (1968).
(18) M. Noelken, *Biochemistry*, **9**, 4122 (1970).

Properties of Organic–Water Mixtures. 11. Self-Diffusion Coefficients of Na^+ in Polyethylene Glycol–Water Mixtures at 25 °C[1,2]

Harold O. Phillips,[3a] Arthur E. Marcinkowsky,[3b] S. Baruch Sachs,[3c] and Kurt A. Kraus*

Chemistry Division, Oak Ridge National Laboratory, Oak Ridge, Tennessee 37830 *(Received October 18, 1976)*

Publication costs assisted by the U.S. Energy Research and Development Administration

Self-diffusion coefficients, D, of Na^+ (NaCl, $m = 0.1$) were measured by the radiometric porous frit method for water mixtures of polyethylene glycol (PEG, molecular weight ca. 20 000) at 25 °C. As the organic fraction of the solution increases, D decreases from 1.28×10^{-5} cm^2/s in water to 0.15×10^{-5} cm^2/s in 48 vol % PEG. The diffusion coefficient–viscosity product increases rapidly with increasing fraction of organic component in solution. At an organic volume fraction of 0.48, the relative diffusion coefficient–viscosity product is over 700 times larger than in water. A plot of the logarithm of the relative diffusion coefficients against logarithm of the volume fraction of water is essentially linear, with slope 3.3. This large slope implies that for self-diffusion of small ions the PEG solution behaves like an assembly of oblate ellipsoids of revolution with an axial ratio substantially different from unity.

In this series of papers, we have been concerned with obtaining information on the equilibrium and kinetic behavior of water–organic–electrolyte mixtures largely because of their possible pertinence to membrane processes such as hyperfiltration. An earlier paper[4] dealt with diffusion in glycol– and glycerol–water solutions. In these low molecular weight viscous systems, diffusion is largely determined by viscosity. The present paper deals with self-diffusion of a small ion in a highly viscous (neutral) polymer–water system. One would expect that in this case diffusion and viscosity would not be closely related.

A number of workers have measured conductance and diffusion of small particles in polymer–water mixtures and in non-Newtonian fluids: Matsumoto[5] and Edelson and Fuoss[6] have measured the conductance of salts in polyvinyl alcohol (PVA)–water systems and found that the conductance is not decreased by the polymer to nearly the degree to which the polymer increases viscosity. Hoshino and Sato[7] showed that the diffusion of small molecules in polymer solutions was much less sensitive to the solution viscosity than expected from similar studies on low molecule weight organic–water solutions.

Nishijima and Oster,[8] Biancheria and Kegeles,[9] Astarita,[10] and Clough, Read, Metzner, and Behn[11] have also found that the diffusion of small particles or molecules in polymer solutions is much larger than could reasonably be expected from bulk viscosity considerations.

Although considerable work has been carried out on the conductance and gradient diffusion of small molecules and particles in polymer solutions, apparently little work has been devoted to the measurement of self-diffusion coefficients of small ions in high molecular weight polymer–water solutions over a wide composition and viscosity range. This study utilizes the radiometric porous frit method, which is a rapid and versatile method for measuring self-diffusion coefficients, D, to determine the effect of polymer (polyethylene glycol, PEG) concentration on D of Na^+ ion in solutions. Measurements were carried to polymer concentrations of 48 vol % and to relative viscosities (compared to 0.1 m NaCl) of ca. 6100.

Experimental Section

Method. The radiometric porous frit method[12] was used for measuring self-diffusion coefficients. In this method the rate of removal ("decay") of tracer from an equilibrated and calibrated[13] frit is measured as the same solution, not containing tracer, is pumped past it. The diffusion coefficients are computed from the exponential portions of the decay rates (corrected for background) obtained in a plateau region where the rate is essentially independent of flow velocity past the frit.

For polymer concentrations of 48.2, 22.6, and 12.6%, the half-time, τ, of tracer removal was obtained over a wide range of flow rates and the plateau region established by

TABLE I: Self-Diffusion Coefficients of Na^+ Obtained with Porcelain and Gold Frits at 25 °C

Material	Frit thickness, cm	% void volume	τ, s (for 1 M NaCl)	$10^5 D_{Na}$, $cm^2\ s^{-1}$ (in 22.6% PEG)
Porcelain	0.047	58	37.2	0.526
Gold	0.066	45	28.7	0.529

plotting τ against flow rate. In the remaining cases at least two measurements at different flow rates in the plateau region were carried out; results were considered representative of the diffusional half-times when the decay rates agreed within ca. ±2%. All measurements were carried out at 25 ± 0.1 °C.

Materials. Two porous frit materials were used: porcelain slabs (Selas) with nominal pore diameters ca. 0.5 and 3.0 μm, and gold compacts prepared from gold powder of <10 μm diameter. Most of the results were obtained with the gold frits, since with the porcelain frits residual tracer activity was considerably larger than with the gold frits and a greater "background" correction was required. In those cases where measurements were carried out on the same solution with both types of frits, agreement was satisfactory. A representative set of results is given in Table I.

Sodium tracer, ^{24}Na ($T_{1/2}$ = 15 h), was obtained from the Isotopes Division of ORNL and used without further purification. The tracer was of high specific activity and had a stated radiochemical purity greater than 99%. Use of the tracer was discontinued after approximately four half-lives to prevent significant impurity buildup.

The solutions were prepared by weight from PEG, designated by the manufacturer (Union Carbide Corp.) to have a molecular weight of ~20 000. This value is in reasonable agreement with a value calculated from our viscosities with the equation given by Bailey and Koleske.[14] All solutions were made 0.1 *m* (moles of salt per kilogram of solvent) in reagent grade NaCl.

The water content of the solutions was checked by Karl Fischer titrations. Viscosities (η) were determined with Cannon–Ubbelohde viscometers. In a few cases (13 and 48% PEG) viscosities were also checked as a function of shear rate with a Brookfield viscometer. There was no significant change in viscosity with shear rate. Densities were determined with 2-cm^3 pycnometers.[15]

The volume fraction of water, f_v, in the solution was computed by the relationship $f_v = f_W\ \rho_{sol}/\rho_1$, where f_W is the weight fraction of water, ρ_{sol} is the density of solution, and ρ_1 the density of water. This definition assumes that the partial molal volume of water in the mixture is essentially equal to the molal volume of water.

Frit–Polymer Equilibration. While equilibration of the frits with radioactive sodium was fast, there was concern that the frit–polymer equilibrations might be excessively slow. Thus, for all results reported here, minimum equilibration time with the polymer–water mixtures was 6 days at 40 °C. This proved to be ample. The results obtained at longer equilibration times were consistent with those at the shorter times and in one experiment where the measurement was repeated after 20 days the diffusion coefficient agreed within experimental error with that obtained after 6 days. We also measured the PEG content in a porcelain frit (1.2 mm thick) after 65 h equilibration with a 30% PEG solution at 40 °C. From the necessary weighings of the frit dry, filled with solution, and dehydrated after saturation with the solution (vacuum desiccator over $Mg(ClO_4)_2$ at 25 °C), the PEG contained in the voids of the frit was found to be in reasonable agreement with the amount computed from the composition of the solution.

TABLE II: Self-Diffusion Coefficients (D) of Na^+ in NaCl (m = 0.1)-Polyethylene Glycol-Water Mixtures at 25 °C

Vol % PEG	$10^5 D$, $cm^2\ s^{-1}$	D/D_{aq}	η, cP	η/η_{aq}[a]	$D\eta/(D\eta)_{aq}$
0.0	1.28	1.00	0.898	1.00	1.0
7.0	0.98	0.77	4.73	5.27	4.03
10.8	0.90	0.70	18.0	20.1	14.1
12.6	0.85	0.66	44.5	49.5	32.8
21.5	0.59	0.46	137	153	70.0
22.6	0.53	0.41	270	301	125
31.1	0.39	0.31	832	926	284
48.2	0.147	0.115	5490	6110	702

[a] η_{aq} is the viscosity of 0.1 *m* NaCl in centipoise (cP) at 25 °C.

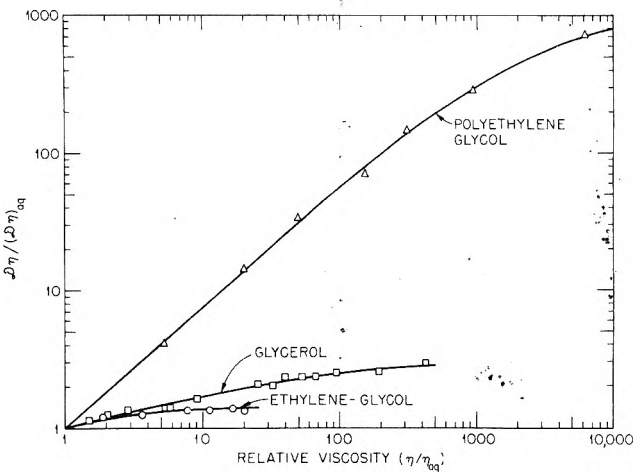

Figure 1. Diffusion–viscosity products of Na^+ in water–organic mixtures.

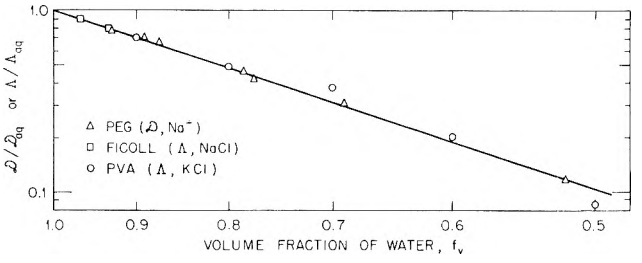

Figure 2. Self-diffusion coefficients, D, and equivalent conductances, Λ, in polymer–water mixtures at 25 °C.

Results and Discussion

The calculated self-diffusion coefficients, D, of Na^+ and the viscosities of the PEG–water mixtures are given in Table II. While the viscosity of the solutions increases from 0.9 to 5500 cP, a factor of ca. 6100, the self-diffusion coefficients decrease only from 1.28×10^{-5} $cm^2\ s^{-1}$ in the aqueous solution to 0.15×10^{-5} $cm^2\ s^{-1}$ in 48 vol % PEG, a factor of 9. Thus, the diffusion–viscosity product is far from constant.

In Figure 1, the relative self-diffusion–viscosity products of Na^+ in the PEG–water mixtures as a function of viscosity are compared with those for ethylene glycol–water and glycerol–water mixtures.[4] While for the ethylene glycol (EG) mixtures, the product is nearly independent of viscosity over the entire composition range studied, for the polymeric EG–water system the product $D\eta/(D\eta)_{aq}$ increases greatly with polymer concentration and reaches a value of 700 at η/η_{aq} = 6110 (f_v = 0.52). Even for gly-

cerol–water mixtures, $D\eta/(D\eta)_{aq}$ increases only slightly with viscosity and reaches a value of ca. 3 at $\eta/\eta_{aq} \approx 420$ ($f_v = 0.06$).

In the PEG–water system we find (Figure 2) that a plot of the logarithm of the relative diffusion coefficients vs. the logarithm of the volume fraction f_v of water is essentially a straight line which follows the relationship

$$\log D/D_0 = S \log f_v \tag{1}$$

The value of the slope S is equal to 3.3 over the water content range studied.

For comparison, Figure 2 also includes relative equivalent conductances of NaCl (at infinite dilutions) obtained by Stokes and Weeks[16] for Ficoll–water solutions (Ficoll is a synthetic sucrose polymer) and of KCl (0.0564 *m*) in poly(vinyl alcohol)–water mixtures at 25 °C, which were interpolated from Matsumoto's data.[5] The data for the Ficoll- and the PVA–water mixtures are in good agreement with the PEG results.

Dependence of diffusion coefficients on water content (or solids content) is expected for polymer solutions if we consider the polymers to be obstructions in the path of the diffusing ions. From this point of view the model for the polymer solution is a heterogeneous system, and one can assume that the relationships developed for suspensions and emulsions (which seem to hold equally for conductance,[17] diffusion, heat conductance, and dielectric constants) are applicable. While in these relationships the shape of the obstructing particle is important, its size is not, provided it is large compared to the size of the diffusing particle. The latter condition is probably not completely met here if we focus attention on the diameter of the (coiled) polymer chains rather than their length. Nevertheless, analysis of the data in terms of existing equations for obstructions in a continuum might be of interest.

The linear log–log relationship of Figure 2 is consistent with the frequently cited linear dependence[17] of diffusion coefficients on volume fraction (ϕ) of the dispersed phase as expressed in the equation

$$D/D_0 = 1 - \alpha_d \phi \tag{2}$$

The slope, S, of the plot of Figure 2 is numerically equal to the coefficient α_d of eq 2; this can be shown if the substitution $\phi = (1 - f_v)$ is made and series expansions of the logarithmic functions carried out in the limit of high water content. The coefficient α_d of eq 2 is 1.5 for spherical particles and is larger for various ellipsoids of revolution. Thus while one expects a straight line relationship of the type shown in Figure 2, one might consider it surprising that the equivalent logarithmic relationship holds over the large water content range studied. Further, since the observed value of S is larger than 1.5, the polymers clearly do not obstruct as spheres would.

An equation similar to eq 2, the Einstein equation

$$\eta/\eta_0 = 1 + \alpha_\eta \phi \tag{3}$$

describes the change in viscosity with volume fraction of solids of dilute suspensions. In logarithmic form this would be $\log \eta/\eta_0 = -\alpha_\eta \log f_v$. The value of the coefficient α_η, like α_d, depends on the shape of the macromolecule in the system. Generally, the value of α_η is larger than the value of α_d. For spheres $\alpha_\eta = 2.5$; for ellipsoids of revolution (prolate and oblate) α_η is substantially larger than for spheres.[18] Combining eq 2 and 3 one expects the ratio $D\eta/D_0\eta_0$ to vary with ϕ in the following manner:

$$D\eta/D_0\eta_0 = 1 + (\alpha_\eta - \alpha_d)\phi - \alpha_\eta \alpha_d \phi^2 \tag{4}$$

In the water content range where both $\log D$ and $\log \eta$ vary linearly with $\log f_v$

$$\log \frac{D\eta}{D_0 \eta_0} = -(\alpha_\eta - \alpha_d) \log f_v \tag{5}$$

Invariance of $D\eta$ with composition ("Walden's rule") is then equivalent to $(\alpha_\eta - \alpha_d) = 0$. This, however, is not expected to occur even if the obstructing particles are spheres, where $(\alpha_\eta - \alpha_d) = 1.0$. For ellipsoids of revolution $(\alpha_\eta - \alpha_d) > 1$, such as in our case where $(\alpha_\eta - \alpha_d) \simeq 20$, Walden's rule is not obeyed and the diffusion coefficient is strongly dependent on viscosity.

For describing conductivities of suspensions, Fricke[19] computed values of α_d for prolate and oblate ellipsoids of revolution; a similar computation for self-diffusion coefficients of small ions in the presence of macromolecules was carried out by Wang.[20] The coefficients are numerically equal for these systems.

While linear equations of the type of eq 2 and the more elaborate equation of Fricke apply principally to dilute suspensions, equations have been developed for conductance in heterogeneous systems with very much higher volume fractions of the dispersed phase by Bruggeman[21] and more recently by Meredith.[17b] These equations when evaluated at zero conductance of the dispersed phase imply that the relative conductivity (and presumably also the relative diffusion coefficient) varies with the volume fraction of the continuous phase raised to an appropriate power. We shall consider eq 23 of ref 17b which for our case may be written as

$$(1 - \phi) = f_v = K_m{}^a = (D/D_0)^a \tag{6}$$

or

$$\log D/D_0 = (1/a) \log f_v \tag{7}$$

where K_m is the conductance ratio defined by Meredith and Tobias (MT). Equation 7 is formally the same as our empirical 1. The (form-sensitive) slope $a = 1/S$ is given by $a = (1 + \beta + \gamma)$, where β and γ are numerical coefficients, defined and tabulated by MT, which are obtained from integrals whose values depend on the axial ratios of the ellipsoids of revolution which are models for the dispersed phase. Using their values of β and γ and our observed value of the slope $S = 3.3$, one concludes that the polymer solutions of Figure 2 behave from the point of self-diffusion of small ions as assemblies of oblate ellipsoids of revolution with axial ratios somewhat smaller than 0.1.

References and Notes

(1) Research jointly sponsored by the Office of Saline Water, U.S. Department of the Interior, and the U.S. Atomic Energy Commission under contract with the Union Carbide Corporation.
(2) Previous paper in series: W. H. Baldwin, R. J. Raridon, and K. A. Kraus, *J. Phys. Chem.* **73**, 3417 (1969).
(3) (a) Present address: EBASCO, New York, N.Y. (b) Present address: Union Carbide Corp., South Charleston, W.Va. (c) Visiting scientist from Weizmann Institute of Science, Israel. Present address: Israel Desalination Engineering, Tel-Aviv, Israel.
(4) A. E. Marcinkowsky, H. O. Phillips, and K. A. Kraus, *J. Phys. Chem.*, **72**, 1201 (1968).
(5) T. Matsumoto, *Koleunshi Kagaku*, **13**, 86 (1956).
(6) E. Edelson and R. M. Fuoss, *J. Am. Chem. Soc.*, **72**, 306 (1950).
(7) S. Hoshino and K. Sato, *Kagaku Kogaku*, **31**, 961 (1967).
(8) Y. Nishijima and G. Oster, *J. Polym. Sci.*, **19**, 337 (1956).
(9) A. Biancheria and G. Kegeles, *J. Am. Chem. Soc.*, **79**, 5908 (1957).
(10) G. Astarita, *Ind. Eng. Chem., Fundam.*, **4**, 236 (1965).
(11) S. B. Clough, H. E. Read, A. B. Metzner, and V. C. Behn, *AIChE J.*, **8**, 347 (1962).
(12) A. E. Marcinkowsky, F. Nelson, and K. A. Kraus, *J. Phys. Chem.*, **69**, 303 (1965).
(13) A. E. Marcinkowsky, H. O. Phillips, and K. A. Kraus, *J. Phys. Chem.*, **69**, 3968 (1965).
(14) F. E. Bailey, Jr., and J. V. Koleske, "Surfactant Science Series", Vol. I, "Nonionic Surfactants", M. J. Schick, Ed., Marcel Dekker,

New York, N.Y., 1967, Chapter 23, p 794.
(15) We thank Mr. John Csurny for making these viscosity and density measurements.
(16) R. H. Stokes and I. A. Weeks, *Aust. J. Chem.*, **17**, 304 (1964).
(17) See, for example, (a) R. H. Stokes and R. Mills, "Viscosity of Electrolytes and Related Properties", Vol. 3, Topic 16 of "The International Encyclopedia of Physical Chemistry and Chemical Physics", Pergamon Press, New York, N.Y., 1965. (b) R. E. Meredith and C. W. Tobias, "Advances in Electrochemistry and Electrochemical Engineering", Vol. 2, Interscience, New York, N.Y., 1962, p 15.
(18) R. Simha, *J. Phys. Chem.*, **44**, 25 (1940).
(19) H. Fricke, *Phy. Rev.*, **24**, 575 (1924).
(20) J. H. Wang, *J. Am. Chem. Soc.*, **76**, 4755 (1954).
(21) D. A. G. Bruggeman, *Ann. Phys.*, **24**, 636 (1935).

Properties of Organic–Water Mixtures. 13. Self-Diffusion Coefficients of Na^+ in Glycerol Triacetate–Water Mixtures[1,2]

Harold O. Phillips,[3] Arthur J. Shor, Arthur E. Marcinkowsky,[4] and Kurt A. Kraus*

Chemistry Division, Oak Ridge National Laboratory, Oak Ridge, Tennessee *(Received November 9, 1976)*

Publication costs assisted by the U.S. Energy Research and Development Administration

Self-diffusion coefficients, D, of Na^+ in water solutions of glycerol triacetate (GTA) were obtained at 25 °C as a function of water fraction, f_v, and sodium perchlorate concentration. The latter was used to produce miscibility of water and GTA over the composition range studied. At constant $NaClO_4$ concentration, D decreases rapidly with water content, qualitatively as expected from the viscosity of the solutions. A plot of log D vs. log f_v is essentially linear, with a slope of 1.5. The diffusion coefficient–viscosity products are not quite constant but have a shallow maximum near $f_v = 0.5$. At constant organic volume fraction of 0.97, an increase in $NaClO_4$ concentration causes a large increase in the viscosity of the solutions and a somewhat smaller increase in diffusion coefficients.

Our earlier thermodynamic studies of glycerol triacetate (GTA)–water mixtures[5] were carried out because we believe that this system, as well as similar ones, are reasonable models for the thermodynamic (equilibrium) properties of cellulose acetate membranes. While one would not expect a water–organic mixture containing a low molecular weight organic compound to be a good kinetic model for a membrane, it seemed nevertheless of interest to examine the diffusional properties of the GTA–water system and, perhaps, even to establish how large the difference between it and a membrane system is.

GTA and water are not miscible in all proportions. This immiscibility makes it impossible to examine the diffusion properties over a broad composition range. Since GTA and water can be made miscible in all proportions through addition of modest quantities of certain salts,[6] we elected to make most of our measurements in GTA–water mixtures containing 1.4 M of $NaClO_4$ (moles per liter of the GTA–H_2O solvent). Since sodium perchlorate has a significant effect on the viscosity of these systems, we have also carried out some measurements as a function of $NaClO_4$ concentration in GTA solutions of very low water content.

Experimental Section

Method. The radiometric porous frit method which was used for measuring the self-diffusion coefficients has been previously described.[7]

Briefly, the method consists of saturating a porous frit with the solution of interest containing a radioactive isotope of the ion of interest and measuring the rate of removal of the radioisotope as a solution of identical composition (not containing the tracer) is pumped past it. The diffusion coefficients can then be calculated from the diffusional decay half-times obtained in a flow regime where the measured half-times of removal are essentially independent of flow rates past the frit. Corrections for radioactive decay are made when necessary.

TABLE I: Self-Diffusion Coefficients of Na^+ in Glycerol Triacetate-Water-$NaClO_4$ Mixtures at 25 °C (1.4 M $NaClO_4$)

Volume fraction H_2O (f_v)	η/η_0[b]	10^5D, cm²/s	$D\eta/D_0\eta_0$
0.934[a]	1.00	1.26	1.00
0.844	1.61	1.03	1.32
0.721	2.38	0.756	1.43
0.469	4.94	0.415	1.63
0.291	10.3	0.196	1.60
0.148	25.3	0.074	1.49
0.045	111.6	0.016	1.42

[a] No GTA. [b] η = 0.952 cP for 1.4 M $NaClO_4$ solution.

Porous gold frits with about 45% void volume were used and calibrated as described earlier.[8,9] In separate experiments, it was shown that the gold frit did not adsorb sodium ions significantly from the GTA–water mixtures. The temperature of the measurements was 25 ± 0.1 °C, except for the more viscous solutions where variations were ±0.2 °C.

Materials. The tracer ^{24}Na ($T_{1/2}$ = 15.05 h) was obtained from the Isotopes Division of ORNL and used without further purification since examination of the γ-energy spectra showed no detectable impurities. Use of the tracer was discontinued after several half-lives as a precaution against significant relative buildup of possible long-lived contaminants.

The solutions were prepared from reagent grade $NaClO_4$ and Eastman Kodak glycerol triacetate. Each solution was checked for water content by Karl Fischer titration. Viscosities were measured by standard techniques (Cannon–Ubbelohde viscometer).

Results and Discussion

The self-diffusion coefficients of Na^+ were measured in GTA–H_2O solutions as a function of solution composition.

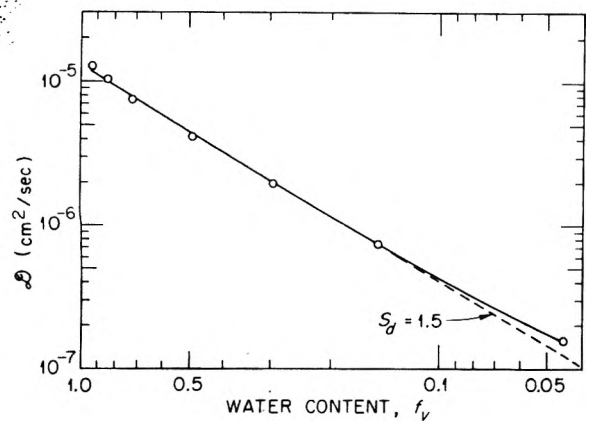

Figure 1. Self-diffusion coefficients of Na^+ in GTA–H_2O mixtures (1.4 M $NaClO_4$, 25 °C).

The salt concentration ($NaClO_4$) was 1.4 M in each solution to ensure miscibility. The effect of water content, expressed as volume fraction f_v, on self-diffusion coefficients, D, of Na^+ in GTA–water–$NaClO_4$ mixtures at constant salt concentration is given in Table I. The values of D decrease from 1.26×10^{-5} cm^2/s in the 1.4 M salt solution (no GTA) to 1.6×10^{-7} cm^2/s in a 95.5% GTA. A plot of log D vs. log f_v (Figure 1) is approximately a straight line over most of the composition range with slope $S_d \approx 1.5$. This slope is very much smaller than the one we observed for the diffusion of sodium ions in polyethylene glycol–water mixtures[10] where S_d was approximately 3.3. This is not surprising since, in the latter case, the organic solute can almost surely be considered an obstruction with a highly nonspherical shape (presumably an oblate elipsoid of revolution). The slope is also very much less than we observed[11] in a number of membranes and porous bodies where S_d was about 4.6.

In an earlier paper[10] we had shown that the log–log slope, S_d, is numerically equal to the coefficient α_d in the linear equation

$$D/D_0 = 1 - \alpha_d\phi$$

where the "solid" fraction is $\phi = (1 - f_v)$ and D_0 is the diffusion coefficient at $\phi = 0$. With spherical "obstructions" α_d is expected to be 1.5;[12] our experimental value of S_d thus implies that for Na^+ diffusion GTA acts similar to a "dispersion" of spherical obstructions.

The relative viscosity, η/η_0 (η_0 is viscosity of aqueous 1.4 M $NaClO_4$), increases from 1.00 in the aqueous salt solution to 112 in 95.5% GTA. A plot of the logarithm of the relative viscosity vs. log f_v has considerable curvature at high water contents with slope S_η much larger than 1.5. The plot eventually becomes a straight line with slope S_η near 1.5. As a result, the relative diffusion–viscosity product $D\eta/D_0\eta_0$ is not quite independent of solution composition but goes through a shallow maximum near $f_v = 0.5$. The fact that the absolute value of S_η is initially much larger than S_d is qualitatively consistent with theory;

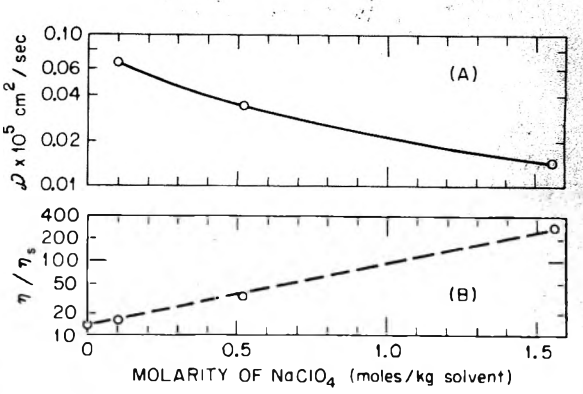

Figure 2. (A) Self-diffusion coefficients of Na^+ and (B) relative viscosity for ca. 95 vol % GTA.

thus, α_η in the (linear) Einstein equation ($\eta/\eta_0 = 1 + \alpha_\eta\phi$) for spherical obstructions is 2.5.

Sodium perchlorate causes a striking increase in the viscosity of GTA solutions and a significant decrease in the self-diffusion coefficient of Na^+. As shown in Figure 2, viscosity (at $f_v = 0.03$) increases by a factor of ca. 20 as the sodium perchlorate concentration increases from 0.1 to 1.6 m; in the same range, D decreases by approximately a factor of 5. While the logarithm of the viscosity increases approximately linearly with molality of $NaClO_4$, the equivalent diffusion coefficient relationship has some curvature. As a result log ($D\eta$) increases (nonlinearly) with sodium perchlorate concentration. We report these observations here, although we do not have an explanation.

References and Notes

(1) Jointly sponsored by the Office of Saline Water, U.S. Department of the Interior, and the U.S. Energy Research and Development Administration under contract with Union Carbide Corporation.
(2) Previous paper in series: R. J. Raridon and K. A. Kraus, *J. Chem. Eng. Data*, **16**, 241 (1971).
(3) Present address: EBASCO, New York, N.Y.
(4) Present address: Union Carbide Corp., South Charleston, W.Va.
(5) See, e.g., (a) K. A. Kraus, R. J. Raridon, and W. H. Baldwin, *J. Am. Chem. Soc.*, **86**, 2571 (1964); (b) J. S. Johnson, L. Dresner, and K. A. Kraus, "Hyperfiltration (Reverse Osmosis)" in "Principles of Desalination", K. S. Spiegler, Ed., Academic Press, New York, N.Y., 1966, p 395.
(6) R. J. Raridon and K. A. Kraus, *J. Colloid. Sci.*, **20**, 1000 (1965).
(7) (a) F. Nelson and K. A. Kraus, "Some Techniques for Isolating and Using Short-Lived Radioisotopes" in "Production and Use of Short-Lived Isotopes from Reactors", Vol. I, IAEA, Vienna, 1962, p 191. (b) A. E. Marcinkowsky, F. Nelson, and K. A. Kraus, *J. Phys. Chem.*, **69** 303 (1965).
(8) A. E. Marcinkowsky, H. O. Phillips, and K. A. Kraus, *J. Phys. Chem.*, **69** 3968 (1965).
(9) A. E. Marcinkowsky, H. O. Phillips, and K. A. Kraus, *J. Phys. Chem.*, **72**, 1201 (1968).
(10) H. O. Phillips, A. E. Marcinkowsky, S. B. Sachs, and K. A. Kraus, *J. Phys. Chem.*, preceding paper in this issue.
(11) K. A. Kraus, H. O. Phillips, and A. E. Marcinkowsky, "Saline Water Conversion Report for 1965", U. S. Department of the Interior, Office of Saline Water, p 24 and unpublished results.
(12) See, e.g., (a) R. H. Stokes, "Mobilities of Ions and Uncharged Molecules in Relation to Viscosity—A Classical Viewpoint", in "The Structure of Electrolytic Solutions", W. J. Hamer, Ed., Wiley, New York, N.Y., 1959, p 293. (b) J. H. Wang, *J. Am. Chem. Soc.*, **76**, 4755 (1954).

COMMUNICATIONS TO THE EDITOR

The Reaction of Chlorine Atoms with Acetylene and Its Possible Stratospheric Significance

Publication costs assisted by the U.S. Energy Research and Development Administration

Sir: The only hydrocarbon considered to have major importance in current models of stratospheric chlorine chemistry is methane,[1,2] which acts as the primary reactant for conversion of Cl to HCl, as in (1). Since the tro-

$$Cl + CH_4 \rightarrow HCl + CH_3 \quad (1)$$

pospheric mixing ratio of CH_4 is about 1.5×10^{-6}, and at stratospheric temperatures reaction occurs for about 1 collision in 10^4 of Cl with CH_4,[3] possible chlorine atom reactions with other species should be considered for any hydrocarbon present in 10^{-10} or larger mixing ratio. We consider here the reactions of chlorine atoms with acetylene, which has been tentatively identified at the $2–7 \times 10^{-10}$ level between 15–21 km altitude, with the concentration decreasing with increasing altitude.[4] The reaction rate for atomic chlorine with acetylene has apparently not previously been discussed in the scientific literature.

The abstraction reaction (2), analogous to (1), cannot

$$Cl + C_2H_2 \rightarrow HCl + C_2H \quad (2)$$

occur because the extremely strong C–H bond in acetylene makes the reaction endothermic by about 9 kcal/mol.[5] Consequently, the only important reaction path available for atomic Cl with acetylene is addition, as shown in (3).

$$Cl + C_2H_2 \rightarrow CHCl{=}\dot{C}H^* \quad (3)$$

The excited $C_2H_2Cl^*$ radical can then undergo either stabilization or decomposition in (4) or (5), the latter

$$CHCl{=}\dot{C}H^* + M \rightarrow CHCl{=}\dot{C}H + M \quad (4)$$

$$CHCl{=}\dot{C}H^* \rightarrow C_2H_2 + Cl \quad (5)$$

releasing the free Cl atom again.[6] No information is available about the fate of a stabilized C_2H_2Cl radical from (4), but probably the radical would react with O_2 and lead eventually to the formation of a chlorine-containing oxy–carbon compound. A previous study of C_2H_2Cl reactions was carried out in the absence of any specific scavenger molecule and consequently was very much concerned with the polymerization products resulting from C_2H_2Cl reaction with acetylene itself.[7]

We have measured the relative rates of (4) and (5) in a system containing $CClF_3$ as the inert molecule, M, with HI present as a scavenger for the stabilized C_2H_2Cl radical, as in (6). The inclusion of HI in the system necessarily

$$CHCl{=}\dot{C}H + HI \rightarrow CHCl{=}CH_2 + I \quad (6)$$

permits the direct reaction of Cl with HI, as in (7). All

$$Cl + HI \rightarrow HCl + I \quad (7)$$

of our experiments have utilized radioactive ^{38}Cl atoms formed by the thermal neutron reaction, $^{37}Cl(n,\gamma)^{38}Cl$. The $CClF_3$ thus serves as the nuclear target, and then as a moderator to remove the excess kinetic energy of the initially "hot" ^{38}Cl atom before reactions 3 or 7 occur.[8]

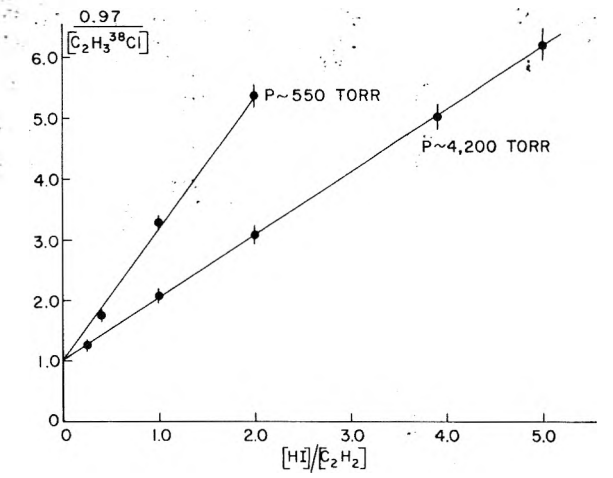

Figure 1. Reciprocal yields of $C_2H_3{}^{38}Cl$ for ^{38}Cl reactions in mixtures of C_2H_2 and HI. (See footnote 9 for explanation of 0.97 in the numerator.)

The key measurement in this system is the yield of $C_2H_3{}^{38}Cl$ from the sequence (3), (4), and (6), as a function of HI concentration. The slope of a plot of reciprocal $C_2H_3{}^{38}Cl$ yield vs. HI/C_2H_2 ratio is a measure of the relative rates of reactions 3 and 7.[9] However, if reaction 3 is followed by (5), the ^{38}Cl is not permanently removed from the system and will once more undergo competition between (3) and (7). This apparent "inefficiency" of reaction 3 in removing ^{38}Cl can be experimentally detected by carrying out the experiments at widely differing pressures, as shown in Figure 1. The two sets of data are consistent with $k_7/k_3 = 0.86 \pm 0.08$ and $P_{1/2}$ (pressure of half stabilization, i.e., $k_4M = k_5$) $= 840 \pm 80$ Torr of $CClF_3$, as shown by the calculated lines of Figure 1.[10] The intercept at 1.0 confirms that reaction 2 is not observed.

Reaction 7 is very fast, with a reaction rate estimated as 10^{-10} cm^3 molecule^{-1} s^{-1}, and the initial addition reaction 3 must therefore also have a rate coefficient that corresponds to addition in not more than 2–5 collisions. If the stratospheric mixing ratio of C_2H_2 is indeed 10^{-10}, then the addition of Cl to C_2H_2 should occur at a rate comparable to that of abstraction with CH_4. However, the fraction of $C_2H_2Cl^*$ molecules which are stabilized is then given by the stratospheric density divided by the density at which $k_4M = k_5$. At 30 km, for instance, the density is about 0.01 times that at sea level, and only about 1% of the $C_2H_2Cl^*$ radicals would be stabilized. A more accurate calculation would require the measurement of $P_{1/2}$ for N_2 and O_2 at stratospheric temperatures. The value of k_5 should be less at 210 K by about a factor of 2, while the smaller size of N_2 and O_2 vs. $CClF_3$ may also reduce k_4 by a comparable amount, leaving the room temperature measurements with $CClF_3$ as a reasonable approximation to the actual stratospheric situation.

Accordingly, the overall conversion of Cl to stabilized C_2H_2Cl has a rate constant of roughly 10^{-12} cm^3 molecule^{-1}

s^{-1} at 30 km, and the removal of Cl through reaction with C_2H_2 is very much less important ($\leq$0.01) on a quantitative basis than the conversion of Cl to HCl through reaction 1. Since Cl is cycled through HCl many times, the amount of Cl which can be bound up in acetylenic compounds is also dependent upon the rate of return of Cl (or ClO) to the ozone-removing catalytic chain. The HCl formed from (1) is returned to the catalytic cycle as Cl through reaction

$$OH + HCl \rightarrow Cl + H_2O \qquad (8)$$

8 in a time period of a few days at 30 km. The oxychlorocarbon molecule presumably formed by C_2H_2Cl reaction with O_2 are likely to be both chemically and photochemically reactive and release of Cl or ClO within a still shorter time seems likely. Nevertheless, a minor amount of stratospheric chlorine atoms may be bound into organic form following addition to acetylene, and the subsequent history of these molecules is of some scientific interest.

Acknowledgment. This research was supported by U.S. ERDA Contract No. AT(04-3)-34, P.A. 126.

References and Notes

(1) F. S. Rowland and M. J. Molina, *Rev. Geophys. Space Phys.*, **13**, 1 (1975).
(2) "Halocarbons: Effects on Stratospheric Ozone", Panel on Atmospheric Chemistry, National Academy of Sciences, Sept 1976.
(3) Recent measurements indicate a rate constant of about 2×10^{-14} cm^3 $molecule^{-1}$ s^{-1} at 210 K for reaction 1. See ref 2 or R. T. Watson, *J. Phys. Chem. Ref. Data*, in press. A summary of such measurements is also given in F. S. C. Lee and F. S. Rowland, *J. Phys. Chem.*, **81**, 86 (1977).
(4) P. Hanst, private communication.
(5) With the following heats of formation, the endothermicity is 9 kcal/mol. ΔH_f(298 K, in kcal/mol), as given in JANAF Thermochemical Tables, *Natl. Stand. Ref. Data Ser., Natl. Bur. Stand.*, **No. 37** (1971); C_2H_2, 54.2; HCl, −22.1; Cl, 28.9; C_2H, 114; C_2HCl, 51 ± 10; H, 52.1.
(6) The loss of H from $C_2H_2Cl^*$ is also endothermic by about 20 kcal/mol from the heats of formation in ref 5.
(7) M. H. J. Wijnen, *J. Chem. Phys.*, **36**, 1672 (1962).
(8) F. S. C. Lee, Ph.D. Thesis, University of California, Irvine, 1975.
(9) Approximately 3% of the ^{38}Cl atoms react with $CClF_3$ while still "hot" and are found as $C^{38}ClF_3$, $CCl^{38}ClF_2$, or $CH^{38}ClF_2$ in this system. These correspond, respectively, to the hot substitution reactions of $^{38}Cl/Cl$, $^{38}Cl/F$, and to the HI-scavenged $C^{38}ClF_2$ radical from the decomposition of $CCl^{38}ClF_2$. The data are therefore plotted with 97% of the total ^{38}Cl available for thermal reaction. Details are given in ref 8, and in an article by F. S. C. Lee and F. S. Rowland, *J. Phys. Chem.*, submitted for publication.
(10) If a single collision (i.e., "strong" collision assumption) is sufficient to stabilize C_2H_2Cl in (4), then the fraction of stabilized C_2H_2Cl is given by $[k_4M/(k_4M + k_5)]$, or by its equivalent, $\theta = [P/(P + P_{1/2})]$ in which P is the actual pressure, and $P_{1/2}$ is the pressure for which $k_4M = k_5$. The ratio of rates of formation of HCl from (7) and $C_2H_2Cl^*$ from (3) is $k_7(HI)/k_3(C_2H_2)$ and of HCl and stabilized C_2H_2Cl is $k_7(HI)/k_3\theta(C_2H_2)$. The ratio of total thermal chlorine reacting to that forming stabilized C_2H_2Cl is given by $\{1 + [k_7(HI)/k_3\theta(C_2H_2)]\}$ and the slope of the graph in Figure 1 for pressure P is given by $k_7/k_3\theta$ or $(k_7/k_3)\{1 + (P_{1/2}/P)\}$. The ratio for k_7/k_3 and the value of $P_{1/2}$ are obtained from slopes of 2.17 and 1.03 for 550 and 4200 Torr, respectively.

Department of Chemistry
University of California
Irvine, California 92717

F. S. C. Lee
F. S. Rowland*

Received December 3, 1976

Dielectric Constants of Liquids from Nuclear Magnetic Resonance Phase Control Studies[1]

Sir: Most chemical laboratories are not equipped with specialized apparatus for measuring dielectric constants of liquids. Today, however, many laboratories are equipped with nuclear magnetic resonance (NMR) spectrometers which can be used for such purposes, after minor modification. The dielectric constant of liquid samples can be determined easily and quickly by measuring the phase control adjustment of a high-resolution NMR spectrometer required to produce a pure absorption mode for the proton signal of an external standard. This is possible because the phase of the NMR signal is dependent upon the dielectric constant of a sample placed in the probe region. Because this dependency is a complicated function of the electrical circuitry involved, special calibration techniques were developed.

An external standard was employed for several reasons: (1) to eliminate the need for the sample to provide the proton signal necessary for observation, (2) to eliminate

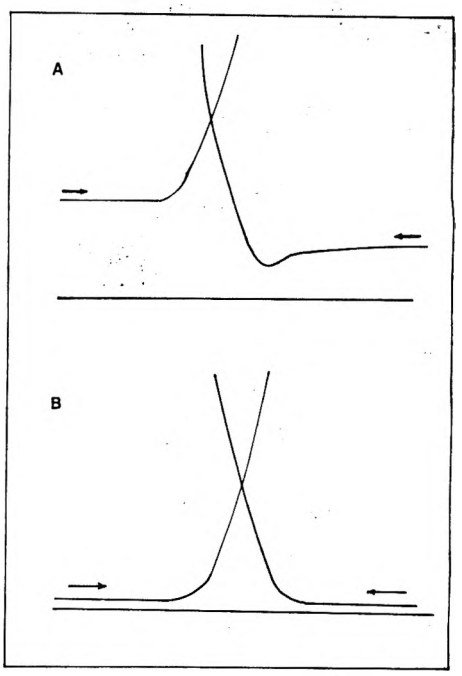

Figure 1. Upfield (→) and downfield (←) traces of high-gain, fast-sweep signal of HMD: (A) signal showing dispersion characteristics; (B) pure absorption mode.

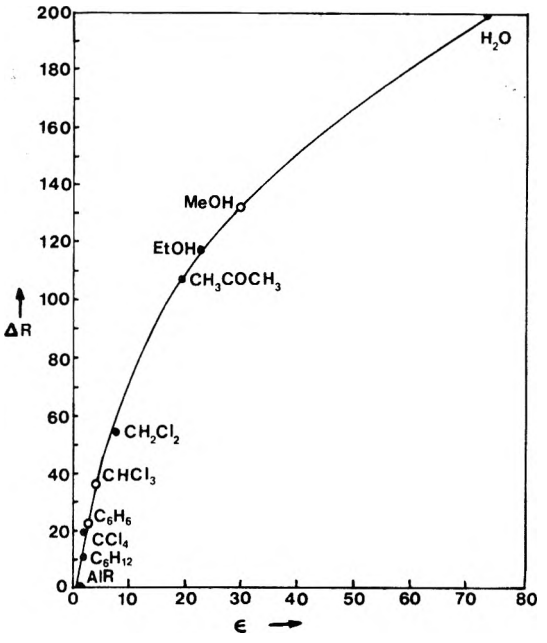

Figure 2. Plot of ΔR as a function of dielectric constant, ϵ: ●, points used for calibration; ○, points used to obtain ϵ for unknowns from NMR phase control data.

TABLE I: Phase Control Readings for Air and Nine Pure Liquids and Reported Dielectric Constants Used for Calibration and Dielectric Constants Obtained from NMR Phase Control Measurements at 39 °C

Sample	R (rf power = 0.05 mG)[c]	ΔR (rf power = 0.05 mG)[c]	ΔR (rf power = 0.03 mG)[c]	ϵ (handbook,[a] 39 °C)	ϵ (from NMR,[b] 39 °C)	% diff
Air	701 ± 1	0	0	1.00[d]		
C_6H_{12}	691 ± 2	10 ± 3		1.99[d]		
CCl_4	682 ± 2	19 ± 3		2.20[d]		
C_6H_6	680 ± 2	21 ± 2		2.25	2.30	2.2
$CHCl_3$	665 ± 1	36 ± 2	33 ± 4	4.48	4.60	2.5
CH_2Cl_2	644 ± 2	57 ± 3		8.40[d]		
CH_3COCH_3	595 ± 2	106 ± 3		19.38[d]		
C_2H_5OH	584 ± 2	117 ± 3		22.27[d]		
CH_3OH	570 ± 1	131 ± 2	130 ± 4	29.97	29.00	3.0
H_2O	500 ± 1	201 ± 2	200 ± 2	73.79[d]		
						Av 2.6

[a] "Handbook of Chemistry and Physics", 54th ed, Chemical Rubber Publishing Co., Cleveland, Ohio. [b] Obtained from calibration chart (Figure 2). [c] Radiofrequency power, in milligauss units, expressed indirectly through linewidth changes on the applied magnetic field axis. [d] Dielectric constants used to obtain calibration chart (Figure 2).

solvent effects which would occur with the use of an internal standard, and (3) to provide a strong signal in order to enhance the accuracy. Hexamethyldisiloxane (HMD), placed in a central 1-mm capillary cell of a 5-mm coaxial cell system, met all of these requirements. The sample under study was placed in the annular region of the coaxial cell.

In order to provide a more precise measurement of the phase reading, the phase control resistor in a Varian A60A NMR spectrometer was replaced with a ten-turn helipot (100 ohm, 2 W).

With air in the annular region ($\epsilon = 1$), the proton signal of HMD was adjusted to give a pure absorption signal. The reading, R_0, of the phase control resistor was recorded. A pure, dry, liquid sample was then placed in the annular region and the phase of the HMD signal was found to have changed, the signal showing dispersion characteristics. The phase control resistor was adjusted to restore the pure absorption mode. High gain was employed in order to provide maximum sensitivity. The baseline near the resonance signal was recorded by rapidly sweeping upfield and then downfield, while the phase control was varied. This was repeated until the upfield and downfield sweeps produced lines which were parallel and equidistant from a horizontal reference line. Figure 1a shows the high-gain fast-sweep trace of an improperly phased signal. Figure 1b shows the same signal after proper phase adjustment. The phase control reading, R, so obtained, was recorded.

Table I shows the data obtained for air and nine pure liquids. Seven liquids, as indicated, were used to generate the calibration curve illustrated in Figure 2. Here ΔR, where $\Delta R = R_0 - R$, is plotted as a function of ϵ, at 39 °C, the temperature at which the NMR experiments were conducted. Although R was found to depend upon the radiofrequency power, ΔR was found to be independent rf power from 0.03 to 0.05 mG (linewidth units) as shown in Table I. Values for ϵ were taken from the literature.

Benzene, chloroform, and methanol were used as unknowns. Their dielectric constants were determined by measuring their ΔR and using the calibration curve. As shown in Table I, the average difference between the NMR determined values and the handbook values was 2.6%. The Varian A60A spectrometer used in this study had a signal-to-noise ratio of only 15 to 1. An improved NMR instrument (such as a Varian EM390 with a signal-to-noise ratio of 50 to 1 or better) should yield considerably more accurate results.

References and Notes

(1) Presented on May 14, 1975, during the Meeting-in-Miniature co-sponsored by the North Jersey and New York Sections of the American Chemical Society and Stevens Institute of Technology, held in Hoboken, N.J.

Department of Chemistry and Chemical Engineering
Stevens Institute of Technology
Hoboken, New Jersey 07030

Edmund R. Malinowski*
Sunil K. Garg

Received November 12, 1976

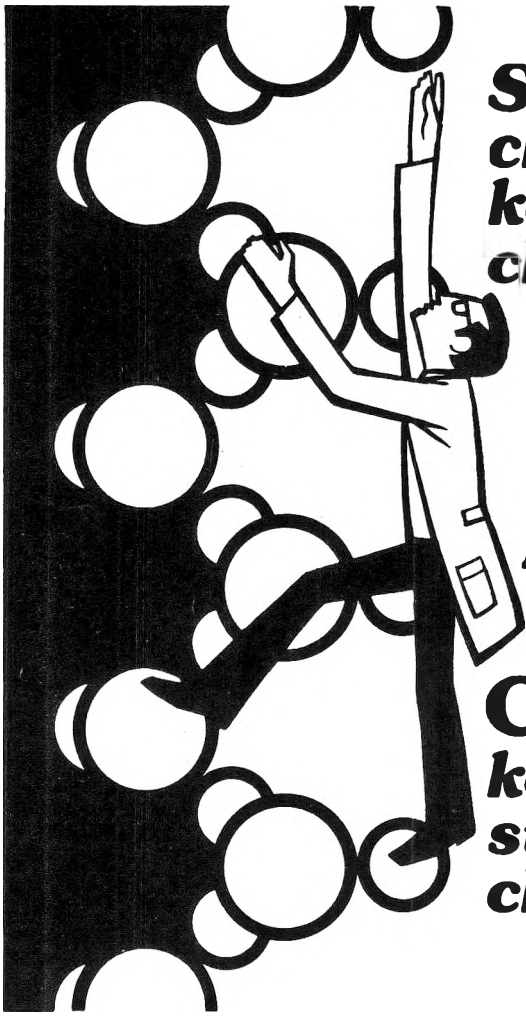

Successful chemists keep up with chemistry

ACS AUDIO COURSES keep up with successful chemists

The best way to keep pace with chemistry's rapid progress is to learn from the chemists who help make it happen.

More than 25 ACS Audio Courses are now available—all prepared and recorded by leading chemists teaching their own specialties. All courses include audiotape cassettes and comprehensive manuals with information, diagrams and other visual material, many with exercises so you can combine the ease of listening with the challenge of doing as you learn.

The courses cover all levels and interests, introductory and refresher topics, specialized subjects and techniques, non-technical courses to aid your personal development.

Best of all, *all ACS Audio Courses are offered on a money-back guarantee basis . . . so you can't lose.*

Send coupon below for more information.

Department of Educational Activities
American Chemical Society
1155 Sixteenth Street, N.W.
Washington, D. C. 20036

Please send information on ACS Audio Courses

Name _____

Organization _____

Address _____

City _____

State _____ Zip _____

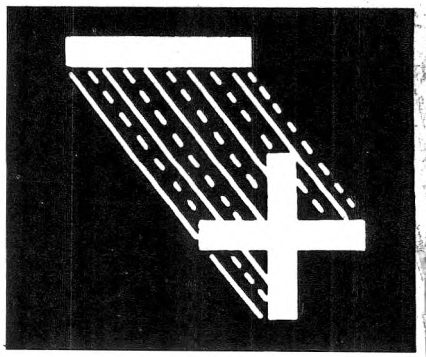

Magnetic Resonance in Colloid and Interface Science

ACS Symposium Series No. 34

Henry A. Resing and Charles G. Wade, *Editors*

A symposium sponsored by the Divisions of Colloid and Surface Chemistry, Physical Chemistry, and Petroleum Chemistry of the American Chemical Society.

This comprehensive collection represents the most current interdisciplinary and international presentation of the state of the science today. It is the first book of its kind to integrate magnetic resonance techniques used in biological systems and inorganic systems of catalytic interest.

Forty-two papers span the range from anisotropy, gas-solid adsorption systems, and surface kinetics to studies of aqueous macromolecular systems, and work with living systems.

Such systems of surface chemical interest and commercial importance as oil shale, cracking catalysts, polymer composites, biological macromolecules, liquid crystals, and surface colloids are covered.

Reports of nuclear, quadrupole, electron paramagnetic resonance, and Mössbauer studies are presented with a proper mix of theory and experiment. All experimental systems in which molecules or ions are bound to interfacial structures or within colloidal systems are included.

541 pages (1976) clothbound $25.50
LC 76-44442 ISBN 0-8412-0342-3

SIS/American Chemical Society
1155 16th St., N.W./Wash., D.C. 20036

Please send _____ copies of *SS 34 Magnetic Resonance in Colloid and Interface Science* at $25.50 per copy.

☐ Check enclosed for $ _____. ☐ Bill me.
Postage at 40 cents per copy if other than U.S. or Canada.

Name _____

Address _____

City _____ State _____ Zip _____

Introduction to the Electron Theory of Small Molecules

By A. C. HURLEY

From the Preface:

This introduction consists of the earlier and simpler chapters of what was originally conceived as a comprehensive one-volume work on the electron theory of small molecules . . . . My primary objective is to provide a "royal road" from basic quantum mechanics, as exemplified by Schrödinger's wave equation and elementary atomic structure to the various theories and techniques of calculation which today are yielding such detailed information on molecular interactions. With this object in mind the simplest available mathematical method is used at each stage in the development; for example, Hartree-Fock theory is developed in terms of Slater determinants rather than density matrices. When unavoidable complications are encountered, as in the explicit reduction of the Hartree-Fock equations for open shell states, the text expanded to assist the mathematically unsophisticated reader

1977, 340 pp., $26.25/£12.00 ISBN: 0-12-362460-6

Electron Correlation in Small Molecules

By A. C. HURLEY

A Volume in the THEORETICAL CHEMISTRY Series

This monograph gives a systematic account of pair theories and other approaches to the correlation problem, starting from molecular Hartree-Fock theory and correlation theory for two-electron systems. Of the two chapters, the first is devoted to the correction of qualitative errors of the Hartree-Fock approximation which arise in cases of degeneracy or near degeneracy and which vitiate any attempt to use traditional Hartree-Fock theory to follow dissociative processes and chemical reactions. The elimination of quantitative errors is the subject of the second chapter. Here the emphasis is on the series of pair theories and their implementation using pair natural orbitals: these appear to provide the most efficient solution available to the correlation problem, but other procedures employing interelectronic coordinates, transcorrelated wavefunctions or overall natural orbitals are also described.

1977, 288 pp., $23.00/£10.50 ISBN: 0-12-362450-9

Dispersion Forces

By J. MAHANTY and B. W. NINHAM

Colloid Science: A Series of Monographs No. 1
Series Editors: R. H. Ottewill and R. L. Rowell

The material in this book ranges from the fundamental level to the investigation of the interaction between colloidal particles of different shapes and to aspects of surface chemistry and physics in which dispersion forces play a role. Starting with a discussion of dispersion forces in the historical context, the various approaches to interactions between microscopic and macroscopic bodies are considered within a single unified semiclassical framework which emphasizes the role of the radiation field, and the connection between surface and interaction energies.

1977, 236 pp., $20.10/£9.20 ISBN: 0-12-465050-3

Send payment with order and save postage plus 50¢ handling charge.
Prices are subject to change without notice.

ACADEMIC PRESS
A Subsidiary of Harcourt Brace Jovanovich, Publishers
111 FIFTH AVENUE, NEW YORK, N.Y. 10003
24–28 OVAL ROAD, LONDON NW1 7DX

Please send me the following:
____copies, Hurley: *Introduction to the Electron Theory of Small Molecules*
____copies, Hurley: *Electron Correlation in Small Molecules*
____copies, Mahanty/Ninham: *Dispersion Forces*
Check enclosed ____ Bill me ____

Name _____

Address _____

City/State/ZIP _____

New York residents please add sales tax.
Direct all orders to Mr. Paul Negri, Media Dept. *JPhyCH/4/77*

SCIENCE SYMPOSIA— ON TAPE

- ☐ **Technology in the Energy Crisis** — Improving chances for self-sufficiency
- ☐ **Coal: Nature's Black Diamond** — America's biggest energy resource
- ☐ **Unusual Fuels Production** — Methanol, ethanol, ammonia
- ☐ **Oil from Shale** — The potential is huge
- ☐ **Interferon** — Powerful new weapon against disease
- ☐ **Drugs from the Cannabinoid Nucleus** — Exciting source of new drugs
- ☐ **Another Side of Marijuana Research** — Exclusive roundtable discussion
- ☐ **Drugs Affecting Learning & Memory** — An exciting area of drug research
- ☐ **New Solid Waste Disposal Processes** — New processes ready to go commercial
- ☐ **Nutrition & U.S. Public Policy—The Issues** — Experts discuss a problem of growing concern

PRICES

	ACS Members	Nonmembers
Cassettes Only	$15.00/title	$18.00/title

(Price includes printed copies of slides used)

10% Discount if payment accompanies order

Name _____

Address _____

_____

Order From: American Chemical Society, 1155 16th St., N.W. Washington, D.C. 20036, ATTN: Dept. AP

(allow 4 to 6 weeks for delivery)

Isotopes and Chemical Principles

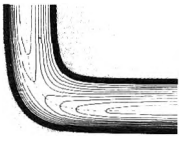

ACS Symposium Series No. 11

Peter A. Rock, *Editor*

A symposium sponsored by the Division of Chemical Education of the American Chemical Society.

Order from:
Special Issues Sales
American Chemical Society
1155 Sixteenth St., N.W.
Washington, D.C. 20036

Here is a unique book on isotopes which can be used by undergraduate chemistry teachers in their discussions of chemical principles, as well as by graduate and professional chemists.

Nine papers examine the fundamental principles of isotope chemistry and its development in connection with quantum chemistry and statistical mechanics. Also covered are various aspects of the physical and theoretical bases of isotope effects including:

- isotope separation processes; quantum-mechanical tunneling
- corrections to the Born-Oppenheimer approximation
- reaction mechanisms; isotope biology; equilibrium constants for isotope-exchange reactions

215 pages (1975) $15.95 clothbound (ISBN 0-8412-0225-7). Postpaid in U.S. and Canada, plus 40 cents elsewhere.